Iowa Research Online
The University of Iowa's Institutional Repository

University of Iowa
Iowa Research Online

Theses and Dissertations

Fall 2015

Understanding and controlling vorticity transport in unsteady, separated flows

James Akkala
University of Iowa

Follow this and additional works at: https://ir.uiowa.edu/etd

 Part of the Mechanical Engineering Commons

Copyright © 2015 James Akkala

This dissertation is available at Iowa Research Online: https://ir.uiowa.edu/etd/1947

Recommended Citation
Akkala, James. "Understanding and controlling vorticity transport in unsteady, separated flows." PhD (Doctor of Philosophy) thesis, University of Iowa, 2015.
https://doi.org/10.17077/etd.8t9jvlnt

Follow this and additional works at: https://ir.uiowa.edu/etd

 Part of the Mechanical Engineering Commons

www.manaraa.com

UNDERSTANDING AND CONTROLLING VORTICITY TRANSPORT IN UNSTEADY, SEPARATED FLOWS

by

James Akkala

A thesis submitted in partial fulfillment of the
requirements for the Doctor of Philosophy
degree in Mechanical Engineering
in the Graduate College of
The University of Iowa

December 2015

Thesis Supervisor: James H. J. Buchholz

www.manaraa.com

Graduate College
The University of Iowa
Iowa City, Iowa

CERTIFICATE OF APPROVAL

PH.D. THESIS

This is to certify that the Ph.D. thesis of

James Akkala

has been approved by the Examining Committee for the thesis requirement for the Doctor of Philosophy degree in Mechanical Engineering at the December 2015 graduation.

Thesis Committee: _____
James H. J. Buchholz, Thesis Supervisor

_____
Christoph Beckermann

_____
Donald Gurnett

_____
Ching-long Lin

_____
Frederick Stern

www.manaraa.com

ACKNOWLEDGEMENTS

I would like to begin by thanking Professor James Buchholz for the tremendous encouragement, guidance and support that he has provided to me throughout this endeavor. Without his inspiration, optimism and confidence in my abilities, this work could not have been accomplished. I would also like to thank him for affording me the privilege of participating in the Air Force Summer Faculty Fellowship Program and for giving me the opportunity to present my work at several conferences.

I would also like to thank my esteemed committee members, Prof. Christoph Beckermann, Prof. Donald Gurnett, Prof. Ching-Long Lin and Prof. Frederick Stern for their valuable time and insightful discussion. My sincere thanks also extends to my close friend Katie Radtke for generously serving as my thesis reader and providing invaluable feedback for improving the quality of this work.

It has been my pleasure to work with an amazing research team at the University of Iowa. Azar Eslam Panah, Kevin Wabick and Craig Wojcik, in particular, have been outstanding co-collaborators and I am fortunate to have had the chance to work with them.

Last but not least, I want to thank my parents for their steadfast support in all that I do, as well as my friends at the University of Iowa for providing me with some of the best times of my life.

This work was supported in part by the Air Force Office of Scientific Research, award number FA9550-11-1-0019, and by IIHR-Hydroscience & Engineering.

www.manaraa.com

ABSTRACT

Vortices interacting with the solid surface of aerodynamic bodies are prevalent across a broad range of geometries and applications, such as dynamic stall on wind turbine and helicopter rotors, the separated flows over flapping wings of insects, birds and micro-air vehicles, formation of the vortex wakes of bluff bodies, and the lift-producing vortices formed by aircraft leading-edge extensions and delta wings. This study provides fundamental insights into the formation and evolution of such vortices by considering the leading-edge vortices formed in variations of a canonical flapping wing problem.

Specifically, the vorticity transport within three distinct experimental cases–2D plunging airfoil, 3D plunging airfoil and 2D plunging airfoil with suction applied at the leading edge–were analyzed in order to characterize the formation and evolution of the leading-edge vortex (LEV).

Three-dimensional representations of the velocity and vorticity fields were obtained via multi-plane particle image velocimetry (PIV) measurements and used to perform a vorticity flux analysis that served to identify the sources and sinks of vorticity within the flow. Time-resolved pressure measurements were obtained from the surface of the airfoil and used to characterize the flux of vorticity diffusing from the solid surface, and a method for correcting dynamic pressure data was developed and validated for the application within the current study.

Upon characterizing all of the sources and sinks of vorticity, the circulation budget was found to be fully accounted for. Interpretation of the individual vorticity balance terms

www.manaraa.com

demonstrated vorticity generation and transport characteristics that were consistent among all three cases that were investigated. Three-dimensional vorticity fluxes were found to be an almost negligible contributor to the overall circulation budget, mostly due to the individual terms canceling each other out. In all cases, the diffusive flux of vorticity from the surface of the airfoil was shown to act primarily as a sink of LEV vorticity, with a magnitude roughly half that of the flux of vorticity emanating from the leading-edge shear layer.

Inspection of the chordwise distribution of the diffusive flux within the 2D case showed it to correlate very well with the evolution of the flow field. Specifically, the diffusive flux experienced a major increase during the phase interval in which the LEV remained attached to the downstream boundary layer. It was also noted that the accumulation of secondary vorticity near the leading edge prevented the diffusive flux from continuing to increase after the roll-up of the LEV. This result was validated within the 3D case, which demonstrated that maintaining an LEV that stays attached to the downstream boundary layer produces a larger diffusive flux of vorticity–presumably enhancing both lift and thrust.

Through the use of a spanwise array of suction ports, the suction case was able to successfully alter the total circulation of the flow by removing positive vorticity from the opposite-signed vortex (OSV) that formed beneath the LEV. This removal of positive vorticity produced a measured increase in the total lift, and it was noted that weakening this region of secondary vorticity allowed the LEV to impose more suction on the surface of the airfoil. However, it was also noted that weakening the OSV resulted in a loss of thrust,

www.manaraa.com

which was attributed to the loss of suction that occurred near the leading edge when the removal of secondary vorticity caused the energetic OSV to be reverted into a low energy region of separated flow.

The physical insights provided by this work can form the basis of novel flow control strategies for enhancing the aerodynamic loads produced in unsteady, separated flows.

www.manaraa.com

PUBLIC ABSTRACT

The interaction between vortices and the solid surface of an aerodynamic body is a ubiquitous feature of high-angle-of-attack aerodynamics associated with a broad range of aerospace structures, including maneuvering and flapping wings, blades on helicopter rotors and gas turbine engines, the aerodynamic forebodes of missiles and high-performance aircraft. This study provides fundamental insights into the development of such vortices by considering the vortex formed at the leading edge of a plunging airfoil.

The primary goal of this work was to rigorously characterize the formation and evolution of the leading-edge vortex (LEV) based on the transport of vorticity both within the bulk flow as well as near the surface of the airfoil. By performing a novel analysis that served to quantify the near-wall dynamics of the flow, this study demonstrated that the strength of the LEV was significantly reduced by its interaction with the solid surface. It was further shown that the near-wall vorticity transport mechanisms associated with this reduction also play a critical role in governing the formation and development of the LEV prior to its detachment.

By explicitly characterizing how the vortex-airfoil interaction affects the evolution of the LEV, the results of this study have significantly enhanced our understanding of why the LEV develops the way it does. The physical insights provided by this work can form the basis of novel flow control strategies for enhancing the aerodynamic loads produced in unsteady, separated flows.

www.manaraa.com

TABLE OF CONTENTS

www.manaraa.com

www.manaraa.com

www.manaraa.com

LIST OF TABLES

Table

www.manaraa.com

LIST OF FIGURES

Figure

www.manaraa.com

www.manaraa.com

www.manaraa.com

www.manaraa.com

www.manaraa.com

www.manaraa.com

www.manaraa.com

www.manaraa.com

NOMENCLATURE

$A = 2h_0$	Peak-to-Peak Plunge Amplitude, m
APG	Adverse Pressure Gradient
AR	Aspect-Ratio
BVF	Boundary Vorticity Flux
c	Chord Length, m
$C_p = \frac{p - p_\infty}{0.5\rho U_\infty^2}$	Pressure Coefficient
f	Oscillation Frequency, Hz
FPG	Favorable Pressure Gradient
Γ	Circulation, m^2/s
h_0	Plunge Amplitude, m
h_0/c	Dimensionless Plunge Amplitude
$k = \frac{\pi f c}{U_\infty}$	Reduced Frequency
LEV	Leading-Edge Vortex
LSB	Laminar Separation Bubble
ν	Kinematic Viscosity, m^2/s
ω	Vorticity, s^{-1}
OSV	Opposite-Signed Vortex
ϕ	Phase Angle, degrees
PIV	Particle Image Velocimetry
ps	Percent Span

www.manaraa.com

ρ	Density, kg/m^3
$Re_C = \frac{U_\infty c}{\nu}$	Chord-Based Reynolds Number
s	Airfoil Span, m
SLV	Shear-Layer Vortex
$St = \frac{fA}{U_\infty}$	Strouhal Number
TEV	Trailing-Edge Vortex
TiV	Tip Vortex
TrV	Tertiary Vortex
u	Velocity, m/s
U_∞	Free-Stream Velocity, m/s

www.manaraa.com

CHAPTER 1
INTRODUCTION AND BACKGROUND

1.1 Motivation and Goals

Vortical structures have long been recognized as the "sinews and muscles of fluid motion" [62], and the study of vortex evolution and stability has consequently become a prominent sub-discipline of fluid mechanics. This interest primarily stems from the fact that interactions between vortices and solid surfaces are ubiquitous in engineering applications. Examples include: dynamic stall vortices shed from the leading edges of helicopter and wind turbine blades (Figure 1.1a), the streamwise vortices separating from the forebodies of high performance air vehicles and submarines at high incidence, leading-edge vortices on delta wings (Figure 1.1b), and the vortices shed from biological and biomimetic, oscillatory wings and fins (Figure 1.1c).

Because the vorticity shed from a solid body has been shown to have a significant impact on aerodynamic forces, vortex-dynamic studies have been performed for a broad range of airfoil motions (e.g. pitching, plunging, rotating, dynamic stall) and geometries (e.g. flat plate, airfoil, rectangular planform, ellipsoid planform, flexible structure) [36, 60, 103, 104, 8, 64, 67, 70, 55]. Studies like Cleaver et al. [27] have shown the strength of the vortex generated at the leading edge of an airfoil to be directly related to the time-averaged lift forces and that the position of this vortex within the bulk flow plays a critical role in governing the propulsive efficiency of the airfoil–i.e. the ratio between thrust and lift production. Furthermore, the evolution of the leading-edge vortex (LEV) has been

www.manaraa.com

shown to significantly influence the topology of the wake [67]. But perhaps one of the most relevant characteristics of an LEV is that many experimental studies have observed stable LEVs to be the primary lift-producing structure used by natural swimmers and fliers [34, 113, 78, 15]. Because of its widespread applicability, studies of unsteady airfoils typically focus on characterizing the dynamics of the leading-edge vortex [91].

In the work presented here, the boundary vorticity flux and other relevant vorticity transport mechanisms will be quantified and examined on three experimental cases, all of which utilize a simple flat-plate airfoil undergoing a pure-plunge motion. By exerting strict control over the various sources and sinks of vorticity within the flow, each of these three cases will be specifically designed to explicate different aspects of the LEV evolution. The overarching goal of this work will be to provide a more thorough description of the LEV formation process that puts great emphasis on determining how and why the LEV develops the way it does.

1.2 Literature Review: The Leading-Edge Vortex

The formation of the leading-edge vortex is due to the instability and roll-up of a separated shear layer, and the evolution of the vortex can alter the *global* dynamics of the flow about the body which, in turn, affects the continued evolution of the separated flow structure. The vortex also affects the *local* flow dynamics in its immediate vicinity, which also governs the fluxes of vorticity entering the flow. For example, surface pressure gradients established by the vortex interacting with the boundary lead to the generation of opposite-sign vorticity [68, 126], which can cause significant destruction of the vortex

www.manaraa.com

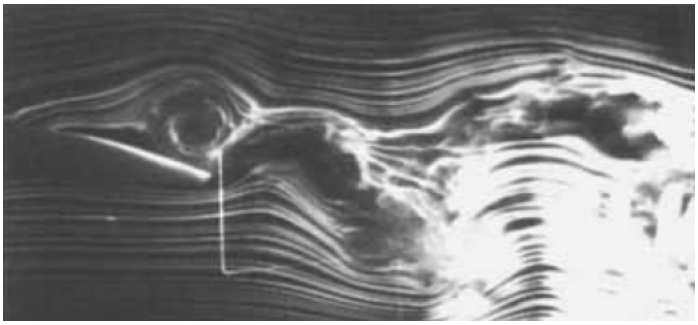

(a) Smoke-wire flow visualization of the dynamic stall vortex formed on a pitching NACA 0012 airfoil. Adopted from Panda and Zaman [86].

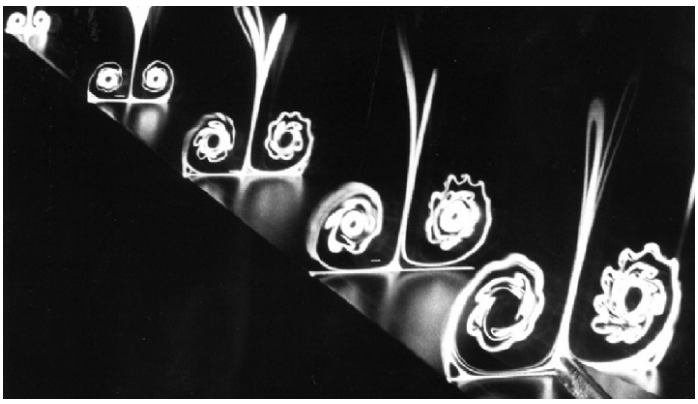

(b) Flow visualization of the leading-edge vortices formed above an 85° swept delta wing. Adopted from Nelson and Pelletier [80].

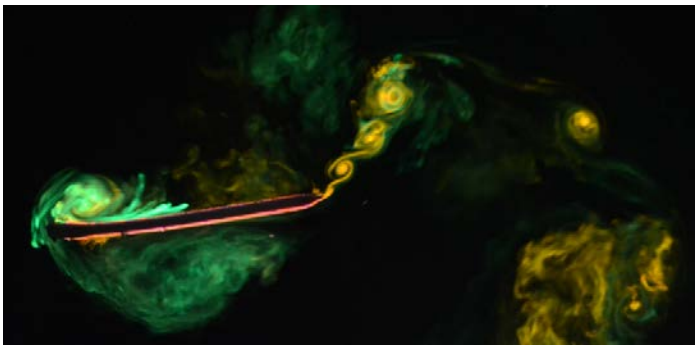

(c) Dye visualization of the leading and trailing edge vortex structures formed by a plunging, flexible wing. Unpublished picture from previous work by the author [3].

Figure 1.1: Flow visualizations of the vortical structures shed from the leading edge of a variety of aerodynamic bodies.

www.manaraa.com

through cross-cancellation [118, 117]. This section serves to review our current understanding of the formation, evolution and aerodynamic effect of the leading-edge vortex.

1.2.1 LEV Formation Process

The appearance of an LEV is preceded by the generation of a boundary layer on the surface of the airfoil via the no-slip condition, and this stage–which is devoid of any coherent vortical structures–is referred to as attached flow. The fundamental dynamic that leads to the formation of an LEV on an airfoil–or wing, fin, plate, etc.–is a changing angle of attack, as it causes the stagnation point on the surface of the airfoil to move away from the leading edge. The relevant result of this process is that it makes it more "difficult" for the flow to navigate around the leading edge, which corresponds to the development of an adverse pressure gradient (APG) upon the surface of the airfoil near the leading edge [33, 44]. The initial formation of the LEV begins when an APG of sufficient strength is imposed on the boundary layer, causing an ejection of vorticity into the bulk flow as the boundary layer separates from the surface [106, 33]. The fundamental physics associated with this separation process was once a point of contention within the fluid dynamics community, but the subject was essentially put to rest in 1980 when Van Dommelen and Shen [106] showed that the formation of a stagnation point on the surface of the airfoil would spontaneously generate a singularity in the laminar boundary layer equation. The separation process has since been characterized as the formation of reversed flow at the surface of the airfoil and once the boundary layer separates, the structure rolls up to create the leading-edge vortex.

Even after the LEV separates, it remains connected to the leading edge via a per-

www.manaraa.com

sisting shear layer that provides a continued flux of vorticity into the LEV to increase its circulation. As the LEV continues to grow, it begins to impose large pressure gradients on the surface of the airfoil. Due to the no-slip condition, this leads to the formation of a layer of opposite-signed vorticity beneath the LEV [1, 46].

Detachment of the LEV occurs when its connection to the leading-edge shear layer is broken, preventing the accumulation of any additional circulation. Some describe the process using ideas from turbulent boundary layer theory, where the approach of the LEV towards the surface of the airfoil results in a "sweep event" that causes an eruption of opposite-signed vorticity [33, 9]. However, the phenomenon is typically characterized as the layer of opposite-signed vorticity accumulating enough circulation for it to break the connection between the LEV and its feeding shear layer [1]. This process was first described by Acharya and Metwally [1] when they showed opposite-sign vorticity cutting off a dynamic-stall vortex from the leading-edge shear layer. In their study of a plunging airfoil, Lewin and Haj-Hariri [67] also found the evolution of the secondary vorticity to play a significant role in the detachment of the LEV.

Visbal [108] performed high-fidelity large eddy simulations on a plunging airfoil and noted the entrainment of opposite-signed vorticity into the LEV. Wojcik and Buchholz [118] observed a similar phenomenon on the attached LEV of a rotating blade. Using qualitative measurements of the fluxes of circulation regulating the LEV strength, they inferred that the rate of annihilation of the LEV due to entrainment of secondary vorticity is often comparable to the flux of vorticity into the LEV via the shear layer. Based on concepts originally identified by Wojcik and Buchholz, Eslam Panah et al. [85] hypothesized that

www.manaraa.com

for the transitional flow on a plunging flat-plate airfoil, the detachment process was not the result of a decisive "cutting" of the shear layer, but rather a gradual weakening of the shear layer through the entrainment of blobs of opposite-signed vorticity that break off of the secondary vortex.

While it has been widely accepted that the detachment of the LEV is caused by the interaction between the LEV and secondary vortex, there are multiple ways in which secondary vorticity can be introduced into the flow. Widmann and Tropea [115] describe two fundamental mechanisms by which the detachment of the LEV can occur: bluff body detachment and boundary layer eruption. They used topological analyses to characterizes these mechanisms, and Figures 1.2 and 1.3 have been adopted from their discussions. In bluff body detachment, the LEV separates from the airfoil but maintains a reattachment point that proceeds to move downstream (Figure 1.2a). When the reattachment point reaches the trailing edge, the LEV detaches and allows reverse flow to extend up the airfoil from the trailing edge (Figure 1.2b). On the other hand, the boundary layer eruption detachment mechanism occurs when the viscous vortex-wall interaction causes an eruption of secondary vorticity from beneath the LEV before the reattachment point of the LEV reaches the trailing edge. This breaks the topology between the shear layer and the LEV by forming a counter-rotating region between the two, the division of which incites detachment. As the advection of the reattachment point of an LEV has been shown to be dependent on reduced frequency [26], this transition to the boundary layer eruption mechanism is associated with high frequency motions. Note: reduced frequency $(k) = \pi f c / U_\infty$ where f is the motion frequency, c is chord length and U_∞ is the free-stream velocity.

www.manaraa.com

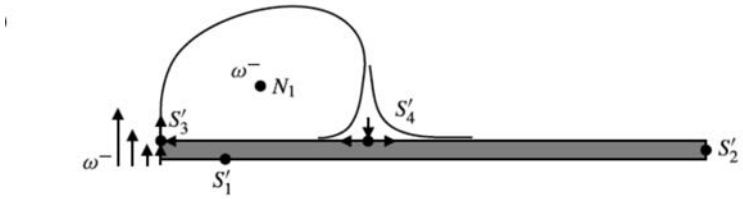

(a)

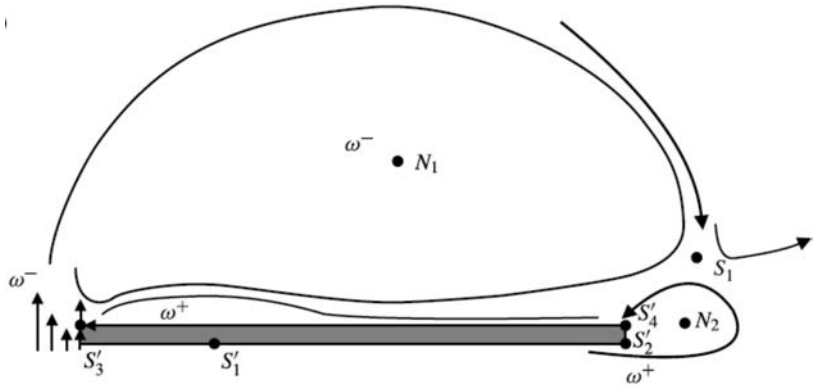

(b)

Figure 1.2: Topological representation of the bluff body detachment mechanism. Adopted from Widmann and Tropea [115].

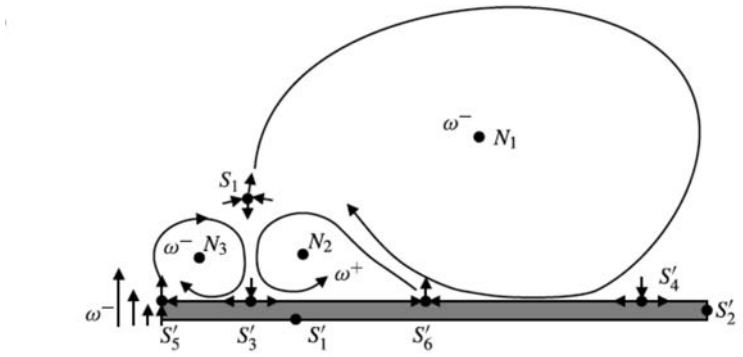

Figure 1.3: Topological representation of the boundary layer eruption mechanism. Adopted from Widmann and Tropea [115].

www.manaraa.com

1.2.2 LEV Scaling

Interest in the LEV primarily stems from its ability to produce large lift values, a byproduct of the high kinetic energy within the LEV generating low pressure regions on the upper surface of the airfoil. It has long since been established that the total lift produced by an airfoil is related to the total circulation of the flow [125] and the fact that most of the circulation about an airfoil is contained within the LEV [88] results in the maximum lift values being achieved just before detachment of the LEV [51]. Thus, developing a non-dimensional circulation-threshold for the detachment of the LEV provides a useful means for characterizing the maximum lift of an airfoil.

Since the bluff body detachment mechanism is characterized by the reattachment point of the LEV arriving at the trailing edge, some studies have demonstrated success in using the chord length to scale the circulation of an LEV [92, 52]. However, Widmann and Tropea [115] showed that this was an insufficient scaling parameter in the case of the eruption-based detachment, as it had no way to account for the viscous effects near the leading edge that inevitably cause the eruption of secondary vorticity. Instead, they found the best way to scale the circulation of the LEV was to use the thickness of the shear layer (Figure 1.4). Alternatively, both Rival et al. [93] and Kriegseis et al. [61] found the effective shear-layer velocity to be a suitable scaling parameter for the LEV circulation. Akkala et al. [4] proposed yet another scaling parameter for leading-edge vortex circulation using a kinematically-based velocity and length scale, which was found to be particularly effective for flexible plunging airfoils. Buchholz et al. [18] demonstrated success in scaling the total circulation shed by finite aspect-ratio pitching panels based on a simple model of

www.manaraa.com

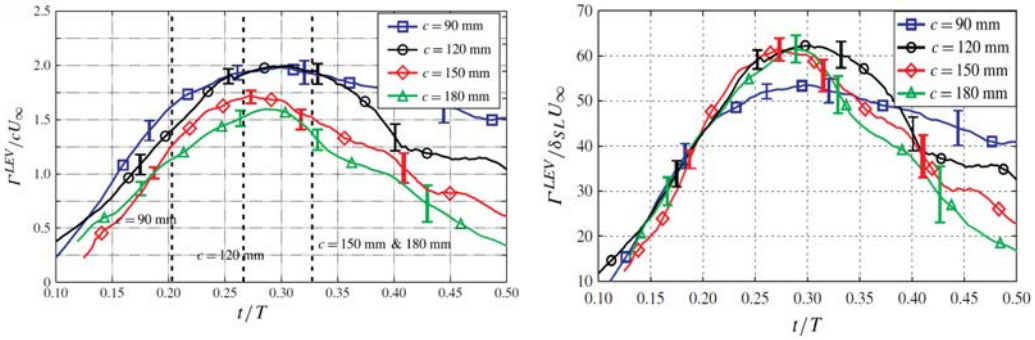

Figure 1.4: Scaled LEV circulation using chord length (left) and shear layer thickness (right) for the four chord lengths tested by Widmann and Tropea. Adopted from Widmann and Tropea [115].

surface pressure gradients. Yet in spite of the many scaling parameters that have been proposed, no robust predictor of LEV circulation has been identified. This is primarily because the boundary layer eruption mechanism is still poorly understood, and without sufficient knowledge of the pertinent flow physics it becomes very difficult to identify any sort of unifying principle.

1.2.3 Evolution of the LEV

In addition to augmenting the aerodynamic loads of an airfoil during its formation [94, 112, 91], the leading-edge vortex has the ability to continue imposing a force on the surface of the airfoil even after it has detached [114, 97, 26]. Choi et al. [26] performed a computational analysis of surging and plunging flat plates and demonstrated that the LEV produced optimal lift when it detached just before the retreating portion of the motion. This was attributed to the fact that it resulted in the LEV remaining closer to the surface

www.manaraa.com

of the airfoil during the retreating motion, thereby producing additional lift. Indeed, many studies have emphasized the importance of stabilizing an LEV so that it remained attached to the airfoil throughout the entire downstroke of the motion, thereby allowing for the LEV to remain a lift-producing structure for a longer period of time. As such, one of the primary motivations within the study of unsteady airfoils is characterizing how to prolong the stability of the LEV and delay detachment.

Jones and Babinksy [52] analyzed the effects of Reynolds number on the formation of the LEV and determined that the fundamental structures within the flow were not greatly affected by Reynolds number. While altering the Reynolds number appeared to have no effect on the non-dimensional circulation value at which detachment of the LEV occurred, they found that increasing the Reynolds number decreased the rate of circulation production–i.e. the LEV grew slower at higher Reynolds numbers. Thus, the LEV was observed to stay attached to the leading edge for a longer period of time at higher Reynolds numbers.

Baik et al. [10] performed experiments on pitching and plunging flat plates and similarly showed the Reynolds number had little effect on the flow. They also found that so long as the time-history of the angle of attack remained the same, the flow evolution was independent of Strouhal number. Note: Strouhal number $(St) = fA/U_\infty$, where f is the motion frequency, A is the peak-to-peak amplitude of the motion and U_∞ is the free-stream velocity. Furthermore, they determined the aerodynamic loads were primarily a function of the angle of attack when the Strouhal number remained low. In their experiments on plunging airfoils, Rival et al. [93] used a variety of different plunge motions to demonstrate

www.manaraa.com

how altering the plunge velocity so that the maximum angle of attack occurred later in the cycle allowed for the production of stronger LEVs that were located closer to the surface of the airfoil at the end of the downstroke. They went on to hypothesize that adding a pitching motion would help to further delay the detachment of the LEV. Trizila et al. [105] experimented with "hovering motions" through the combination of pitching and plunging motions, and by maximizing the angle of attack they achieved optimal airfoil performance. Milano and Gharib [73] similarly optimized the flapping motion of a flat plate by prescribing a pitch-plunge trajectory that maximized the circulation within the LEV.

While pitching and plunging motions are fundamentally different, they can be prescribed in such a way that they produce the same angle of attack. Figure 1.5 presents a sample of the dye visualizations obtained by Ol [82], who performed a series of experiments on airfoils undergoing either a pitching or a plunging motion, yet which had their kinematics defined such that both motions produced equivalent angles of attack. While the kinematics produced vastly different trailing-edge vortex (TEV) structures, the LEVs exhibit essentially the same formational behavior, which provides very convincing evidence that it is the angle of attack that governs the evolution of the LEV.

As opposed to altering the dynamics of the LEV by modifying aspects of the airfoil's motion, a recent trend has emerged within the literature wherein three-dimensional sources of vorticity are utilized in an attempt to stabilize the LEV. This method was inspired by the dynamics observed on delta wings, where spanwise flow has been shown to drain vorticity from the LEV so that it remains stable at the leading edge [71, 89, 74]. Ellington et al. [34] characterized this process as being necessary for the stabilization of

www.manaraa.com

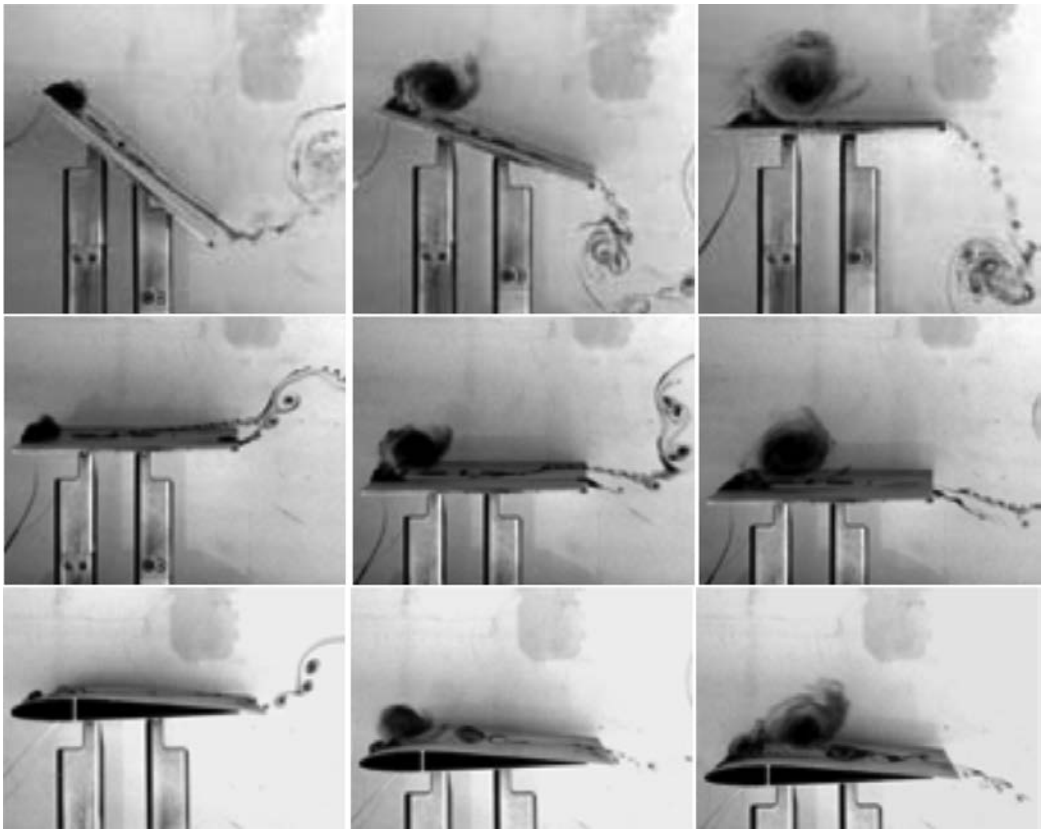

Figure 1.5: Dye visualization for pitching flat plate (top row), plunging flat plate (middle row) and plunging SD7003 airfoil (bottom row). Adopted from Ol [82].

www.manaraa.com

LEVs produced by rotating blades; however, subsequent analyses have found that rotating kinematics do not produce a significant spanwise flux of vorticity [13, 52]. Lim et al. [69] claimed the stability of the LEV was a byproduct of vortex stretching, while the works of Carr et al. [22] and Shyy et al. [98] characterized the downwash induced by the tip vortex as being the mechanism that anchors the LEV to the leading edge. However, when Wojcik and Buchholz [118] performed a novel vorticity transport analysis on a rotating wing, they determined that it was the annihilation of primary vorticity via the entrainment and cross-cancellation of secondary vorticity that limited the circulation of the LEV.

Although studies of LEV stability are typically associated with rotating or waving kinematics, both Beem et al. [12] and Wong et al. [120] attempted to modify the circulation within the LEV of a plunging airfoil (NACA 0012 [12] and flat plate [120]) through vortex stretching, producing spanwise flow by varying the sweep angle of the airfoil. Ultimately both studies showed that spanwise flow had no effect on either the circulation of the LEV nor the force history. This reinforced the idea that spanwise flow does not mitigate the circulation of the LEV [37, 52, 25]. While many of these studies maintain that there are no two-dimensional mechanisms for the stabilization of the LEV, Eslam Panah et al. [85] demonstrated that the diffusive flux of vorticity emanating from the surface of a nominally two-dimensional airfoil beneath the LEV acts as a major sink of primary vorticity. In their experiments on a plunging flat plate, they showed that approximately half of the vorticity that was introduced into the flow at the leading edge could be lost through this diffusion mechanism.

www.manaraa.com

1.2.4 Effect of Cross-Sectional Shape of an Airfoil

The dye visualization shown in Figure 1.5, Ol [82] illustrates how the LEV produced by a plunging SD7003 airfoil is similar to one generated by a flat plate. Kang et al. [54] performed both computational and experimental studies of plunging airfoils and found the sharp leading edge of the flat plate produced stronger LEVs than those seen on a SD7003 airfoil. While the LEV began forming slightly earlier on the flat plate than on the airfoil, they reiterated the conclusion that the flows followed the same evolution.

Cleaver et al. [27] compared the flow field and the lift coefficients of a plunging flat plate to data from a NACA 0012 airfoil in identical flow conditions at a Reynolds number of 10,000. At lower Strouhal numbers ($St < 1$) the flat plate produced a slightly higher lift coefficient, which was attributed to a smaller separation region. Because the leading edge of the flat plate had a smaller radius of curvature, the flow would separate closer to the leading edge (Figure 1.6). While increasing the Strouhal number reduced the separation zone of both airfoils, this reduction was greater for the flat plate. Despite these variations, Figure 1.7 shows that the flow fields of the two airfoils evolve very similarly; while the shear layer of the NACA airfoil has a slightly lower incident angle, the overall shape, size and positions of the LEV and opposite-signed vorticity are similar.

Rival et al. [92] also studied the effect of airfoil shape on the evolution of the flow field, and they too demonstrated that the shape of the leading edge had a noticeable effect on the initial separation of the LEV. However, they went on to show that the growth rate of the LEV was not strongly affected by airfoil shape, thereby characterizing why the vorticity fields remained similar.

www.manaraa.com

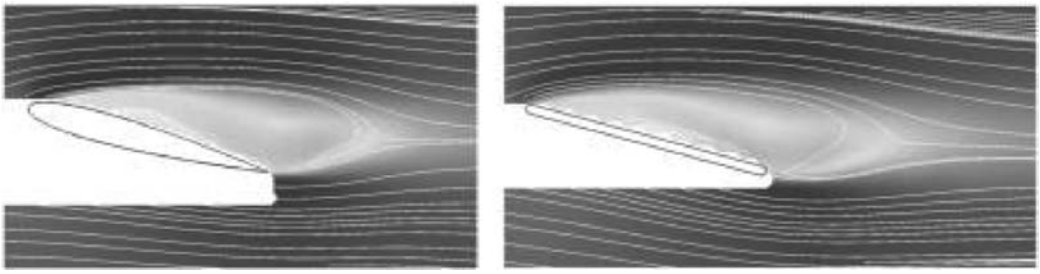

Figure 1.6: Time-averaged velocity magnitude and superimposed streamlines for stationary NACA 0012 and flat-plate airfoils. Adopted from Cleaver et al. [27].

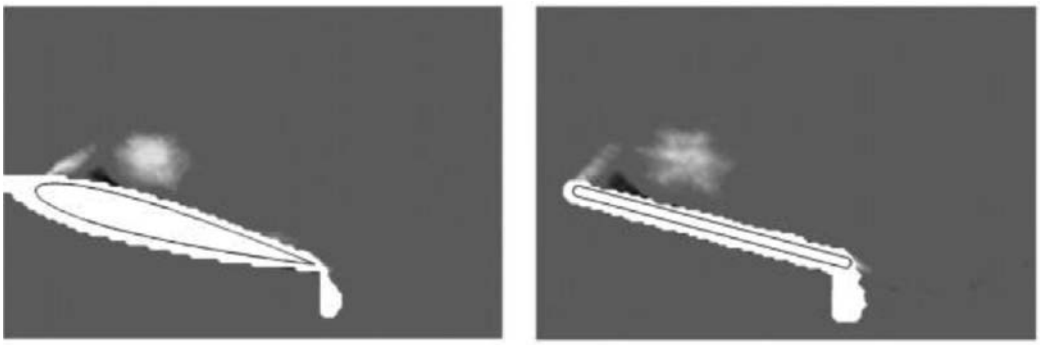

Figure 1.7: Vorticity contours for the NACA 0012 and flat-plate airfoils at the end of the downstroke (St = 0.5). Adopted from Cleaver et al. [27].

www.manaraa.com

1.2.5 Three-Dimensional Vortex Structure

While Eslam Panah et al. [85] demonstrated that the stabilization of an LEV does not inherently require large-scale three-dimensionality, prominent three-dimensional mechanisms of vorticity transport do exist. Yilmaz and Rockwell [130] used quantitative imaging to study a plunging finite aspect-ratio ($AR = span/chord$) plate and the development of large-scale patterns of streamwise-oriented vorticity. Strong axial flows were reported in the LEV, directed towards the symmetry plane on the wing. Visbal et al. [107] computed this flow and developed a model of the aforementioned three-dimensional flow structures. Figure 1.8 presents the measured arch-type vortex using a Q-criterion isosurface. Yilmaz et al. [129] extended these results and characterized the type of three-dimensional vortex structures experimentally observed by Yilmaz and Rockwell [130] and computed by Visbal [109].

Granlund, Ol and Bernal [42] studied the effect of planform shape (rectangular and elliptical) on a pitch-up maneuver using dye visualization and force measurements. While they found the elliptical planform produced weaker spanwise flow–potentially due to the spanwise variation in the chord length–they found the aerodynamic loads of the two planforms to be very similar. Trizila et. al [105] considered how the overall LEV and tip vortex structure affects the vortices shed into the wake. They found the tip vortices to evolve more slowly than the LEVs, with the tip vortex remaining as an attached coherent structure until the LEV detaches.

Volumetric, three-component PIV measurements were performed by Calderon et al. [20] on finite aspect-ratio wings with rectangular and elliptical platforms that were un-

www.manaraa.com

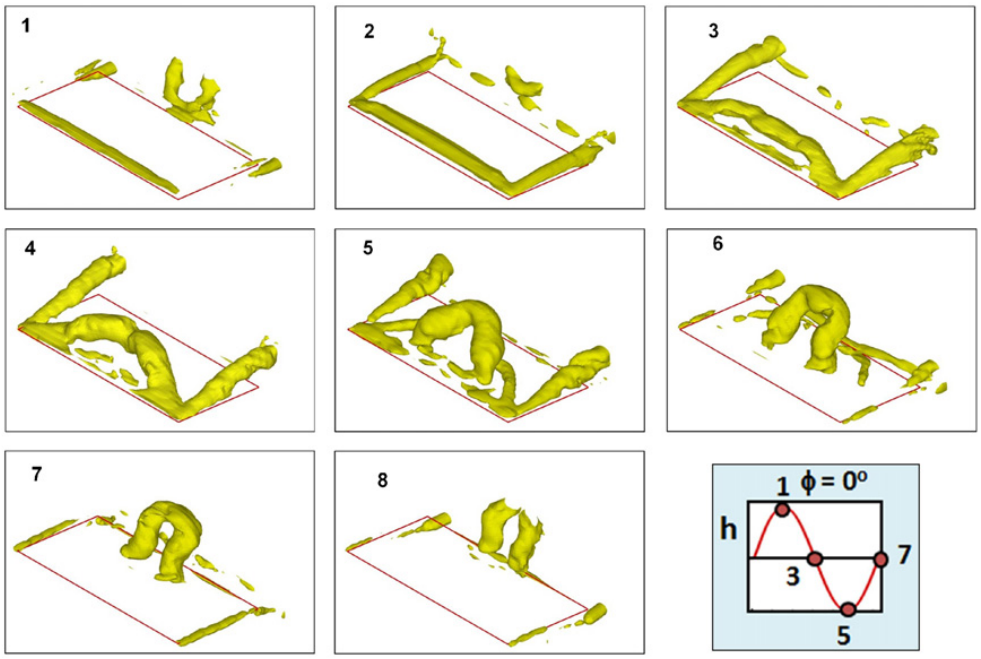

Figure 1.8: Q-Criterion isosurface of experimentally phase-averaged at selected phases of the plunging motion. Adopted from Visbal et al. [107].

dergoing a small amplitude, pure-plunge motion with a static angle of attack $\alpha = 20°$. This prescribed kinematics produced highly three-dimensional LEVs that exhibited a strong dependence on oscillatory frequency. At low frequencies, the LEV would evolve into an arch-type structure with an anchor point that advects towards the root of the wing. A full-arch on the half span was also observed for a AR = 2, and a half-arch was detected on the half-span wing for AR = 1.

Kim and Gharib [59] studied the vorticity transport of plunging wings with an aspect ratio of 3.75 and found the vortex created at the tip of the airfoil produced spanwise flow that was directed towards the root of the airfoil. They also showed that the LEV was positioned closer to the airfoil's surface near the tip (Figure 1.9) and observed reduced

www.manaraa.com

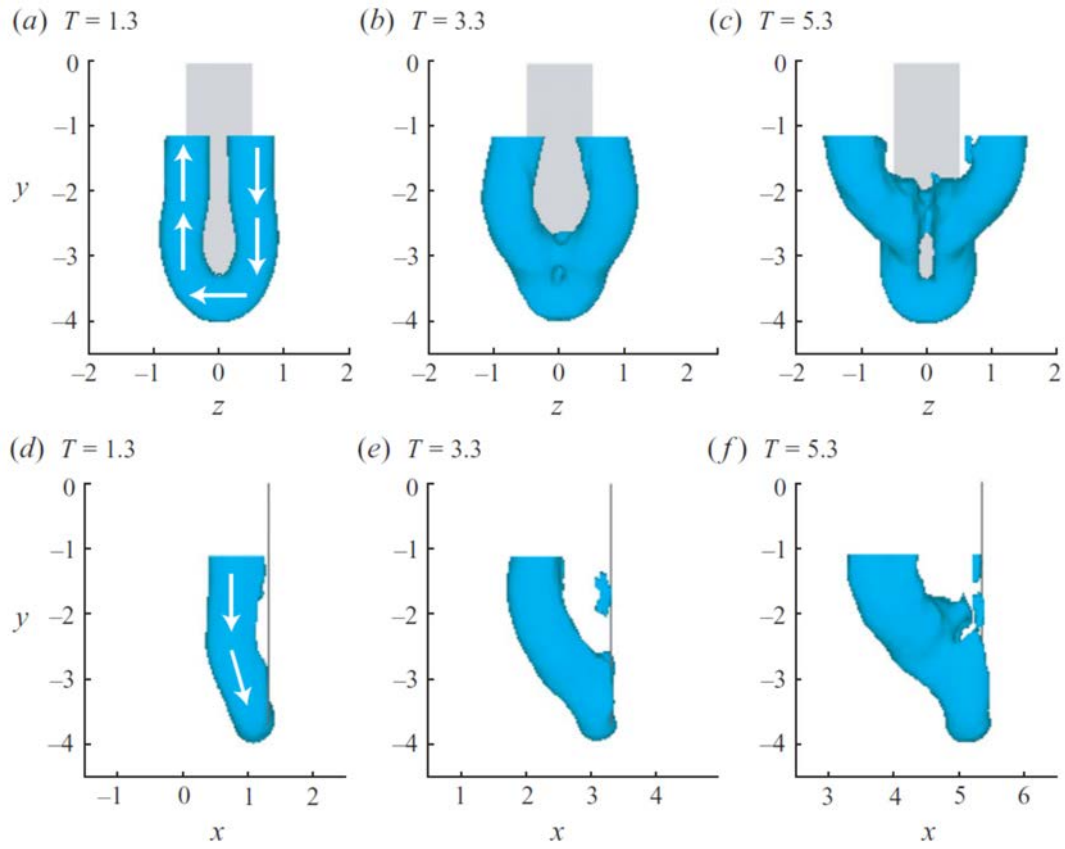

Figure 1.9: Front and side views of the vortical structure measured by Kim and Gharib [59] for a plunging flat plate. Adopted from Kim and Gharib [59].

circulation values within these regions. Based on these results, they concluded that the spanwise flow forced the upper LEV away from the surface of the airfoil (Figure 1.10). Jantzen et al. [51] similarly saw the tip vortex of a pitching flat plate (AR = 2) kept the LEV closer to the surface of the airfoil than a two-dimensional counterpart. They went on to hypothesize that this effect prevented the LEV from detaching.

There has been some disagreement regarding the effect that the tip vortex (TiV) has on the aerodynamics of an airfoil. The standard belief is that the downwash created

www.manaraa.com

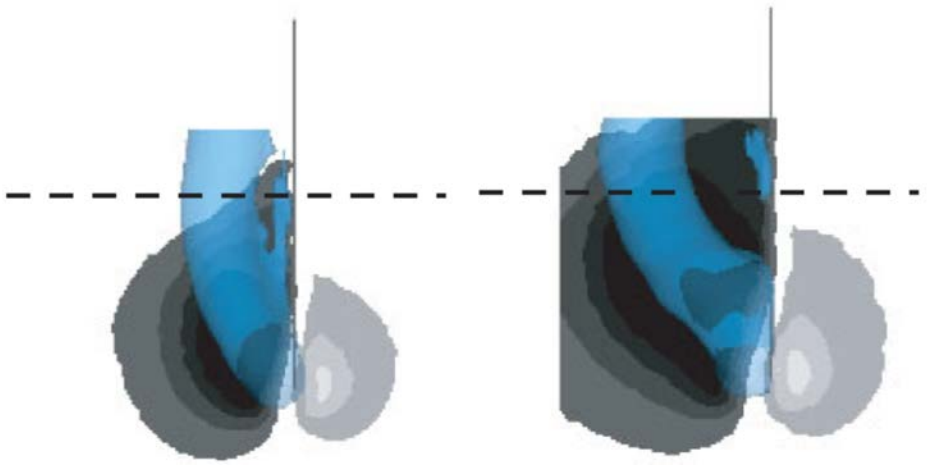

(a) T = 1.8 (b) T = 3.8

Figure 1.10: Vortical structure measured by Kim and Gharib [59] for a plunging flat plate, overlaid with contours of spanwise flow. Adopted from Kim and Gharib [59].

by the TiV reduces lift. Kang et al. [54] looked at a plunging flat plate with AR = 2 and indeed found the TiV reduced the lift. However, Lee et al. [65] performed a unique analysis on a series of plunging flat plates with aspect ratios ranging from 1 to 3. By identifying the negative pressures that the LEV and TiV induced on the surface of the airfoil, they determined both structures acted to generate lift. While they did observe an overall reduction in lift, they determined that the TiV was not an inherently "lift reducing" structure.

1.3 Literature Review: Boundary Vorticity Dynamics

While the literature contains a wealth of information regarding the evolution of vortical structures, discussion of the local dynamics of vorticity on a boundary is more limited. Ever since Lighthill's [68] work in 1963, it has been recognized that all vortical structures

www.manaraa.com

within a flow originate at the solid-fluid interface, which is why it is not surprising that these on-wall physics have been shown to govern aerodynamic performance [125]. In this regard, characterization of the unsteady production and diffusion of vorticity is essential for understanding the flow dynamics [1].

1.3.1 Vorticity Transport at Boundaries

Laminar separation bubbles (LSB) have been observed to be the incipient vortical structures at the leading edge of pitching NACA airfoils operating at low Reynolds numbers (Re = $O(10^4)$-$O(10^6)$), and the bursting of these bubbles has been related to the onset of dynamic stall [1, 95, 110, 66]. The effect of an LSB on the surface pressure distribution has been well established, as there exists a well-defined plateau in the surface pressure distribution beneath the LSB. The physics associated with this plateau are summarized in Figure 1.11 [47]. The plateau begins when the LSB separates from the surface (point S in Figure 1.11b), as the slow moving fluid within the "dead air" region of the bubble does not affect a pressure gradient. This plateau ends once turbulent reattachment begins to take effect (point T in Figure 1.11b), and the flow is considered "reattached" once the pressure returns to its inviscid distribution (point R in Figure 1.11b).

In their analysis of a pitching NACA airfoil, Acharya and Metwally [1] obtained time-resolved surface pressure measurements of a bursting LSB, and they found great success in characterizing the dynamic stall process based on the transient behavior of critical features within the pressure distributions. Their results indicated that there were two distinct mechanisms by which dynamic stall occurs, characteristic of either high or low

www.manaraa.com

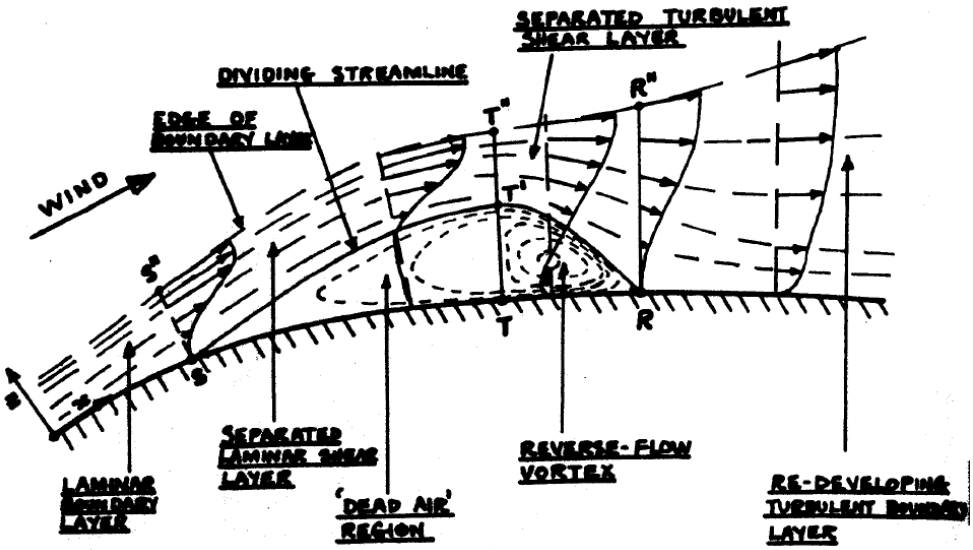

(a) Sectional view of laminar separation bubble

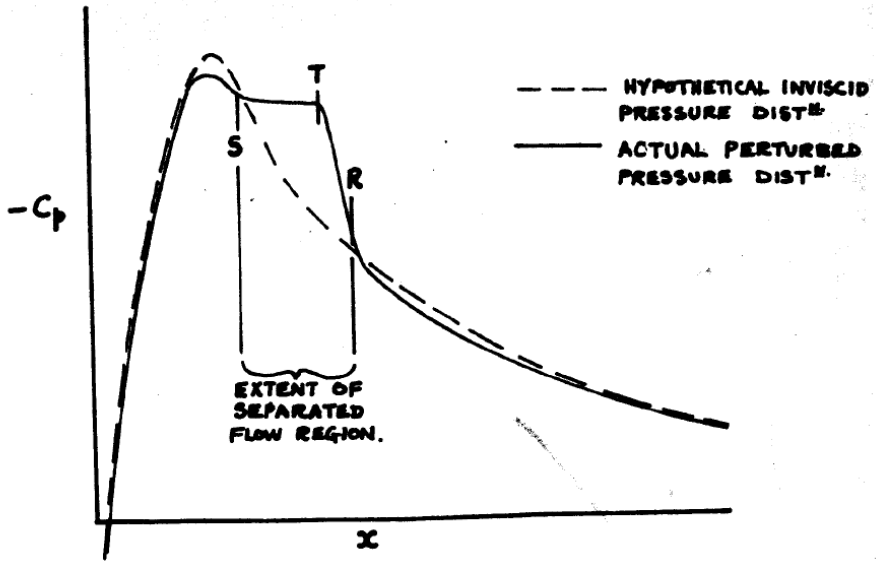

(b) Corresponding surface pressure distribution

Figure 1.11: Pressure distribution characteristic of an LSB. Adopted from Horton [47].

www.manaraa.com

frequency pitch motions. Figure 1.12 presents the three different pressure distributions that Acharya and Metwally [1] used to characterize the two classes of behavior. Within these figures, the leading-edge suction peak (labeled "LESP") characterizes the source of primary vorticity that is formed when the flow accelerates around the leading edge. The pressure plateau that forms downstream of this point (labeled "CCP") is associated with the unsteady separation of the boundary layer near the leading edge, and the suction peak produced by the dynamic stall vortex (labeled "DSVP") is also shown.

At low motion frequencies, Acharya and Metwally [1] found the magnitude of the pressure plateau would increase until it became equal to that of the leading-edge suction peak, after which the two structures would merge and form the DSVP. The DSVP was observed to begin spilling as soon as it was formed (see Figure 1.12c), indicating the detachment of the dynamic stall vortex. This concept of "spilling" is a common term within dynamic stall literature that is used to explicitly reference the behavior seen within the surface pressure distribution when a dynamic stall vortex is shed from the leading edge [66]. Specifically, this term describes how the suction peak of the dynamic stall vortex (DSVP) moves downstream while simultaneously opening up and decreasing in magnitude–note, this "opening up" references how the chordwise spread of the entire DSVP distribution becomes elongated in the downstream direction.

At higher motion frequencies, Acharya and Metwally [1] found the pressure plateau would deform into the DSVP before it was able to reach the same magnitude as the leading-edge suction peak (see Figure 1.12b). Unlike the previous class of behavior, the formation of the DSVP downstream of the leading-edge suction peak resulted in the dynamic stall

www.manaraa.com

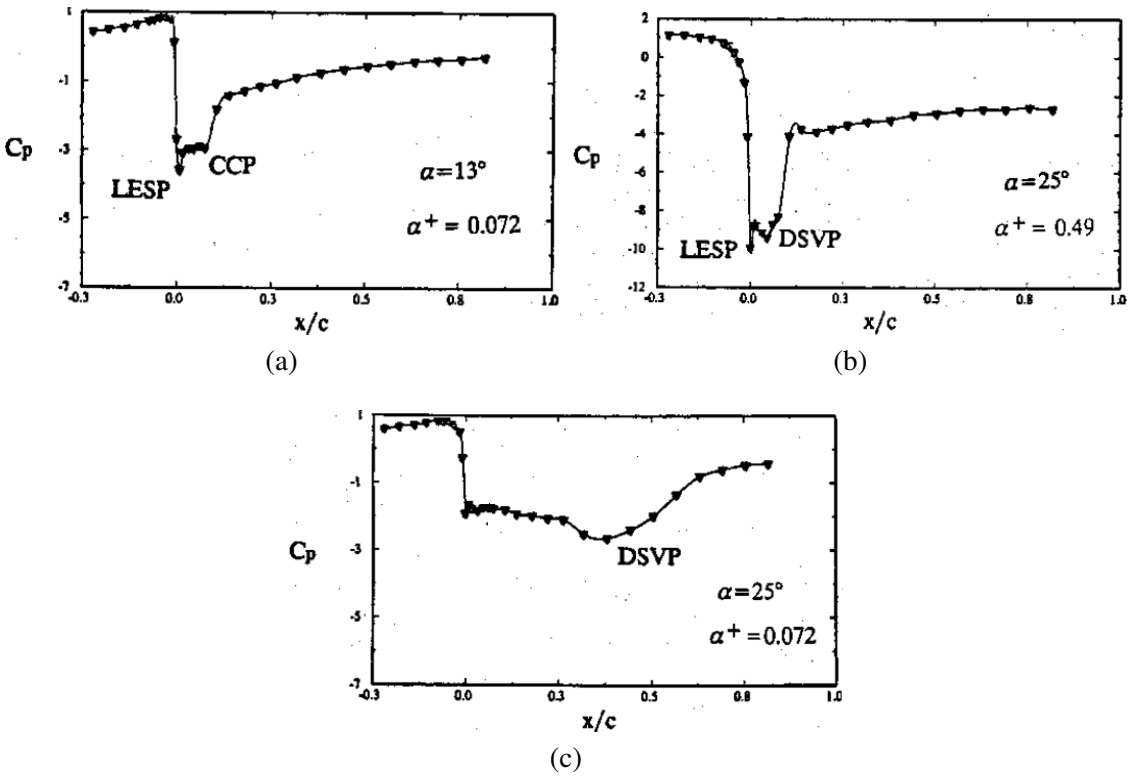

Figure 1.12: Pressure distributions on a pitching NACA 0012 airfoil. Adopted from Acharya and Metwally [1].

vortex remaining close to the leading edge, thereby enhancing lift. However, once leading-edge suction peak began to drop, the DSVP slowly began to spread downstream and the dynamic stall vortex was considered to have detached.

Although time-resolved measurements of surface pressure distribution are still uncommon within studies of unsteady airfoils, several noteworthy examples do exist. In addition to characterizing the surface pressure distribution of a pitching airfoil, Lee and Su [66] performed novel measurements on a NACA 0012 airfoil undergoing heaving and combined pitch-heave motions as well. They found the pressure time-histories produced by

www.manaraa.com

heaving motions to be very similar to those produced by pitching motions, which appeared to follow the low-frequency behavior described by Acharya and Metwally [1]. However, the combined pitch-heave motions were observed to significantly alter the surface pressure distributions. A phase shift of $\phi = 0°$ between the pitch and heave motions was observed to maximize the suction on the surface of the airfoil as it allowed for larger effective angles of attack. Interestingly, when the phase shift between the two motions was $\phi = 180°$, the surface pressure distribution was observed to remain almost completely unchanged throughout the entire cycle of the motion.

Acharya and Metwally [1] found the pressure plateau produced by the LSB to be an important feature for characterizing dynamic stall, but Conger and Ramaprian [28] found no evidence of a plateau within the surface pressure distribution when they studied a pitching NACA 0015 airfoil within a water channel. In the absence of this pressure plateau, the DSVP was observed to form out of the leading-edge suction peak once it began to move downstream. Despite observing this behavior within their results, Conger and Ramaprian were unable to identify what sort of behavior within the flow led to the elimination of the pressure plateau due to the fact that their experiments did not include any form of flow visualization.

Kiedaisch and Acharya [57] measured the shear stress distribution on the same NACA 0012 airfoil model used by Acharya and Metwally [1] and found the relevant features denoted within the pressure gradients were similarly represented in the shear stress data. Figure 1.13 compares a set of results from the two studies; the data corresponds to the flux of vorticity introduced into the flow at a specific chordwise location. While the scales

www.manaraa.com

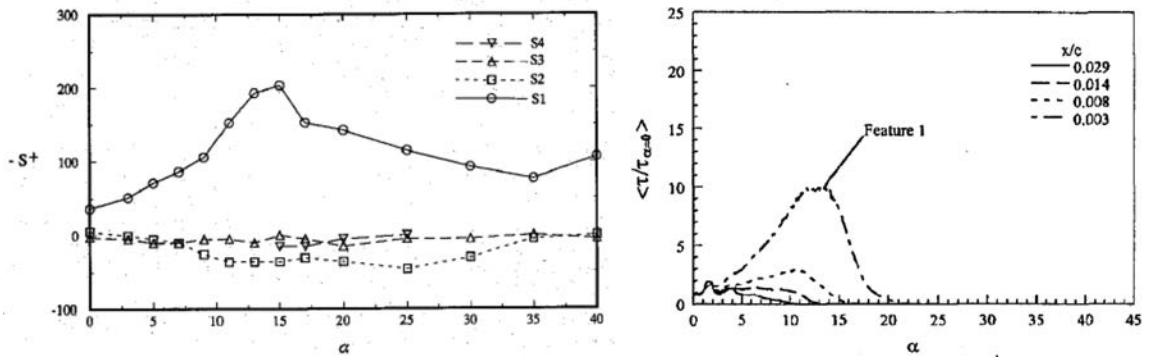

(a) Adopted from Acharya and Metwally [1] (b) Adopted from Kiedaisch and Acharya [57]

Figure 1.13: Comparison of (A) pressure gradient and (B) shear stress distributions reported by Acharya and Metwally [1] and Kiedaisch and Acharya [57] for a pitching NACA 0012 airfoil. The larger profiles in either plot correspond to the region near the leading edge.

between the two plots are different, the distributions shown for the leading edge are clearly similar.

While an adverse pressure gradient provides the necessary physics to incite flow reversal, it is not a sufficient condition for boundary layer separation; the presence of an APG is only a sufficient condition for separation if the incoming fluid contains no vorticity [9]. Because the boundary layer is rotational by definition, it is able to withstand some finite APG without separating. On the other hand, the shear stress on the surface of the airfoil is a deterministic indicator of flow reversal. This idea was utilized by Ramesh et al. [91] when they showed that regions of positive shear stress on the surface of the airfoil coincided with flow reversal. They went on to develop a leading edge suction parameter (LESP) based on the shear stress and hypothesized that the shedding of vorticity was a

www.manaraa.com

result of the airfoil attempting to maintain a critical LESP value. A sample of their results are presented in Figure 1.14, which shows the separation of the LEV occurring while the LESP values has reached its threshold.

Despite the fact that shear stress correlates very well with the velocity field near the surface of the airfoil [81]–and is therefore a good indicator of stagnation points [91]–the fact that the wall shear stress is derived solely from the wall-normal velocity field makes it a poor indicator of the distribution of events within the velocity field. However, the pressure at any given point on the wall is related to the velocity field in the half-space above the wall [81]. This spatial awareness of the pressure field allows the surface pressure distribution to be a better indicator of the dynamics within the flow field and the associated pressure gradients to provide a superior model of the flux of vorticity that is diffusing from the surface of the airfoil.

In addition to characterizing the dynamics of a bursting LSB, the results provided by Acharya and Metwally [1] are one of the few examples within the literature wherein the diffusive flux of vorticity associated with surface pressure gradients were correlated to the dynamics of the vorticity field. By interpreting pressure distributions similar to Figure 1.12, Acharya and Metwally [1] determined that all of the vorticity that was generated at the leading edge and fed into the LEV via the shear layer was generated in the first 1% of the chord. They went on to the show that the formation of the stationary DSVP was concurrent with the diffusion of secondary vorticity from the surface of the airfoil beneath the LEV, and they hypothesized that the accumulation of this secondary vorticity near the leading edge was what eventually led to the reduction of the leading-edge suction peak.

www.manaraa.com

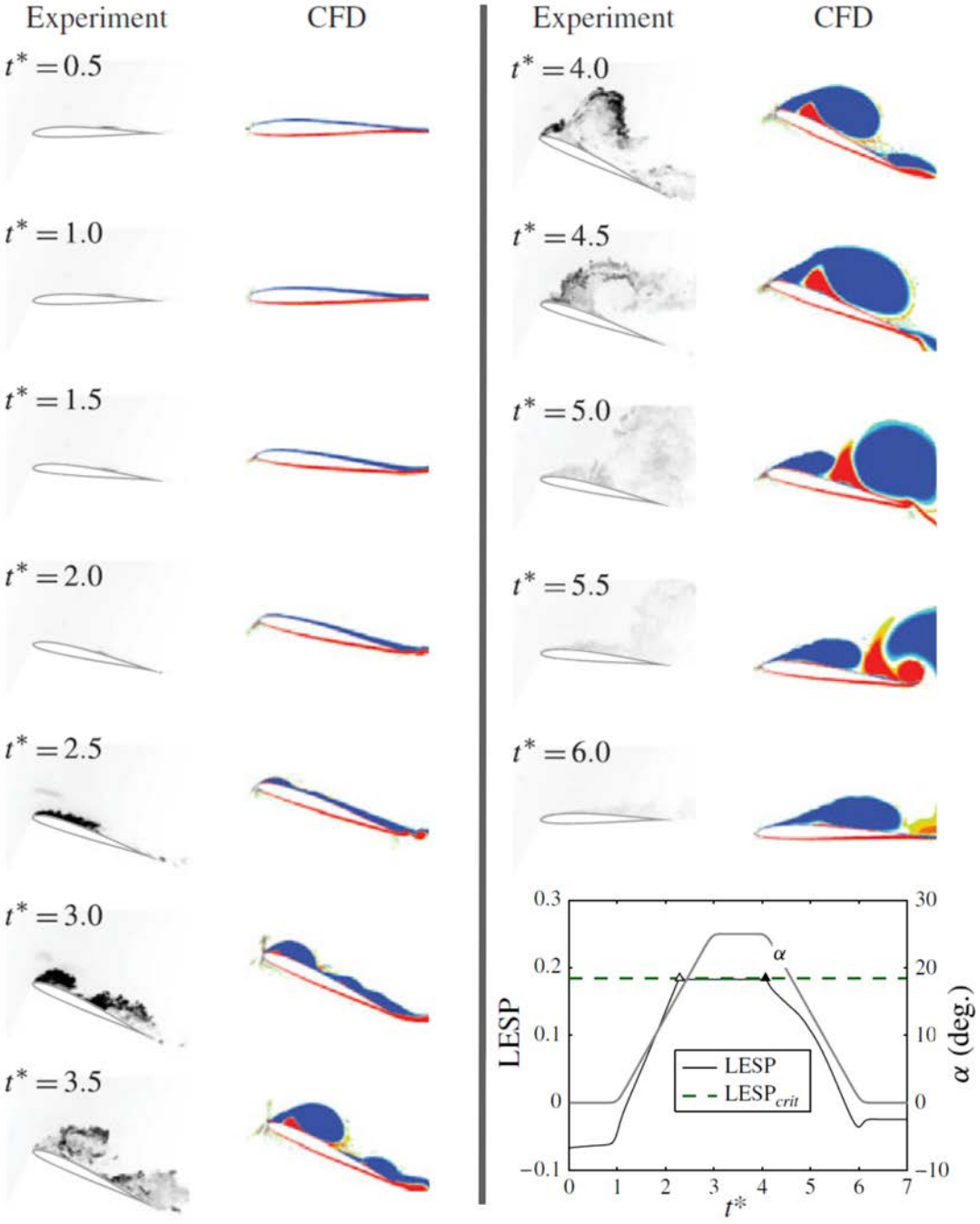

Figure 1.14: Experimental and computational flow fields for a pitching airfoil and the associated LESP time history. Adopted from Ramesh et al. [91]

www.manaraa.com

Visbal and Shang [111] also measured the flux of vorticity diffusing from the surface of a pitching airfoil and showed that the net flux of vorticity was only non-negligible during the period of angular acceleration. But while this net diffusive flux approached zero once a constant pitch rate was reached, they found significant–and equivalent–amounts of positive and negative vorticity were still being diffused into the flow after this point. Thus, it can be inferred that the chordwise distribution of the diffusive flux may play an important role in determining its effect on the evolution of the flow.

Shih and Ho [96] characterized the vorticity transport on a NACA 0012 airfoil being held at a static stall angle of 5° in a sinusoidally oscillating free-stream. Through the use of Laser Doppler Anemometry, velocity profiles were measured very near to the surface of the airfoil. By calculating the gradients of these velocity profiles, they were able to quantify the total flux of opposite-signed vorticity that was being diffused from the surface of the airfoil. In the end, they concluded that the flux of vorticity from the surface of the airfoil governs the dynamics of an LEV while it remains attached to the leading edge. However, once the LEV detached at the end of the deceleration period, the total diffusive flux dropped to zero. After this point, the dynamics of the LEV were characterized as being purely a function of convection.

While the work of Shih and Ho [96] was some of the first to demonstrate that the vortex-airfoil interaction has a significant impact on the development of the LEV, their results were based on a magnitude analysis that showed diffusive effects to be on the same order of magnitude as convective effects during the formation of the LEV. No discussion was provided regarding how the vortex-airfoil interaction might actually affect the evolu-

www.manaraa.com

tion of the LEV; indeed, no such explicit characterization appears to exist anywhere within the literature.

In a work that was similar to Shih and Ho [96], Kuo and Hsieh [63] studied the trajectory of the LEV formed by a pitching NACA 0012 airfoil. Using a control volume analysis, they characterized the flux of vorticity from the surface of the airfoil at nine different chordwise locations and also reported significant fluxes of vorticity from the surface of the airfoil. Furthermore, they showed the magnitude and chordwise-distribution of the surface vorticity flux to be very well correlated with the position and strength of the LEV. In accordance with the work of Shih and Ho [96], it was also demonstrated that the detachment of the LEV led to the surface vorticity flux falling to zero. By tracking the core of the LEV, Kuo and Hsieh [63] characterized this drop in the surface vorticity flux as being caused by the LEV moving away from the surface of the airfoil, thereby weakening the interaction between the two.

These examples demonstrate how the fundamental vorticity transport within the flow can be used to elucidate the intricate flow dynamics associated with an LEV. However, it can also be shown that the aerodynamic performance of a non-accelerating body in an incompressible flow is a direct function of the boundary vorticity flux [125]. Therefore, as the instigator of all the physics within the flow, the study and characterization of boundary vorticity dynamics has the potential to significantly enhance our understanding of complex aerodynamic flows that can aid in the development of effective strategies for flow control.

www.manaraa.com

1.3.2 Flow Control and Boundary Vorticity Manipulation

The topic of flow control relates to any mechanism that manipulates the flow field on or around a solid boundary. In the current context, these systems attempt to improve the performance of an airfoil–or other rigid body–by modifying the distribution of vorticity along its surface by affecting the boundary vorticity flux (BVF). While BVF analyses are not very common, the studies that do exist have produced some important results.

One approach to BVF manipulation uses the fact that an accelerating body within a fluid will create vorticity [125]. By inducing some form of acceleration on the body (e.g. flexibility effects or traveling waves), these techniques attempt to modify the BVF distribution in some favorable manner.

Molki and Sattari [76] studied the vorticity generation on a plunging, deforming arc airfoil. By quantifying the pressure distribution and correlating it with the vorticity field, they were able to show that the asymmetric accelerations seen by the upper and lower surfaces resulted in an increased time-averaged vorticity flux. Zhao et al. [133] showed that reducing the turbulent friction on a flexible wall will result in spanwise oscillations. They also showed that these oscillations would generate traveling waves that would be used to control the BVF. Wu et al. [121] were able to generate similar BVF modifying waves by eliminating vortical structures within the wake using a flexible wall.

Another fundamental flow control technique used for BVF manipulation is the modification of the model geometry. Chandrasekhara et al. [23, 24] performed experiments on an airfoil with a dynamically deforming leading edge that allowed for a means of flow control. By first quantifying the BVF distribution, they were able to orient the flap in a manner

www.manaraa.com

that decreased the large BVF peak at the leading edge and spread it over a larger surface and cause the flow to reattach.

A very powerful example of BVF manipulation was presented by Wu et al. [125] in the optimization of an airfoil's design, the results of which are in Figure 1.15. The first image of Figure 1.15 depicts the original cross section of the airfoil, with an approximation of the baseline BVF distribution. Wu et al. asserted that in order to optimize lift, the peak BVF regions on the top surface need to be concentrated near the leading and trailing edges, and that drag reduction can be achieved by concentrating the peak BVF regions near the middle of the airfoil's lower surface. The second image in Figure 1.15 shows the qualitative attempt by Wu et al. [125] to do this. The final image of Figure 1.15 shows the result of a similar procedure performed by Yamamoto [127] using an optimization algorithm.

The striking similarity between the two results–which were generated independently–demonstrates the robustness of this method. This led Wu et al. [125] to the conclusion that optimization of the BVF only needs to occur in a few key regions for performance optimization.

Another study performed by Wu et al. [124] demonstrated the broad range of applicability of vorticity flux analyses through the diagnosis of flows over delta-wings and bluff-bodies. Not only were parallels drawn between the two geometries, but the fundamental fluid-structure interactions being observed were utilized in the optimization of a compressor rotor and wind turbine blade.

Another approach to geometry-based BVF manipulation was presented by Glezer [39] through the use of synthetic jet actuation. This approach sought to modify aerody-

www.manaraa.com

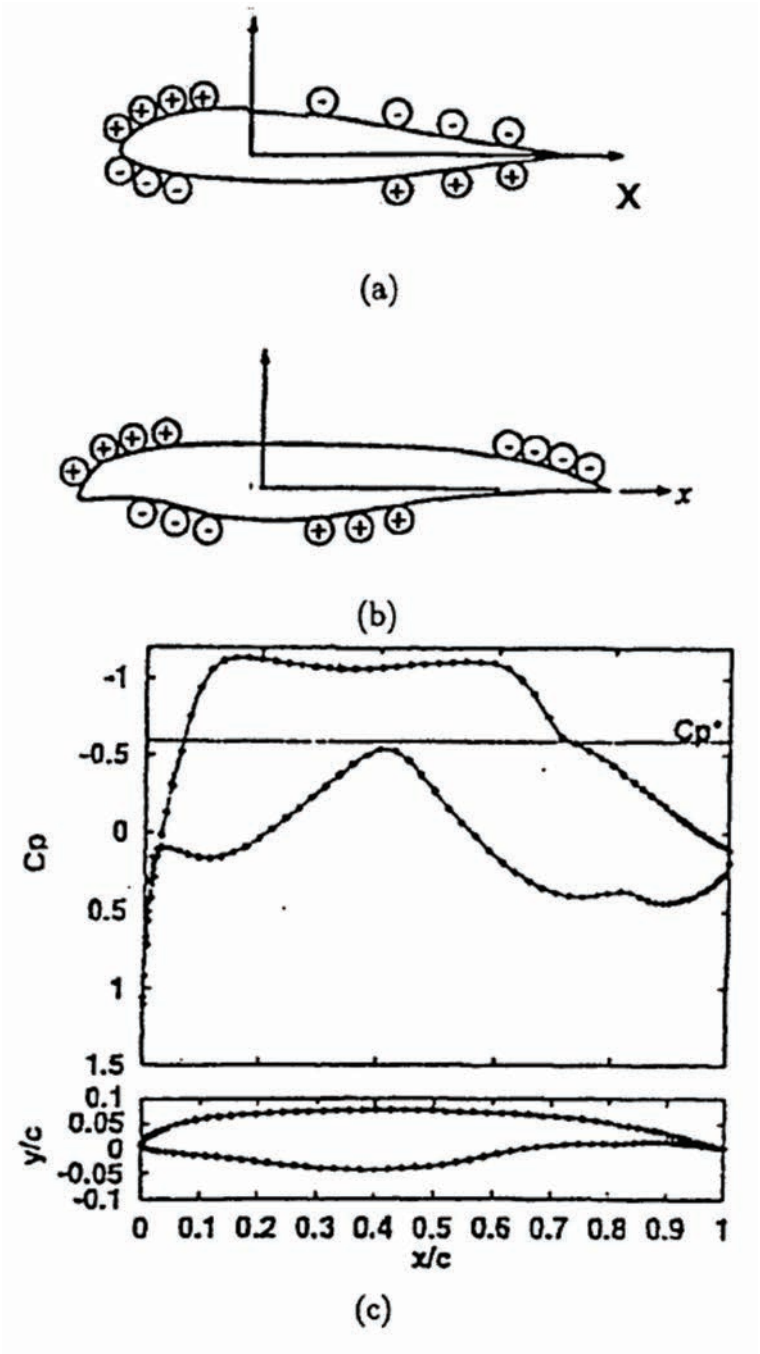

Figure 1.15: Demonstration of boundary vorticity based design optimization. Adopted from Wu et al. [125].

www.manaraa.com

namic forces through the creation and control of "trapped" vorticity on the model's surface via synthetic jets. This aeroforming technique essentially modified the aerodynamic shape of the airfoil. Similarly, Amitay et al. [6] used zero-net mass-flux jets to alter the apparent shape of an object and showed the effect to cause significant changes in the pressure distribution.

1.4 Objective

As reviewed within Section 1.2, the formation and evolution of an LEV has been thoroughly characterized within the literature. However, the works of both Wojcik and Buchholz [118] and Eslam Panah et al. [85] have demonstrated that the diffusion of vorticity from the surface of the airfoil plays a prominent role in governing the stability and strength of an LEV, and thus the performance of an airfoil. This conclusion highlights a major deficit within our understanding of unsteady airfoils and their interaction with vortex dominated flows, as it provides evidence that the critical dynamics for stabilizing an LEV are associated with a term from the Navier-Stoke equation (i.e. viscous diffusion) that is almost always neglected within experimental studies [59, 25, 50, 120].

The works of Shih and Ho [96] and Kuo and Hsieh [63] have further demonstrated that the diffusive flux of vorticity also plays a significant role in the formation and development of the LEV prior to its detachment. It can therefore be assumed that characterizing the near-wall dynamics of an LEV has the potential to significantly enhance our understanding of its evolution.

The primary goal of this dissertation will be to provide a rigorous characterization

www.manaraa.com

of the formation and evolution of a leading-edge vortex that is based on the transport of vorticity both within the bulk flow as well as near the surface of the airfoil. In order to limit the factors governing the development of the LEV, the nominally two-dimensional flow produced by a high aspect-ratio, flat-plate airfoil undergoing a pure-plunge motion will be studied first. Once a baseline description of the flow has been provided, two additional cases will be studied wherein slight modifications will be made to the evolution of the LEV through the introduction of additional source of vorticity. These additional cases will be used to both validate the results of the baseline case as well as to provide a more thorough description of the vorticity transport mechanisms that govern the development of the LEV. The first of these additional cases will consider a finite aspect-ratio plate, which will introduce three-dimensional vorticity transport mechanisms into the flow. Through the use of suction ports on the surface of the plate, the final case will seek to alter the evolution of the LEV by physically removing vorticity-carrying fluid particles from the flow. The specific objectives of this work will be to:

(1) Quantify the sources and sinks of vorticity within the flow in order to elucidate the physical mechanisms that govern the circulation of the LEV.

(2) Identify the on-wall signature that coherent structures from the vorticity field produce within the pressure distribution on the surface of the airfoil.

(3) Determine how the salient features within the pressure distribution couple with the vorticity field to affect the evolution of the LEV.

(4) Propose control strategies for optimizing lift and thrust production by characterizing

www.manaraa.com

the aerodynamic effect of the dominant vorticity transport mechanisms within the evolution of the LEV.

1.5 Overview

In Chapter 2, the framework for a proposed vorticity flux analysis will be derived by integrating the vorticity transport equation over an arbitrary surface. A substantial derivation follows, which breaks the equation down into fundamental transport mechanisms that can be used to identify sources and sinks of vorticity. A second derivation is then presented, which characterizes the vorticity generation mechanisms on a solid-fluid interface in order to identify an alternative method for quantifying the diffusive flux of vorticity from the surface of the airfoil that does not require the use of PIV data.

Chapter 3 describes the experimental models, apparatus and methodologies used to obtain the relevant flux analysis data (three-dimensional velocity field and surface pressure data) for the three distinct experimental investigations. Chapter 4 reviews methods for correcting dynamic signals and then goes on to develop and validate a new methodology for correcting the amplitude and phase attenuation associated with dynamic pressure measurements.

Chapter 5 introduces the results of the vorticity flux analysis from the unforced, nominally-two-dimensional plunging case in order to establish a baseline description for the evolution of the LEV. These results are then interpreted in parallel with the surface pressure distribution in Chapter 6, and conclusions are made about the relationship between vortex structures and their interaction with boundary vorticity. The aerodynamic

www.manaraa.com

implications of these vortex-airfoil interactions are then discussed within Chapter 7. The results of the finite aspect-ratio and suction cases are then presented with Chapters 8 and 9 respectively.

Finally, Chapter 10 provides a summary of the conclusions from this dissertation along with suggestions for future work.

www.manaraa.com

CHAPTER 2
DEVELOPMENT OF THE VORTICITY FLUX ANALYSIS

The first objective of this work that was specified within Section 1.4 was to quantify the sources and sinks of vorticity within the flow field surrounding a plunging, flat-plate airfoil. These sources and sinks of vorticity will be characterized within this dissertation through the implementation of a vorticity flux analysis, which uses a vorticity flux equation to quantify the circulation budget of a specified control region within the flow as well as the amount of vorticity entering and leaving that region. The precise form of this vorticity flux equation will be derived within Section 2.1, after which Section 2.2 will modify one of the terms in order to allow for a more accurate implementation within the experimental cases that were considered.

2.1 Derivation of Vorticity Flux Equation

The purpose of the vorticity flux equation is to quantify the sources and sinks of vorticity within a flow field. As the behavior of the vorticity at any given point within the flow is governed by the vorticity transport equation, its integration over a control region will characterize the dynamics of the vorticity field within that region. Figure 2.1a shows a sample control surface (A_z), which has a surface normal $\hat{z}$ in the z-direction. In order to identify the sources and sinks of vorticity within this control region, the scalar product of the vorticity transport equation with $\hat{z}$ is taken before integration. The boundary of A_z also needs to be defined for this analysis, which is shown in Figure 2.1b as ℓ. The unit vector $\hat{t}$ lies tangent to ℓ and points in the counterclockwise direction. The unit vector $\hat{n}$ is the

www.manaraa.com

(a) (b)

Figure 2.1: (*a*) Control region A_z and (*b*) its boundary ℓ.

outward normal of the boundary, defined such that $\hat{n} = \hat{t} \times \hat{z}$.

Deriving the vorticity flux equation begins with the vorticity transport equation for a fluid with constant properties:

$$\frac{\partial \vec{\omega}}{\partial t} = (\vec{\omega} \cdot \nabla)\,\vec{u} - (\vec{u} \cdot \nabla)\,\vec{\omega} + \nu \nabla^2 \vec{\omega} \tag{2.1}$$

Since this dissertation is concerned with characterizing the sources of spanwise vorticity, the control region A_z will always be specified such that $\hat{z}$ points in the spanwise direction. Thus, only the z-component of the vorticity transport equation (Equation 2.1) needs to be considered. In order to explicate the specific mechanism by which vorticity can be transported, this z-component of Equation 2.1 is presented below in index notation.

$$\frac{\partial \omega_z}{\partial t} = \omega_x \frac{\partial u_z}{\partial x} + \omega_y \frac{\partial u_z}{\partial y} + \omega_z \frac{\partial u_z}{\partial z} - u_x \frac{\partial \omega_z}{\partial x} - u_y \frac{\partial \omega_z}{\partial y} - u_z \frac{\partial \omega_z}{\partial z} + \nu \nabla^2 \omega_z \tag{2.2}$$

The specific nature of these transport mechanisms on the RHS of Equation 2.2 are as follows: the first two terms represent the tilting of vorticity into the z-direction from the x- and y-directions, the third term is associated with the stretching of the vorticity field, the next three terms quantify the convection of vorticity in the x-, y-, and z-directions

www.manaraa.com

respectively and the final term characterizes the diffusion of vorticity. Because Equation 2.2 captures the transport of vorticity at a specific point within the flow, the vorticity flux equation is derived by integrating Equation 2.2 over the control region A_z.

$$\int_{A_z}\left(\frac{\partial \omega_z}{\partial t}\right) dA_z = \int_{A_z}\left(\omega_x\frac{\partial u_z}{\partial x} + \omega_y\frac{\partial u_z}{\partial y} - u_z\frac{\partial \omega_z}{\partial z}\right) dA_z + \int_{A_z}\left(\omega_z\frac{\partial u_z}{\partial z} - u_x\frac{\partial \omega_z}{\partial x} - u_y\frac{\partial \omega_z}{\partial y}\right) dA_z + \int_{A_z}\left(\nu\nabla^2\omega_z\right) dA_z \quad (2.3)$$

In addition to integrating over A_z, Equation 2.3 also rearranges some of the RHS terms for the purpose of clarity. It should be noted that the circulation within the control region is specified as:

$$\Gamma_z = \int_{A_z} \omega_z \, dA_z \quad (2.4)$$

and that Equation 2.3 describes the budget of this circulation within A_z. The LHS characterizes the rate of circulation accumulation within the control region, while the RHS represents the transport mechanism by which vorticity can enter or leave the control region in order to affect this change in the total circulation.

The first group of terms on the RHS of Equation 2.3 represents the three-dimensional vorticity transport mechanisms and the second group captures the two-dimensional (i.e. within the xy-plane) mechanisms for vorticity transport. Note that these first two groups on the RHS are associated with two- and three-dimensional transport mechanisms that are convection-based. The final term on the RHS isolates the diffusive transport mechanisms, which can act in all directions. While a vorticity flux analysis can be performed using Equation 2.3 in its current form, the subsequent discussion goes through some additional modifications that will help to elucidate the underlying physical phenomena that is being

www.manaraa.com

represented by these transport terms.

To begin, Equation 2.5 demonstrates how specifying the control region A_z such that it is time-invariant results in the LHS of Equation 2.3 being equivalent to the time-rate-of-change in the amount circulation contained within the control region, A_z.

$$\int_{A_z} \left(\frac{\partial \omega_z}{\partial t} \right) dA_z = \frac{d}{dt} \int_{A_z} \omega_z dA_z = \frac{d\Gamma_z}{dt} \tag{2.5}$$

The three-dimensional transport terms contained within the first area-integral on the RHS of Equation 2.5 are sufficiently represented as they are; however, modifications will be made to the second group of terms on the RHS so that the stretching, x-convection and y-convection terms are consolidated into a single convective flux. Through the use of the continuity equation for an incompressible flow ($\nabla \cdot \vec{u} = 0$), Equation 2.6a illustrates how the z-derivative within the stretching term can be expressed via x- and y-derivatives. Equation 2.6b goes on to specify how this allows for the stretching term to be consolidated with the x- and y-convection terms.

$$\int_{A_z} \left(\omega_z \frac{\partial u_z}{\partial z} - u_x \frac{\partial \omega_z}{\partial x} - u_y \frac{\partial \omega_z}{\partial y} \right) dA_z = \int_{A_z} \left(-\omega_z \left(\frac{\partial u_x}{\partial x} + \frac{\partial u_y}{\partial y} \right) - u_x \frac{\partial \omega_z}{\partial x} - u_y \frac{\partial \omega_z}{\partial y} \right) dA_z \tag{2.6a}$$

$$= - \int_{A_z} \left(\frac{\partial}{\partial x} (\omega_z u_x) + \frac{\partial}{\partial y} \left(\omega_z u_y \right) \right) dA_z \tag{2.6b}$$

By specifying these two-dimensional transport terms in the form shown in Equation 2.6b, Equation 2.7 illustrates how the area integral can now be expressed as the divergence of the two-dimensional vector field $\omega_z \vec{u}_\Pi$, where $\vec{u}_\Pi$ specifies the velocity field of the xy-plane–i.e. $\vec{u}_\Pi = \langle u_x, u_y, 0 \rangle$.

$$- \int_{A_z} \left(\frac{\partial}{\partial x} (\omega_z u_x) + \frac{\partial}{\partial y} \left(\omega_z u_y \right) \right) dA_z = - \int_{A_z} \left(\nabla \cdot (\omega_z \vec{u}_\Pi) \right) dA_z \tag{2.7}$$

www.manaraa.com

Using Green's theorem, this surface integral over region A_z from Figure 2.1a can be transformed into a line integral about the boundary ℓ from Figure 2.1b.

$$-\int_{A_z} (\nabla \cdot (\omega_z \vec{u}_\Pi))\ dA_z = -\oint_{\partial A_z} (\omega_z \vec{u}_\Pi) \cdot \hat{n}\ d\ell \tag{2.8a}$$

$$= -\oint_{\partial A_z} \omega_z\, (\vec{u}_\Pi \cdot \hat{n})\ d\ell \tag{2.8b}$$

$$= -\oint_{\partial A_z} \omega_z\, (\vec{u} \cdot \hat{n})\ d\ell \tag{2.8c}$$

It should be noted that unit vector $\hat{n}$ is the outward normal of boundary ℓ and is therefore implicitly defined within xy-plane. Thus, the $\vec{u}_\Pi \cdot \hat{n}$ term indicated within Equation 2.8b can be equivalently represented as $\vec{u} \cdot \hat{n}$, as demonstrated by Equation 2.8c.

Equation 2.8c presents the final form of the term within the vorticity flux equation that accounts for the two-dimensional transport of vorticity. By specifying this term as a line integral, it essentially quantifies the amount of vorticity that is convecting through the boundary of the control region within the xy-plane. The term is negative because $\hat{n}$ is the outward normal of ℓ, thus the term characterizes the amount of vorticity leaving the control region.

It is also necessary to modify the final term on the RHS of Equation 2.3. Since this term represents a diffusive flux of vorticity, it can be assumed to be fairly small within the fluid itself, where diffusion is a poor transport mechanism [59, 25]. For this reason, the term only becomes relevant if ℓ lies along a solid boundary. For the cases considered within this dissertation, it is therefore more useful to express the surface integral from this term as a line integral, noting that the associated diffusive flux will only develop a non-negligible contribution if the path of this line integral is specified along a solid-fluid

www.manaraa.com

interface–i.e. the surface of the airfoil. Equation 2.9 begins this transformation of the integral by characterizing the Laplacian of the z-vorticity field as the divergence of the gradient of the vorticity field.

$$\int_{A_z} \left(\nu \nabla^2 \omega_z\right)\, dA_z = \nu \int_{A_z} \left(\nabla \cdot \nabla \omega_z\right)\, dA_z \tag{2.9}$$

Equation 2.10a uses the divergence theorem to express the surface integral of Equation 2.9 as a line integral, which is then simplified and presented in Equation 2.10b. For annotation purposes, any portion of ∂A_z that lies along the surface of the airfoil will be called S.

$$\nu \int_{A_z} \left(\nabla \cdot \nabla \omega_z\right)\, dA_z = \nu \oint_{\partial A_z} \left(\nabla \omega_z\right) \cdot \hat{n}\, d\ell \tag{2.10a}$$

$$= \nu \int_{S} \frac{\partial \omega_z}{dn}\, d\ell \tag{2.10b}$$

By substituting Equations 2.5, 2.8c and 2.10b into Equation 2.3, Equation 2.11 presents the vorticity flux equation.

$$\frac{d\Gamma_z}{dt} = \int_{A_z} \left(\omega_x \frac{\partial u_z}{\partial x} + \omega_y \frac{\partial u_z}{\partial y} - u_z \frac{\partial \omega_z}{\partial z}\right) dA_z - \oint_{\partial A_z} \omega_z \left(\vec{u} \cdot \hat{n}\right)\, d\ell + \nu \int_{S} \frac{\partial \omega_z}{\partial n}\, d\ell \tag{2.11}$$

Summarizing Equation 2.11, the LHS corresponds to the time rate-of-change in the circulation of control region A_z. The first two terms within the surface integral on the RHS of the equation account for the tilting of vorticity into the z-direction from the x- and y-directions. The third term within this surface integral quantifies the amount of vorticity that is entering the control region via a spanwise convective flux, which can be seen to be dependent on the spanwise-gradient of the vorticity field. The first line integral on the RHS captures the convection of vorticity across the boundary of the control region (ℓ), and

www.manaraa.com

the final term on the RHS quantifies the diffusive flux of vorticity from the surface of the airfoil. It should be noted that this diffusive flux of vorticity is equivalent to the boundary vorticity flux that was discussed within Section 1.3.2.

2.2 Characterization of the Diffusive Flux of Vorticity

While most of the terms within Equation 2.11 are in their final form, the term that accounts for the diffusion of vorticity from the surface of the airfoil–the final term on the RHS of Equation 2.11–needs some additional modification. In order to quantify the diffusive flux in its current form, the gradient of the vorticity field at the surface of the airfoil would need to be measured. This would require the velocity field near the surface of the airfoil to be very accurately resolved. This was achieved within the works of both Shih and Ho [96] and Kuo and Hsieh [63] through the use of Laser Doppler Anemometry (LDA). Particle Image Velocimetry (PIV) will be used within the current work, and while this will allow for the characterization of the entire velocity field above the surface of the airfoil, laser reflections will decrease the accuracy of measurements made near the surface of the airfoil. Furthermore, particle seeding considerations will limit the resolution at which the velocity field can be specified. It is therefore desirable to modify the final term on the RHS of Equation 2.11 so that it can be characterized without the use of the near-wall velocity field.

Lighthill [68] tells us that all the vorticity within a barotropic flow must be generated on a solid boundary, as the no-slip condition allows forces within the flow to impose a rotation on wall-bounded fluid elements. The term expressed within Equation 2.10b essen-

www.manaraa.com

tially characterizes how much vorticity is diffused into the flow after this on-wall generation occurs. It is therefore possible to derive an alternate form for this diffusive flux term by actually identifying the specific vorticity generation mechanisms that are present at the wall.

All of the subsequent derivations have been adapted from the works of Wu et al. [126, 122, 53], who pioneered the development of an equation that fully characterizes the vorticity generation mechanisms of any arbitrary fluid-structure interface. While the following derivation follows the same approach used by Wu et al. [126, 122], the current analysis uses a variety of assumptions and simplifications in order to present a concise characterization of the physics relevant to the types of fluid-structure interactions that are considered within this dissertation.

As this generation of vorticity requires a force within the flow, we begin by considering the Navier-Stokes equation:

$$\rho\left(\frac{d\vec{u}}{dt} + \vec{u}\cdot\nabla\vec{u}\right) = -\nabla p + \mu\nabla^2\vec{u} \tag{2.12}$$

In an attempt to simplify the appearance of the following analysis, the left-hand side of Equation 2.12 will be represented as Equation 2.13.

$$\frac{d\vec{u}}{dt} + \vec{u}\cdot\nabla\vec{u} = \vec{a} \tag{2.13}$$

It also helps to expand the second term on the RHS of Equation 2.12 using the vector identity reported in Equation 2.14a. Equation 2.14b then simplifies the result based on the fact that the divergence of the velocity field within an incompressible fluid is zero ($\nabla\cdot\vec{u} = 0$),

www.manaraa.com

after which the remaining term is modified using the definition of vorticity, $\vec{\omega} = \nabla \times \vec{u}$.

$$\mu\nabla^2\vec{u} = \mu\nabla\left(\nabla \cdot \vec{u}\right) - \mu\nabla \times \left(\nabla \times \vec{u}\right) \tag{2.14a}$$

$$= -\mu\nabla \times \vec{\omega} \tag{2.14b}$$

Equation 2.13 and 2.14b can then be substituted into Equation 2.12, which yields Equation 2.15 after all of the terms have been gathered on one side.

$$\vec{a} + \frac{\nabla p}{\rho} + \nu\nabla \times \vec{\omega} = 0 \tag{2.15}$$

As defined by Wu and Wu [126]–and illustrated within Figure 2.2–vorticity is generated at the surface of the airfoil when a force is applied to a surface-bound fluid element so that the principal axes of its strain-rate tensor is rotated out of the wall-normal direction. This precise definition was posed following an assertion by Wu and Wu [126] that the no-slip condition prevents a wall-bound fluid element from actually rotating and that a vorticity-containing fluid element only develops an angular velocity after it has been diffused into the flow. Thus, the "rotation of the principle axis of the strain-rate tensor" was used to characterize a way for a wall-bound fluid elements to contain vorticity without actually rotating. While it is worth considering, this precise description is not particularly relevant to the mechanics of vorticity generation, and a majority of studies are content with characterizing the process as if the wall-bound fluid element were actually allowed to rotate [68, 77, 123, 16]. Therefore, for the purpose of this dissertation, it is sufficient to say that the generation of vorticity occurs when a force–directed tangential to the surface of the airfoil–acts on a wall-bound fluid element, thus imposing a rotation on that element due to the no-slip condition.

www.manaraa.com

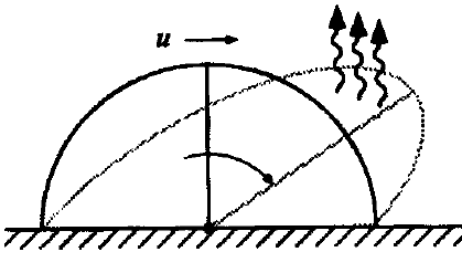

Figure 2.2: Schematic depicting the generation of vorticity via the deformation of a wall-bound fluid element. Adopted from Wu and Wu [126].

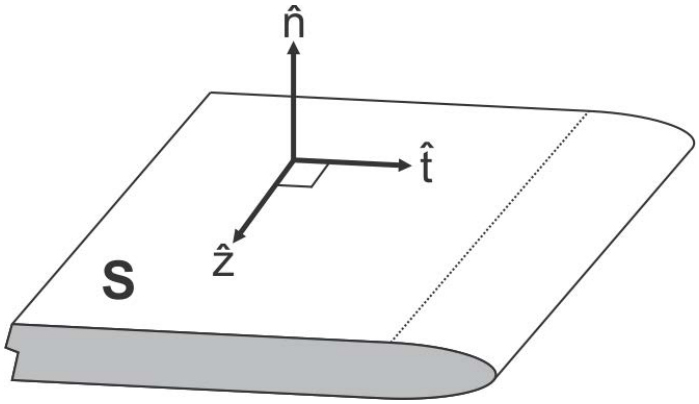

Figure 2.3: Coordinate system of an arbitrary solid surface S upon which vorticity is generated.

Consider the arbitrary solid surface S shown in Figure 2.3 that has the surface-normal unit vector $\hat{n}$ and surface-tangent unit vectors $\hat{t}$ and $\hat{z}$, which are defined such that $\hat{z} = \hat{t} \times \hat{n}$. Note that all subsequent derivation within this section will utilize this coordinate system shown in Figure 2.3, and not the one shown in Figure 2.1. However, it can be noted that $\hat{z}$ will once again be specified in the spanwise direction, so that this analysis is concerned with characterizing the mechanism for the generation of ω_z at the boundary.

www.manaraa.com

The generation of vorticity on surface S can be quantified by taking the cross product of the surface-normal unit vector ($\hat{n}$) and Equation 2.15, the result of which is shown in Equation 2.16.

$$0 = (\hat{n} \times \vec{a}) + (\hat{n} \times \frac{\nabla p}{\rho}) + \nu(\hat{n} \times (\nabla \times \vec{\omega})) \tag{2.16}$$

Equation 2.17 breaks down the terms from Equation 2.16 and presents them in their explicit index-notation, with the unit vectors defined as shown in Figure 2.3.

$$(\hat{n} \times \vec{a}) + (\hat{n} \times \frac{\nabla p}{\rho}) + \nu(\hat{n} \times (\nabla \times \vec{\omega})) = \left(a_z + \frac{1}{\rho}\frac{\partial p}{\partial z} + \nu\left(\frac{\partial \omega_n}{\partial t} - \frac{\partial \omega_t}{\partial n}\right)\right)\hat{t} + \left(-a_t - \frac{1}{\rho}\frac{\partial p}{\partial t} + \nu\left(\frac{\partial \omega_n}{\partial z} - \frac{\partial \omega_z}{\partial n}\right)\right)\hat{z} \tag{2.17}$$

where a_t and a_z are the components of the acceleration vector $\vec{a}$ in the tangential ($\hat{t}$) and spanwise ($\hat{z}$) directions. Similarly, $\partial/\partial t$ and $\partial/\partial z$ represent derivatives taken in the tangential ($\hat{t}$) and spanwise ($\hat{z}$) directions. Finally, $[\omega_t, \omega_n, \omega_z]$ are the components of the vorticity vector $\vec{\omega}$ in the $\hat{t}$, $\hat{n}$ and $\hat{z}$ directions (from Figure 2.3) respectively.

The objective of the current analysis is to quantify the diffusion of the spanwise component of vorticity from the surface of the airfoil, and will therefore only utilize the z-component that is defined in Equation 2.17. This z-component is isolated in Equation 2.18.

$$0 = -a_t - \frac{1}{\rho}\frac{\partial p}{\partial t} + \nu\left(\frac{\partial \omega_n}{\partial z} - \frac{\partial \omega_z}{\partial n}\right) \tag{2.18}$$

once again, where $\partial/\partial t$ represents the derivative in the tangential direction and a_t is the tangential-component of acceleration vector.

Equation 2.18 can then be rearranged to provide an expansion for the wall-normal

www.manaraa.com

gradient of ω_z, which represents the diffusive flux of spanwise vorticity from the surface.

$$\nu\frac{\partial\omega_z}{\partial n} = -a_t - \frac{1}{\rho}\frac{\partial p}{\partial t} + \nu\frac{\partial\omega_n}{\partial z} \tag{2.19}$$

The first two terms on the RHS of Equation 2.19 represent vorticity generated by the tangential component of the wall acceleration and the tangential gradient of the surface pressure distribution. The physics associated with the third term on the RHS of Equation 2.19 are less transparent. This term has been associated with vorticity generation mechanisms that occur on curved surfaces [126, 7]. However no additional derivation is required for the current analysis, as the use of a flat-plate airfoil of uniform span within the experiments performed for this thesis means that both ω_n and its spanwise gradient will be zero. It should be noted that in order for this simplification to be valid, any portion of the airfoil's surface from which the diffusive flux of vorticity is considered must have zero curvature. Thus, boundary ℓ from Figure 2.1b cannot be prescribed along the rounded leading or trailing edges of the airfoil.

Equation 2.19 can be further reduced based on the fact that this dissertation considers a pure-plunge motion, as this means the acceleration of the airfoil will always be defined normal to the portion of the airfoil's surface being considered–noting that the aforementioned curvature-restriction requires that the leading and trailing edge not be included within this analysis. Thus, a_t will always be zero and Equation 2.19 can be rewritten as:

$$\nu\frac{\partial\omega_z}{\partial n} = -\frac{1}{\rho}\frac{\partial p}{\partial t} \tag{2.20}$$

As it is the only pertinent generation mechanism, Figure 2.4 presents a schematic from Wu et al. [123] to show how a surface pressure gradient leads to the generation

www.manaraa.com

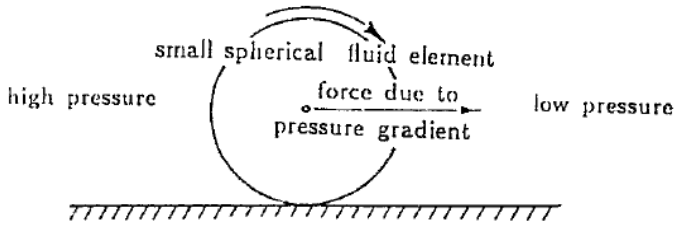

Figure 2.4: Schematic depicting the generation of vorticity via a surface pressure gradient. Adopted from Wu et al. [123].

of vorticity. The figure illustrates how a wall-bound fluid element exposed to a pressure gradient will experience a force that is directed opposite the pressure gradient. Since the fluid-element remains stationary at the surface of the airfoil due to the no-slip condition, this force will impose a torque on the element that results in the generation of vorticity that can then diffuse into the flow.

While deriving Equation 2.20 has helped to more sufficiently resolve the physics associated with the diffusive flux of vorticity by characterizing the vorticity generation mechanism acting at the surface of the airfoil, this correlation will also help with the implementation of the vorticity flux analysis. As stated at the beginning of this section, it would be very difficult to quantify the wall-normal gradient of ω_z based on the PIV data that was collected for this work. However, Equation 2.20 indicates that this term can be equivalently modeled by surface pressure gradients. In order to avoid the arduous task of resolving the near-wall vorticity field, transient pressure data were obtained for each of the cases being considered within this dissertation in order to quantify the diffusive flux of vorticity.

www.manaraa.com

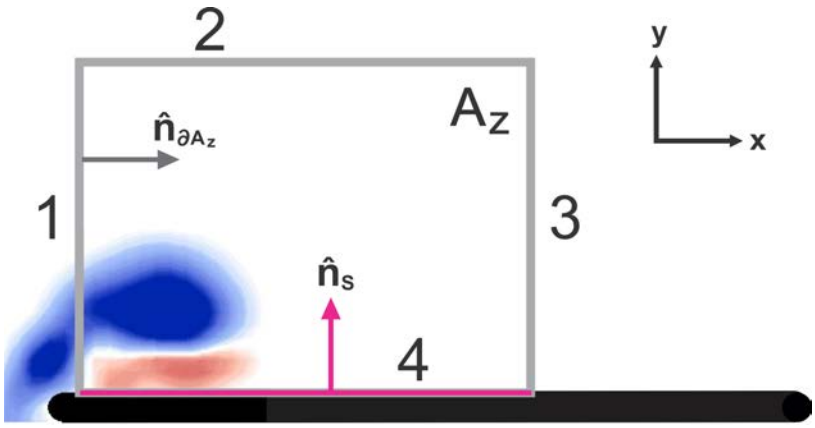

Figure 2.5: Control region used for the vorticity flux analyses within this dissertation.

2.3 Model Implementation

When developing the final form of the vorticity flux equation that will be used within this dissertation, it is necessary to first specify the control region (A_z) that will be used. Because the LEV will be the main focus of this work, it should remain within the control region throughout the downstroke of the airfoil. Part of the control region must also lie on the surface of the airfoil so the diffusive flux of vorticity from the surface of the airfoil–which is an important component of the budget–can be calculated using the surface pressure gradients. To satisfy these conditions, a rectangular control region was chosen, with one side prescribed along the surface of the airfoil.

Figure 2.5 depicts this control region within a representative approximation of the vorticity field produced by a plunging airfoil. The blue and red isocontours within Figure 2.5 represent regions of either negative vorticity (i.e. the leading-edge vortex) or positive vorticity (i.e. the opposite-signed vortex), and the blacked out region represents the cross-sectional shape of the flat-plate airfoil being used within these experiments.

www.manaraa.com

Each boundary segment of the control region within Figure 2.5 is numbered so that the individual contributions of the fluxes through each segment can be considered. It should be noted that since Boundary 4 is prescribed along the surface of the airfoil, this is the boundary over which the diffusive flux will be calculated, which is why the segment is highlighted in pink. Based on the previously established terminology, this portion of the control region boundary ∂A_z that lies on the surface of the airfoil is denoted as S. In order to properly account for the diffusion of vorticity from this surface, the normal unit vector of this boundary ($\hat{n}_S$) must be directed in the surface-normal direction (i.e. in the positive y-direction).

In order to remain consistent, specifying $\hat{n}_S$ as the inward pointing normal of Boundary 4 requires that the unit normal of Boundaries 1-3 ($\hat{n}_{\partial A_z}$) also be specified as an inward pointing normal. While this change in the convention that was specified in Figure 2.1b will require some minor alterations to Equation 2.11, it should be noted that this modification is useful for the sake of terminology as well as consistency. By specifying $\hat{n}_{\partial A_z}$ as an inward normal, it allows a "source" of vorticity to be defined as vorticity entering the control region.

The first step in deriving the final form of the vorticity flux equation is to apply this coordinate transformation to Equation 2.11, yielding Equation 2.21.

$$\frac{d\Gamma_z}{dt} = \int_{A_z} \left(\omega_x \frac{\partial u_z}{\partial x} + \omega_y \frac{\partial u_z}{\partial y} - u_z \frac{\partial \omega_z}{\partial z} \right) dA_z + \oint_{\partial A_z} \omega_z \left(\vec{u} \cdot \hat{n} \right) \, d\ell - \nu \int_S \frac{\partial \omega_z}{\partial n} \, d\ell \qquad (2.21)$$

Because this coordinate transformation would only affect line integrals, the only difference between Equations 2.11 and 2.21 is a change in the sign of the last two terms on the RHS.

The next step is to use Equation 2.20 to eliminate the wall-normal derivative of ω_z

www.manaraa.com

within the final term on the RHS of Equations 2.21 in favor of the surface pressure gradient in the tangential direction. Referencing the coordinate system of Figure 2.5, it can be noted that this surface-tangent direction corresponds to the positive x-direction. For the purposes of this dissertation, Equation 2.20 can therefore be equivalently represented as:

$$\nu \frac{\partial \omega_z}{\partial n} = -\frac{1}{\rho}\frac{\partial p}{\partial x} \tag{2.22}$$

Now, substituting Equation 2.22 into Equation 2.21 produces:

$$\frac{d\Gamma_z}{dt} = \int_{A_z} \left(-u_z \frac{\partial \omega_z}{\partial z}\right) dA_z + \int_{A_z} \left(\omega_x \frac{\partial u_z}{\partial x} + \omega_y \frac{\partial u_z}{\partial y}\right) dA_z + \oint_{\partial A_z} \omega_z \left(\vec{u} \cdot \hat{n}\right) d\ell + \frac{1}{\rho} \int_S \frac{\partial p}{\partial x} d\ell \tag{2.23}$$

Note that Equation 2.23 breaks the total three-dimensional flux of vorticity within the area integral of Equation 2.21 into the individual spanwise convection and tilting terms.

While the terms within Equation 2.23 are now all in their final form, the geometry of the control region specified in Figure 2.5 can be used to simplify the integrals. Specifically, because Boundary 4 lies on a solid surface, no vorticity can convect through that boundary. Thus the two-dimensional convective flux of vorticity ($\omega_z \left(\vec{u} \cdot \hat{n}\right)$) will only be evaluated along Boundaries 1-3. Alternatively, since the diffusive flux is only evaluated along the surface of the airfoil, the line integral over boundary S can be equivalently represented as the line integral over Boundary 4. Furthermore, since Boundary 4 lies entirely in the x-direction, the $d\ell$ within the diffusive flux term can be replaced with dx.

Applying these modifications to Equation 2.23 results in:

$$\frac{d\Gamma_z}{dt} = \int_{A_z} \left(-u_z \frac{\partial \omega_z}{\partial z}\right) dA_z + \int_{A_z} \left(\omega_x \frac{\partial u_z}{\partial x} + \omega_y \frac{\partial u_z}{\partial y}\right) dA_z + \int_{1-3} \omega_z \left(\vec{u} \cdot \hat{n}\right) d\ell + \int_4 \frac{\partial p}{\partial x} dx \tag{2.24}$$

Noting that the convective flux through Boundaries 1-3 can be explicitly written for each

www.manaraa.com

boundary as:

$$\int_{1-3} \omega_z \left(\vec{u} \cdot \hat{n}\right) d\ell = \int_{1} \omega_z u_x dy - \int_{2} \omega_z u_y dx - \int_{3} \omega_z u_x dy \tag{2.25}$$

Summarizing Equation 2.24 one final time, the LHS corresponds to the time-derivative of the amount circulation contained within the control region A_z. The first term on the RHS of the equation quantifies the amount of vorticity that is entering the control region via a spanwise convective flux, and the next set of terms accounts for the tilting of vorticity into the z-direction from the x- and y-directions. The first line integral on the RHS captures the convection of vorticity across Boundaries 1-3 of the control region shown in Figure 2.5, and the final term on the RHS quantifies the diffusion of vorticity from the surface of the airfoil through Boundary 4. It should be noted that while Chapters 5-9 will present the values that have been calculated for these fluxes within each experimental case, an uncertainty analysis of these calculations is provided in the Appendix.

In order to evaluate all of the terms within Equation 2.24, two experiments need to be performed for each of the three cases being considered: one for characterizing the three-dimensional velocity and vorticity fields and one to measure the pressure distribution on the surface of the airfoil.

In the cases to be presented, the three-dimensional characterization of the velocity and vorticity fields was done in one of two ways. In the baseline and suction cases, Stereo Particle Image Velocimetry (Stereo PIV) was used to define the three-dimensional velocity field at three different, closely spaced spanwise planes. Collecting these three planes of data made it possible to calculate the spanwise gradients of the velocity and vorticity fields that are required for characterizing the three-dimensional transport of vorticity (first term

www.manaraa.com

on RHS of Equation 2.23). Alternatively, two-component, planar PIV was implemented within the finite aspect-ratio case. Three-dimensional flow characterization was achieved by imaging multiple horizontal and vertical planes whose two-dimensional data could be compiled into a three-dimensional reconstruction of the velocity field.

Within the second set of experiments, time-resolved pressure measurements needed to be obtained at the surface of the airfoil. These measurements were acquired via an array of pressure taps that were spaced out along the airfoil chord, thus allowing for the computation of chordwise pressure gradients ($\partial p/\partial x$). Unfortunately, obtaining reliable transient pressure data can be difficult, as the response of the measurement system will have some characteristic phase and amplitude error. Generally, transient pressure data are only measured when the resonant frequency of the system (which includes the sensor and any fluid-transmission lines) is much higher than that of the signal being measured. However, the use of water as a working fluid–due to the fact that experiments were performed in a water channel–caused the pressure measurement system being used within this dissertation to have a non-negligible response time. It was therefore necessary to develop a robust method for correcting the response data for any non-ideal pressure measurement system so as to obtain a more reliable estimate of the true input.

The details of these experiments are presented next in Chapter 3, after which Chapter 4 presents the method that was developed for the dynamic correction of the pressure data.

www.manaraa.com

CHAPTER 3
METHODOLOGY

3.1 Overview

Three different experimental cases are considered within this dissertation. The first case studied was a rigid, flat-plate airfoil of aspect-ratio 4 (AR4) oscillating in a pure-plunge motion. The high aspect ratio resulted in a nominally two-dimensional flow that was further promoted by considering the flow at the spanwise centerline of the airfoil. As this case was used to establish the baseline dynamics of the flow, it will be referred to as the "baseline case."

The experimental conditions for the second test case were identical to those of the baseline, except a flat-plate airfoil of aspect-ratio 2 (AR2) was used. This case introduced more three-dimensionality into the flow and will be referred to as the "AR2 case" or "finite-AR case."

The final experimental case used the exact same experimental model and setup as the baseline case. However within this "suction case," suction ports on the surface of the airfoil were used to remove vorticity-containing fluid from beneath the LEV.

All experiments were performed in a recirculating, free-surface water channel at Reynolds numbers on the order of typical micro-air vehicles and smaller birds [131]. Similarly, the kinematics of the plunge motion were prescribed to be within the parameter space relevant to biological locomotion [101].

Details about the airfoil geometry and kinematics of these three cases are reported

www.manaraa.com

in Section 3.2, along with a description of the water channel within which experiments were performed. Section 3.3 then provides details about the suction system that was used within the "suction case," including a description of the system setup as well as a characterization of the actual suction that was applied. Section 3.4 goes on to describe the PIV experiments that were used to characterize the velocity field around the airfoil. Section 3.5 provides details about the force measurements that were collected for the baseline and suction cases, and Section 3.6 describes the method used for resolving the pressure distribution on the surface of the airfoil, covering both the pressure measurement system as well as the experimental approach.

3.2 Model Geometries and Experimental Techniques

All three experimental cases considered flat-plate airfoils–with varying aspect ratios–that were oscillated in a pure-plunge motion. The airfoil used in the baseline and suction cases had an aspect ratio of 4 (span = 304.8 mm), and the airfoil from the AR2 case had an aspect ratio of 2 (span = 152.4 mm). The airfoils were constructed out of aluminum, and both had a chord length (c) of 76.2 mm, thickness of 3.175 mm and circular rounds on the leading and trailing edges. A schematic of the cross section of the two airfoils is given in Figure 3.1a. Figure 3.1b shows the spanwise dimensions of the two airfoils as well as the spanwise planes (in red) at which pressure data were collected at the surface of the airfoil. This figure also shows the mounting brackets at the top of each airfoil by which their kinematics were driven. The plunge motion was created using a scotch yoke mechanism that was driven by a Emerson Control Techniques XVM-6011-TONS motor and an

www.manaraa.com

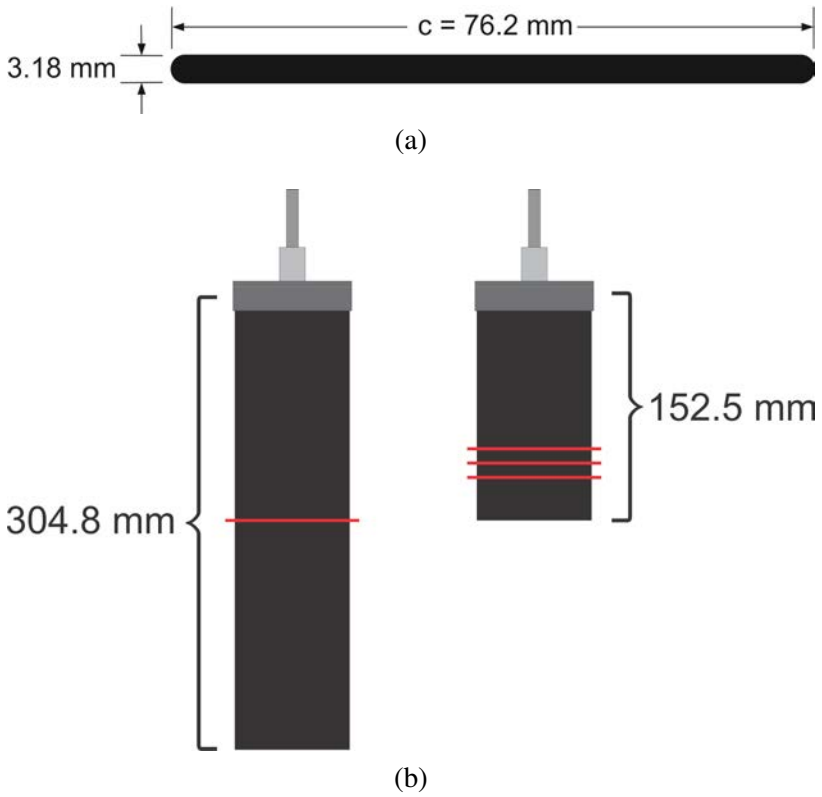

Figure 3.1: (*a*) chordwise and (*b*) spanwise dimensions of the flat-plate airfoils.

Emerson EP-B amplifier. The leading edge was thus oscillated in a sinusoidal motion with the transverse displacement specified as:

$$h(t) = -h_0 sin(2\pi f t) \tag{3.1}$$

The airfoil's position was measured using a US Digital EM1 Transmissive Optical Encoder Module and a 120-counts-per-inch Linear Strip with an index channel that could be used to trigger PIV data acquisition at specific phases of the plunge motion. Within the suction case, the signal from this linear encoder was also used to trigger the application of suction over a specified portion of the airfoil's motion.

The motor was programmed and operated using a Galil DMC-4040 motion control

www.manaraa.com

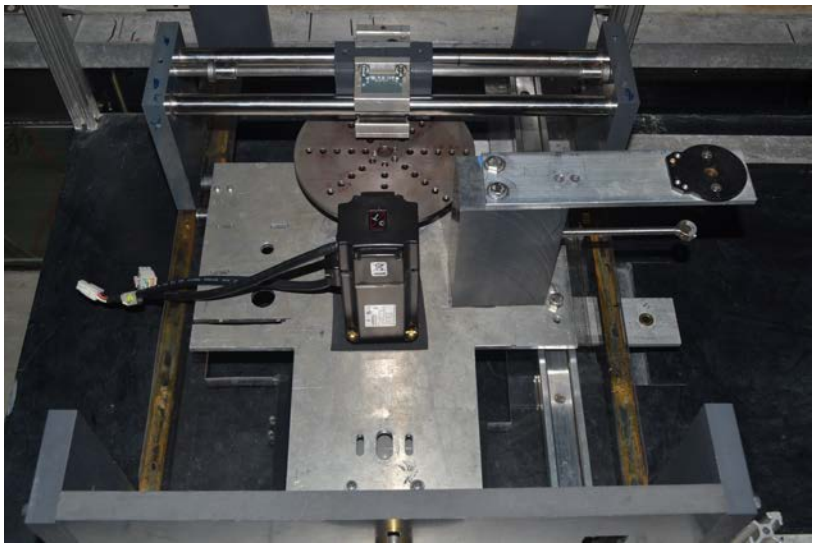

Figure 3.2: Scotch yoke mechanism used to generate the sinusoidal plunge motion.

system. The kinematics of the motion were specified such that the dimensionless plunge amplitude (h_0/c) and the Strouhal number ($St = 2fh_0/U_\infty$) were both equal to 0.3, which also correlated to a reduced frequency of $k = (2\pi f/U_\infty) = \pi/2$. The scotch yoke mechanism (Figure 3.2) was placed atop a free-surface water channel that had a width of 0.61 meters and depth of 0.33 meters. The free surface of the channel was constrained by rigid plates that extended 0.6 meters both up and downstream of the airfoil to prevent the formation of surface waves. The water channel flow was conditioned using a honeycomb, five screens and an 8:1 plenum-to-channel contraction ratio, resulting in a turbulence intensity of less than 0.3 percent. The airfoil was approximately 0.75 meters downstream of the contraction. Figure 3.3 shows the position of the scotch yoke, free-surface plates and the water channel contraction. The free-stream velocity for all experimental cases was maintained at U_∞ = 0.13 m/s, resulting in a chord-based Reynolds number of $Re_c = 10,000$.

www.manaraa.com

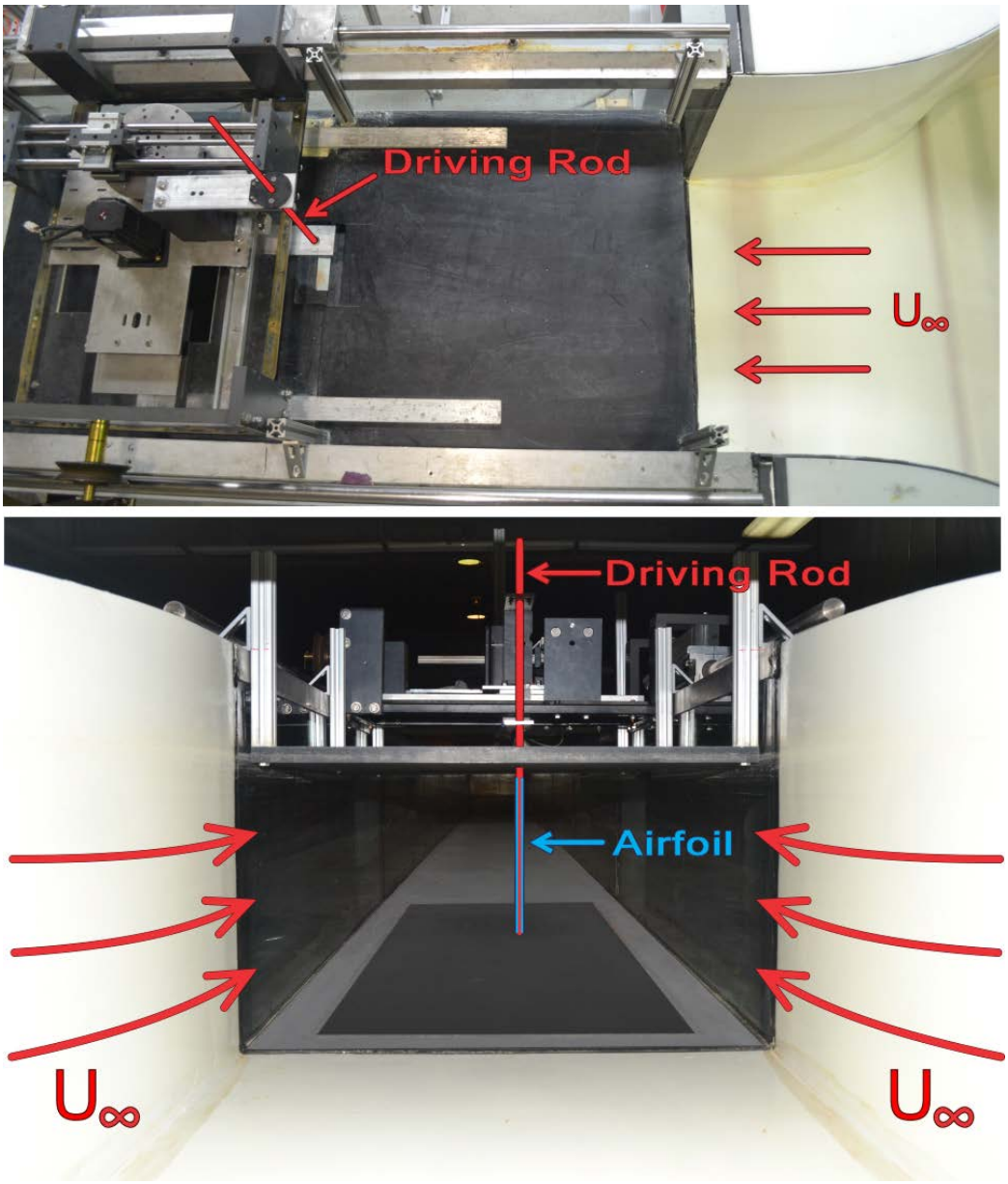

Figure 3.3: Water channel and the position of the scotch yoke.

www.manaraa.com

3.3 Suction System and Internal Fluid Transmission Lines of the AR4 Airfoil

The experimental objective of the suction case was to remove vorticity-containing fluid particles from the flow by applying suction at the surface of the airfoil. In order to implement this suction, an internal transmission system was built into the AR4 airfoil that was used to connect an external suction reservoir to the suction ports on the surface of the airfoil. In addition to this internal suction system, a completely separate internal transmission system was also made within the AR4 airfoil in order to allow for the measurement of the surface pressure distribution without having to use any external tubing. This resulted in there being an intricate network of fluid-transmission lines contained within the AR4 airfoil, which are shown in Figure 3.4a and characterized below. It should be emphasized that the suction ports and their associated internal transmission lines within the AR4 airfoil form an actuator that is used to remove fluid from the flow. On the other hand, the pressure taps and their associated internal transmission lines are instruments used for the measurement of surface pressures.

The suction (blue) and pressure (red) transmission systems depicted within Figure 3.4a were milled into the pressure-side of the airfoil, which corresponds to the underside of the airfoil depicted in Figure 3.1a. This ensured that the suction-side of the airfoil–upper surface in Figure 3.1a–would remain relatively unmarred (see Figure 3.4b). In addition to the suction and pressure transmission systems, Figure 3.4a also shows a dark gray region covering a majority of the airfoil's surface. The first step in machining the pressure-side of the airfoil was to recess this dark gray region by 0.3 mm, and all of the transmission lines were subsequently machined within this recessed region. Once all of the internal systems

www.manaraa.com

had been created, a rigid piece of shim stock was epoxied into this recessed region in order to reseal the suction-side of the airfoil so that the sealed surface was flush with the rest of the airfoil.

Figure 3.4a shows the suction transmission system in blue, which can be seen to start at the root of the airfoil at x/c = 0.792 as a narrow channel that extends down towards the mid-span (note: x is the distance from the leading edge of the airfoil). This narrow channel eventually splits in two, with one of the branches continuing down past the mid-span and the other moving in the chordwise direction towards the leading edge. In order to keep these branches from intersecting the pressure transmission lines, the portion of these suction channels shown in light blue within Figure 3.4a were milled out of the suction-side of the airfoil. A picture of the suction-side of the airfoil is shown in Figure 3.4b, within which this portion of the suction transmission line is plainly visible–note the slight recess around the edge of these channels. When this small portion of the suction channel was sealed, an "L"-shaped piece of shim stock was epoxied to this recessed surface, leaving the surface of the shim stock flush with the rest of the airfoil.

Figure 3.4a shows that at x/c $\approx$ 0.375, the two branches of the original suction channel expand into a large upper and lower suction cavity. The purpose of these cavities was to diffuse the suction being transmitted through the system so that it could be applied at the suction ports with relative uniformity–note that these ports cover 75% of the airfoil's span. These suction ports–which had a diameter of 0.8 mm–are shown in yellow within Figure 3.4a at the very end of the suction cavities at a chordwise location of x/c = 0.125. Each cavity contained 36 of these suction ports, uniformly spaced in the spanwise direction

www.manaraa.com

at 3.175 mm intervals. Because there was a pressure tap located at x/c = 0.125 at the mid-span, the first suction ports within the upper and lower cavities were specified 1.588 mm above and below the spanwise-centerline. Thus, when the suction case PIV data is collected at the mid-span of the airfoil, the imaging plane is not situated directly above a suction port, but rather halfway between two suction ports. It should also be noted that the presence of the pressure tap at x/c = 0.125 prevented the upper and lower cavities from being connected to each other.

In addition to the suction transmission system, Figure 3.4a depicts two pressure transmission lines (in red) that were used to connect the chordwise array of twenty-four pressure taps (each having a diameter of 1.19 mm) at the airfoil mid-span to the pressure transducer located above the water channel. Both of these pressure transmission lines start at the root of the airfoil, but while one extends straight down to the mid-span, the other cuts toward the leading edge so that it can navigate around the upper suction cavity before extending down towards the mid-span. Though not visible within Figure 3.4a, these two pressure transmission lines connect to two distinct, chordwise channels once they reach the mid-span. The first six pressure taps–the last of which is located at x/c = 0.125–are contained within the upstream channel. The other eighteen pressure taps are located within the second channel, which starts at x/c=0.146 and ends at x/c=0.917. The actual chordwise position of these twenty-four pressure taps will be listed in Section 3.6, along with a description of how pressure measurements were taken at each port.

Figure 3.4b displays a picture of the pressure-side of the airfoil. The chordwise distribution of holes at the mid-span are the pressure taps. The spanwise distribution of

www.manaraa.com

holes are the suction ports, and it should be noted that when the airfoil is placed within the water channel, these holes are actually located near the leading edge. At the root of the airfoil (top of the picture) are three hypodermic tubes that extend through the surface of the airfoil and into the three channels shown in Figure 3.4a. These hypodermic tubes allow the three internal systems of the airfoil–two pressure systems and one suction system–to be connected to external tubing that either go to the pressure sensor or the suction reservoir. The two hypodermic tubes that were epoxied into the pressure channels were barbed Scannivalve Inc. TUBN-063-1.0 stainless steel tubulations (1.08 mm ID and 1.59 mm OD). Alternatively, 12 gauge stainless steel hypodermic tubing (2.31 mm ID and 2.77 mm OD) was used for the suction channel tubulation.

Once the airfoil had been constructed, a series of dye visualization experiments were performed in order to characterize the spanwise distribution of the pressure being applied at the suction ports. For these experiments, the airfoil was submerged in quiescent water and a syringe filled with an aqueous Rhodamine B solution was attached to the suction system tubulation at the root of the airfoil via a short length of Tygon tubing. The syringe was then compressed so that the Rhodamine was forced through the internal suction system of the airfoil and blown out of the suction ports. Figure 3.4c presents an image (obtained with a Nikon D3100 SLR camera that was placed downstream of the airfoil) of the Rhodamine jets that were formed at the suction ports by this blowing process. While this image depicts some minor spanwise variation in the length of these jets, the inner 40% or so appears to be applied with relative uniformity. Figure 3.4c depicts an approximate step change between the magnitude of the jets within this inner region and those within

www.manaraa.com

the outer regions–i.e. the 30% or so near the root and tip of the airfoil. Yet after undergoing this approximate step change, the outboard jets once again appear to contain very little spanwise variation. Based on the magnitude ratio of the jet lengths within these two regions, it appears that the suction ports will affect a velocity within the outboard region that is approximately 65% of that being produced near the mid-span.

Due to the fact that the suction experiments will only consider a small region near the mid-span of the airfoil–located in the center of the relatively uniform inner-distribution of jets–it seems appropriate to conclude that any spanwise variation in the pressure being affected at the suction ports will be negligible. Because the internal suction system of the airfoil is rigid, it can be assumed that the spanwise-uniformity of the suction-port pressure distribution will not be altered when the system is operated in a suction mode during the suction case experiments.

In order to physically affect the negative gauge pressure at the suction ports that was required for the suction case experiments, the suction tubulation at the root of the airfoil was connected to an external suction system, which is depicted in Figure 3.5. The main component of this external system was a vacuum tank, which acted as both a suction reservoir as well as a holding tank for any fluid that was removed. This cylindrical vacuum tank was 0.343 m tall and had a diameter of 0.127 m, and the negative gauge pressure was generated within the tank using a Gast DOA-P707-AA vacuum pump. In order to control the internal pressure of the vacuum tank, it was attached to an Airtrol RV-5200 pressure relief valve. This valve allowed air to flow into the tank and could be adjusted so that the negative pressure within the tank could be specified anywhere between 0 and 24

www.manaraa.com

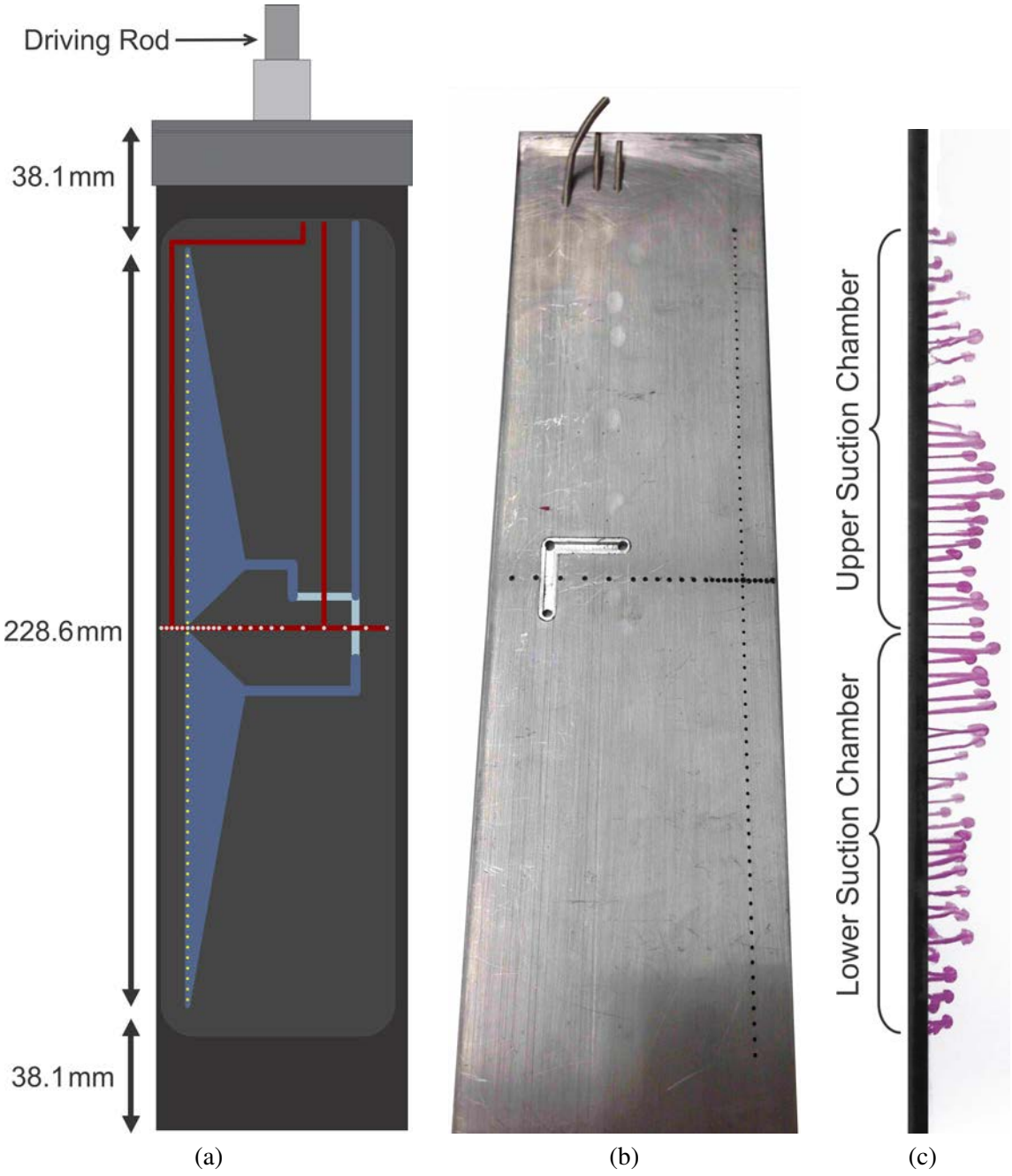

Figure 3.4: (a) Suction (blue) and pressure (red) transmission systems that were milled into the pressure-side of the airfoil. (b) Photo of the suction-side of the airfoil. (c) Rhodamine jets formed at the suction ports during the dye visualization experiments that were used to characterize the spanwise-uniformity of the suction-port pressure distribution.

www.manaraa.com

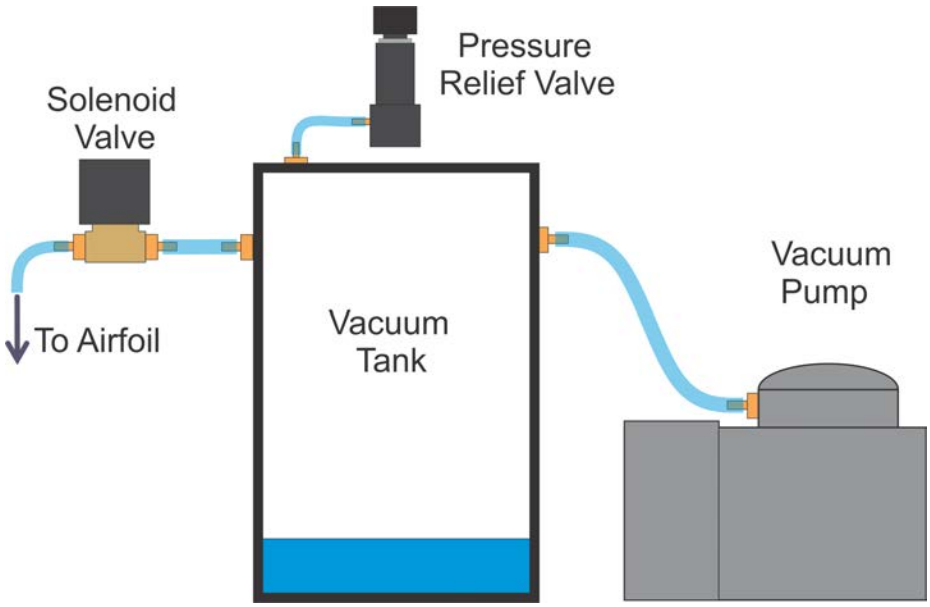

Figure 3.5: System used to control the application of suction within the suction case.

kPa. During the actual experiments of the suction case, a negative pressure of 2 kPa was specified within the vacuum tank.

Because the vacuum pump was operated continuously during experiments, the vacuum tank was connected to a CNYUXI 2W-025-08 solenoid valve so that suction could be applied over a specific phase interval within the motion of the airfoil. This valve was then connected to the suction tubulation at the root of the airfoil using 127 mm of Tygon 2375 Tubing (2.38 mm ID and 3.97 mm OD). The solenoid valve was normally closed and was opened by supplying the valve with a 12 VDC signal. Using the linear encoder on the scotch yoke mechanism, this valve could be opened and closed at specific phases within the plunge motion. The details of this triggering process are discussed next.

Using the position data provided by the linear encoder, a National Instruments USB-

www.manaraa.com

6216 16-bit data acquisition board (DAQ board) was used to generate a 2 VDC signal during the suction application interval. The limited current supplied by the DAQ board was amplified using a simple transistor current amplifier circuit and then used to power an IMO Precision Controls EV1N-CWL-5VDC subminiature relay that switched a 12 VDC power source to activate the solenoid valve. Activating–i.e. opening–this valve allowed the internal suction system of the airfoil to access the suction reservoir of the vacuum tank. The spanwise array of suction ports shown in Figure 3.4b would remove fluid from the flow above the suction-surface of the airfoil once the negative pressure supplied by the solenoid valve propagated through the internal transmission system to the suction ports.

In order to determine how long it took for the suction applied at the suction ports to reach steady state, the frequency response of the suction system was characterized with a dynamic calibration. During this calibration, the airfoil was attached to scotch yoke mechanism and was submerged in the water channel; the airfoil was held stationary in quiescent water. A dynamic calibration was then obtained by activating the solenoid valve of the suction system and measuring the response of the pressure field near the suction ports. In order to measure this response, the pressure measurement system (described later in Section 3.6) was set up to collect pressure data from the pressure tap located at the same chordwise position as the suction ports (x/c = 0.125).

This calibration was performed ten times, and Figure 3.6 plots the average of these responses in black. The red dotted line within this figure represents the first-order dynamic system that was fitted to this response by minimizing the distance between the two curves, yielding a time constant of $\tau = 0.0264$ seconds. This corresponds to 8.08 degrees of motion

www.manaraa.com

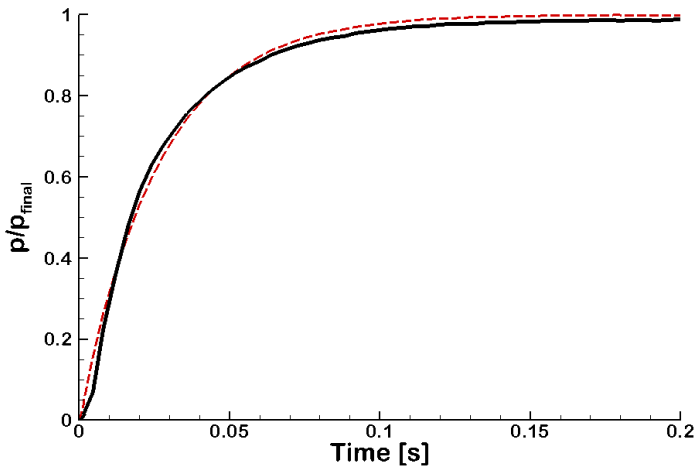

Figure 3.6: Pressure response measured at the suction ports after triggering the suction system. The black line corresponds to the measured data and the dotted red line depicts the best-fit first-order dynamic system (wherein $\tau = 0.0264$ seconds).

within the prescribed kinematics of the airfoil.

In addition to this calibration of the suction system's response time, applying suction within a quiescent fluid allowed for the characterization of the amount of suction being supplied. After referencing some preliminary surface pressure measurements–partially reported by Eslam Panah et al. [85]–it was noted that the LEV created by the current plunging motion could be expected to produce a maximum suction on the surface of the airfoil of approximately 100 Pa. Based on this, it was determined that using suction to reduce the pressure on the surface of the airfoil by approximately 50 Pa should provide a suitable case for study. By adjusting the pressure regulator valve while simultaneously measuring the pressure at $x/c = 0.125$, it was found that this desired surface (gauge) pressure could be achieved within the quiescent fluid if a negative pressure of 2 kPa was prescribed within

www.manaraa.com

the vacuum tank, which is why this vacuum pressure was used during experiments.

These results indicate that there is a ratio of 40:1 between the suction pressure within the vacuum tank and the suction pressure on the surface of the airfoil, which means there is a significant loss of suction that occurs within the internal transmission system of the airfoil. It can by noted that the ratio between the area of the suction tubulation at root of airfoil and the cumulative area of the suction ports is about 8.6, meaning that some of these losses simply come from the internal transmission system diffusing the input pressure so that it can be applied uniformly along the span. The remaining losses are expected to be caused by frictional losses within the internal channels of the airfoil.

In order to determine the average velocity imposed at the suction ports, a secondary set of calibration experiments were performed on the airfoil while it was undergoing the prescribed plunging motion. The calibration involved triggering the suction during a specific phase interval for 150 plunge cycles, and then subsequently measuring the volume of water that had been collected within the vacuum tank. This allowed for the calculation of the average volumetric flow rate at which the suction removed fluid, which was then divided by the total area of the suction ports in order to obtain the average suction velocity being applied at the ports. During the first round of calibration, the suction was triggered between $\phi = -30^\circ$ and $\phi = 60^\circ$, which is the interval that was used during the suction case experiments (the reasons for selecting this interval will be discussed at the beginning of Chapter 9.) Based on this test, it was determined that an average suction velocity of $U_s = 0.131$ m/s was prescribed within the suction case, which corresponds to a velocity ratio of $U_s/U_\infty = 1.014$ where U_∞ is the free-stream velocity. Two additional phase in-

www.manaraa.com

tervals were tested in order to characterize how the acceleration of the airfoil might affect the suction process: $\phi = -30°$ to $\phi = 0°$ and $\phi = 0°$ to $\phi = 30°$. Both phase intervals were observed to remove the same amount of fluid–corresponding to a magnitude ratio of $U_s/U_\infty = 0.984$–thereby indicating that the inertia of the airfoil had no noticeable effect on the suction process.

3.4 Digital Particle Image Velocimetry

In order to characterize the velocity field above the suction-side of the airfoil, two techniques were implemented. For the baseline and suction cases, Stereo PIV was used to measure the three-dimensional velocity field of three, closely-spaced spanwise planes. For the AR2 case, two-dimensional PIV was performed at multiple horizontal and vertical planes, the data from which was compiled into a three-dimensional reconstruction of the velocity field. The following section describes these PIV methods and experimental setups.

3.4.1 Stereo Particle Image Velocimetry: Baseline and Suction Cases

The three-dimensional velocity field of the baseline and suction cases was characterized using a LaVision Flowmaster Stereo PIV system, the setup of which is depicted within Figure 3.7. In order to allow for the characterization of spanwise gradients within the velocity and vorticity fields, measurements were taken at three spanwise planes, spaced 3.2 mm apart. A central difference approximation using the upper and lower planes could then be used to calculate the relevant spanwise gradients of the velocity and vorticity fields.

The first step in performing the PIV measurements was to seed the water channel with hollow glass spheres that had a mean diameter of 10 μm and a density of 1.1 g/cc.

www.manaraa.com

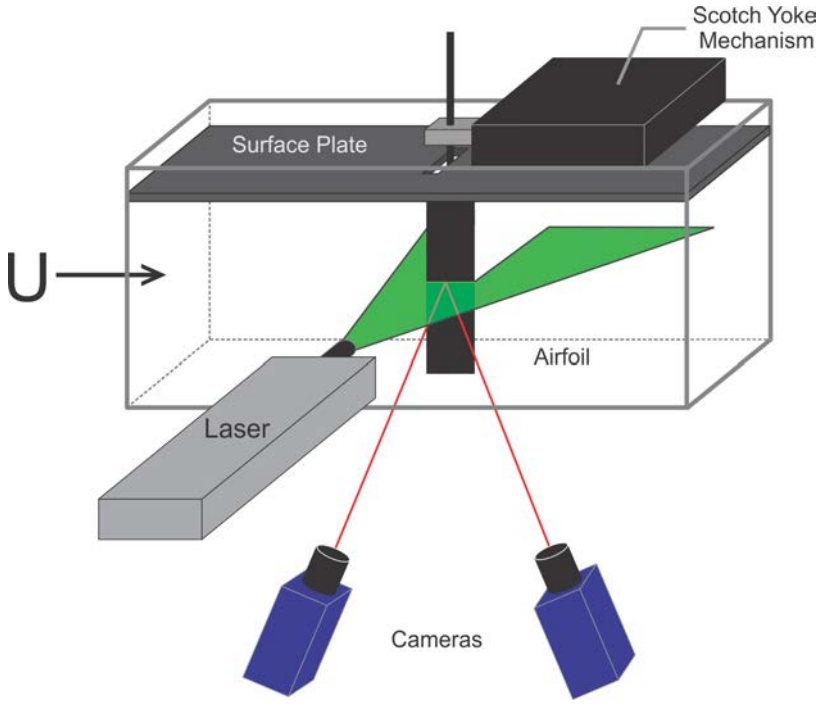

Figure 3.7: Stereo PIV setup used for the baseline and suction cases.

Stereo PIV data were acquired at a given spanwise location by using a dual-cavity 200 mJ/pulse Nd:YAG laser (Figure 3.8) with light sheet optics to illuminate the particles within the imaging plane. Images were acquired using two 14-bit Imager ProX CCD cameras with 2048×2048 pixel resolution and 14-bit dynamic range, equipped with Scheimpflug mounts and Nikon Micro-Nikkor 50 mm lenses (Figure 3.9) with f-stops set to 8.0. The cameras were placed 42 degrees to each other, with each camera being tilted 21 degrees from the vertical.

The cameras were also oriented with an elevation angle from the airfoil surface of approximately 4 degrees in order to prevent the bottom edge of the airfoil from obscuring the measurement plane due to parallax. Each camera was also fitted with a 532 nm (± 10

www.manaraa.com

Figure 3.8: Nd:YAG laser used for PIV measurements.

nm) bandpass filter to remove any background noise and allow for more distinct correlation peaks–note: the Nd:YAG laser produces a 532 nm beam, so the filters would only pass light from the laser that was reflecting off of particles within the flow.

The linear encoder that was attached to the scotch yoke mechanism was used to trigger the PIV data acquisition at specific phases in the plunging motion. Data were collected at 38 different phase locations for the baseline and suction cases, all of which are listed within Table 3.1. Summarizing these values, phase-locked locations were specific every 10 degrees between $\phi = -90°$ and $\phi = -30°$, and every 5 degrees from $\phi = -30°$ until the end of the downstroke at $\phi = 90°$. Phase locations were then specified every 20 degrees during the upstroke between $\phi = 100°$ and $\phi = 220°$. Figure 3.10 provides a plot showing where each of these phases fall within the plunge motion of the airfoil. It should be noted that the locations specified during the downstroke were spaced closer together so

www.manaraa.com

Figure 3.9: Imager ProX CCD cameras used for PIV measurements.

as to better resolve the formation and development of the LEV. Since $\phi = -30°$ marked the beginning of the suction application interval within the suction case, an even finer spatial resolution was defined after this point in order to sufficiently resolve any effects that the suction process might have on the evolution of the flow field.

Table 3.1: Phases at which PIV data were collected for the Baseline and Suction Cases.

−90°,	−80°,	−70°,	−60°,	−50°,	−40°,	−30°,	−25°,	−20°,	−15°
−10°,	−5°,	0°,	5°,	10°,	15°,	20°,	25°,	30°,	35°
40°,	45°,	50°,	55°,	60°,	65°,	70°,	75°,	80°,	85°
90°,	100°,	120°,	140°,	160°,	180°,	200°,	220°		

www.manaraa.com

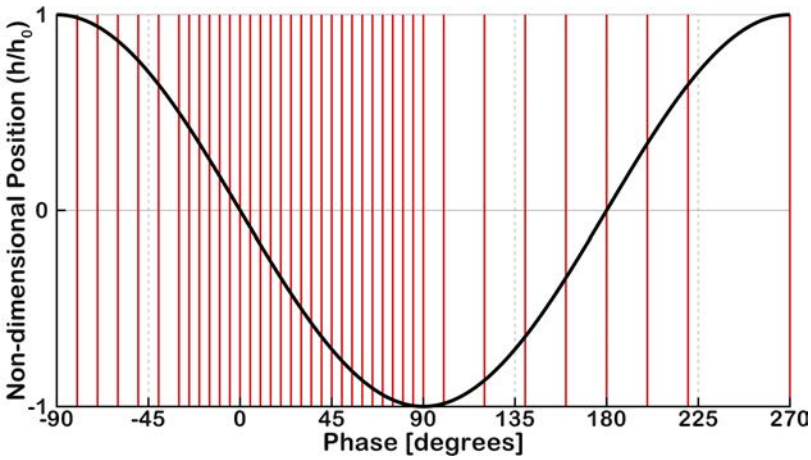

Figure 3.10: Phase-locked locations (in red) at which Stereo PIV data were acquired for the baseline and suction cases. Black line represents the position of the airfoil as specified by Equation 3.1. The LEV forms on the suction-side of the airfoil–i.e. the side that is being imaged–during the downstroke, which begins at -90° and ends at 90°.

At each of the three spanwise locations being investigated within the baseline and suction cases, 100 Stereo PIV image sets were acquired at each of the 38 phase-locked locations. In order to verify that 100 trials would be an appropriate sample size for the characterization of the vorticity field, a series of 500 image sets were obtained at the $\phi = 0^\circ$ phase-locked location of the baseline case at the mid-span of the airfoil. The instantaneous circulation of the LEV was computed within each image set and the results were then progressively averaged over the 500 trials. Figure 3.11 depicts the average circulation of the LEV that was calculated as a function of the number of trials that were averaged (in red). Based on the 500 trials, the average circulation of the LEV was found to be $-0.01295 \pm 1.55 \times 10^{-}5$ m^2/s at a 95% confidence interval. This "true" average is shown within Figure

www.manaraa.com

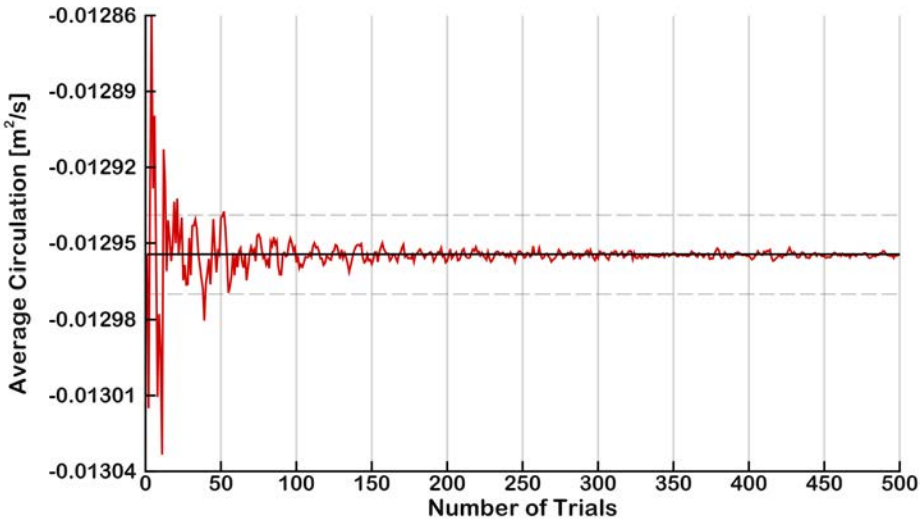

Figure 3.11: Convergence of the LEV circulation as a function of the number of PIV image sets being averaged. The "true" circulation is indicated by a black line, with the 95% confidence interval marked by dashed gray lines. Data for the 500 trials was obtained at $\phi = 0°$ with the baseline plunging case.

3.11 as a black line, with the bounds of the confidence interval marked by dashed gray lines. Because Figure 3.11 shows the phase-averaged circulation data converging within the confidence interval of the true value after approximately 60 trials, it can be concluded that an average of 100 Stereo PIV image sets will sufficiently characterize the flow field.

Stereo PIV data were processed using LaVision DaVis 8.1.6 software and GPU to perform an adaptive multi-pass direct-correlation analysis. The first pass had an interrogation window size of 48×48 pixels and the next two had a window sizes of 24×24, all of which used 50% overlap and median filter between passes. While the PIV images were pre-processed using a particle intensity normalization (with scale of 5 pixels), the vector fields obtained by the direct-correlation analysis were not post-processed.

www.manaraa.com

3.4.2 2D Particle Image Velocimetry: AR2 Case

The three-dimensional flow field was characterized within the AR2 case by compiling two-dimensional PIV data that had been obtained at multiple horizontal (x-y) and vertical (y-z) planes into a three-dimensional reconstruction of the flow. These 2D PIV data were collected under the same experimental conditions as the Stereo PIV measurements, using the same LaVision Flowmaster system, ND:YAG laser and Imager ProX CCD camera–although only one camera was used for the 2D PIV measurements.

Horizontal planes were obtained by placing a camera beneath the water channel and looking up at the plane being illuminated by a laser aimed at the top surface of the airfoil. This setup is depicted in Figure 3.12. For the vertical planes, the laser was projected upward through the floor window. The camera was placed downsteam of the airfoils, aimed downwards at a mirror submerged in the flow at a 45 degree angle, which would redirect the camera's view to the streamwise direction. This setup is shown in Figure 3.13. These experiments were performed by Azar Eslam Panah with the assistance of Kevin Wabick, the full details of which are detailed within the Ph.D. thesis of Eslam Panah [84].

While the same linear encoder from the baseline and suction cases was used to trigger the PIV image acquisition of the AR2 case, a different set of phases ended up being investigated. PIV data for the AR2 case was acquired at 16 phase-locked locations, beginning at $\phi = -90^\circ$ and continuing throughout the rest of the plunge motion at evenly spaced, 22.5 degree intervals. Table 3.2 provides an explicit list of these interrogated phases and Figure 3.14 shows their spread within the plunge cycle. Similar to the baseline and suction cases, 100 PIV images were obtained at each of these phase-locked locations.

www.manaraa.com

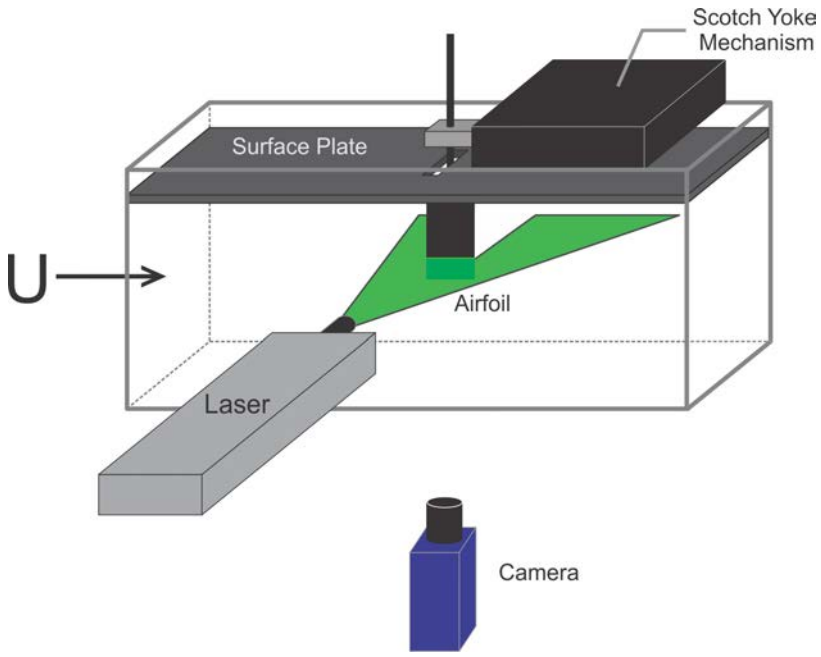

Figure 3.12: PIV setup for horizontal planes.

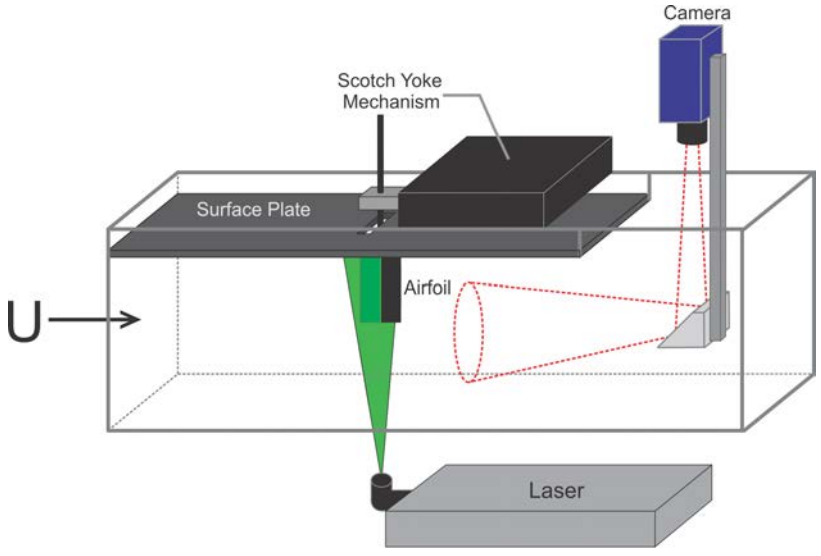

Figure 3.13: PIV setup for vertical planes.

www.manaraa.com

Table 3.2: Phases at which PIV data were collected for the AR2 Case.

Downstroke:	−90°,	−67.5°,	−45°,	−22.5°,	0°,	22.5°,	45°,	67.5°
Upstroke:	90°,	112.5°,	135°,	157.5°,	180°,	202.5°,	225°,	247.5°

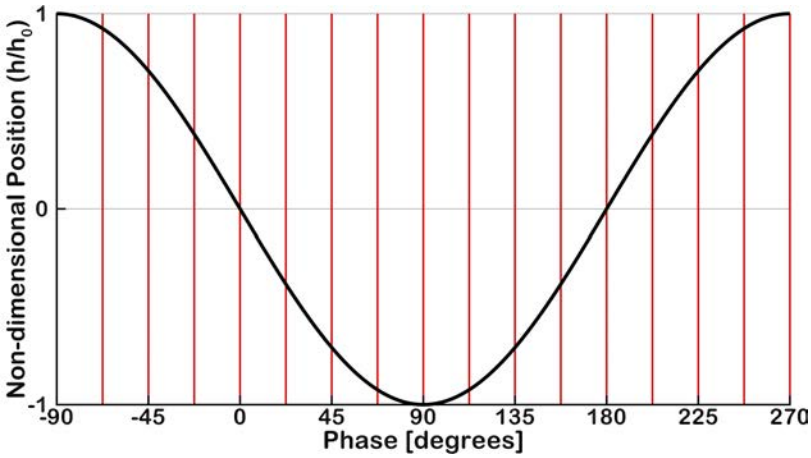

Figure 3.14: Phase-locked locations (in red) at which PIV data were acquired for the AR2 cases. Black line represents the position of the airfoil as specified by Equation 3.1.

3.5 Force Measurements

In order to begin understanding how specific flow structures affect the aerodynamics of the airfoil, time resolved force measurements were acquired for both the baseline and suction. This was done using an ATI Mini40-E Six-Axis Force Transducer (Figure 3.15a) that was factory calibrated to measure forces up to 20 Newtons and torques up to 1 Newton-meters. Mounting brackets were secured to either side of the transducer, and–as shown in Figure 3.15b–the top bracket was then attached to the driving-rod of the scotch yoke

www.manaraa.com

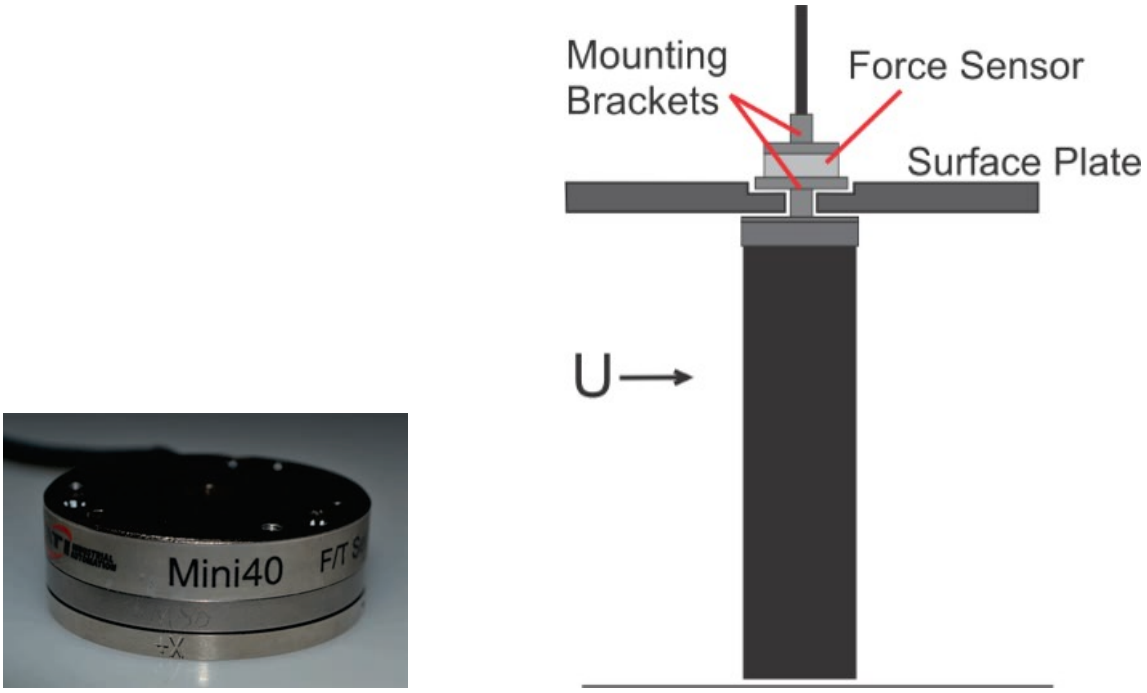

(a) (b)

Figure 3.15: (a) ATI Mini40-E Six-Axis Force Transducer. (b) Schematic showing the experimental configuration used to conduct force measurements on the AR4 airfoil.

mechanism, and the bottom bracket was attached to the airfoil. Data were collected over 500 cycles at 10,000 Hz using a National Instruments USB-6216 16-input, 16-bit, 400kS/s DAQ board, the results of which were averaged to get the final force measurements. The total uncertainty of these force measurements was calculated as 0.0046 Newtons, which includes the factory-reported accuracy as well as repeatability errors.

www.manaraa.com

3.6 Transient Pressure Measurements

3.6.1 Baseline and Suction Cases

As discussed in Section 3.3 (and shown in Figure 3.4a), the AR4 airfoil used within the baseline and suction cases contained two pressure transmission systems. Pressure taps within these systems were located at the mid-span location and consisted of a chordwise-array of holes that were drilled through the suction-side of the airfoil into the internal pressure transmission lines of the airfoil. These internal channels–one upstream of the suction ports and one downstream–served to transmit the pressure sensed at the location of a pressure tap to a hypodermic tube that was pressed into the channel at the root of the airfoil, onto which 50 mm of Tygon tubing (ID 1.6 mm, OD 2.86 mm) was attached. The other end of the tubing was connected to the input of the pressure transducer.

While both of the internal pressure systems were connected to multiple pressure taps, the taps were all sealed when they were not being used. The 1.19 mm diameter holes of these pressure taps were threaded for a #0-80 screw, allowing each one to be sealed with a #0-80 set screw that had a length of 1.59 mm. After a hole was sealed with a set screw, it was covered with Dow Corning 112 silicone valve-packing grease that was pressed flush to the surface of the airfoil with a razor blade. The thick grease would fill any non-uniformities so that the surface of the airfoil remained smooth.

The AR4 airfoil contained a total of twenty-four pressure taps, the first of which was located 1.59 mm downstream of the leading edge. The next thirteen taps were made at 1.59 mm intervals so that the fourteenth tap was located 22.23 mm from the leading edge. The next five taps were placed every 3.18 mm, and the final final five taps were made at

www.manaraa.com

6.35 mm intervals. Table 3.3 explicitly lists the chordwise position of these twenty-four pressure taps, with the distance from the leading edge being reported in both millimeters and inches. Figure 3.16a provides an illustration showing the chordwise position of these taps. The pressure distribution beneath the LEV was a critical part of this investigation, which motivated the increased spatial resolution near the leading edge. As mentioned in Section 3.3, the first six pressure taps were located within the upstream pressure transmission system, and tap numbers seven through twenty-four were located in the downstream system.

Table 3.3: Chordwise position of the twenty-four pressure taps on the surface of the AR4 airfoil. Expressed as distance from the leading edge in both millimeters and inches.

Tap Number	1	2	3	4	5	6	7	8
Position [mm]	1.59	3.18	4.76	6.35	7.94	9.53	11.11	12.7
Position [in]	0.0625	0.0125	0.01875	0.25	0.3125	0.375	0.4375	0.5
Tap Number	9	10	11	12	13	14	15	16
Position [mm]	14.29	15.88	17.46	19.05	20.64	22.23	25.4	28.58
Position [in]	0.5625	0.625	0.6875	0.75	0.8125	0.875	1.0	1.125
Tap Number	17	18	19	20	21	22	23	24
Position [mm]	31.75	34.93	39.1	44.45	50.80	57.15	63.5	59.85
Position [in]	1.25	1.375	1.5	1.75	2.0	2.25	2.5	2.75

www.manaraa.com

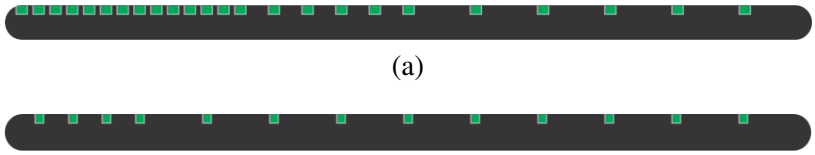

(a)

(b)

Figure 3.16: Position of the pressure taps (in green) in the (a) AR4 and (b) AR2 airfoils.

3.6.2 Finite-AR Case

The pressure transmission lines that were constructed within the AR2 airfoil were slightly different than those contained within the AR4 airfoil, as chordwise-arrays of pressure taps were made at several different spanwise planes. An illustration of the internal system that was made within the AR2 airfoil is presented within Figure 3.17. As was the case with the AR4 airfoil, the first step in machining this internal system was to counterbore the region around the transmission lines by 0.3 mm (shown in dark gray within Figure 3.17). Once all of the internal channels had been made, a 0.3 mm thick piece of shim-stock was epoxied into this counterbored region in order to reseal the airfoil. The actual pressure transmission lines are shown in Figure 3.17 in red, and this system began at the root of the airfoil (0% span) at $x/c = 0.25$ as a 1.6 mm $\times$ 1.6 mm channel that extended straight down the airfoil to the 75% span location. Two wider channels were also made in the chordwise direction: a 9.5 mm wide channel at the 50% span, and a 22.2 mm wide channel at the 75% span. Thirteen pressure taps of diameter 0.8 mm were drilled in the airfoil in a chordwise line, starting 3.2 mm downstream of the leading edge and ending 6.4 mm before the trailing edge. The first four holes were spaced 3.2 mm apart, followed by nine more spaced 6.4 mm apart. Table 3.4 explicitly lists the chordwise position of these thirteen pressure taps, with

www.manaraa.com

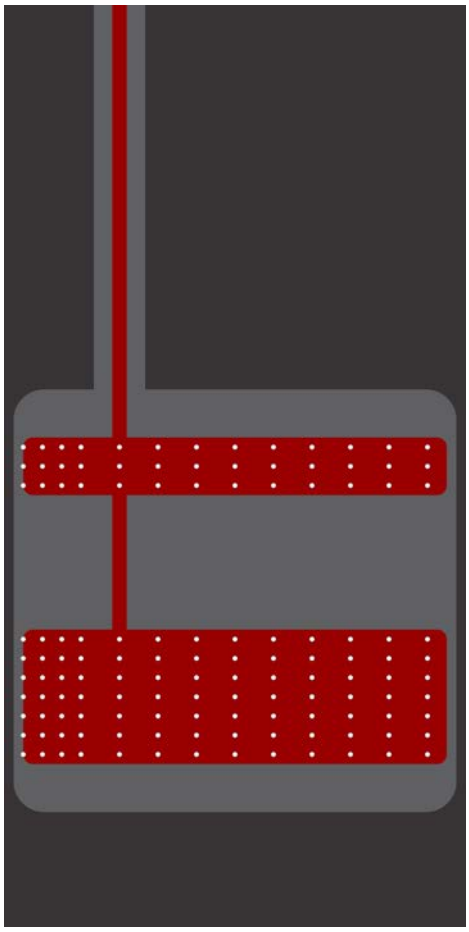

Figure 3.17: Illustration of the pressure transmission lines contained within the AR2 airfoil.

www.manaraa.com

Table 3.4: Chordwise position of the thirteen pressure taps on the surface of the AR2 airfoil. Expressed as distance from the leading edge in both millimeters and inches.

Tap Number	1	2	3	4	5	6	7
Position [mm]	3.18	6.35	9.53	12.7	19.05	25.4	31.75
Position [in]	0.125	0.25	0.375	0.5	0.75	1.0	1.25
Tap Number	8	9	10	11	12	13	
Position [mm]	38.1	44.45	50.8	57.15	63.5	69.85	
Position [in]	1.5	1.75	2.0	2.25	2.5	2.75	

the distance from the leading edge being reported in both millimeters and inches. Figure 3.16b provides an illustration showing the chordwise position of these taps. Ten of these chordwise patterns of pressure taps were made in the airfoil, located at the 48-, 50-, 52-, 69-, 71-, 73-, 75-, 77-, 79- and 81-percent span locations. The resulting matrix of pressure taps is shown within Figure 3.17 in white.

Only the 69-, 75- and 81-percent span locations were utilized within this dissertation. Since all the holes were connected to the same channel within the airfoil, all but one had to be sealed for measurements to be taken at a specific point. All of the holes located on the seven spanwise planes not being considered were sealed with #000-120 screws. At the 69-, 75- and 81-percent span locations, Dow Corning 112 silicone valve-packing grease was spread over the unused holes and pressed flush to the airfoil's surface with a razor

www.manaraa.com

blade. The thick grease would seal the holes but could be sucked out of the airfoil with a syringe when necessary.

A barbed hypodermic tube (Scannivalve Inc. TUBN-063-1.0 stainless steel tubulations, 1.08 mm ID and 1.59 mm OD) was pressed into the root of the airfoil and epoxied into the vertical channel located at the quarter chord. This tubulation was connected to the pressure transducer using 50 mm of Tygon tubing (ID 1.6 mm and OD 2.86 mm).

3.6.3 Pressure Data Acquisition

A Kistler 4264A piezoresistive, unidirectional differential pressure transducer with a range of 10.3 kPa and overall uncertainty of 0.1% full scale was used for pressure measurements. The stated uncertainties were reported by the manufacturer and include errors due to non-linearity, hysteresis, and repeatability. Distributions of the surface pressure coefficient ($C_p = [p - p_\infty]/0.5\rho U_\infty^2$) will be presented throughout this dissertation, the total uncertainty of which has been conservatively calculated as $\sigma_{Cp} = 0.1003$.

Pressure transducer output was acquired and stored using a National Instruments USB-6216 16-input, 16-bit, 400kS/s DAQ board and LabVIEW software running on a PC. For each pressure tap being measured, data for 150 oscillation cycles was obtained and then phase-averaged to obtain the final results. Static pressure transducer calibration was achieved using a Rouse manometer as the standard. The dynamic correction technique described within the next chapter was also performed on the pressure data in order to account for any phase and amplitude errors introduced by the high-density fluid within the pressure transmission lines.

www.manaraa.com

CHAPTER 4
CORRECTION OF DYNAMIC PRESSURE MEASUREMENTS

Accurate time-resolved measurements of the surface pressures on an aerodynamic body can provide significant insight into aerodynamic performance and the related flow physics. When the Reynolds numbers become moderately large, the aerodynamic forces and moments are dominated by the surface pressure distribution so that the unsteady aerodynamic loads can be accurately computed if the pressure distribution is resolved with sufficiently high spatial and temporal resolution. The passage of vortical flow structures over the surface can be inferred from the pressure distribution [1, 96], and since the boundary flux of vorticity from the body is generally dominated by the surface pressure gradients [123, 126], sources and sinks of vorticity on the boundary can be estimated by measuring the pressure gradients (as demonstrated in Section 2.2).

Unfortunately, obtaining reliable transient pressure data–especially in water–can be difficult, as the response of the measurement system will introduce phase and amplitude errors. These effects are introduced due to the dynamics of the sensor itself as well as within the pressure lines connecting the sensor to the point of interest within the flow. Although no standard exists, it is generally desirable to design a system with a resonant frequency much higher than that of the signal being measured.

Still, there exist many scenarios in which dynamic effects cannot be minimized. If it is not possible to mount a pressure sensor within the experimental model so that it can be located near the measurement location, the connective tubing will adversely impact the frequency response of the system. Also, measurement of transient pressures in water is

www.manaraa.com

uncommon due to the low dynamic pressures associated with the typically low convection velocities in water tunnels and the significantly increased inertia and damping within a water-filled pressure measurement system. Still, experiments in water are particularly well-suited for studies at low Reynolds numbers since aerodynamic force measurement is facilitated by the high fluid density (i.e. similar Reynolds numbers in air would yield even lower dynamic pressures). It is therefore desirable to develop a robust method for correcting measured transient pressure data in order to accurately resolve the true pressure variations.

4.1 Methods for Assessment and Correction of Transient Pressure Measurements

In 1950, Iberall [49] presented the first theoretical model describing the fluid dynamics within a transmission line, which served as the foundation for the development of increasingly complex models in the years since. Unfortunately, Iberall's original model, and those it inspired, all deal with the forward identification method–i.e. predicting the response of a system given a known input. However, for the application being considered within this dissertation, an inverse identification method is required–i.e. determining the true input of the system based on the known output that has been measured. Unlike the forward identification method, the literature contains very few examples of techniques for the implementation of an inverse identification method. In fact, only four techniques have been developed, mainly due to the complexity associated with the invertibility of transfer functions. The nuances of this problem are described next, after which the existing techniques for realizing an invertible transfer function are discussed.

www.manaraa.com

When characterized in terms of the Laplace operator s, the dynamic response of a system ($P_{out}(s)$) can be found by applying the transfer function of that system ($H(s)$) to an arbitrary inlet pressure ($P_{in}(s)$) by solving the inverse Laplace transformation as:

$$P_{out}(s) = H(s) \cdot P_{in}(s) \tag{4.1}$$

On the other hand, the inverse identification problem requires the use of an inverse transfer function ($H^{-1}(s)$):

$$P_{in}(s) = H^{-1}(s) \cdot P_{out}(s) \tag{4.2}$$

However, the problem within implementing Equation 4.2 is that the inverse transfer function ($H^{-1}(s)$) does not always exist as a physically implementable system. Specifically, the system $H(s)$ becomes a non-invertible system if $H^{-1}(s)$ is an improper transfer function–i.e. the polynomial in the denominator is of a lower degree than that in numerator. Akiyama [2] discussed how the dynamic system of a pressure transmission line is an inherently non-invertible system since it will always include a time delay effect. Therefore, the key to performing an inverse identification method on the response data measured with a pressure transducer is to realize an inverse transfer function ($H^{-1}(s)$) of the pressure system that can be physically implemented.

Akiyama [2] demonstrated a method for inverse identification, where an approximation of a the inverse transfer function was numerically calculated using FFT and then applied to the measurement data. Instead of solving for the exact inlet pressure using an inverse Laplace transformation method, an approximation of the inlet pressure was calculated using an inverse FFT. While their results seemed to show that approximating the

www.manaraa.com

inverse Laplace transform with an inverse FFT resulted in a small numerical error, representing the inverse transfer function with an FFT approximation led to the production of non-negligible modeling errors. Because their work considered idealized transfer functions of basic phenomena (e.g. a pure time delay taking the form e^{-Ls}, where s is the Laplace operator) in the first place, this modeling error would be expected to become even larger for more complex, real world transfer functions.

Batil and Nebres [11] approached the problem in a different manner by developing a methodology that was defined in the frequency domain but evaluated in the time domain. They performed a step function calibration, converting the discrete input and response data into the frequency domain using a z-transform. The resulting transfer function was converted back into the time domain and implemented using an autoregressive moving average model that solved for the current input value based on past inputs and the full time history of the output. While this method was able to recover a significant portion of the true input, the approach requires that the transfer function of the pressure system be characterized as a second-order dynamic system. Similar to the work of Akiyama [2], the applicability of the approach developed by Batil and Nebres [11] is therefore limited to idealized pressure systems with relatively simple transfer functions.

Conger and Ramaprian [28] also developed a correction method that was limited to second-order systems and performed within the time domain. Keeping their analysis in the time domain allowed them to avoid invertibility issues and directly calculate input values based on the output and its derivatives. In addition to this being the only method that made direct use of time derivatives, it is also the only method that was developed based on a

www.manaraa.com

system with water as its working fluid. To the author's knowledge, this is also the only method that has been implemented in the published literature to correct experimentally-measured transient pressures [29, 87].

The final technique presented in the literature was developed by Greenblatt et al. [43], which operated solely in the frequency domain using FFT and inverse FFT analyses. Instead of a typical transfer function, their system was characterized by determining the attenuation factor and phase lag for a range of applied acoustic frequencies. These variables could then be used to determine the true input from whatever signal they measured with the system. Despite the success of this model, its application does not lend itself very well to water-based systems, as the relevant frequencies would be difficult–if not impossible–to calibrate acoustically.

The method developed here is an evolution of the Conger and Ramaprian [28] method, in that a transfer function was developed by fitting a generalized equation to calibration data. However, in order to better characterize the responses, a system was generated through the combination of multiple first and second-order damped systems. The invertibility issue cause by the addition of extra terms was solved by applying part of the transfer function in the time domain (similar to Conger and Ramaprian [28]), while the other portion of the transfer function was applied in the frequency domain using the Laplace and inverse Laplace transforms. A second, easier-to-implement method developed at the end of this chapter is entirely based in the frequency domain and solves the invertibility issue through the addition of high frequency poles.

www.manaraa.com

4.2 Test Case

In order to verify the validity of the inverse identification method to be presented, the method was applied to data from a test case that was similar in nature to the plunging cases that were previously discussed in Section 3.2. The data used in this test case was acquired at the mid-chord, mid-span position of a flat-plate airfoil of aspect-ratio 4 that was oscillating in a pure-plunge motion within a free-surface water channel. The pressure tap being used had a diameter of 0.8 mm and was connected to an internal channel that ran up the airfoil (channel depicted in red within Figure 4.1a). Approximately 30 mm from the free surface, a barbed hypodermic tube (OD 1.5875 mm) was pressed into the airfoil at the end of the channel, onto which a 50 mm length of tygon tubing (ID 1.6 mm, OD 2.86 mm) was attached. The other end of the tubing was connected to a Kistler 4264A piezoresistive, unidirectional differential pressure transducer. Since the fluid transmission lines within the system just described were minimized as much as possible, it will be denoted as the *optimized* system and is shown in Figure 4.1b. In order to gauge the success of the inverse identification methodology, this correction method was also applied to data from a second system, denoted the *impaired* system, whose signal underwent severe damping. These additional losses were introduced into the system by adding an extra 60 mm length of Tygon tubing with inner diameter 25.4 mm, as shown in Figure 4.1c.

4.3 Dynamic Calibration

Similar to Conger and Ramaprian [28], a dynamic calibration was performed through the generation of a step response. This was done by first placing the pressure measurement

www.manaraa.com

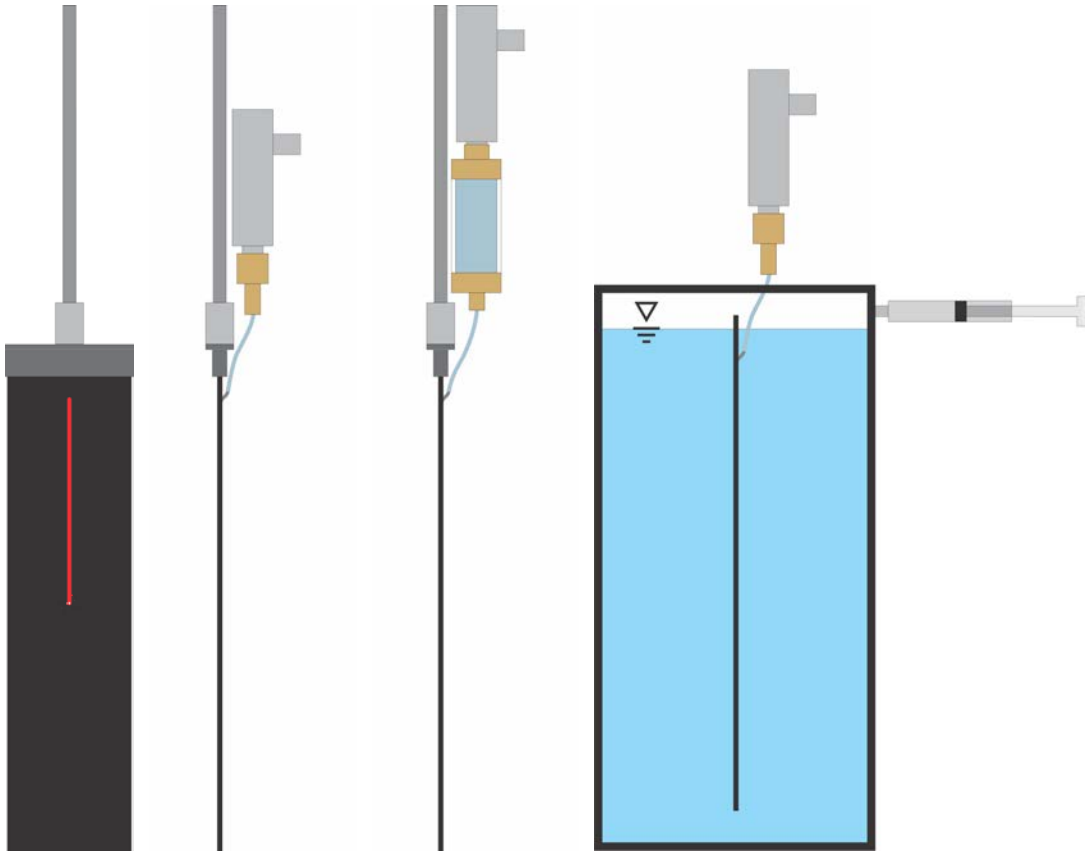

Figure 4.1: Schematics showing the (*a*) planform and (*b*) streamwise view of the optimized pressure measurements system, (*c*) the impaired pressure measurement system (streamwise view) and (*d*) the dynamic calibration setup.

www.manaraa.com

system within a calibration tank and then connecting it to the pressure transducer (located outside of the tank). The calibration tank was filled with water and sealed, as depicted in Figure 4.1d. A syringe was attached to the tank, and used to modify the internal pressures. A small hole was located in the top of the tank that could be sealed with tape while the vessel was being pressurized and then impulsively opened by ripping off the tape, creating a step-response pressure change inside the tank back to atmospheric pressure.

Sample step responses obtained for the two systems are shown in Figure 4.2, where every 20th value of the measured data is plotted as a discrete point. The blue line represents the best fit obtained using the second-order model used by Conger and Ramaprian [28], whereas the red lines represent the transfer function obtained in this analysis, as described below.

As Figure 4.2 illustrates, a second-order function (blue line) does not represent either system very well. Therefore, a procedure for developing an appropriate transfer function had to be devised. This was achieved through the combination of multiple first- and second-order linear, damped systems:

$$H_{\text{f.o.}} = \frac{k}{\tau s + 1} \tag{4.3}$$

$$H_{\text{s.o.}} = \frac{k\omega_0^2}{s^2 + 2\zeta\omega_0 s + \omega_0^2} \tag{4.4}$$

where k is the function gain, τ is the time constant, ω_0 is the natural frequency and ζ is the damping ratio. These parameters were uniquely defined in each of the constituent transfer functions and were determined using the Matlab function `fminsearch`, which uses a multi-dimensional unconstrained nonlinear minimization. The parameters were iteratively varied to optimize the fit between the step response of the transfer function and the measured data.

www.manaraa.com

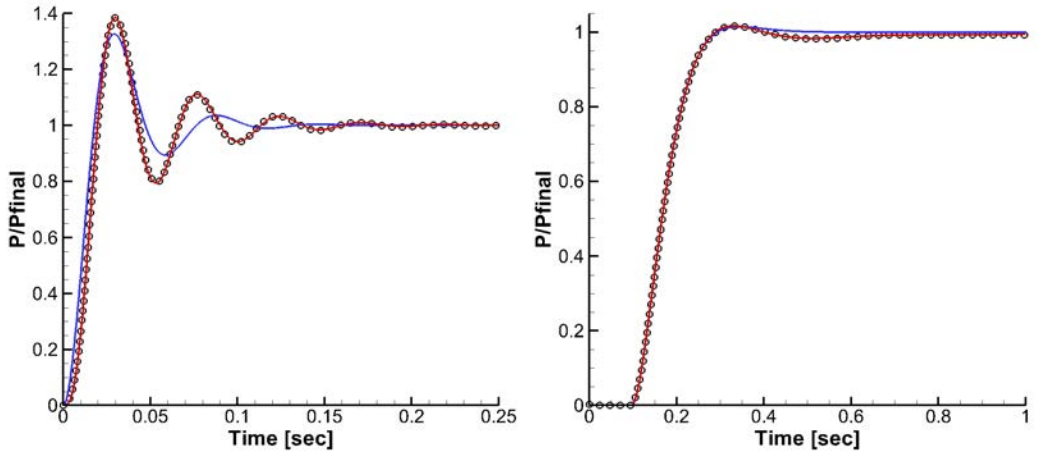

(a) Ideal Frequency Response (b) Damped Frequency Response

Figure 4.2: Step response and of the (*a*) ideal and (*b*) damped measurement systems. Open circles represent the measured data. The closest-fit second-order system is shown in blue and the red line is the fitted transfer function.

An efficient means of determining the general form of the transfer function was developed, which began with fitting a second-order system to the step response (this would result in the blue lines shown in Figure 4.2). The transfer function was then modified by adding additional second-order systems and re-optimizing the parameters. The end goal of this step was to characterize the ringing of the step response, i.e. model everything after the initial rise time. Once this portion of the data was modeled, the transfer function was multiplied by a first-order system. This multiplication allowed for the modification of the transfer function within the rise time of the step response without changing the fit that had already been achieved in the later part of the signal. The transfer function continued to be multiplied by first-order systems until the initial rise of the step response was characterized.

www.manaraa.com

The fitted transfer functions used to create the red lines in Figure 4.2 were generated according to Equation 4.5 (optimized) and Equation 4.7 (impaired).

$$H_{\text{opt}}(s) = H_{\text{s.o.,A}} * H_{\text{s.o.,B}} \tag{4.5}$$

$$H_{\text{opt}}(s) = \frac{1.25 \times 10^5}{s^2 + 2720s + 4.16 \times 10^5} * \frac{6.19 \times 10^4}{s^2 + 53.53s + 1.85 \times 10^4} \tag{4.6}$$

$$H_{\text{imp}}(s) = (H_{\text{f.o.,A}} + H_{\text{s.o.,A}} + H_{\text{s.o.,B}}) * H_{\text{f.o.,B}} * H_{\text{f.o.,C}} \tag{4.7}$$

$$H_{\text{imp}}(s) = \left(\frac{0.46}{0.18s + 1} + \frac{1053}{s^2 + 62.89s + 1903} + \frac{194.3}{s^2 + 17.95s + 176.2} \right) * \frac{0.54}{0.002s + 1} * \frac{0.88}{0.038s + 1} \tag{4.8}$$

Use of these transfer functions to recover the original pressure signals is discussed in the following section.

4.4 Inverse Identification Methods

In order to determine the true input of the system ($X(s)$), the output data ($Y(s)$) must be transformed using the inverse transfer function $H^{-1}(s)$:

$$X(s) = H^{-1}(s)Y(s). \tag{4.9}$$

The coefficients of the inverse transfer function can be expressed as a ratio of polynomials:

$$H^{-1}(s) = \frac{\sum_{i=0}^{N} a_i s^i}{\sum_{j=0}^{M} b_j s^j}. \tag{4.10}$$

www.manaraa.com

Since $H(s)$ was created through the combination of strictly proper functions (i.e. functions with a polynomial in the denominator that is of higher degree than that of the numerator), it is also guaranteed to be strictly proper. Therefore, $H^{-1}(s)$ takes the form of an improper transfer function – that is, the polynomial in the denominator is of a lower degree than that in numerator ($N > M$). As a result, any attempt to transform the results of Equation 4.10 into the time domain using the inverse Laplace transform will yield a solution that does not converge [31]. This is the fundamental invertibility problem that is often encountered with inverse identification models, for which two solutions are developed and presented here.

One way to realize the improper transfer function is to split it into two parts, a strictly proper portion $R(s)$ and a polynomial $P(s)$:

$$H^{-1}(s) = R(s) + P(s) = \frac{\sum_{i=0}^{M-1} A_i s^i}{\sum_{j=0}^{M} B_j s^j} + \sum_{k=0}^{N-M} C_k s^k \tag{4.11}$$

The input can then be solved for according to:

$$X(s) = R(s)Y(s) + P(s)Y(s) \tag{4.12}$$

Since $R(s)$ now has a numerator of lower degree than the denominator, the proper portion of the input can be calculated and transformed into the time domain using a numerical inverse Laplace transform. The polynomial portion, however, cannot be computed in the frequency domain. Instead, its functional form is converted into the time domain, with each s^k variable becoming a k$^{\text{th}}$-order derivative.

$$x(t) = \mathcal{L}^{-1}\{G(s)Y(s)\} + \sum_{k=0}^{N-M} C_k \frac{d^{(k)}y}{dt^{(k)}} \tag{4.13}$$

www.manaraa.com

Now that it is in the time domain, the polynomial portion of the input can be computed by taking the appropriate derivatives of the response data, as shown by Conger and Ramaprian [28]. In order to preserve smoothness, the response data should be smoothed with a moving average before each differentiation. Once the proper and polynomial portions are obtained, the input can be found by summing them together.

An alternative approach to the inverse problem is to modify $H^{-1}(s)$ so that it can be implemented in its raw form yet still maintains the characteristics of the original function. This is achieved by introducing high frequency poles to Equation 4.10 that increase the order of the denominator until it exceeds that of the numerator. These frequencies need to be high enough such that they do not interfere with the relevant behavior of the transfer function [79, 90]. One very efficient way of introducing these poles was found to be through the use of an $(N - M + 1)$-order, lowpass butterworth filter:

$$L(s) = \frac{1}{B_{N-M+1}\left(\frac{s}{f_N}\right)} \tag{4.14}$$

By setting the cutoff frequency equal to half the Nyquist frequency (f_N), the filter $L(s)$ should pass all relevant frequencies and have negligible phase and amplitude shifts.

The inlet pressure can now be solved using:

$$x(t) = \mathcal{L}^{-1}\{H^{-1}(s)L(s)Y(s)\} \tag{4.15}$$

Within the current investigation, the two inverse identification methods yielded virtually identical results, as demonstrated in Figure 4.3. For this reason, all of the inverse identification corrections made from this point on will make use of the second methodology, as it is both computationally faster and easier to implement.

www.manaraa.com

4.4.1 Validation

In order to validate the inverse identification technique presented, the results of the impaired system of Figure 4.1b and the optimized system of Figure 4.1a are compared. As the data sets both measured the same pressure signal, the corrected responses should match. Figure 4.4 shows the measured pressure response for the damped system in red, and the corrected signal for the damped and ideal systems in blue and black respectively. Although the transformed signals do not exhibit a perfect match, the damped signal does experience significant phase and amplitude corrections. It should be noted that the manner in which the modified system achieved the significant damping necessary for a good test case basically consisted of increasing the mass of the system by roughly a factor of 50. Although this yielded the desired result, it also damped out a lot of the information within the signal. Theoretically, a transfer function should be able to recover all the damped-out data of a system; however, with real-world devices, the information needed to recover the true input can get lost within the uncertainty of the data.

4.5 Model Implementation and Correction of Plunging Airfoil Data

The dynamic calibration procedure described in Section 4.1 was performed on the AR4 and AR2 airfoils described in Section 3.6 by placing each of the airfoils in the calibration tank shown in Figure 4.1d and following the procedure from Section 4.3. Using the inverse identification method that has been developed, the transfer functions derived from the calibration were then used to correct for the dynamic losses within the pressure data.

www.manaraa.com

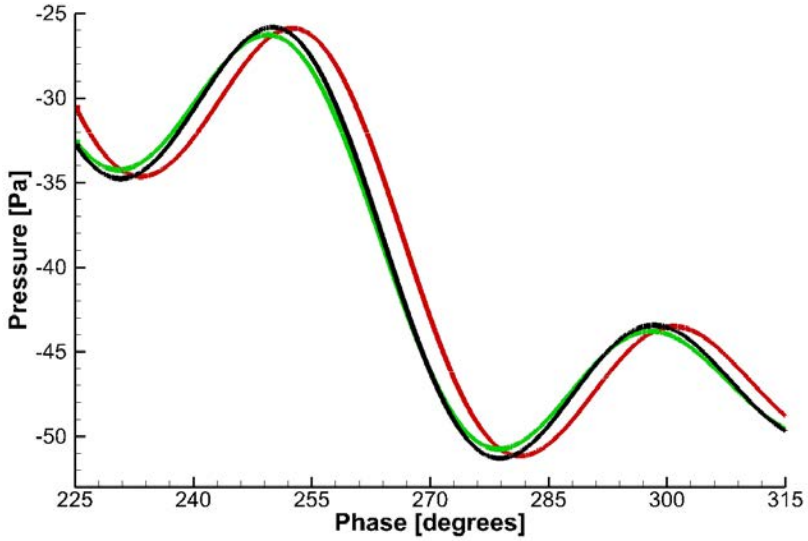

Figure 4.3: Portion of the measured signal (red) from the optimized system compared to the results of the first (green) and second (black) inverse identification methodologies presented.

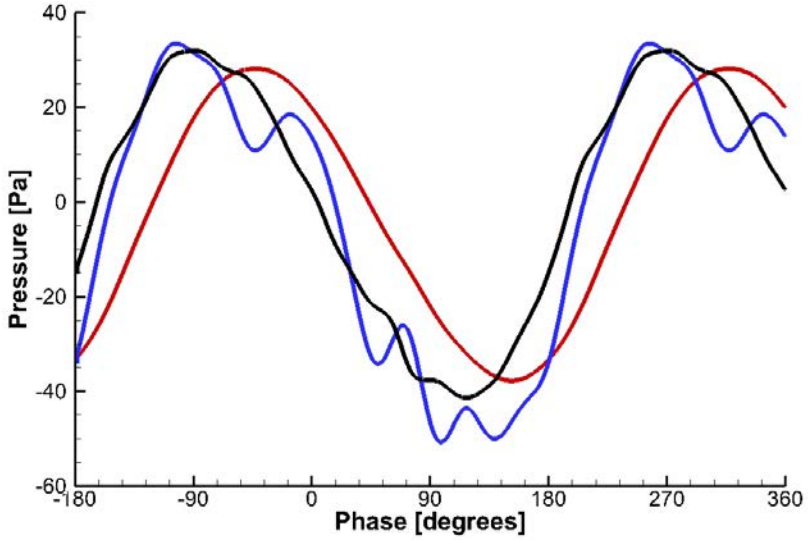

Figure 4.4: Comparison of the uncorrected (red) and corrected (blue) data of the damped system with the corrected measurements of the ideal system (black).

www.manaraa.com

CHAPTER 5
RESULTS FOR THE BASELINE CASE

5.1 Introduction

The overarching goal of this dissertation is to determine how and why the leading-edge vortex develops the way it does. While characterizing the vorticity transport within the flow helps to provide a superior description of the LEV dynamics, the problem being considered should be simplified as much as possible in order to make any underlying physics governing the growth and evolution of the LEV more pronounced.

This was the primary motivation for testing a high aspect-ratio airfoil, as the nominally two-dimensional flow field that it produced would be more conducive to the identification of fundamental formation and growth mechanisms of the LEV. Minimizing the three-dimensionality within the flow serves to emphasize the dynamics that are associated with the intrinsic development of the LEV. Furthermore, the use of a plunging flat plate means that the only acceleration-based sources of vorticity (i.e. from accelerations prescribed tangent to the surface–first term on RHS of Equation 2.19) will be located at the rounded leading and trailing edges, which simplifies the dynamics of the vortex by reducing the nonlinear coupling between the LEV and the upper surface of the airfoil. As a whole, these experimental constraints limit the factors governing the evolution of the LEV.

5.2 Global Flow Dynamics and LEV Evolution

In order to observe the development of the LEV, isocontours of spanwise vorticity are examined in Figure 5.1. A simple vorticity threshold was used as a vortex identification

www.manaraa.com

criterion, which was specified as 5-percent of the maximum vorticity value, and is shown in Figure 5.1 as a black line. Using the raw PIV images, the outline of the airfoil was determined and inserted into the figures in black, and the shadow created by the airfoil has been superimposed in gray. In these images, the flow is from left to right and the airfoil is plunging downwards, with the beginning of the downstroke at $\phi = -90°$ and the end of the downstroke at $\phi = 90°$.

Figure 5.1 also depicts the gradients of the surface pressure (dp/dx) that was measured at each phase (see Section 3.6) as lines projecting normal to the airfoil's surface, with the line length proportional to the magnitude of the pressure gradient. A central difference scheme was used to calculate the pressure gradients using the data obtained at two adjacent pressure ports, and the chordwise location of the calculated gradient was specified as halfway between the two ports. The red/blue color-coding is used to specify the direction of the gradient, with red lines corresponding to an adverse pressure gradient (APG: $dp/dx > 0$) and blue representing a favorable pressure gradient (FPG: $dp/dx < 0$).

Beginning at $\phi = -90°$ with the initiation of the downstroke, Figure 5.1a indicates the presence of an attached boundary layer over the majority of the airfoil. While there are no signs of vortex formation near the leading edge in Figures 5.1a-5.1d, the pressure gradients within this region do show some interesting dynamics. The FPG shown at the leading edge in Figure 5.1a transitions to an APG by Figure 5.1c which then proceeds to spread downstream. When the LEV begins to form at $\phi = -50°$, Figure 5.1e shows the reemergence of a FPG right at the leading edge due to the low-pressure region beneath the nascent LEV.

www.manaraa.com

The LEV continues to grow in strength in Figure 5.1f and appears to roll-up at $\phi = -30°$ in Figure 5.1g and begins accumulating secondary vorticity into an opposite-signed vortex (OSV). This growth of the LEV also leads to the formation of a large, narrow APG peak downstream of the core, which eventually spreads downstream once the LEV rolls up, weakening in magnitude as it does so. Through the middle of the downstroke (Figures 5.1g-5.1s), it is difficult to identify any specific evolutionary stages of the LEV within the vorticity isocontours. However, the pressure gradients do indicate a change in the flow at $\phi = -5°$, as Figure 5.1l indicates the appearance of two suction peaks (i.e. transition from blue to red pressure gradients within the figures). The final stage in the evolution of the LEV is the detachment from the leading-edge shear layer, which takes place between $\phi = 30°$ and $\phi = 65°$. Within this interval, Figures 5.1s-5.1z depict an unsteadiness in the connection between the shear layer and the LEV, with appears to be caused by the intermittent shedding of small blobs of vorticity from the shear layer.

Briefly summarizing this analysis of Figure 5.1, the main events seen within the vorticity field are as follows:

1. The flow remains attached between $\phi = -90°$ and $\phi = -70°$.

2. Separation of the boundary layer and appearance of the LEV at $\phi = -60°$.

3. Roll-up of the LEV at $\phi = -30°$.

4. Detachment of the LEV between $\phi = 35°$ and $\phi = 65°$.

With the important events in the evolution of the flow now identified, a control volume analysis of the vorticity fluxes within the flow will be used to characterize the

www.manaraa.com

vorticity budget. The details of this analysis will then be used to provide additional insight into the flow physics when the LEV formation process is investigated more closely.

5.3 Characterization of the Vorticity Budget

The first step in applying a vorticity flux analysis is to specify the control region (A_z) that will be investigated. Figure 5.2 depicts the same control region that was shown in Figure 2.5, and it can be noted that the only thing missing from this representation of the control region are the specific dimensions. For the current analysis of the baseline case, the specified control region (A_z) starts 1.59 mm downstream of the leading edge, ends 40 mm downstream of the leading edge and extends 35 mm vertically into the flow.

The finalized form of the vorticity flux equation that was obtained as Equation 2.24 is once again presented here as Equation 5.1.

$$\frac{d\Gamma_z}{dt} = \int_{A_z} \left(-u_z \frac{\partial \omega_z}{\partial z}\right) dA_z + \int_{A_z} \left(\omega_x \frac{\partial u_z}{\partial x} + \omega_y \frac{\partial u_z}{\partial y}\right) dA_z + \int_{1-3} \omega_z \left(\vec{u} \cdot \hat{n}\right) d\ell + \int_{4} \frac{\partial p}{\partial x} dx \quad (5.1)$$

It should be noted that Equation 5.1 assumes that the control region remains connected to the surface of the plunging plate, and therefore the coordinate system in which the analysis is performed is non-inertial. Since the PIV measurements were obtained in an inertial frame–as illustrated by Figure 5.1–the data were corrected by uniformly subtracting the plunge velocity from the y-components of the velocity field at each phase-locked location. Because this modification was applied uniformly across the entire field-of-view, the vorticity distributions from Figure 5.1 are invariant to the transformation. Thus, the vortex-dynamics that were described within the previous section remain consistent between the inertial and non-inertial frames.

www.manaraa.com

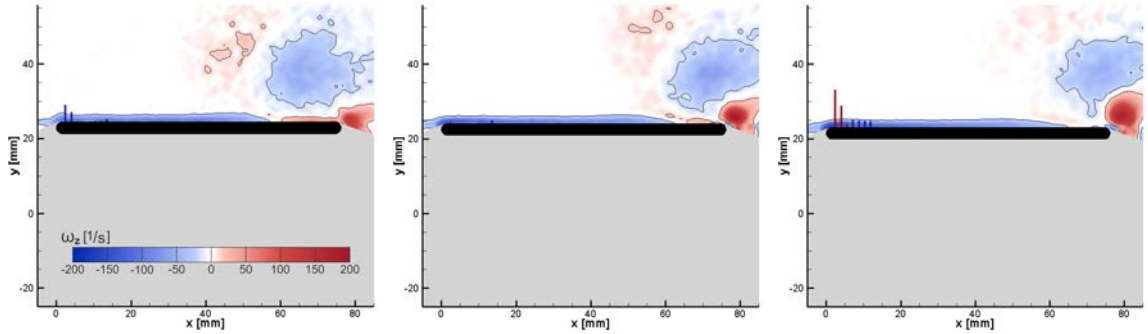

(a) $\phi = -90°$ (b) $\phi = -80°$ (c) $\phi = -70°$

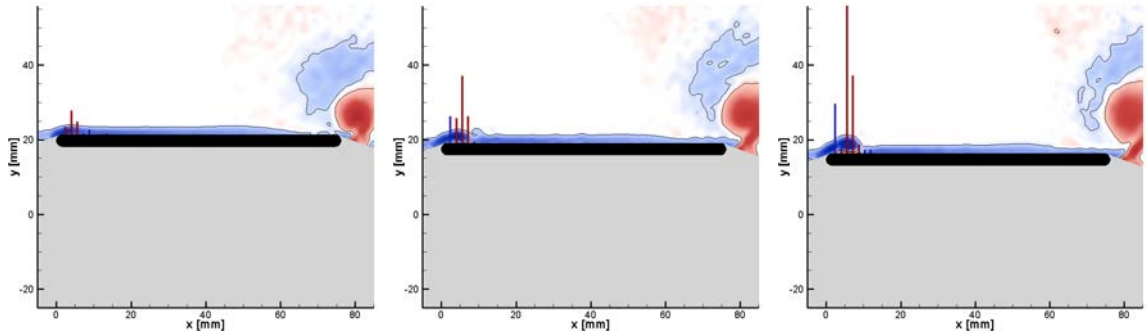

(d) $\phi = -60°$ (e) $\phi = -50°$ (f) $\phi = -40°$

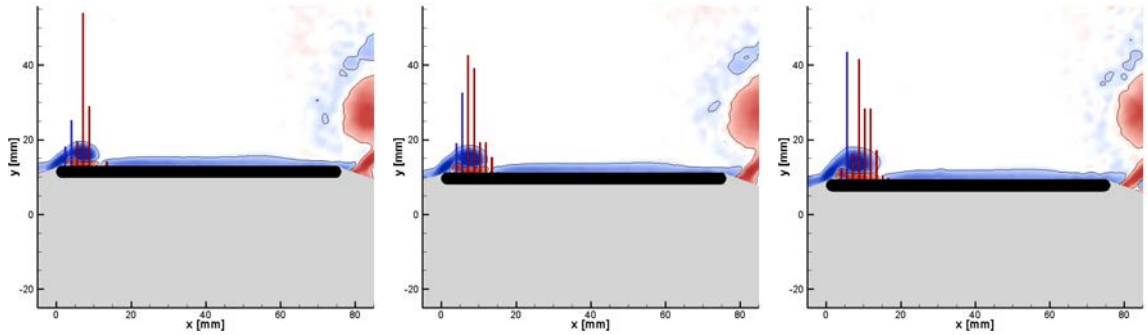

(g) $\phi = -30°$ (h) $\phi = -25°$ (i) $\phi = -20°$

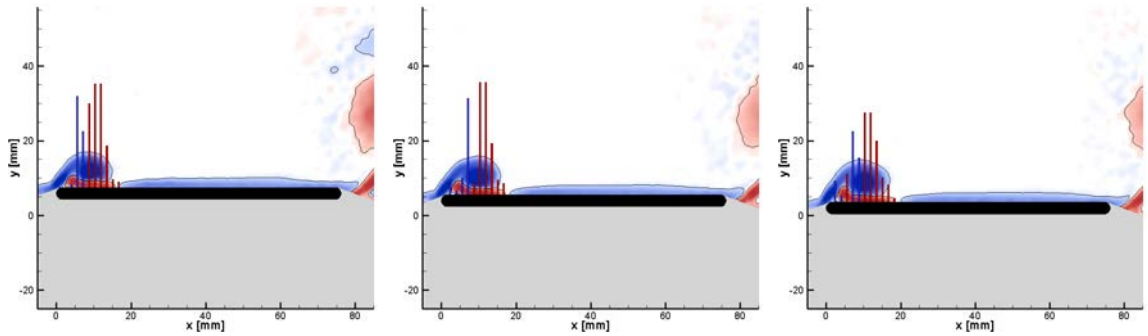

(j) $\phi = -15°$ (k) $\phi = -10°$ (l) $\phi = -5°$

Figure 5.1: Evolution of the vorticity field from the baseline case.

www.manaraa.com

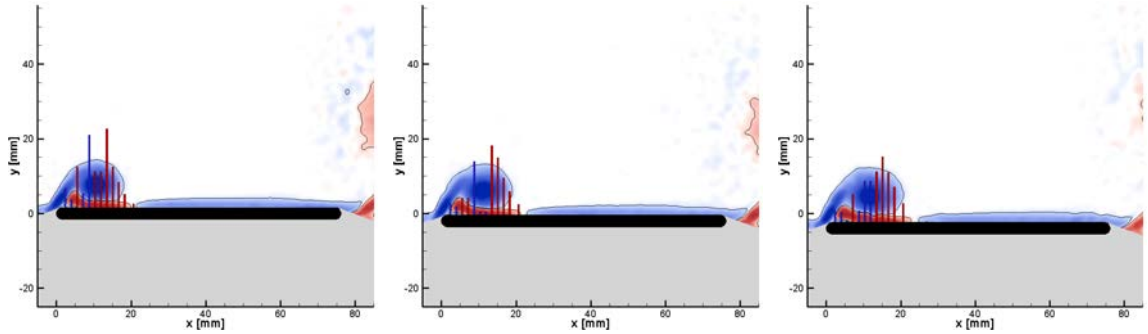

(m) $\phi = 0°$ (n) $\phi = 5°$ (o) $\phi = 10°$

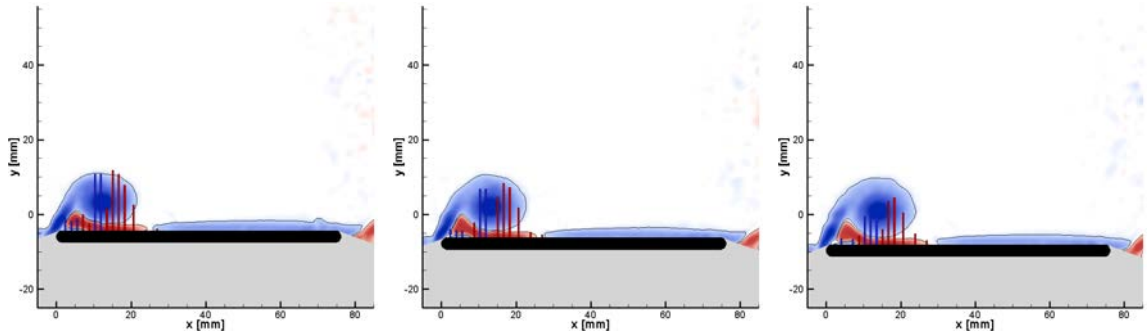

(p) $\phi = 15°$ (q) $\phi = 20°$ (r) $\phi = 25°$

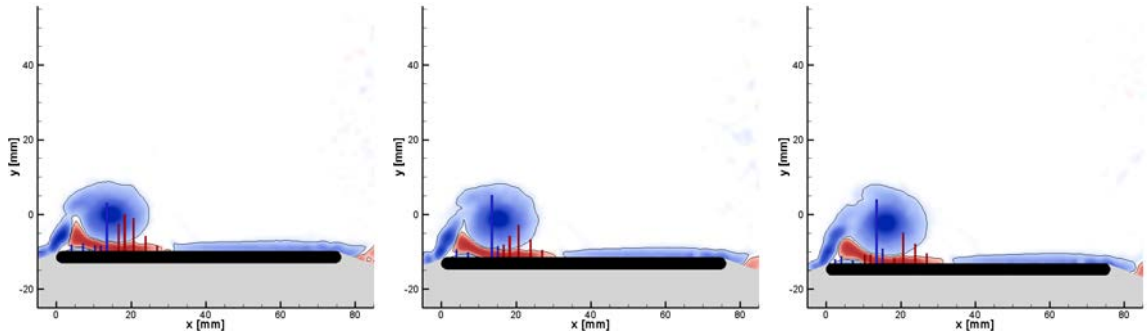

(s) $\phi = 30°$ (t) $\phi = 35°$ (u) $\phi = 40°$

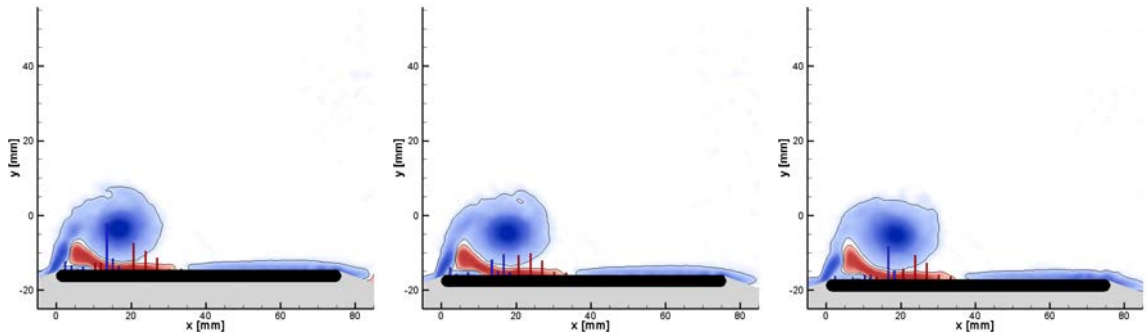

(v) $\phi = 45°$ (w) $\phi = 50°$ (x) $\phi = 55°$

Figure 5.1: Evolution of the vorticity field from the baseline case.

www.manaraa.com

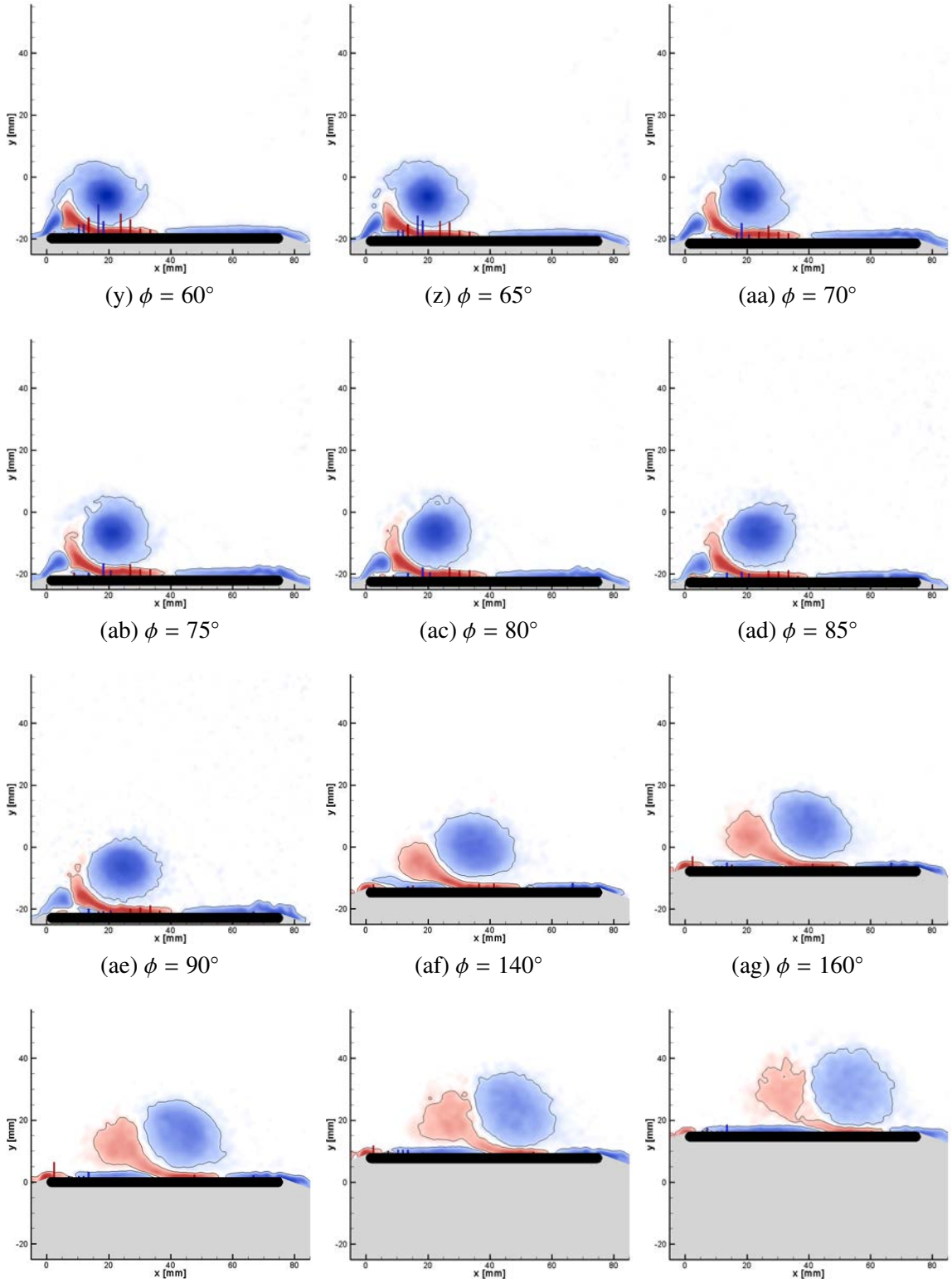

(y) $\phi = 60°$ (z) $\phi = 65°$ (aa) $\phi = 70°$

(ab) $\phi = 75°$ (ac) $\phi = 80°$ (ad) $\phi = 85°$

(ae) $\phi = 90°$ (af) $\phi = 140°$ (ag) $\phi = 160°$

(ah) $\phi = 180°$ (ai) $\phi = 200°$ (aj) $\phi = 220°$

Figure 5.1: Evolution of the vorticity field from the baseline case.

www.manaraa.com

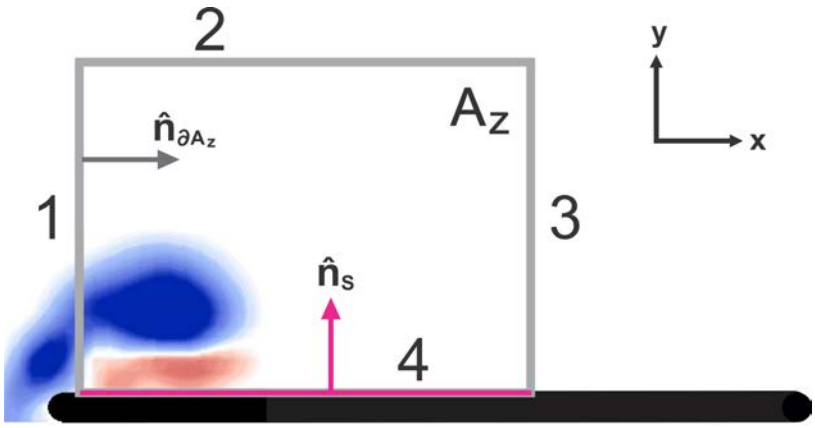

Figure 5.2: Control region used for vorticity flux analysis in the baseline case.

In order to evaluate the LSH of Equation 5.1, the temporal derivative of the circulation was approximated using a central difference approximation. All of the spatial derivatives that were needed in order to evaluate Equation 5.1 (e.g. $\partial\omega_z/\partial z$) were also computed using central difference approximations. As there can be no convection of vorticity through the plate, the in-plane convection term is only calculated along Boundaries 1-3. The control region was chosen so that Boundary 2 was located within predominantly irrotational fluid so that the convective flux of vorticity through Boundary 2 was negligible. As such, this term is neglected in all subsequent discussions. The convective flux of vorticity through Boundary 1 all comes from the leading-edge shear layer, and as such this term will be referred to as the shear-layer flux. As discussed in Chapter 2, since the diffusive flux of vorticity is small except at a solid boundary, it is only evaluated along Boundary 4 (via the surface pressure gradients as per Equation 2.20).

The phase-averaged fluxes of vorticity throughout the downstroke were calculated throughout the downstroke using Equation 5.1 and plotted in Figure 5.3. The most impor-

www.manaraa.com

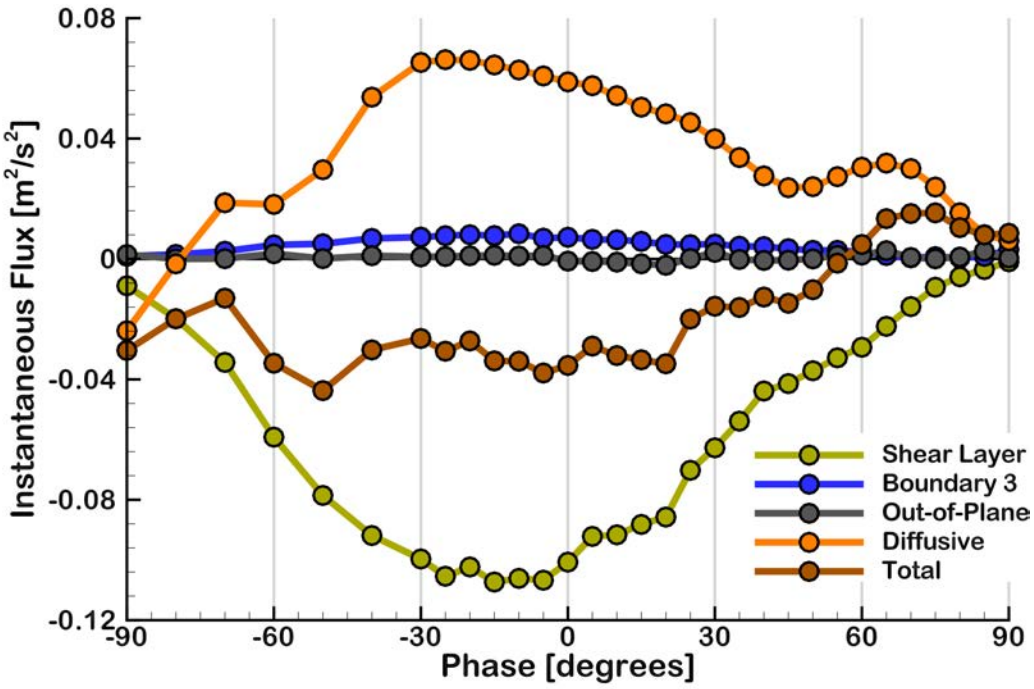

Figure 5.3: Instantaneous fluxes of vorticity during the downstroke of the baseline case.

tant of these fluxes are the convective flux into the control region via the shear layer and the diffusive flux from the surface pressure gradients. The flux of vorticity through Boundary 3 is also shown, which is small due to the fact that LEV remains within the control region throughout the entire downstroke. It can be noted that the total three-dimensional flux of vorticity (via tilting and spanwise convection) is negligible. The total flux of vorticity into the control region (labeled "Total" in Figure 5.3) is found by summing the entire RHS of Equation 5.1, and should be equal to the change in circulation.

Neglecting any three-dimensional effects, as well as realizing that the flux of vorticity through Boundary 3 is merely a byproduct of the boundary layer convecting downstream, leaves the shear-layer and diffusive fluxes as the primary terms that govern the

www.manaraa.com

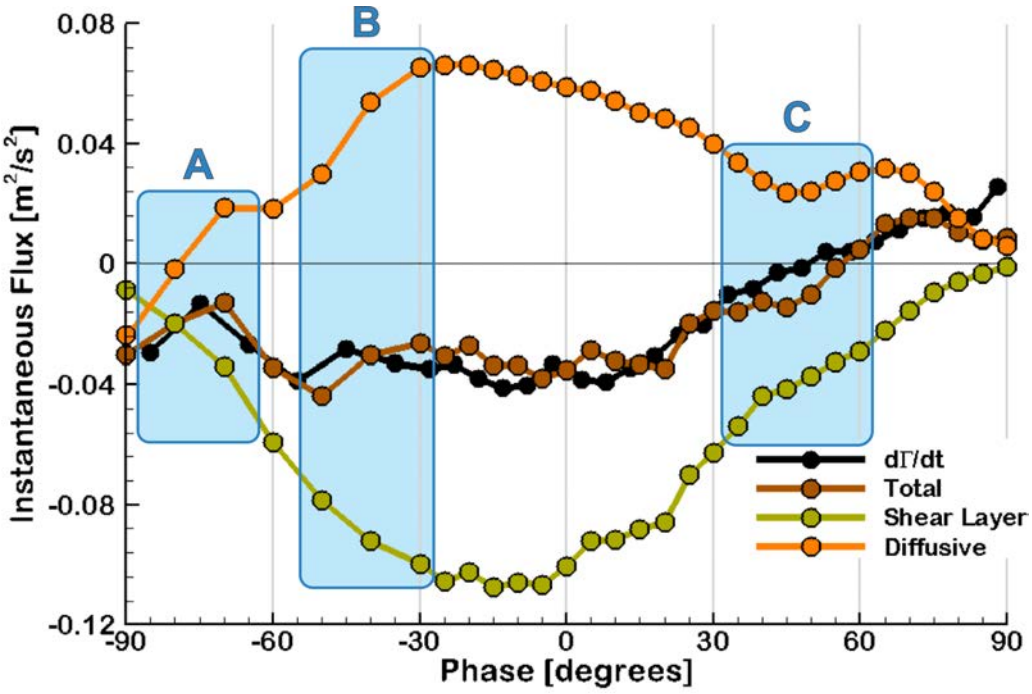

Figure 5.4: Primary fluxes of vorticity during the downstroke of the baseline case.

vorticity budget. These terms are therefore once again plotted in Figure 5.4, along with the total flux of vorticity (RHS of Equation 5.1) and the change in circulation (LHS of Equation 5.1). The close agreement between $d\Gamma/dt$ and the total flux of vorticity indicates the vorticity budget is being appropriately characterized. Furthermore, showing this budget is essentially the sum of the shear-layer and diffusive fluxes is an important result because it helps to elucidate the fundamental physics present within the flow, and analyzing the dynamics within these principal sources can provide superior insight into the formation and evolution of the LEV.

Figure 5.4 indicates the largest source of vorticity is the shear-layer flux, which is unsurprising since this term accounts for all of the vorticity that was generated and released

www.manaraa.com

from the leading edge. Overall, this flux approximates a cosine function that is similar to the plunge velocity. This is to be expected as both the vorticity concentration and velocity magnitude within the shear layer have been shown to increase with the plunge velocity [120]. This distribution does appear to have a slight phase shift with the data showing noticeable zero-offset at $\phi = -90^\circ$ and reaching a minimum around $\phi = -10^\circ$.

As it appears to be highly correlated to the kinematics of the airfoil, the shear-layer flux lends itself very well to modeling. Indeed, many models of vortex growth–especially inviscid ones–only account for physics associated with the convection of vorticity [112, 120]. However, Figure 5.4 shows that the magnitude of the diffusive flux is approximately half that of the shear-layer flux. The importance of this result is accentuated by the fact that the majority of existing studies tend to neglect the effects of vorticity diffusing from the surface [59, 25, 50, 120]. This trend is particularly surprising given that the few studies which have characterized the diffusive flux properly have shown it to take a prominent role in the development of a vortex. Didden [32] found the net vorticity flux into a vortex ring to be significantly diminished by the secondary vorticity generated on the outer wall of the nozzle from which it was generated. Similarly, in their vorticity budget analysis of a rotating wing, Wojcik and Buchholz [118] found the flux of secondary vorticity from the surface of the wing acted to stabilize the LEV and prevent the vortex from detaching. Eslam Panah et al. [85] actually measured the diffusive flux using the same experimental platform as this study, and–similar to what is shown in Figure 5.4–found the magnitude of the diffusive flux to be approximately half that of the shear-layer flux. Based on the dynamics that were characterized by Eslam Panah et al. [85], it can be expected within the

www.manaraa.com

current study that up to half of the vorticity added to the LEV via the shear-layer flux can be cross-canceled by vorticity diffusing from the surface of the airfoil.

Because of the limited attention it has received, the effect of the diffusive flux on the development of an LEV has yet to be rigorously explored. An analysis of the diffusive flux of vorticity thus begins with the identification of key features within the data. The regions containing these features have been highlighted and labeled in blue within Figure 5.4 and are identified as follows:

(A) The rapid transition from a negative to positive diffusive flux between $\phi = -90°$ and $\phi = -70°$.

(B) A significant increase in the diffusive flux between $\phi = -60°$ and $\phi = -30°$.

(C) A loss and subsequent recovery of the diffusive flux from $\phi = 35°$ to $\phi = 60°$, with a local minimum around the same phase at which $d\Gamma/dt$ becomes positive.

The physical sources of theses features, as well as their overall effect on the vorticity budget, are investigated within Sections 5.3.1-5.3.3 through a closer examination of the flow field. Isocontours of vorticity are once again used to characterize the evolution of the flow field; however, these contours will be magnified so as to provide a better picture of the LEV. Velocity vectors and pressure gradients are also shown in Figures 5.5-5.7 in order to thoroughly characterize the flow field.

www.manaraa.com

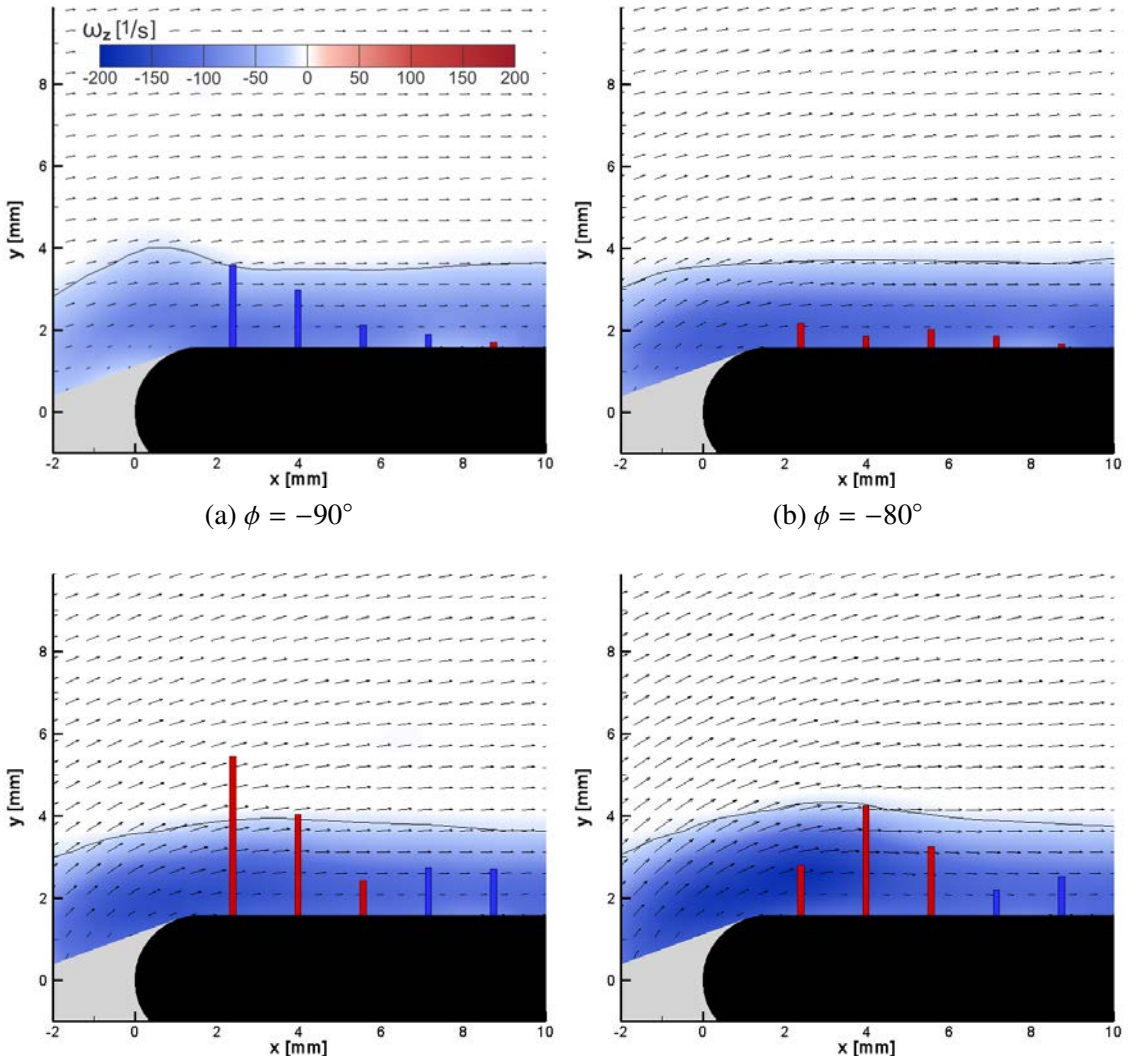

(a) $\phi = -90°$ (b) $\phi = -80°$

(c) $\phi = -70°$ (d) $\phi = -60°$

Figure 5.5: Evolution of the vorticity field prior to the formation of the LEV.

www.manaraa.com

5.3.1 Region *A*: Attached Flow

The provisional analysis of the flow field that was performed in Section 5.2 revealed that the LEV structure begins to form around $\phi = -50°$, indicating the flow near the leading edge should be attached from $\phi = -90°$ to $\phi = -60°$. Figure 5.5 presents a magnified view of the flow field during this phase interval, and the presence of a boundary layer near the leading edge confirms the increasing diffusive flux within Region **A** of Figure 5.4 is associated with an attached flow. Because there are no vortical structures near the leading edge, the formation of this adverse pressure gradient must be related to the increasing effective angle of attack as the plate begins to plunge downward and the stagnation point begins migrating to the underside of the plate [33, 44].

Referencing the vorticity fields above the plate at the end of the upstroke, Figures 5.1ah-5.1aj show a pressure maximum (transition from APG to FPG) beginning to move towards the leading edge, which corresponds to the motion of the stagnation point on top of the plate at the end of the upstroke. The FPG that is seen in Figure 5.5a is similarly a result of the stagnation point increasing the pressure at the leading edge, which would be expected to produce significant pressure drag. As the downstroke begins and the angle of attack starts to increase, the stagnation point moves to the underside of the airfoil. This motion first reduces the high pressure at the leading edge and the associated FPG (see Figure 5.5b), and ultimately forms an APG at the leading edge (see Figure 5.5c) as it becomes more difficult for the flow to navigate around the leading edge [33].

The formation of the APG at the leading edge provides a necessary condition for flow separation; however, the leading-edge boundary layer is able to withstand some finite

www.manaraa.com

APG without separating [38, 33]. Within the current example, the APG surpasses this threshold value somewhere between $\phi = -70°$ and $\phi = -60°$, as both the accumulation of vorticity near the leading edge and the diminished APG within Figure 5.5d indicate a transition to a separated flow. Referencing Figure 5.4, the plateau that forms in the diffusive flux from $\phi = -70°$ to $\phi = -60°$ essentially marks a transition towards a separated flow, with the suction peak moving downstream from the leading edge to the location of the vortex.

To summarize the relevant aspects of this section, the location of the stagnation point at $\phi = -90°$ causes negative vorticity to be diffused into the flow, thereby strengthening the boundary layer near the leading edge and decreasing its susceptibility to separation. This process is very short-lived, as the increasing angle of attack causes the flow to accelerate around the leading edge when the stagnation point moves to the underside of the airfoil. The suction produced by this acceleration creates an APG, which, once it has reached a critical magnitude, causes the flow to separate. Overall, this process has a significant effect on the time-history of the vorticity budget. As illustrated in Figure 5.4, contributions from the diffusive flux cause the magnitude of the total vorticity flux to have a local maximum early in the downstroke and then subsequently decrease until the onset of separation, despite the fact that the shear-layer flux is continually increasing. Separation occurs as $d\Gamma/dt$ approaches zero, with the balance of the shear-layer flux and the diffusive flux indicating a balance between convective and viscous forces.

www.manaraa.com

5.3.2 Region *B*: Separation at the Leading Edge

The concentration of vorticity that forms above the leading edge at $\phi = -60°$ (Figure 5.5d) signals the transition to a separated flow, allowing for the formation and subsequent growth of the LEV (Figure 5.6). While the separation process–and the appearance of a vortical structure–is very distinct within the flow fields, Figure 5.6 shows that the LEV undergoes two different stages of separation. When the LEV originally forms, it remains connected to the downstream boundary layer, and this reattachment implies the flow has only "partially" separated. It should be noted that there is no rigorous method for identifying when the LEV stops reattaching, but for the purpose of this discussion, the process is simply understood to occur once Figure 5.6 shows the vorticity-threshold contour around the LEV is no longer connected to the downstream boundary layer.

One important characteristic of the partially separated LEV is the extremely thin region of reversed flow at the surface of the airfoil. Visbal [110] was able to resolve these small pockets of reversed flow at the leading edge of a pitching SD7003 airfoil using a high-fidelity large-eddy simulation, yet the region appears to be too small to be resolved within the presented data until $\phi = -40°$. Because of this limitation of sufficiently resolving the near-wall flow, a more definitive indication of separation within Figure 5.6a is the formation of an FPG upstream of the LEV core and a strong APG downstream of the core, which is caused by the separated structure accelerating fluid away from (FPG) or towards (APG) the surface of the airfoil [33].

As the circulation of the LEV continues to increase, Figures 5.6a-5.6b show how the APG downstream of the core grows into a large, narrow peak, the formation of which

www.manaraa.com

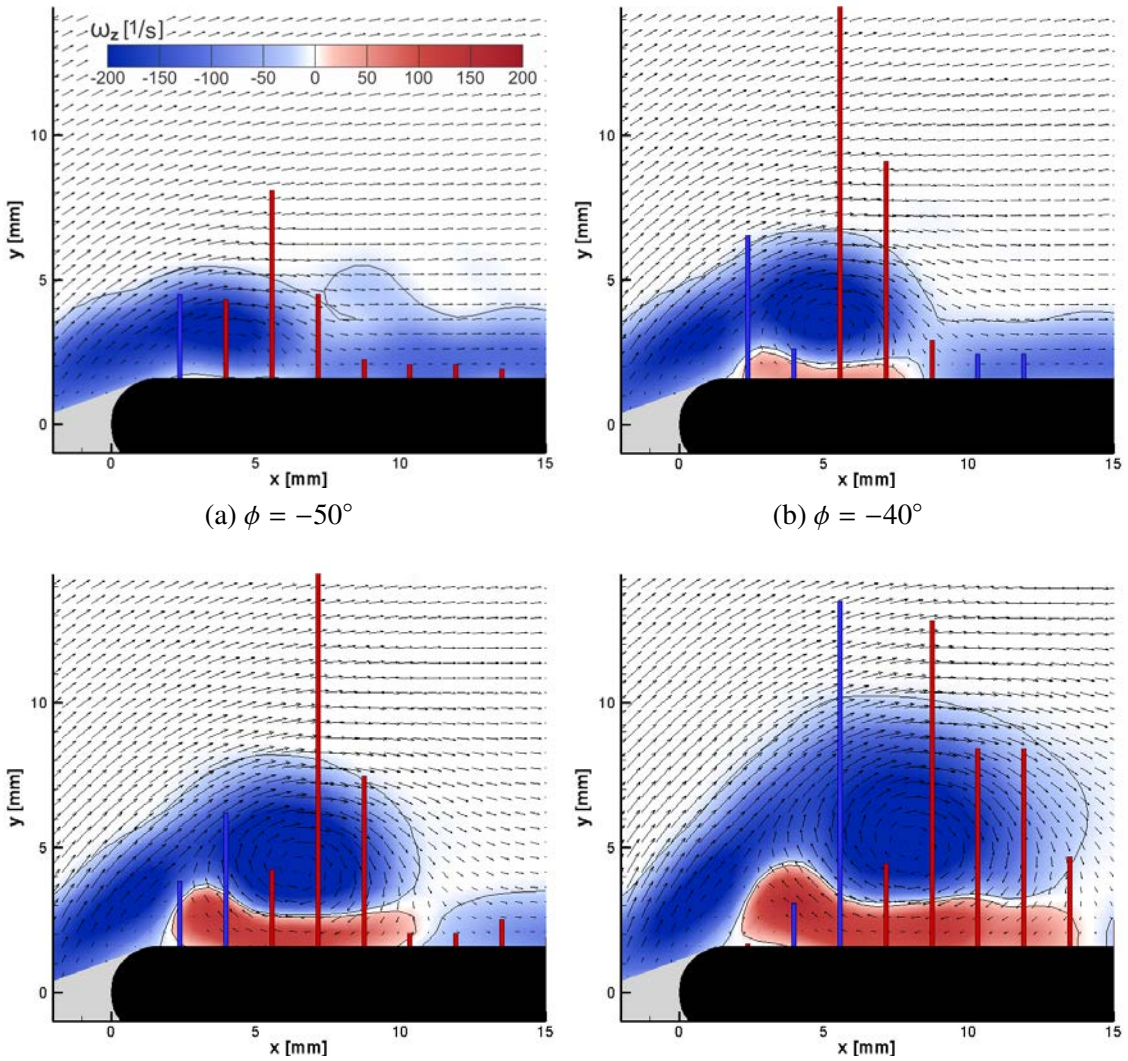

(a) $\phi = -50°$ (b) $\phi = -40°$

(c) $\phi = -30°$ (d) $\phi = -20°$

Figure 5.6: Separation of the LEV and formation of OSV.

www.manaraa.com

amplifies the diffusive flux within Region **B** of Figure 5.4. This rise in the diffusive flux data lasts until $\phi \approx -30°$, which Figure 5.6c shows to coincide with the LEV detaching from the downstream boundary layer and becoming "fully" separated. After this roll-up of the LEV occurs, Figure 5.6d shows the narrow APG peak begins to spread out downstream of the LEV, decreasing in magnitude as it does so. This process–i.e. the LEV detaching from the downstream boundary layer–is concomitant with the formation of a distinct OSV within Figures 5.1g-5.1i, the simultaneity of which has been noted within several other studies [26, 54, 91, 115].

Interpreting Region **B** of Figure 5.4 as a whole provides some interesting insight into the dynamics of the LEV. While the shear-layer flux–which approximately follows a cosine distribution in time–experiences a gradual leveling off during the initial separation of the LEV, there is a drastic increase within the diffusive flux while the LEV remains attached to the downstream boundary layer. Given enough time, the combination of these two effects eventually leads to a reduction in the total vorticity flux. Once the LEV rolls up and the OSV forms, the diffusive flux abruptly levels off and the magnitude of the total vorticity flux begins to increase once more. This characterization reveals a critical component of the separation process: the reattachment of the LEV leads to the formation of a massive sink of negative vorticity at the surface of the airfoil. While a significant diffusive flux is still maintained once the LEV has rolled-up, these results indicate that maximizing the diffusive flux is associated with prolonging the reattachment of the LEV to the downstream boundary layer. Therefore, the roll-up of the LEV–and thereby the formation of the OSV–limits the diffusive flux.

www.manaraa.com

5.3.3 Region *C*: LEV Detachment

The final stage within the evolution of the flow that will be considered is the detachment of the LEV from the leading edge. Region **C** of Figure 5.4 highlights a distinct drop within the diffusive flux between $\phi = 35°$ and $\phi = 60°$, which an analysis of the pressure distributions has revealed to be caused by the formation of a minor FPG (creating a flux of negative vorticity) at the leading edge. Figure 5.7 illustrates the evolution of the vorticity field over this phase interval, wherein the diffusive flux caused by this FPG can be seen to strengthen the region of negative vorticity (i.e. the tertiary vortex) beneath the upstream portion of the OSV. This tertiary vortex grows until it connects with the shear layer at $\phi \approx 45°$, and the subsequent loss of the FPG between $\phi = 50°$ to $\phi = 60°$–and the corresponding increase within the diffusive flux in Figure 5.4–is concomitant with the shear layer rotating down towards the surface of the airfoil as it partially reattaches. Figure 5.4 shows that the local minimum of the diffusive flux within Region **C** is concurrent with the circulation of the control region beginning to decrease (i.e. $d\Gamma/dt > 0$), which is a clear indication of a detached vortex as it implies the shear layer is no longer feeding vorticity into the LEV [115].

Although the specific dynamics are not clear within the available data, these results suggest that the formation of an FPG near the leading edge–or the growth of the tertiary vortex–plays a roll during the detachment of the LEV by promoting the reattachment of the shear layer. Note that the causality has not been established, so it is not clear if the tertiary vortex and the leading-edge FPG actually cause the detachment. However, the presence of an FPG beneath a reattaching shear layer can be understood to aid in the reattachment

www.manaraa.com

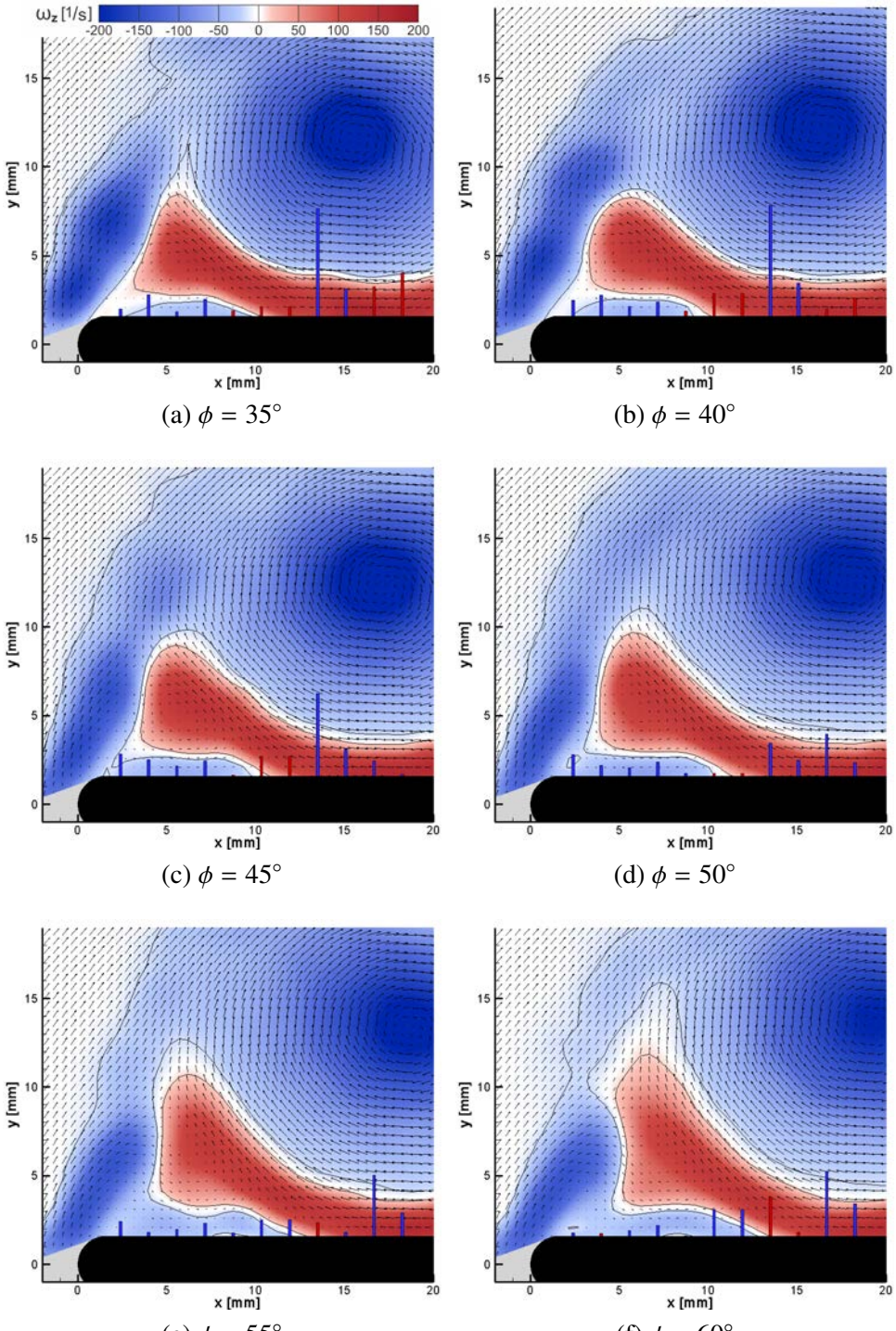

(a) $\phi = 35°$ (b) $\phi = 40°$

(c) $\phi = 45°$ (d) $\phi = 50°$

(e) $\phi = 55°$ (f) $\phi = 60°$

Figure 5.7: Detachment of the LEV.

www.manaraa.com

process itself. Even though the physical source of the FPG is unclear, its effect on the vorticity budget is captured very well within Region **C** of Figure 5.4.

5.3.4 Summary

After characterizing the vorticity budget of the leading-edge vortex, the growth of the structure was observed to be governed by two dominant sources of vorticity. The shear-layer flux was identified as the larger source, and its magnitude was observed to be well correlated with the plunge velocity. However, the results also showed the total circulation of the control region was substantially reduced by the vorticity diffusing from the surface beneath the LEV, which is in accordance with the limited number of studies available in which the diffusive flux was properly characterized [32, 1, 96, 85]. Demonstrating the relevance of this source has served to identify a major deficit within our understanding of leading-edge vortex formation on unsteady profiles, as many examples within the literature overlook the effects of the diffusive flux of vorticity from the surface of the airfoil [59, 25, 50, 120]. Cursory attempts–to great effect–have been made to correct this oversight by relating the major trends within the diffusive flux to the evolution of the LEV. Specifically, three trends were identified within the data from Figure 5.4 and related to the flow dynamics as follows:

www.manaraa.com

(A) The rapid transition from a negative to positive diffusive flux between $\phi = -90°$ and $\phi = -70°$ is related to the transience in the leading-edge pressure gradients that is caused by the stagnation point traversing the leading edge while the flow is attached.

(B) The drastic increase in the diffusive flux between $\phi = -60°$ and $\phi = -30°$ coincides with the initial separation of the LEV. However, the physics associated with this increase are short-lived, and the leveling off of the diffusive flux occurs once the LEV rolls up and the OSV forms.

(C) The loss and subsequent recovery of the diffusive flux from $\phi = 35°$ to $\phi = 60°$, highlights a novel behavior within the diffusive flux that is associated with the growth of the tertiary vortex, which is hypothesized to play a roll in the detachment of the LEV.

The impressive correlation between the diffusive flux trends and the flow field indicates the on-wall pressure gradients are highly correlated to stages in the LEV evolution (i.e. separation, roll-up and detachment). Identifying this behavior is a substantial contribution in and of itself, but it also establishes a new paradigm for analyzing the vortex dynamics of the flow in parallel with those observed at the wall. Eslam Panah et al. [85] demonstrated the importance of the diffusive flux of vorticity by showing its magnitude to be approximately half that of the shear-layer flux. The present discussion has helped to establish the physical relevance of this idea by relating the diffuse flux data from Figure 5.4 to the flow fields of Figure 5.6 and concluding that the pronounced diffusive flux is achieved while the nascent LEV remains attached to the downstream boundary layer. Because the

www.manaraa.com

rich vorticity-transport behavior associated with this process has yet to be discussed within the literature, characterizing the physics of the LEV before and after its roll-up is of particular interest. As such, Chapter 6 delves further into the dynamics of the LEV in order to establish how the diffusion of vorticity influences the evolution of the global vorticity field.

www.manaraa.com

CHAPTER 6
CHARACTERIZATION OF THE FLOW PHYSICS GOVERNING THE FORMATION OF THE LEV

6.1 Introduction

Based on the vorticity flux analysis that was performed within the previous chapter, it has been well established that the flux of vorticity diffusing from the surface of the airfoil beneath the LEV acts as a prominent sink of vorticity within the flow. More importantly, the time-history of this diffusive flux was shown to be highly correlated to the evolution of the flow field, as different stages within the formation and evolution of the LEV were observed to be well represented by specific features or trends within the diffusive flux data. It is the role of this chapter to delve further into this relationship, so as to establish a basic model for how this airfoil-vortex interaction influences the formation of the LEV. In addition to characterizing how specific vortical structures within the flow affect the distribution of pressure gradients upon the surface of the airfoil, great care will be taken to identify how the diffusive flux of vorticity that results from these imposed pressure gradients is able to, in turn, perturb the flow field. The end goal of these analyses will be to establish a model for the highly-coupled relationship between the diffusive flux of vorticity, local vortex dynamics and overall flow evolution.

6.2 Formation of the LEV

Approximately two-thirds of the total diffusive flux is generated within Region **B** of Figure 5.4 ($\phi = -60°$ to $\phi = -30°$), which has been established within Section 5.3.2 to

www.manaraa.com

be the phase interval over which the nascent LEV reattaches to the downstream boundary layer. Although this result stems from a correlation between the vorticity field and surface pressure gradients, the physics associated with this interaction can be further characterized through an analysis of the surface pressure distributions. While the reattachment of the LEV does not impose a specific pressure gradient on the surface, it does require the pressure beneath the LEV to be approximately recovered to its inviscid value [100], which is why it is helpful to look at the surface pressure distributions.

Distributions of the surface pressure coefficient ($C_p = [p - p_\infty]/0.5\rho U_\infty^2$) obtained throughout the initial formation of the LEV are shown in Figure 6.1. The total uncertainty in the surface pressure coefficient data was conservatively calculated to be 0.1003. Isocontours of the corresponding vorticity fields, along with velocity vectors and surface pressure gradients, are shown in Figure 6.2. The pressure recovery associated with the reattachment of the LEV is apparent in the data presented for $\phi = -60°, -50°$ and $-40°$, as the pressure coefficient for each case falls to a minimum prior to the location of the reattachment point at $x \approx 8$ mm. This effect becomes more significant as the LEV continues to grow, since an increase in the circulation will induce more suction at the surface of the airfoil and require the reattachment process to coerce a larger pressure recovery. In terms of the vorticity fields from Figures 6.2b-6.2c, this results in the formation of the narrow APG peak downstream of the LEV core.

Through the development of the Crabtree criterion, Crabtree [30] demonstrated that there is a maximum pressure recovery–or pressure gradient–that can be supported by the surface of an airfoil within the reattachment region of a laminar separation bubble (LSB),

www.manaraa.com

and exceeding this threshold is what causes dynamic stall. Extending this basic principle to the current example, it is expected that achieving some threshold pressure gradient downstream of the LEV will eliminate the connection to the downstream boundary layer and cause the vortex to roll up. Considering Figure 6.1, it would appear that such a critical pressure gradient is achieved sometime between $\phi = -40°$ and $\phi = -30°$, as this is the point at which the slope of the pressure distributions downstream of the suction peak stops increasing. Eliminating the reattachment point causes the adverse pressure gradient to relax by allowing it to extend downstream, as illustrated in the distributions for $\phi = -30°, -25°$ and $-20°$. This process is similarly characterized by the chordwise spreading of the APG distribution within Figures 6.2d-6.2f, after Figure 6.2d does indeed show the LEV rolling-up at $\phi = -30°$.

While its basic principle may seem applicable, the Crabtree criterion technically models the bursting of laminar separation bubbles, and the maximum pressure recovery that it predicts is related to the minimum effective distance over which turbulent reattachment can occur within an LSB [30, 33, 110]. Despite this fact, the concept of a critical surface pressure gradient appears to be well-applied within the current investigation of an LEV. In fact, Ramesh et al. [91] have found great success in modeling the shedding of vorticity from an airfoil based on a threshold in the amount of suction that can be supported by the surface. By using unsteady, thin airfoil theory, their "leading-edge suction parameter" was established based on a critical chordwise-gradient within the bound vorticity of an airfoil. While their work was primarily focused on calculating this leading-edge suction parameter, the current investigation is more concerned with establishing how the evolution of the flow

www.manaraa.com

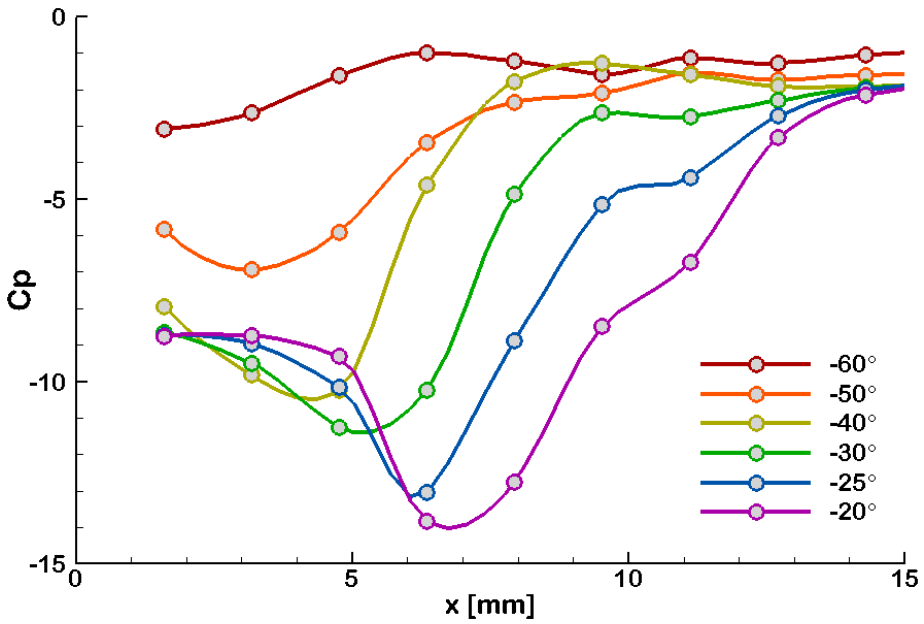

Figure 6.1: Surface pressure distributions associated with the initial formation of the LEV.

field eventually leads to this critical suction value being exceeded.

As discussed earlier, the growth of the APG downstream of the LEV core that is seen within Figures 6.2a-6.2c results from the increased strength of the LEV–corresponding to an increase in the suction peak beneath the vortex–requiring a greater pressure recovery during the reattachment process. In terms of the boundary vorticity flux, the resulting APG represents a source of positive vorticity within the flow. However, Figure 6.2 shows no major accumulation of secondary vorticity until after the LEV rolls-up at $\phi = -30°$. This indicates that the exacerbation of the diffusive flux within Region **B** of Figure 5.4 produces an effect within the flow field that may be considered a sink of negative vorticity rather than a source of positive vorticity.

Since the reattachment of the LEV is concomitant with the pressure recovery, the

www.manaraa.com

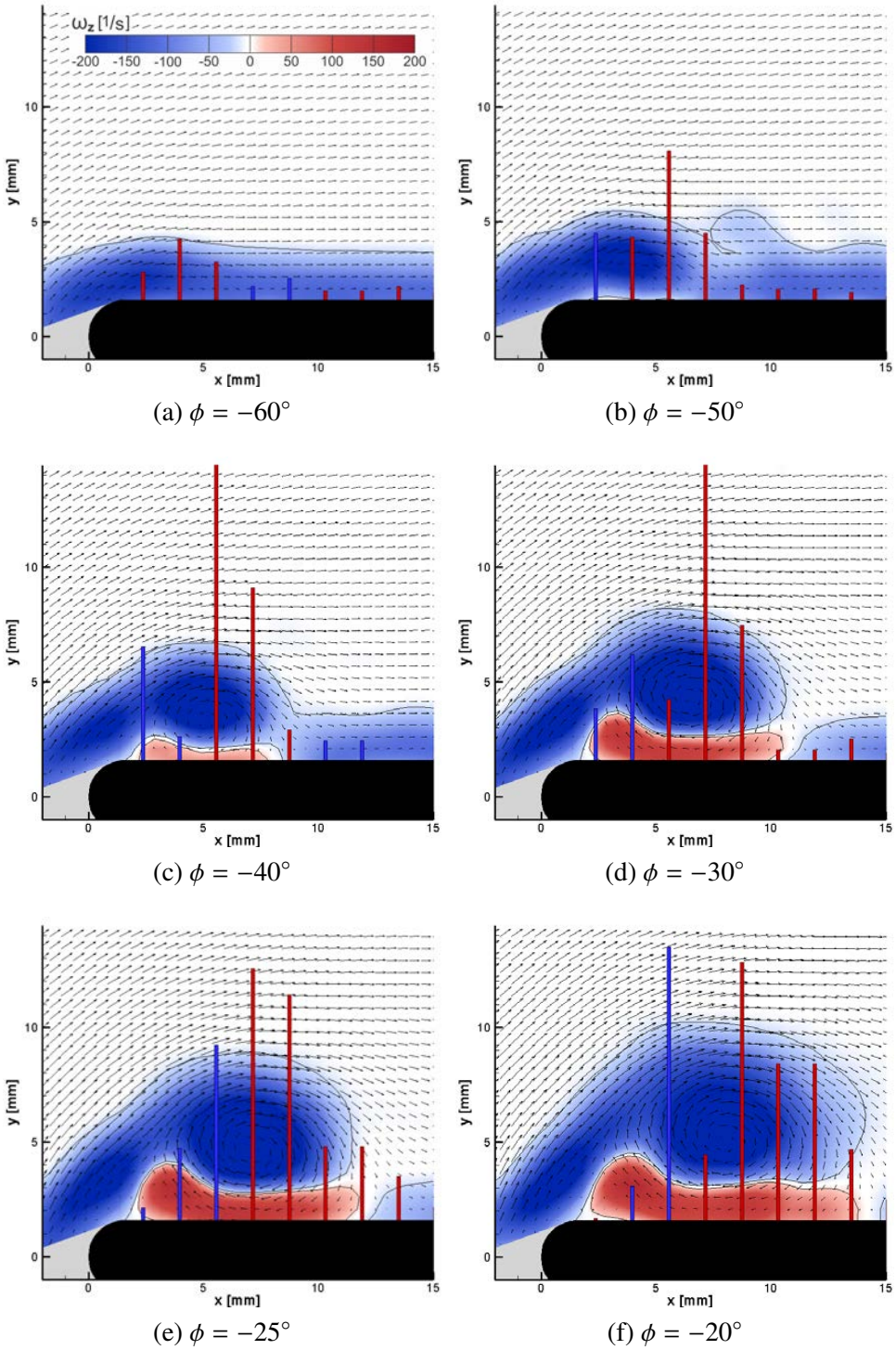

(a) $\phi = -60°$ (b) $\phi = -50°$

(c) $\phi = -40°$ (d) $\phi = -30°$

(e) $\phi = -25°$ (f) $\phi = -20°$

Figure 6.2: Vorticity fields associated with the initial formation of the LEV.

www.manaraa.com

strongest pressure gradients along the surface–and thus the greatest fluxes of secondary vorticity–are located within the reattachment region. The very nature of "reattachment" indicates a repositioning of primary vorticity so that it is concentrated near the wall, which means any secondary vorticity that is diffused should be immediately cross-canceled by the reattached boundary layer. This cross-cancellation of negative vorticity accounts for the distinct weakening of the vorticity field depicted within Figures 6.2a-6.2c in the region above the APG, eventually leading to this connection between the LEV and boundary layer being completely eliminated by Figure 6.2d. When there is no more negative vorticity for the diffusive flux to cross-cancel–i.e. when the LEV detaches from the downstream boundary layer–the accumulation of positive vorticity can finally begin. This characterization is an example of how an analysis of the local vorticity budget–i.e. within the reattachment region–can elucidate the dynamics of the flow. It has been well established within the literature that the formation of a distinct OSV is concomitant with the roll-up of the LEV [26, 54, 91, 115], yet these results are the first to discern that the roll-up of the LEV inherently requires the appearance of the OSV, as eliminating the reattachment region necessitates the diffusion of positive vorticity.

The primary conclusion from Section 5.3.2 was that the diffusive flux of vorticity was significantly augmented during the phase-interval in which the nascent LEV was seen to undergo reattachment. However, because the total diffusive flux of vorticity from the surface of the airfoil is governed by the pressure difference between the leading edge and the downstream end of the control region (see the last term on the RHS of Equation 5.1), it is important to note that the actual reattachment process does not govern the growth of

www.manaraa.com

the total diffusive flux of vorticity. This is made clear by the fact that Figure 6.1 shows the downstream pressure is recovered well before the end of the control region, regardless of whether the LEV reattaches ($\phi = -60°, -50°$ and $-40°$) or not ($\phi = -30°, -25°$ and $-20°$). The peak within the diffusive flux at $\phi = -30°$ must therefore be related the pressure at the leading edge reaching a minimum. This is well illustrated within Figure 6.1, as the $\phi = -30°, -25°$ and $-20°$ data sets all report the same pressure coefficient being measured at the leading edge (at x = 1.6 mm) once roll-up has occurred. Interestingly, the datasets plotted within Figure 6.1 show this effect is related to the formation of a pressure plateau upstream of the suction peak after $\phi = -40°$, and inspection of the flow field near the leading edge of Figures 6.2d-6.2f indicates that this phenomenon is related to the formation of the OSV. This effect, as well as further characterization of the OSV, is discussed next in Section 6.3.

6.3 Development of the OSV

Figure 6.3 shows distributions of the surface pressure coefficient obtained near the leading edge after the appearance of the OSV at $\phi = -30°$, with the associated vorticity fields being shown in Figure 6.4. Based on these plots, it appears that the OSV does not initially have a significant effect on the LEV, as the suction peak produced by the LEV continues to increase until $\phi = -15°$. However, as mentioned in the previous section, the appearance of the OSV does lead to the formation of a pressure plateau near the leading edge, which is characteristic of a low-energy region of separated flow [100, 47]. These results suggest that during its initial formation, the OSV simply acts to slow down the fluid

www.manaraa.com

near the leading edge to produce a region of separated flow between the shear layer and LEV.

As discussed many times already, a novel aspect within the diffusive flux data shown in Figure 5.4 is that it experiences a major increase while the LEV remains attached to the downstream boundary layer, and it was established within the previous section that this positive diffusive flux is actually realized within the flow as a sink of negative vorticity. Interestingly, once the LEV rolls-up at $\phi = -30°$, Figure 6.1 demonstrates how the appearance of the OSV immediately causes the leading-edge pressure to stop decreasing. Because of this, the diffusive flux data plotted in Figure 5.4 stops increasing as soon as it begins to act as a source of positive vorticity at $\phi = -30°$. At least within the current example, it is observed that the diffusive flux of vorticity produced by the interaction between the LEV and the airfoil can only be increased if it is affected as a sink of negative vorticity.

The maintenance of a significant diffusive flux after $\phi = -30°$ eventually leads to the OSV accumulating enough circulation to roll up and become a counter-rotating, vortical structure. While it may be difficult to characterize this roll-up based on the velocity or vorticity fields of Figure 6.4, the roll-up is well indicated within Figure 6.3 by the transition of the pressure plateau into a secondary suction-peak, since the formation of this secondary peak would require the OSV to exhibit a distinct rotational, vortex-like behavior [33]. While Figure 6.3 shows this secondary peak to have definitively formed by $\phi = -5°$, the FPG that can be seen at the leading edge of the $\phi = -10°$ data suggests that the OSV actually rolls-up at $\phi = -10°$, with the spatial resolution of the pressure taps being insufficient to resolve the initial APG produced by this secondary suction-peak. Looking very

www.manaraa.com

closely at Figures 6.4d-6.4f, this roll-up of the OSV does appear to be concomitant with the formation of a small region of negative, "tertiary" vorticity beneath the upstream portion of the OSV. While the reduced accuracy of the PIV measurements within this near-wall region makes it unlikely that the flow is being sufficiently resolved, at the very least, its presence does serve as a minor validation of the roll-up event indicated within the pressure data.

In addition to producing two distinct suction peaks on the surface of the airfoil, the current data suggest that the roll-up of the OSV has a distinct effect on the dynamics of the LEV. As seen in Figure 6.3, the deformation of the leading-edge pressure plateau into a secondary suction-peak at $\phi = -10^{\circ}$ coincides with the magnitude of the primary suction-peak beginning to decrease. Because Figure 5.4 indicates the total circulation of the flow is still increasing at $\phi = -10^{\circ}$, this reduction of the primary suction-peak is indicative of the LEV beginning to detach from the surface of the airfoil. This phenomenon appears to be well represented by standard topological analyses, as the formation of a counter-rotating OSV between the shear layer and LEV will theoretically require the detachment of the LEV [92, 115].

While this correlation between the roll-up of the OSV and the detachment of the LEV is an important result, it should be noted that the causality between the two phenomena is not established. Even so, showing that the two behaviors are concomitant illustrates a very distinct connection between the dynamics of the vorticity field and the "on-wall" signature that is seen within the pressure distribution–i.e. the formation of a secondary suction-peak is indicative of the LEV beginning to decouple from the surface of the airfoil.

www.manaraa.com

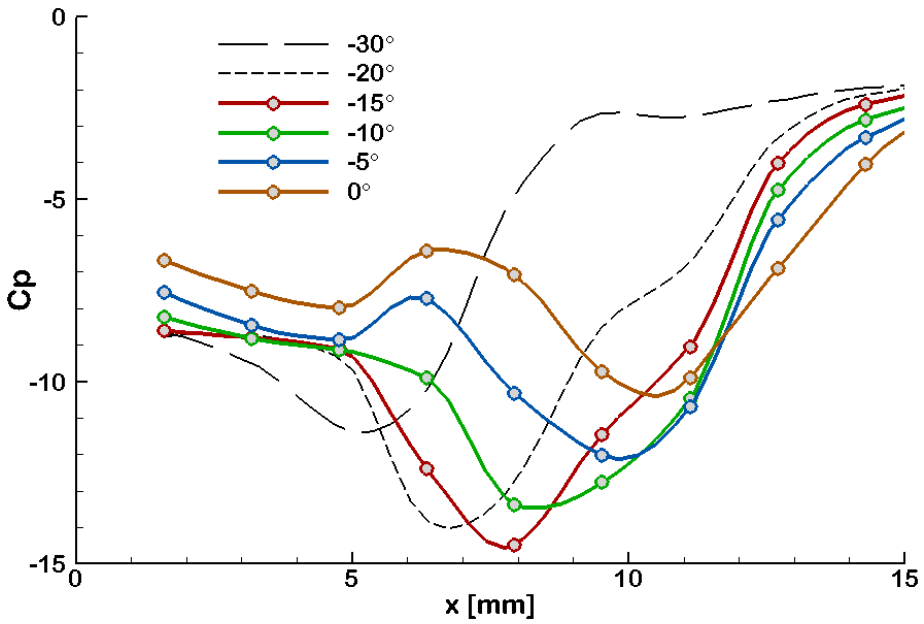

Figure 6.3: Surface pressure distributions associated with the initial formation of the OSV.

6.4 Discussion

By discussing the evolution of the vorticity field in parallel with the boundary vorticity flux, Section 5.3 successfully correlated features and trends within the diffusive flux data of Figure 5.4 to different stages within the development of the LEV. In addition to demonstrating the diffusive flux to be a relevant sink of vorticity, these results also demonstrate that different flow topologies prescribe different dynamics on the surface of the airfoil. In order to explicate this relationship, Sections 6.2-6.3 used the on-wall pressure-signature of the vorticity field to further characterize the dynamics of the flow.

By analyzing the pressure distributions of Figures 6.1 and 6.3, three distinct stages have been identified within the development of the LEV based on the presence of specific flow features. Figure 6.5 provides a simplified overview of these stages, with the pertinent

www.manaraa.com

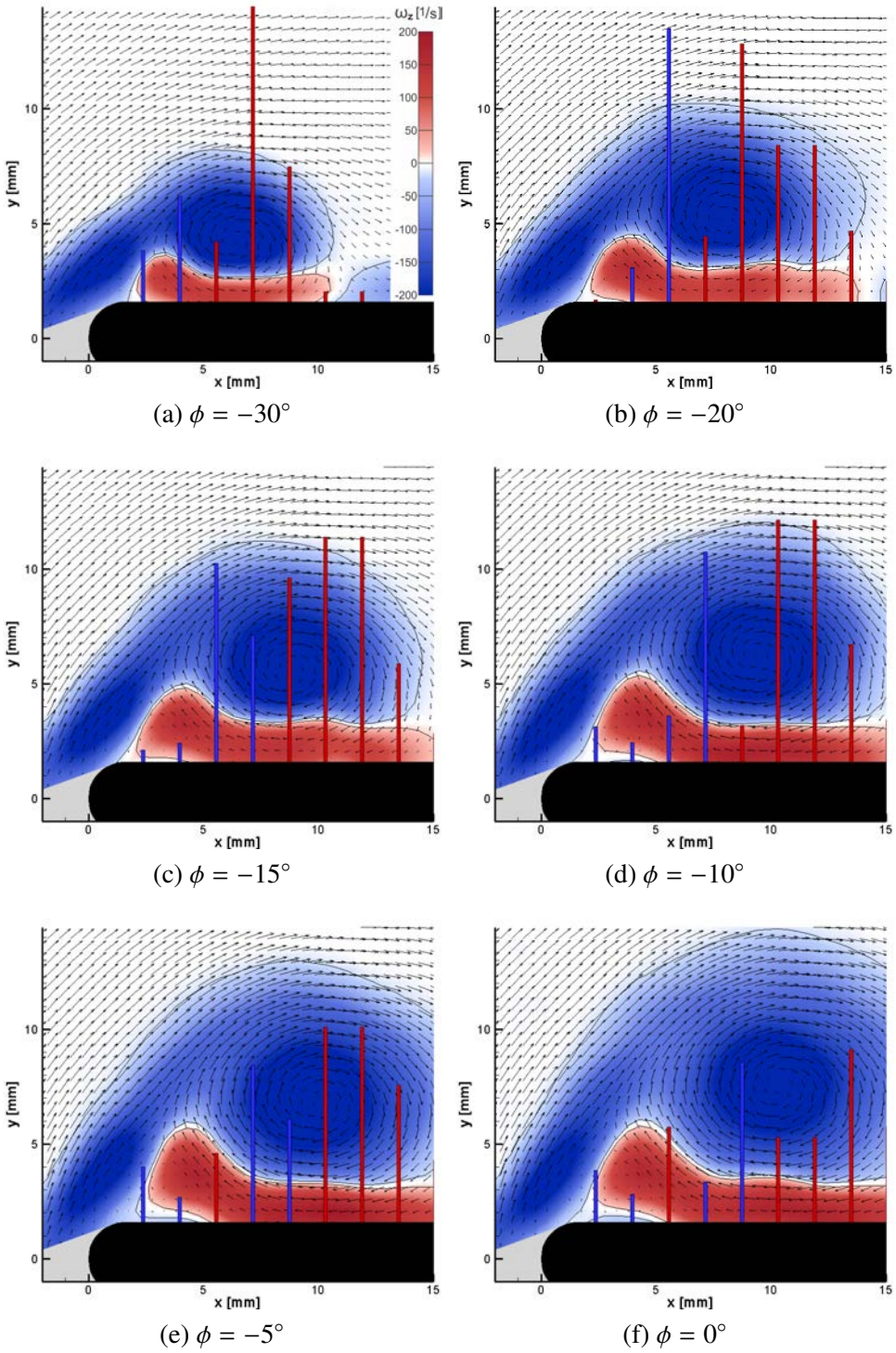

(a) $\phi = -30°$ (b) $\phi = -20°$

(c) $\phi = -15°$ (d) $\phi = -10°$

(e) $\phi = -5°$ (f) $\phi = 0°$

Figure 6.4: Vorticity fields associated with the initial formation of the OSV.

www.manaraa.com

flow structures being illustrated within Figures 6.5a-6.5c by a representative vorticity field, as well as by the defining pressure signature. The following discussion reviews the progression of the LEV through these stages, which serves to both summarize and re-emphasize the relevant flow physics that have been described throughout this chapter.

When the LEV initially forms, Figures 6.2a-6.2c illustrate how the reattachment of the LEV to the downstream boundary layer leads to the formation of an APG downstream of its core. While this APG indicates a positive diffusive flux, the lack of any secondary vorticity within the flow fields suggests that the APG is affecting a sink of negative vorticity rather than a source of positive vorticity. With the LEV being the only pertinent structure within the flow, the surface pressure distribution is characterized by a single suction peak (see Figure 6.5a).

As the circulation of the LEV initially increases, the APG downstream of the core grows into a large, narrow peak, the formation of which amplifies the diffusive flux (see Figures 6.2a-6.2c). The resulting cross-cancellation leads to a distinct weakening of the vorticity field in the region above the APG, eventually causing this connection between the LEV and boundary layer to be competently eliminated. As per the Crabtree criterion [30], this balance between the convective and diffusive fluxes downstream of the LEV core suggests there is a maximum pressure gradient that can be prescribed upon the surface of the airfoil.

Once the LEV detaches from the downstream boundary layer, it is observed to roll up (or fully separate) within Figures 6.4a-6.4c and form a distinct, circinate vortical structure. Without reattachment, the boundary conditions imposed by the primary suction-

www.manaraa.com

peak require the APG downstream of the LEV core to begin acting as a source of positive vorticity, which is diffused from the surface and then convected upstream by the reversed flow beneath the LEV. The presence of secondary vorticity at the leading edge slows down the local fluid, creating a pocket of separated flow between the shear layer and the LEV (shown in gray within Figure 6.5b). This low-energy region of separated flow isolates the leading edge from the influence of the LEV, producing a plateau in the pressure distribution upstream of the primary suction-peak, as depicted within Figure 6.5b.

With positive vorticity continuing to be diffused into the flow, the OSV eventually obtains enough circulation to roll up and cause the region of separated flow near the leading edge to exhibit a distinct, vortex-like behavior. This marks the point at which the region of secondary vorticity transitions from a wall-bounded shear layer into a counter-rotating, opposite-signed vortex. This roll-up is indicated by the deformation of the pressure plateau into a secondary suction-peak. Figure 6.5b depicts how a coherent LEV (blue) and OSV (red) produce a double suction-peak pressure distribution. It has also been noted within the current data set that the formation of this secondary suction-peak is concomitant with a reduction of the primary suction-peak, marking the beginning of the detachment of the LEV from the surface of the airfoil.

By characterizing the formation and evolution of the LEV based on the different signatures identified within the surface pressure distribution, the aerodynamic impact of the observed flow events can be interpreted. To this end, Figure 6.6 provides a qualitative representation of how the characteristic pressure distributions from Figure 6.5 evolve over time. Figure 6.6 illustrates the salient features in the evolution of the pressure distribution

www.manaraa.com

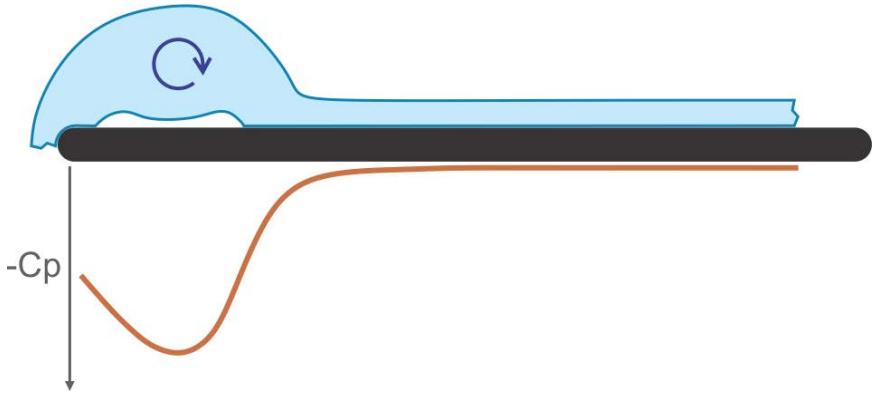

(a) **Reattaching LEV** – Single suction-peak pressure distribution.

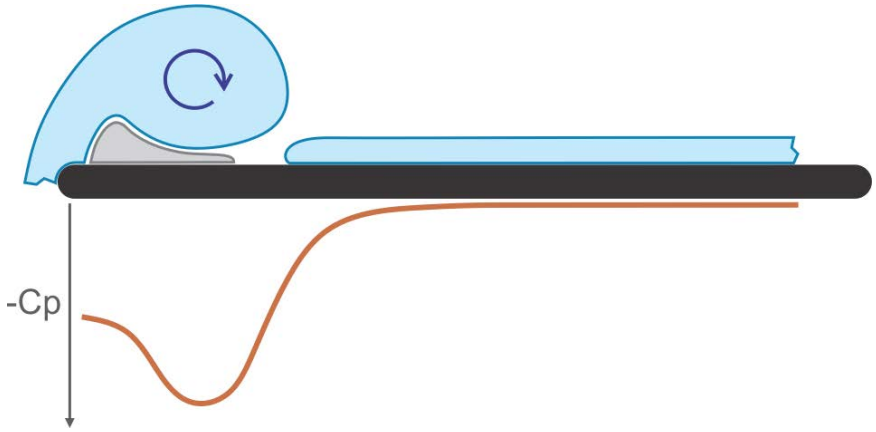

(b) **LEV Roll-up** – Pressure plateau upstream of a primary suction-peak

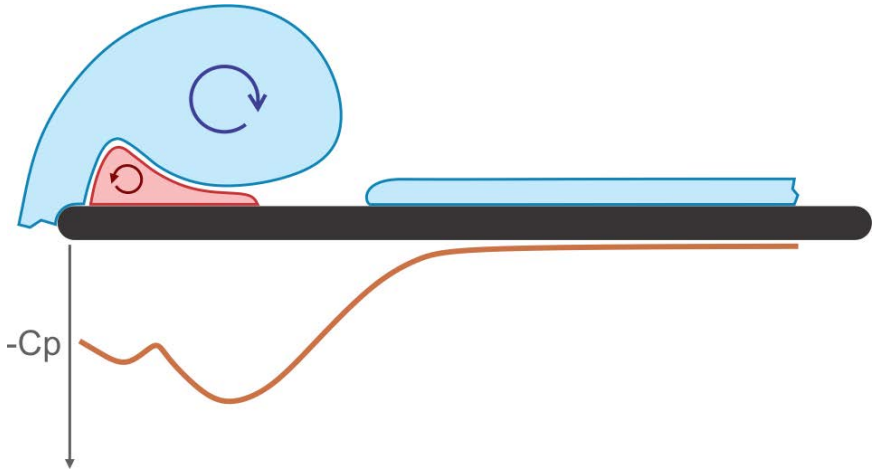

(c) **OSV Roll-up** – Double suction-peak pressure distribution.

Figure 6.5: Characteristic vorticity field and surface pressure distribution from the three stages of LEV formation.

www.manaraa.com

on the suction surface at seven representative times, T1-T7.

$T1$ depicts the primary suction-peak that is created when the LEV first begins to form, with $T2$ and $T3$ characterizing the growth of this primary peak as the reattaching LEV continues to accumulate circulation. Eventually, the growth of this primary suction-peak causes the slope of the pressure distribution downstream of the peak to exceed a critical value and the LEV rolls-up. Corresponding to Figure 6.5b, $T4$ and $T5$ depict the formation of a pressure plateau near the leading edge once this roll-up of the LEV has occurred. While this plateau hinders any additional suction from being imposed upon the leading edge, its appearance does not prevent the primary suction-peak from continuing to increase as the circulation of the LEV continues to grow–although it is possible that the presence of secondary vorticity beneath the LEV might have some minor effects on the amplitude of the primary peak. Finally, $T6$ and $T7$ model the deformation of the pressure plateau into a secondary peak that occurs once the OSV rolls-up, as in Figure 6.5c. While this secondary peak becomes a prominent feature within the pressure distribution, these final two time-steps illustrate how the detachment of the LEV leads to a simultaneous loss of suction across the entire surface of the airfoil.

Based on this characterization of the surface pressure, several hypothesis can be made regarding the production of lift through an intuitive chordwise-integration of these pressure distributions. Furthermore, the magnitude of the leading-edge pressure can be used to infer the behavior of the thrust. To begin, the growth of the primary suction-peak during the reattachment of the LEV is expected to produce a significant increase in both lift and thrust. But once the LEV rolls-up, the plateau that forms at the leading edge is

www.manaraa.com

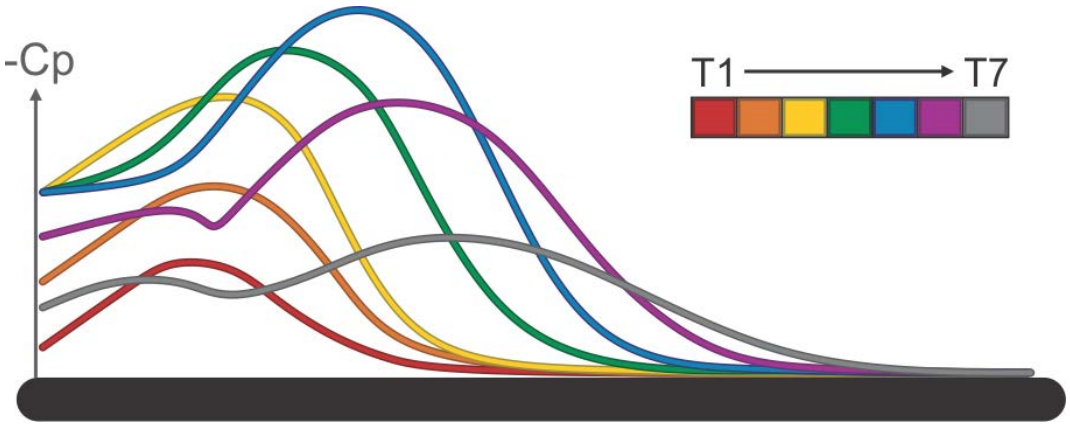

Figure 6.6: Hypothetical evolution of the pressure distributions associated with the development of the LEV.

expected to cause the thrust to stop increasing. While the continued growth of the primary suction-peak indicates the lift will continue to increase after the LEV has rolled-up, the presence of the plateau does seem to imply that the region of separated flow formed near the leading edge may have some detrimental effect on the total lift. Quite obviously, the detachment of the LEV is expected to result in a loss of both lift and thrust, since the magnitude of the entire suction distribution drops. However, the effect of the secondary suction-peak on the aerodynamic loads is not clear, as there are currently no means of establishing what the pressure distribution would look like without the secondary peak. But if one assumes that its formation does not affect the primary suction-peak, a preliminary hypothesis would be that the presence of a secondary peak near the leading edge allows for a favorable contribution to both lift and thrust. In the next chapter, the flow evolution will be considered along with load cell measurements to better understand the physical mechanisms governing the the fluctuations in aerodynamic loads.

www.manaraa.com

CHAPTER 7
FORCES ON A 2D PLUNGING PLATE

7.1 Introduction

At the end of Chapter 6, several hypotheses were made regarding the aerodynamic impact of the LEV. It is the goal of this chapter to objectively examine the aerodynamic loads of the baseline plunging case and to correlate trends from the lift and thrust data to specific dynamics seen within the vorticity field. This should not only help to further characterize the overall physics of the flow, but should also allow for the identification of specific vorticity transport mechanisms within the evolution of the LEV that produce desirable aerodynamic behaviors.

In order to set the stage for this discussion, vorticity isocontours obtained throughout the downstroke are shown in Figure 7.1 using data from the next half cycle to reconstruct the full flow field. As the surface pressure can be used to establish the aerodynamic loads of a specific flow features, the pressure values measured at each port are also displayed atop these contours; the magnitude of these bars is proportional to the *pressure magnitude* and *not* the magnitude of the pressure gradients, as was the case in previous sections. The coloring of these bars is also different than the convection that has been previously used, as the red/blue scheme doesn't refer to positive/negative pressures, but rather positive/negative contributions to the the overall lift. Red bars indicate positive lift, which would be associated with positive gauge pressures on the underside of the airfoil and negative gauge pressures acting on the upper surface. Conversely, blue bars are associated with

www.manaraa.com

negative lift and correspond to negative gauge pressures on the underside of the airfoil and positive gauge pressure on the upper surface.

Phase averaged lift and thrust measurements from the baseline plunging case are shown in Figure 7.2. A cursory inspection of these data indicates that both lift and thrust increase until approximately $\phi \approx -10°$, or the point at which the OSV rolls-up and the LEV begins to detach from the surface of the airfoil. While there is a distinct drop within the lift data after this point, the broader peak within the thrust data prevents any prominent losses from occurring until after $\phi \approx 15°$. Furthermore, the thrust data appears to level off momentarily between $\phi \approx 35°$ and $\phi \approx 65°$, which coincides with the reattachment of the shear layer that occurs within Region **C** of Figure 5.4 (see Section 5.3.3).

Although these distinct trends within the thrust data represent a rich correlation between thrust production and the dynamics of the LEV, a more appropriate representation of the lift must be obtained before an effective discussion of LEV aerodynamics can occur. Because Figure 7.2 reports the total lift produced by the airfoil, very little can be inferred from the relatively featureless data being plotted. Figures 7.1c-7.1f clearly show the development of the LEV to affect distinct loads near the leading edge, but they also depict significant loads being produced on the underside of the airfoil as well. Because this discussion is concerned with the aerodynamic impact of the developing LEV, the total lift plotted in Figure 7.2 must be decomposed so as to resolve the contribution being made by the LEV. This decomposition is explored within Sections 7.2-7.3, after which Section 7.4 uses the decomposed lift, as well as the thrust data from Figure 7.2, to characterize how lift and thrust production varies throughout the evolution of the LEV.

www.manaraa.com

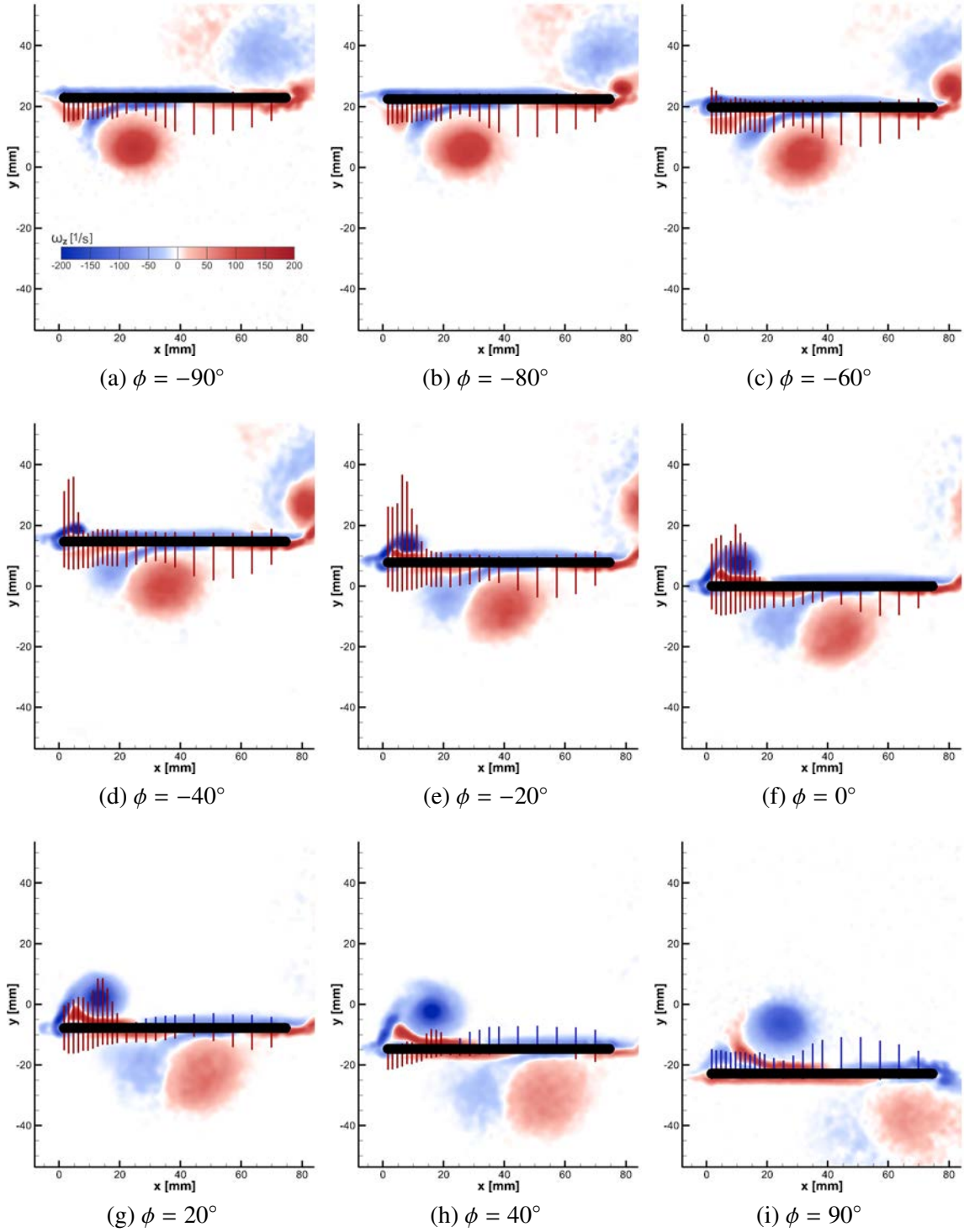

(a) $\phi = -90°$ (b) $\phi = -80°$ (c) $\phi = -60°$

(d) $\phi = -40°$ (e) $\phi = -20°$ (f) $\phi = 0°$

(g) $\phi = 20°$ (h) $\phi = 40°$ (i) $\phi = 90°$

Figure 7.1: The evolution of pressure-based lift during the baseline case.

www.manaraa.com

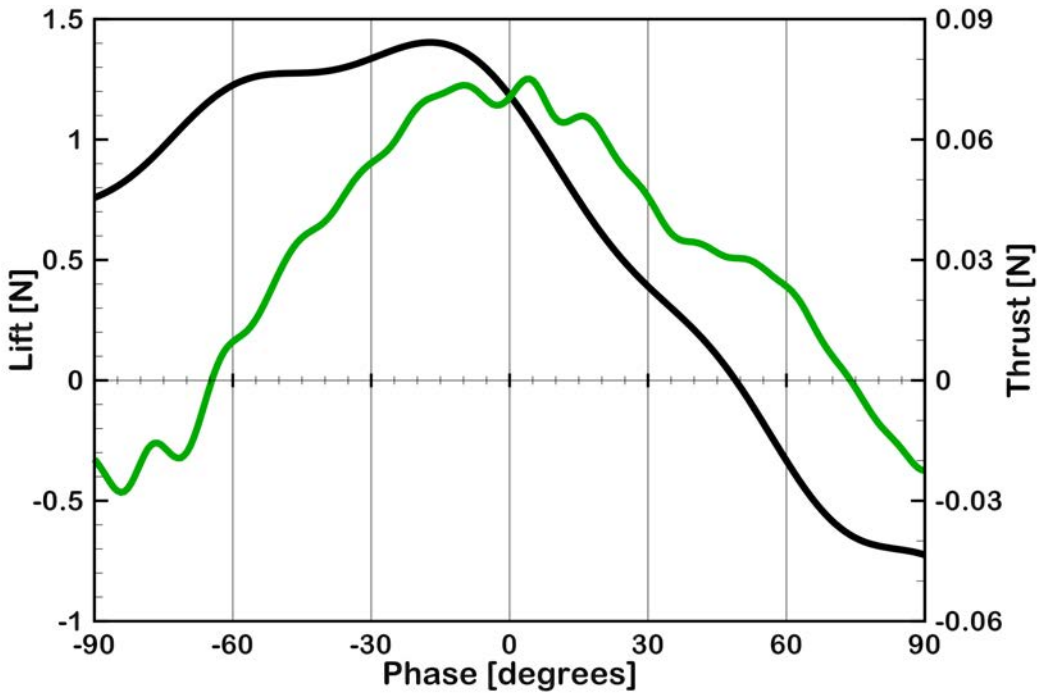

Figure 7.2: Time histories of lift (black) and thrust (green) from the baseline case.

7.2 Lift Decomposition: Contributions from Upper and Lower Surfaces

In order to better characterize the production of lift, Figure 7.3 decomposes the total lift into the contributions from the upper and lower surfaces of the airfoil, which were obtained through a chordwise-integration of the pressure data. Standard aerodynamic terminology identifies the upper and lower surfaces of the airfoil as the "suction" and "pressure" surfaces respectively. Continuing this terminology, the "Suction-Lift" and "Pressure-Lift" data shown in Figure 7.3 are obtained by integrating the pressure data on either side of the airfoil. Because pressure taps were only located on one side of the airfoil, the pressure-lift was calculated using the suction-surface data that was measured during the upstroke (i.e. when the upper surface becomes the "pressure side"). Figure 7.3 shows the sum of the two

www.manaraa.com

lift components ("Calculated Lift"), which should be equivalent to the lift measured with the force transducer ("Measured Lift") if the pressure profiles measured at the centerline were assumed to be constant in the spanwise direction. The close agreement between the calculated-lift and measured-lift data within Figure 7.3 helps to validate this assumption of spanwise-uniformity, which serves to further demonstrate the two-dimensionality of the flow.

Figure 7.3 shows no significant suction-lift being produced until approximately $\phi = -70°$, and Figures 7.1c-7.1d indicate that the rise that eventually occurs from $\phi = -70°$ to $\phi = -40°$ is associated with the generation of a low pressure region beneath the reattaching LEV. While the amount of suction-lift that is produced during this phase interval ends up accounting for approximately 40-percent of the total lift, even more relevant is the fact that this production of suction-lift all occurs within a localized region near the leading edge. In accordance with the work of Wu et al. [125], this suggests that significant aerodynamic changes could be made to the flow by targeting the vorticity transport within this small region.

The suction-lift is held steady as the LEV rolls-up, but $\phi \approx -10°$ marks the beginning of a significant reduction that persists through the rest of the downstroke, and the magnitude of this reduction appears nearly sinusoidal from $\phi = 0°$ to $\phi = 90°$. Figures 7.1f-7.1h indicate this loss of lift is caused by a decline of the entire suction-surface pressure distribution, and the fact that this pressure rise appears to be affected uniformly along the chord suggests that it is not related to the dynamics of the LEV–which Figures 7.1c-7.1f indicate to have a distinct, local effect.

www.manaraa.com

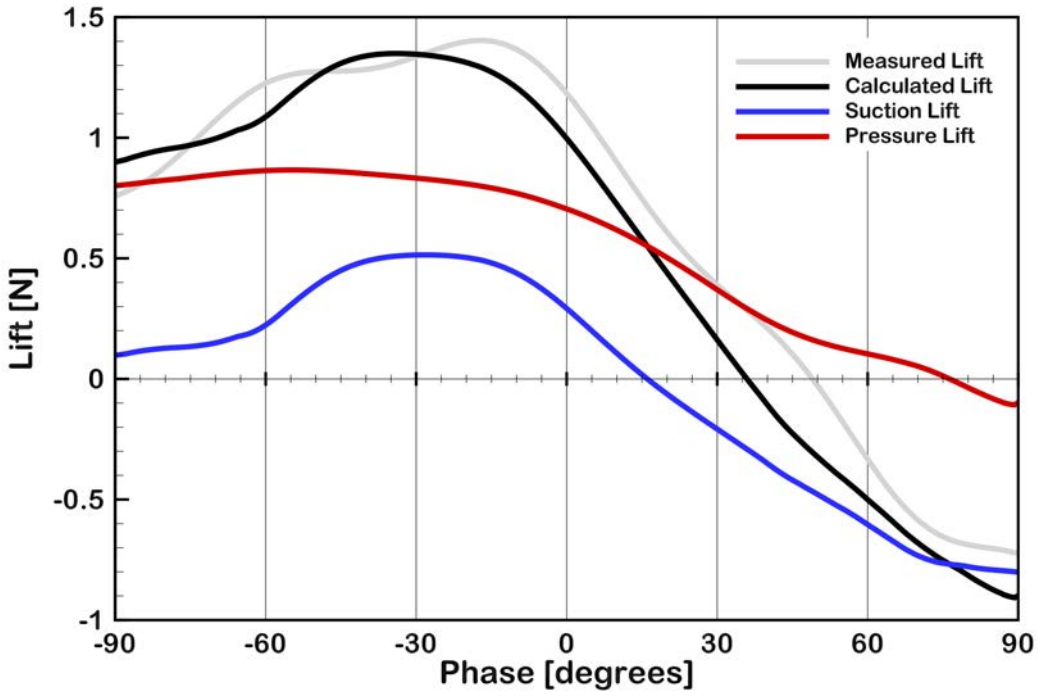

Figure 7.3: Contribution to the total lift from pressure acting on the suction and pressure sides of the airfoil during the downstoke of the baseline case.

www.manaraa.com

By the end of the downstroke, Figure 7.1i showed the suction-lift to be affected with relative uniformity along the chord–with the exception of the minor fluctuations seen downstream of the LEV. In order to continue following the dynamics of this pressure distribution, we look to the data shown on the suction side of the airfoil within Figures 7.1a-7.1e.

Interestingly, Figures 7.1a-7.1e show the pressure distributions on the underside of the airfoil remaining relatively unchanged throughout the first half of the downstroke, which is supported by the pressure-lift data within Figure 7.3 remaining approximately constant during the first half of the downstroke. Figure 7.3 indicates the pressure-lift drops to zero during the second half of the downstoke, which Figures 7.1f-7.1i show to be associated with the entire pressure distribution on the underside of the airfoil being reduced to zero.

The goal of this section was to decompose the total lift plotted in Figure 7.2 so as to isolate the contribution made by the formation of the LEV, i.e. the positive loads seen beneath the LEV in Figures 7.1c-7.1f. Decomposing the lift into the components produced on the upper and lower surfaces of the airfoil has provided a better characterization of the suction produced by the developing LEV, as it appears to be well-captured by the suction-lift plotted in Figure 7.3 during the first half of the downstroke. However, further analysis of Figures 7.1 and 7.3 has lead to the identification of distinct, chordwise-invariant dynamics within the pressure distribution on the suction side of the airfoil during the second half of the downstroke that do not appear to be related to the local effects of the leading-edge suction-peak. A different approach for decomposing the total lift is therefore required, wherein the lift produced by the LEV can be completely isolated from any other global

www.manaraa.com

effects–i.e. contributions to the pressure distribution that are made uniformly along the chord–that may be present within the flow.

7.3 Lift Decomposition: Viscous/Inviscid Contributions

Theodorsen's Theory [102]–referred to as "Theodorsen"–is one of the most broadly applied aerodynamic models for predicting the total lift produced by an oscillating airfoil. Equation 7.1 reports the form of Theodorsen's lift model that is obtained for an airfoil undergoing a pure-plunge motion, which is seen to be a function of the fluid density (ρ), airfoil semi-chord (b), free-stream velocity (U_∞), reduced frequency (k), Strouhal number (St), plunge frequency (f), span (s) and the Theodorsen function ($C(k)$).

$$F_y = -\pi^2 \rho b U^2 \Big[\underbrace{[k \cdot St \cdot sin\,(2\pi f t)]}_{\text{non-circulatory}} - \underbrace{[2St \cdot cos\,(2\pi f t)\, C(k)]}_{\text{circulatory}} \Big] s \tag{7.1}$$

In deriving the model, Theodorsen used linear, potential flow analysis to predict the lift generated by a thin airfoil undergoing small amplitude pitching and plunging oscillations. The model has two components: the non-circulatory and circulatory terms. The non-circulatory term–or the "added mass term"–is governed by the acceleration of the airfoil and essentially accounts for the inertial effects associated with displacing the surrounding fluid.

The circulatory term is associated with the bound circulation about the airfoil that is introduced through a combination of the Kutta condition (which ensures a unique velocity at the trailing edge) and the effective angle of attack produced by the plunge motion. One of the major contributions of Theodorsen's work [102] was characterizing how the vorticity within the wake of an airfoil would mitigate this circulatory term, as downwash from

www.manaraa.com

the wake would reduce the effective angle of attack and thus the bound circulation of the airfoil. In order to account for this attenuation within Equation 7.1, the quasi-steady lift is multiplied by the Theodorsen function ($C(k)$).

Based on this description, it can be understood that Equation 7.1 serves to identify the lift contributions of two major inviscid effects: the added mass effect as well as the effect of a changing angle of attack. As neither of these terms are related to the vortex induced lift that is currently of interest, subtracting the contribution of these inviscid effects from the total lift of the airfoil should help to reveal the lift contribution associated with the formation of the LEV.

The total lift is once again plotted within Figure 7.4, along with the inviscid lift contribution (from circulatory and non-circulatory effects) predicted by Theodorsen. The difference between these two data sets is also plotted within Figure 7.4 as the "Vortex Lift," which characterizes the lift contribution associated with the formation of the LEV. However, before the results of this lift decomposition are discussed, several clarifications should be made regarding the applicability of Theodorsen's lift model. Theodorsen [102] derived this lift model to predict the lift generated by a thin airfoil undergoing small amplitude pitching and plunging oscillations, and these assumptions have been significantly violated within the current experiment. Because Equation 7.1 is not technically valid, subtracting the predicted circulatory and non-circulatory forces from the total lift is not guaranteed to provide an accurate representation of the vortex-induced lift that is currently of interest.

The primary point of concern is that the circulatory effect within the context of Theodorsen's [102] derivation is associated with the bound circulation of the airfoil. Pitt

www.manaraa.com

Ford and Babinsky [88] attempted to correlate potential flow models with experimental results obtained from a translating (surging) flat-plate airfoil with a 15° fixed angle of attack; they found that when the Kutta-condition was violated, the circulation within the LEV was comparable to the bound circulation that would have been predicted by potential flow theory. Thus, within examples like the one being considered, the bound circulation is presumably zero. However, there still appears to be a circulatory lift contribution within the current data that somehow derives from the changing effective angle of attack.

It should also be noted that in a viscous, separated flow, the added mass derived from potential flow assumptions may also be inaccurate because the flow patterns are not the same as in potential flow. Several studies have attempted to characterize the added mass coefficient associated with airfoils undergoing unsteady motion, yet they have been unsuccessful in isolating the non-circulatory term from the viscous effects associated with separation [132, 93]. As such, it is not clear how the added mass of an airfoil within a separated flow varies from its potential flow counterpart.

Despite the questionable applicability of Equation 7.1, the results depicted within Figure 7.4 seem to justify its use. Not only does this figure show Theodorsen to be an extremely good predictor of the total lift prior to $\phi = -60°$ and after $\phi = 30°$, but the "vortex lift" that is identified by the regions of mismatch between Theodorsen and the total lift appears to be highly representative of the suction peak that grows beneath the LEV in Figures 7.1c-7.1e and is subsequently dissipated in Figures 7.1f-7.1h.

In addition to this simple fact that the results of this decomposition appear to be well-correlated with the evolution of the flow field–which will be discussed more in the

www.manaraa.com

next section–many examples within the literature have found Theodorsen's model to be a robust predictor of lift production for plunge-based airfoil kinematics, even when the small-perturbation assumption has been significantly violated [17, 83, 72]. More importantly, many studies of plunging airfoils have demonstrated regions of mismatch between the measured lift and the lift predicted by Theodorsen that are very similar to what is seen within Figure 7.4 [83, 108, 72, 10, 91]. While this discrepancy is not typically characterized, Baik et al. [10] have attributed it to the leading-edge suction produced by the developing LEV. So while the accuracy of the "vortex lift" being identified in Figure 7.4 cannot be verified, its derivation and subsequent interpretation as the lift contribution made by the developing LEV is justifiable. Correlating the time-history of this vortex-induced lift to the dynamics of the LEV, along with a similar correlation between the thrust data and the LEV evolution, will be the focus of the next section.

7.4 Aerodynamics of the LEV

Now that the lift and thrust contributions made by the LEV have been identified, the trends within the data can be related to the evolution of the vorticity field. So as to make for a better comparison, Figure 7.5 plots the vortex lift and a scaled version of the thrust that was measured with the force sensor. In order to streamline this discussion with that of Chapter 6, Figure 7.6 breaks down the representative evolution of the pressure distributions shown in Figure 6.6 into the three developmental stages of the LEV. Correlating these pressure distributions–and by extension the flow dynamics that they represent–to the lift and thrust data is performed next.

www.manaraa.com

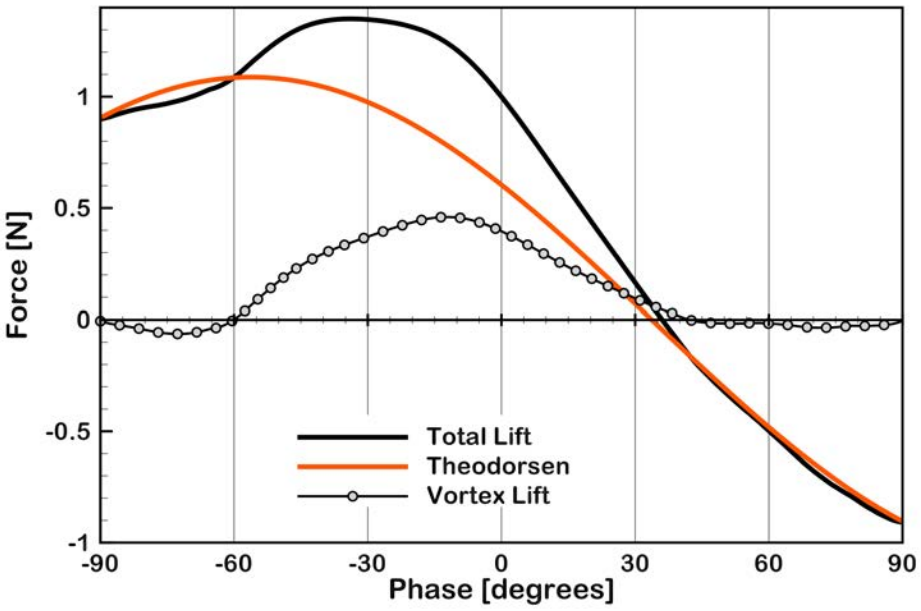

Figure 7.4: Measured lift (black) and the lift predicted by Theodorsen (Equation 7.1, orange), and the vortex lift (circles) identified as the difference between the two.

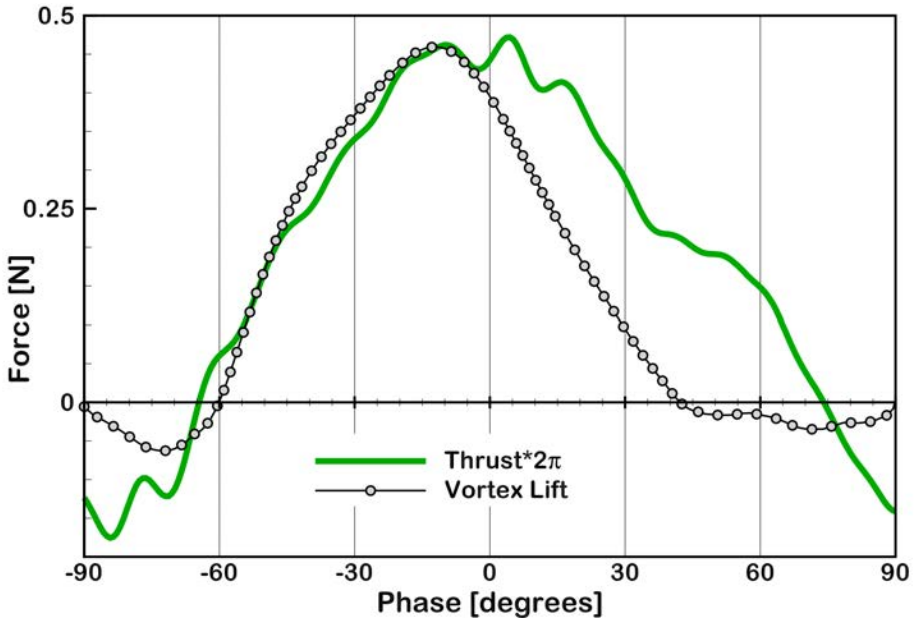

Figure 7.5: Vortex lift (circles) and measured thrust scaled by 2π (green.)

www.manaraa.com

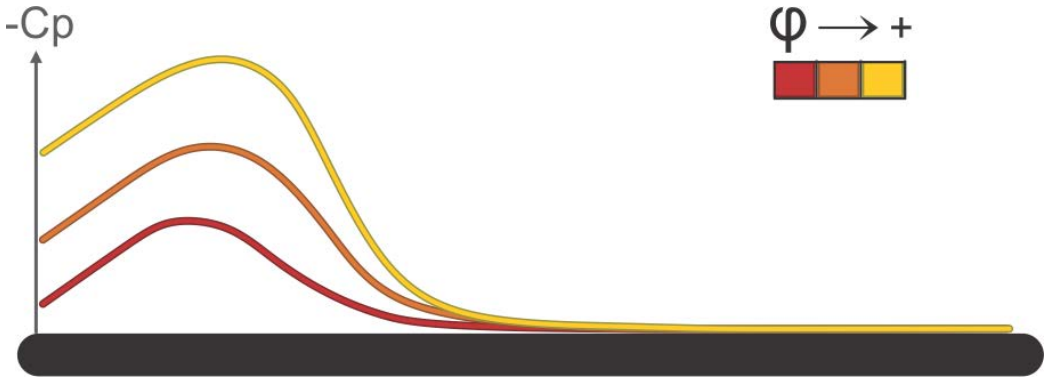

(a) Reattaching LEV: $\phi = -60°$ to $\phi = -30°$

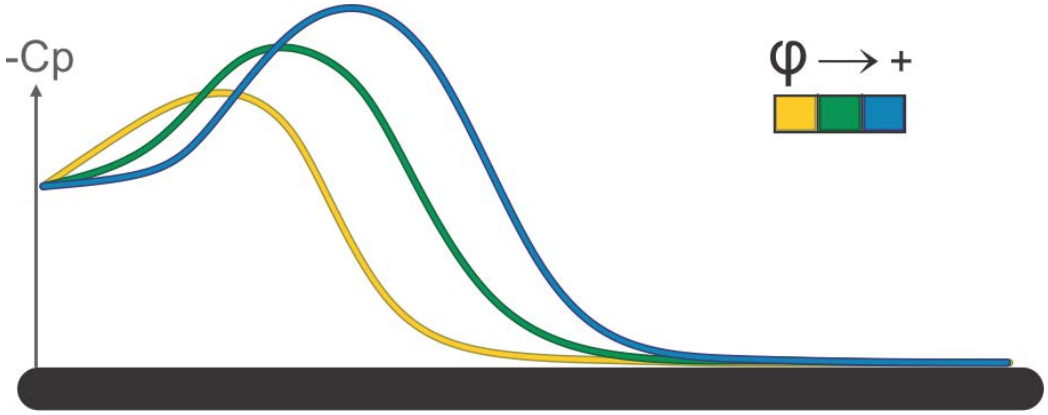

(b) LEV Roll-up: $\phi = -30°$ to $\phi = -10°$

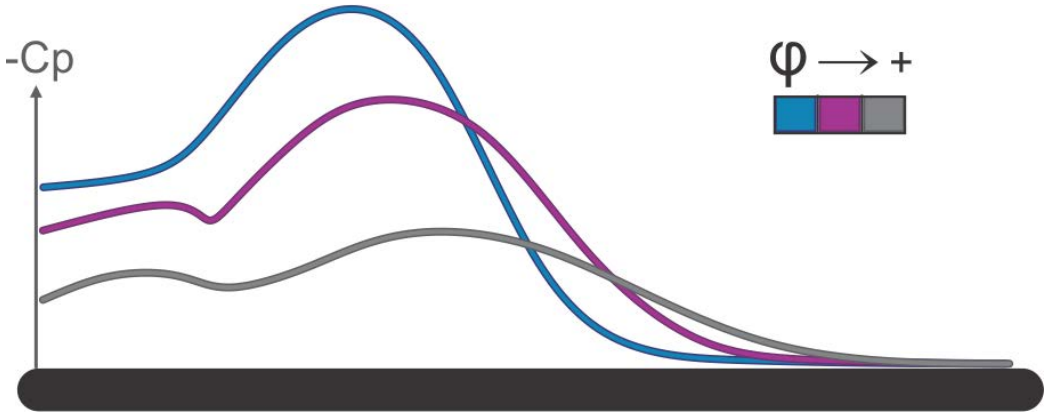

(c) OSV Roll-up: $\phi = -10°$ until LEV detachment

Figure 7.6: Qualitative representation of the dynamics of the pressure distribution during the three stages of LEV formation.

www.manaraa.com

The initial separation of the leading-edge boundary layer at $\phi = -60°$ marks the first appearance of the LEV, which Figure 7.5 shows to approximately coincide with the point at which positive components of both lift and thrust begin to be generated. As the circulation of a reattaching LEV increases, Figure 7.6a depicts how the growth of the primary suction-peak extends around the leading edge. As per Figure 7.5, this leads to an augmentation of both lift and thrust, the magnitudes of which appear to be approximately proportional. Interestingly, this proportionality continues within Figure 7.5 until the detachment of the LEV at $\phi = -10°$, despite the roll-up of the LEV that occurs at $\phi = -30°$.

Because the magnitude of the suction peak continues to increase until the detachment of the LEV at $\phi = -10°$, it is not surprising that Figure 7.5 also shows the vortex-lift as increasing up until this point. Yet the roll-up of the LEV leads to the formation of a pressure plateau, as illustrated in Figure 7.6b, that causes the pressure at the leading edge to stop decreasing. The presence of this plateau should intuitively prevent, or at least hinder, the thrust from continuing to increase, but Figure 7.5 shows the thrust growing approximately monotonically between $\phi = -60°$ and $\phi = -10°$. While the effect is small, it is worthwhile to note that the slope of the lift data appears to decrease slightly after $\phi = -30°$, which would appear to indicate that the formation of the pressure plateau does slightly hamper the production of lift.

Once the OSV rolls-up at $\phi = -10°$, the associated detachment of the LEV leads to a loss of suction across the entire surface of the airfoil (see Figure 7.6c). Figure 7.5 shows this detachment causes the peak of both the lift and thrust data to be located around $\phi = -10°$, yet this also marks the point at which the behavior of the two data sets begins

www.manaraa.com

to diverge. Figure 7.5 shows this loss of suction causes the lift to decrease approximately linearly until it reaches zero at $\phi \approx 35°$, which happens to be the point at which the LEV was observed to begin detaching from the shear layer. This is an interesting correlation, as it seems to imply that the detachment of the LEV from the shear layer may simply be the final step of its detachment from the surface of the airfoil, and not the byproduct of some variation in the "attachment" of the LEV and the shear layer.

In comparison to the distinct drop within the lift data after $\phi = -10°$, the broader peak within the thrust data prevents any prominent losses from occurring until after $\phi \approx 15°$. As the lift and thrust data appeared to be so well correlated within Figure 7.5 prior to $\phi = -10°$, it seems likely that this prolonged thrust is caused by the formation of the secondary suction-peak once the OSV rolls-up. While the overall effect on the lift is still not clear, the formation of a distinct OSV appears to prolong the production of thrust. Figure 7.5 also shows the thrust data leveling off momentarily between $\phi \approx 35°$ and $\phi \approx 65°$, which is coincident with the reattachment of the shear layer. So while the detachment of the LEV from the shear layer is associated with the vortex-lift approaching zero, the rotation of the shear layer back down towards the surface of the airfoil appears to prolong thrust.

Summarizing these results, the formation of a leading-edge vortex contributes favorably to both lift and thrust so long as it remains attached to the leading-edge shear layer. While the roll-up of the LEV was observed to have a significant effect on the vorticity field and diffusive flux, Figure 7.5 indicates the formation of a pressure plateau at the leading edge does not prevent the growth of the primary suction-peak from continuing to augment both lift and thrust. However, once the LEV begins to detach from the surface of the air-

www.manaraa.com

foil, the loss of suction leads to a reduction in the lift and thrust. Even so, the secondary suction-peak that forms once the OSV rolls up provides a means for thrust augmentation during this detachment process.

7.5 Overview of Subsequent Chapters

The remainder of this dissertation will focus on validating the dynamics that have been proposed throughout Chapter 6 regarding the role that both the diffusive flux and OSV have in governing the evolution of the LEV. While a thorough analysis of the baseline data has led to the identification of several defining stages within the formation of the LEV, assessing the validity of these ideas will require a comparison to the results of the finite-aspect-ratio and suction cases.

Within Chapter 8, the finite-AR case will be used to further characterize the roll-up of the LEV and provide additional validation that the augmentation of the diffusive flux requires a reattaching LEV. Discussion will also focus on how enhancing the diffusive flux effects lift and thrust production.

Within Chapter 9, the suction case will be used to explicate the interaction between the OSV and LEV. By providing an example wherein the strength of the OSV is modified, the suction case will also be used to establish the aerodynamic qualities of the secondary suction-peak.

www.manaraa.com

CHAPTER 8
RESULTS FOR THE FINITE ASPECT-RATIO CASE

8.1 Global Flow Dynamics and Evolution

Using data obtained by Eslam Panah [84], a three-dimensional reconstruction of the flow field was generated for a plunging flat plate with aspect-ratio 2. The flow evolution within the entire field-of-view is reported in Figure 8.1, where isocontours of Q-criterion are used to identify any vortical structures. This field-of-view begins at $z/s = 0.166$, where s is span and z is the spanwise distance from the root of the airfoil–note that the root of the plate is constrained by the free-surface plate shown in Figure 3.12-3.13 while the tip of the airfoil is unconstrained (tip of the plate is located at $z/s = 1$). The field-of-view within Figure 8.1 extends past the tip of the plate and ends at $z/s = 1.166$.

Figures 8.1a-8.1c show the initial formation of the LEV occurs with relative uniformity along the span, though the same does not appear to be true for the TEV, as spanwise variations within the spacing of the vortices shed from the trailing edge can be seen even early in the downstroke. Figure 8.1c in particular demonstrates how the TEV structure that is formed near the tip of the plate consists of several smaller vortices that are immediately advected downstream after they are shed into the wake, while the TEV formed near the root rolls-up into a single structure. As a result of this transition, four TEV structures can be seen near the tip of the plate, while only three TEV structures can be seen to have formed around the mid-span. The exact cause of this spanwise variation within the TEV is not clear, however it is potentially an effect of the tip vortex (TiV) that was formed dur-

www.manaraa.com

ing the upstroke. This structure is still visible within Figure 8.1a, and the fact that it is located over the downstream portion of the tip would explain why it might have an effect on the three-dimensionality of the TEV, while the LEV remains roughly two-dimensional in Figure 8.1a-Figure 8.1c.

When the new TiV begins to form during the downstroke around $\phi = -22.5°$, Figure 8.1d shows the spanwise uniformity of the LEV beginning to break down, yet the ensuing three-dimensionality does not develop symmetrically about the midspan. Figures 8.1e-8.1g illustrate how the outboard portion of the LEV remains closer to the surface of the airfoil. Figure 8.1g, in particular, demonstrates how this outboard pinning of the LEV to the surface of the airfoil eventually produces a distinct arch-shaped vortical structure. Similar dynamics were observed both computationally and experimentally by Visbal et al. [107] within the LEV of a heaving, low aspect-ratio wing; however, they observed the formation of a full-arch structure with pinned legs that formed at both the tip and the root of the wing. Only a half-arch is observed within the current data set, as the presence of the free-surface plate at the root of the airfoil appears to prevent the inboard pinning of the LEV. Similar to what was seen by Calderon et al. [19], this root-boundary condition causes the inboard portion of the LEV within Figures 8.1e-8.1g to retain some of its two-dimensionality, in that the core of the structure remains predominantly aligned in the spanwise direction.

While there are a wide range of studies that have analyzed the three-dimensional evolution of an arch-shaped LEV, the vorticity transport phenomena that led to the formation of the arch are still unclear. Taira and Colonius [99] characterized the pinning of the LEV to the surface of the airfoil as a result of the TiV inducing a downward velocity that

www.manaraa.com

would essentially push the LEV down towards the surface of the airfoil, and this mechanism of reattachment has also been proposed by Shyy et al. [97] and Lee et al. [65]. On the other hand, Kim and Gharib [58] characterized the velocity field induced by the TiV as being oriented primarily in the spanwise direction, not towards the surface of the airfoil. They proposed that the arch structure was therefore caused by this spanwise flow forcing the LEV near the mid-span away from the surface of the airfoil. Although the actual vorticity transport mechanism that leads to the three-dimensionality of the LEV is of interest, its identification will not be the focus of this chapter. However, it will be discussed briefly within Section 8.5, as the vorticity flux analysis performed within this study provide some novel insight into the physics associated with this three-dimensionality.

Within the context of this dissertation, the relevant feature within Figure 8.1 is the pinning of the LEV to the surface of the airfoil. While this process results from three-dimensionality within the flow, it effectively serves to counteract the roll-up of the LEV and reattach it to the downstream boundary layer. The overall goal of this chapter will be to establish how this reattachment of the LEV affects the diffusive flux of vorticity. In order to best elucidate these dynamics, the transport of spanwise-vorticity will be characterized within several different spanwise planes using a vorticity flux analysis similar to that employed in Chapter 5. More specifically, these analyses will be performed in the xy-coordinate system on the data obtained by Eslam Panah [84] at the 68.75-percent span (68-ps), 75-percent span (75-ps) and 81.25-percent span (81-ps) locations.

Figure 8.2 depicts the evolution of the spanwise vorticity within each of the horizontal planes that were measured by Eslam Panah [84], with the vorticity fields from the

www.manaraa.com

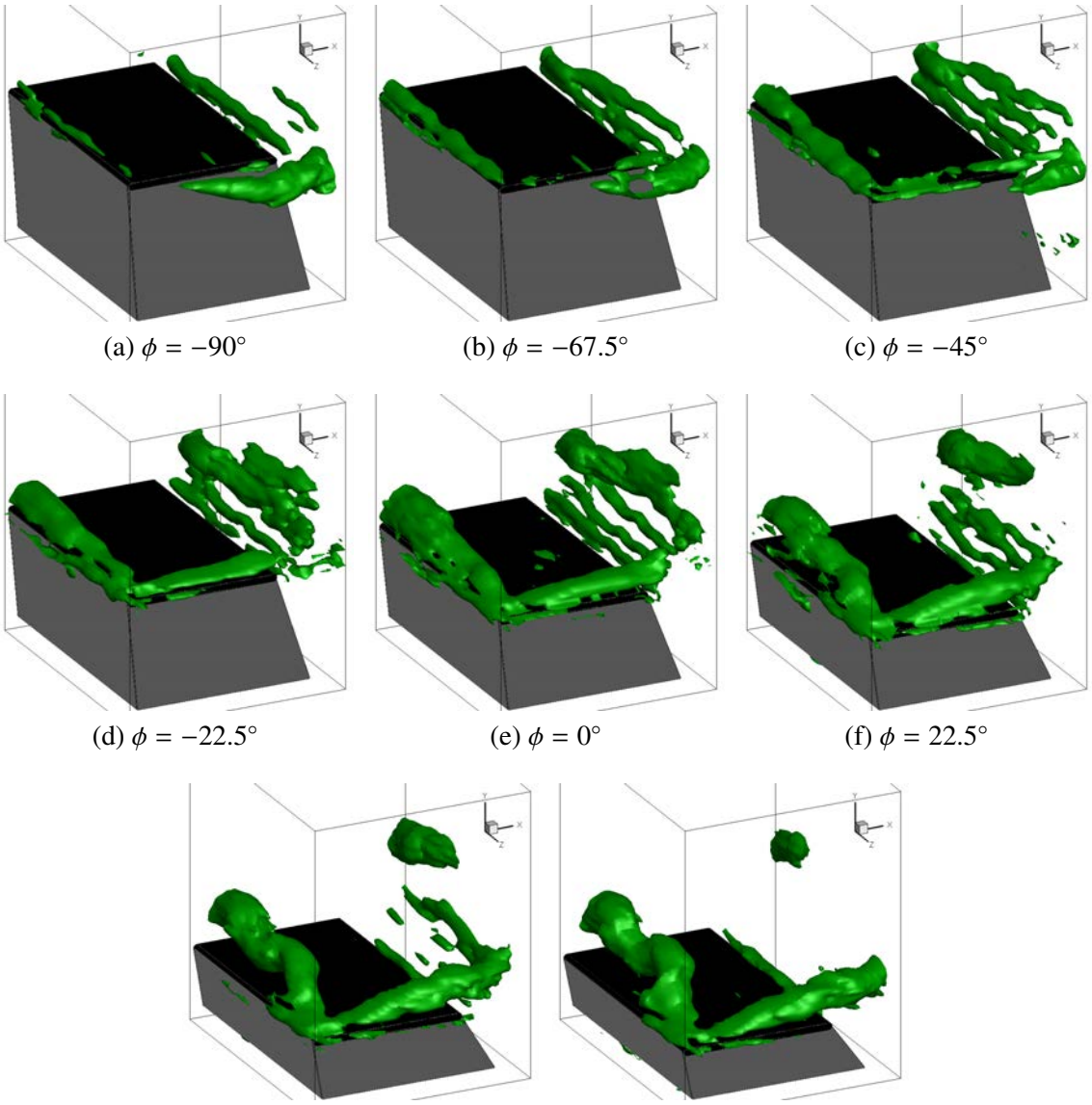

(a) $\phi = -90°$ (b) $\phi = -67.5°$ (c) $\phi = -45°$

(d) $\phi = -22.5°$ (e) $\phi = 0°$ (f) $\phi = 22.5°$

(g) $\phi = 45°$ (h) $\phi = 67.5°$

Figure 8.1: Isocontour of Q-criterion (Q = 10) depicting the evolution of the flow field from the AR2 case.

www.manaraa.com

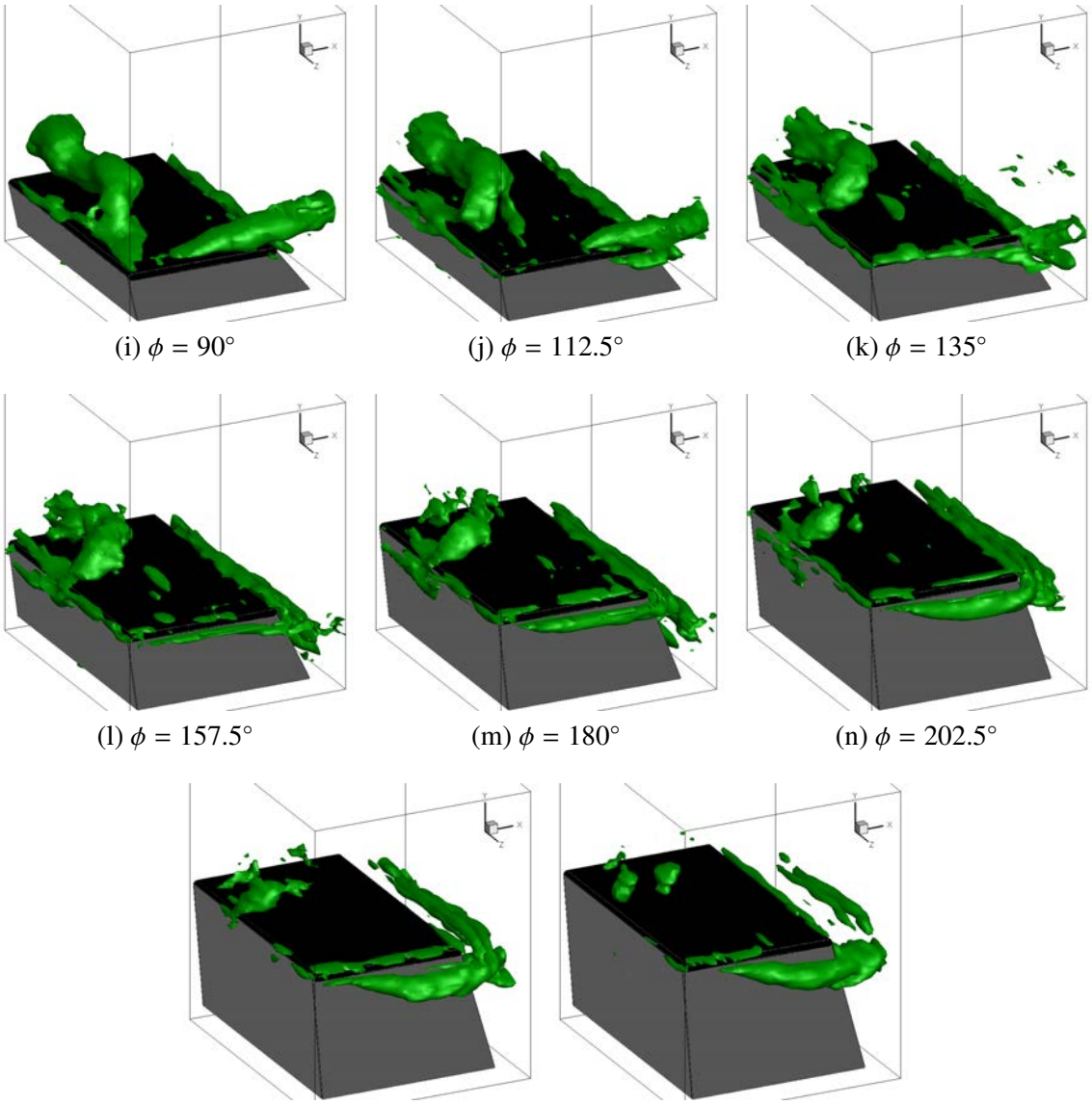

Figure 8.1: Isocontour of Q-criterion (Q = 10) depicting the evolution of the flow field from the AR2 case.

www.manaraa.com

three planes of interest being highlighted by a purple contour. Figure 8.2 shows the LEV to remain approximately two-dimensional around the planes of interest throughout the first half of the downstroke, with Figure 8.2e depicting very similar LEV structures–in terms of both position and size–within each of the highlighted planes at $\phi = 0°$; yet during the second half of the downstroke, the evolution of the LEV begins to vary significantly between the three planes. Figures 8.2f-8.2j illustrate how the LEVs within each of the three highlighted planes are successively drawn back down towards the surface of the airfoil and eventually merge with the boundary layer. For the sake of terminology, this reversal of the LEV roll-up and the reinstatement of an LEV that reattaches to the downstream boundary layer will be referred to as "restabilization." Section 8.5 will provide a full characterization of how this restabilization is affected, but at the moment it is sufficient to state that it caused by three-dimensional effects that are propagating inboard from the tip of the plate.

Because of the spanwise variation of this three-dimensionality, the LEVs within the three highlighted planes of Figures 8.2f-8.2j are affected over different phase intervals. Based on a qualitative inspection of Figures 8.2f-8.2j, the LEV is restabilized between $\phi \approx 22.5°$ and $\phi \approx 67.5°$ for the 81-ps case, between $\phi \approx 45°$ and $\phi \approx 90°$ for the 75-ps case, and between $\phi \approx 67.5°$ and $\phi \approx 112.5°$ for the 68-ps case. A comprehensive analysis of the vorticity fields within these phase intervals will be presented within Section 8.3 for each of the three spanwise locations.

Figure 8.3 compares the vorticity fields of the baseline (AR4) case with those from the 68.75-, 75- and 81.25-percent span locations of the AR2 case at $\phi = 0°$. Ideally, the data from these three spanwise planes would be compared to the baseline example;

www.manaraa.com

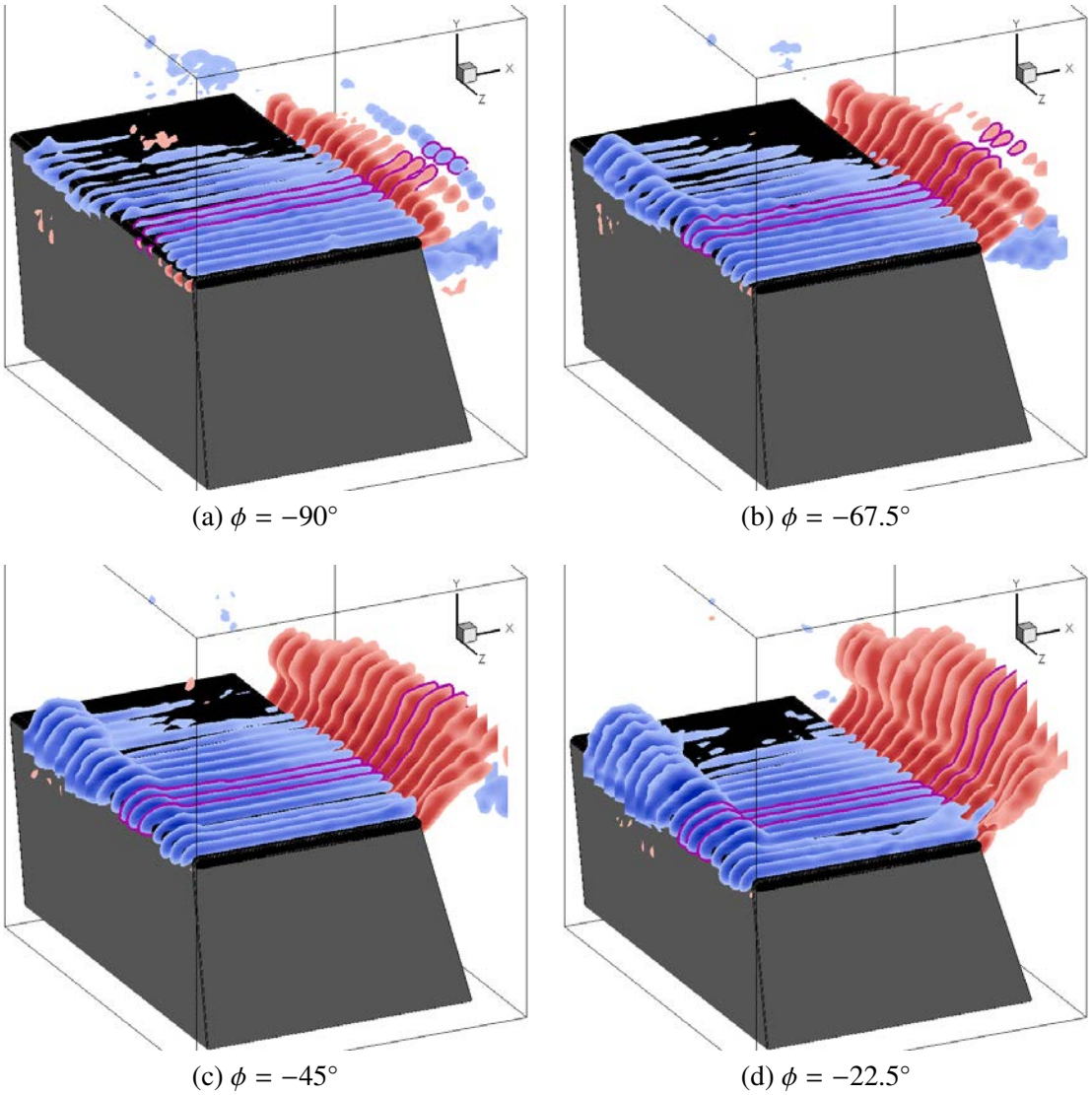

(a) $\phi = -90°$ (b) $\phi = -67.5°$

(c) $\phi = -45°$ (d) $\phi = -22.5°$

Figure 8.2: Vorticity isocountours from the AR2 case with the 68.75-, 75- and 81.25-percent span locations highlighted.

www.manaraa.com

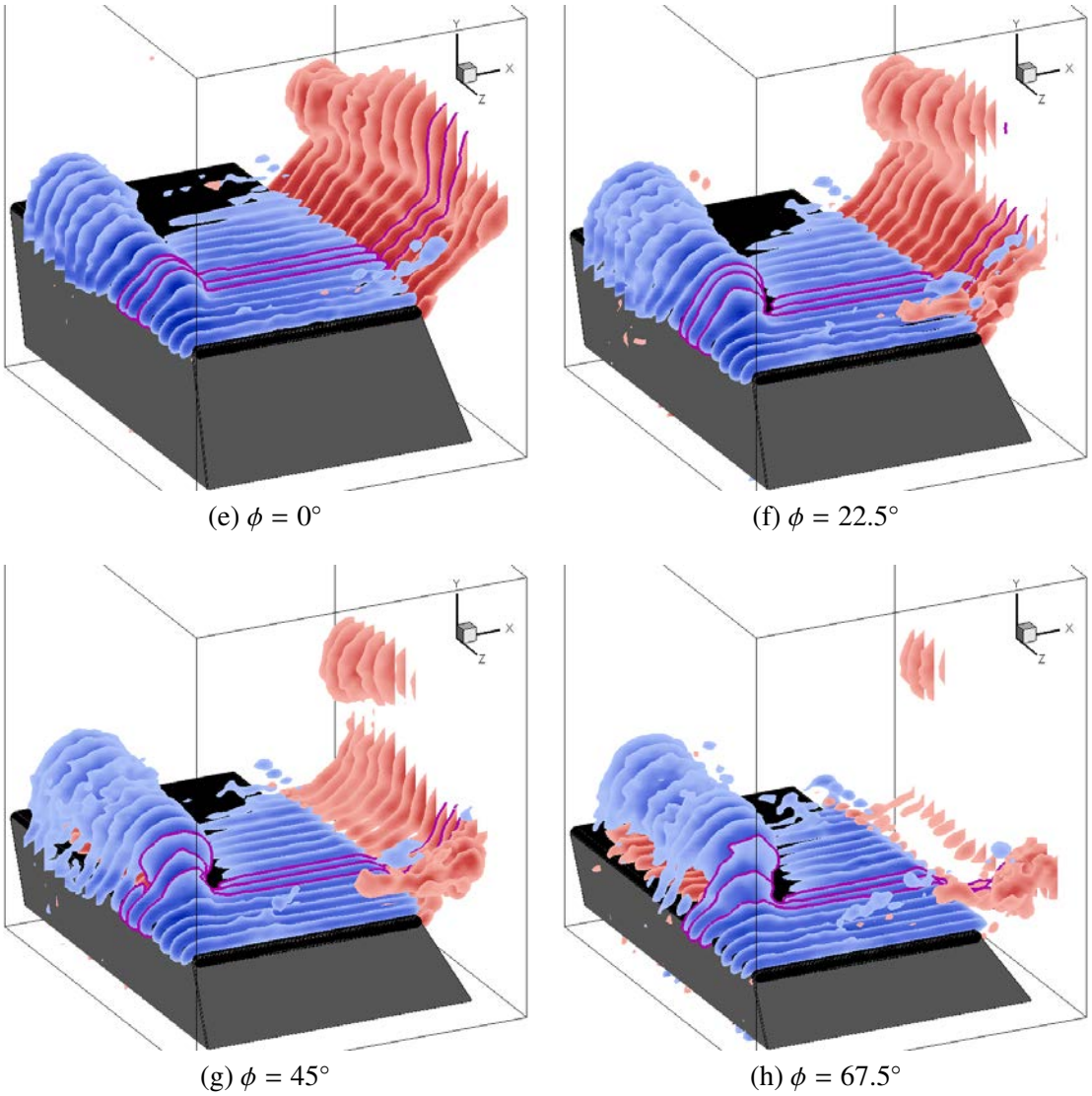

(e) $\phi = 0°$ (f) $\phi = 22.5°$

(g) $\phi = 45°$ (h) $\phi = 67.5°$

Figure 8.2: Vorticity isocountours from the AR2 case with the 68.75-, 75- and 81.25-percent span locations highlighted.

www.manaraa.com

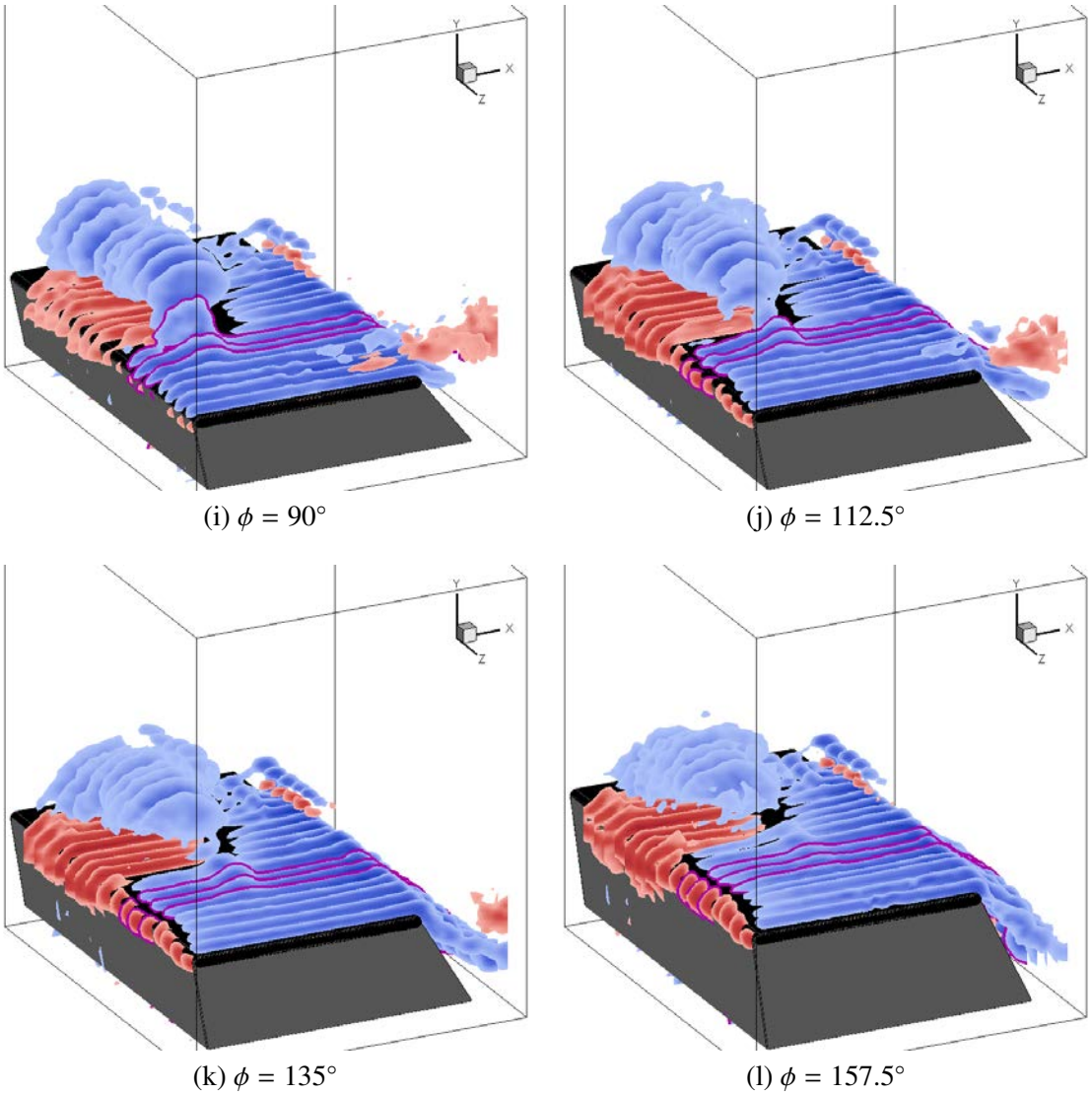

(i) ϕ = 90° (j) ϕ = 112.5°

(k) ϕ = 135° (l) ϕ = 157.5°

Figure 8.2: Vorticity isocountours from the AR2 case with the 68.75-, 75- and 81.25-percent span locations highlighted.

www.manaraa.com

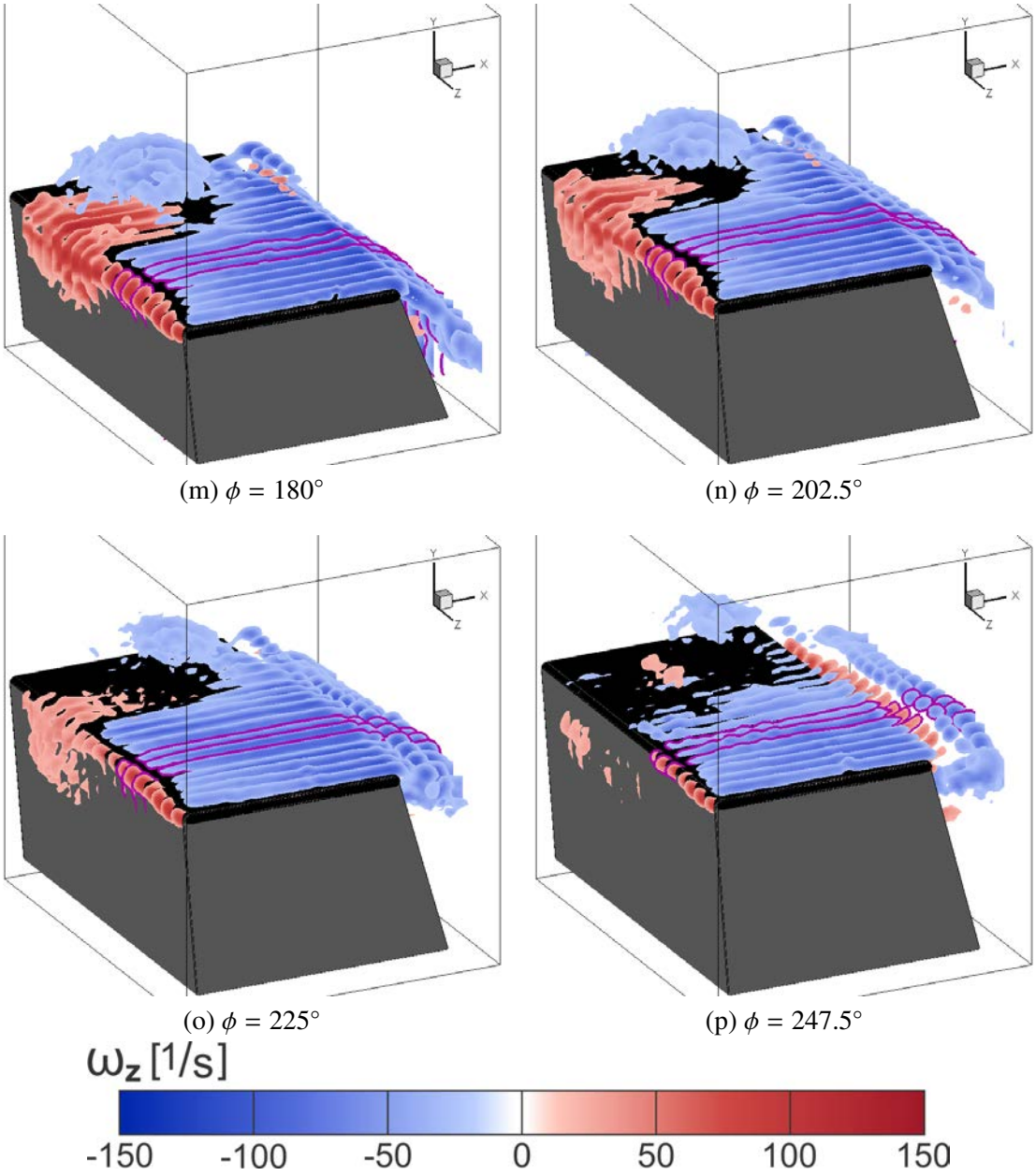

Figure 8.2: Vorticity isocountours from the AR2 case with the 68.75-, 75- and 81.25-percent span locations highlighted.

www.manaraa.com

however, Figure 8.3 shows there is a visible variation in the evolution of the LEV between the AR4 and AR2 cases, even before the three-dimensionality within the AR2 case begins to significantly alter the vorticity field of the three spanwise planes being investigated. As described in Chapter 5, both the LEV and the OSV of the baseline case have already rolled up by $\phi = 0°$, yet Figures 8.3b-8.3d show the LEV is still attached to the downstream boundary layer at $\phi = 0°$ within the AR2 case.

To a certain extent, this inconsistency between the baseline and AR2 cases may derive from the different experimental setups, as the field-of-view of the baseline case was about 75% the size of the AR2 case. This means the baseline case had a spatial resolution that was approximately 1.3-times that of the AR2 case, which may be why Figure 8.3a is able to resolve a more distinct LEV structure than those shown in Figures 8.3b-8.3d. Furthermore, the lack of any OSV structure within Figures 8.3b-8.3d could be due to the fact that this decrease in the resolution of the AR2 case prevented the near-wall structure from being sufficiently resolved within the PIV measurements. On the other hand, there may be some unidentified mechanism within the AR2 case that causes the evolution of the LEV to lag behind that of the baseline case. Regardless of the actual reason, this variation between the flow fields of the two airfoils indicates that a direct correlation cannot be made between the two–i.e. the nominally two-dimensional AR4 case does not act as an effective "baseline" for the results of the AR2 case.

Instead, the analytical approach of this chapter will be to further characterize the development of the LEV by comparing the vorticity fields of the three spanwise plane to one another. Figure 8.2 shows the restabilization of the LEV occurs over different phase

www.manaraa.com

intervals for each plane, which means each spanwise location will exhibit distinct variations in the evolution of the flow field. By correlating these dynamics within the vorticity field to those observed within the surface pressure distributions, the discussion of this chapter will serve to further characterize the roll-up process of the LEV. Not only will additional validation be provided for the conclusion (from Chapter 6) that the roll-up of the LEV limits both the diffusive flux as well as the growth of the primary suction peak, but an analysis of the "restabilization" process observed within Figure 8.2 will also help to characterize the aerodynamic benefit associate with reversing the roll-up process and reestablishing a reattaching LEV, which has the potential to inform future studies on flow control.

8.2 Flux Analysis

Before delving into a more thorough inspection of the flow fields, a vorticity flux analysis is used to objectively quantify the vortex dynamics within each of the three cases. Using the same methodology that was implemented within Section 5.3 for the baseline analysis, Equation 5.1 is used to calculate the circulation budget within the defined control region. It should be noted that the control region had to be modified slightly for the analyses of the AR2 data sets. Because the chordwise position of Boundary 1 (see Figure 5.2) was defined to coincide with the location of the first pressure tap, it had to be shifted 1.59 mm downstream for the AR2 analysis. As such, the results reported within this section have been obtained using a control region that was defined as starting 3.18 mm downstream of the leading edge, ending 40 mm downstream of the leading edge and extending 35 mm vertically into the flow.

www.manaraa.com

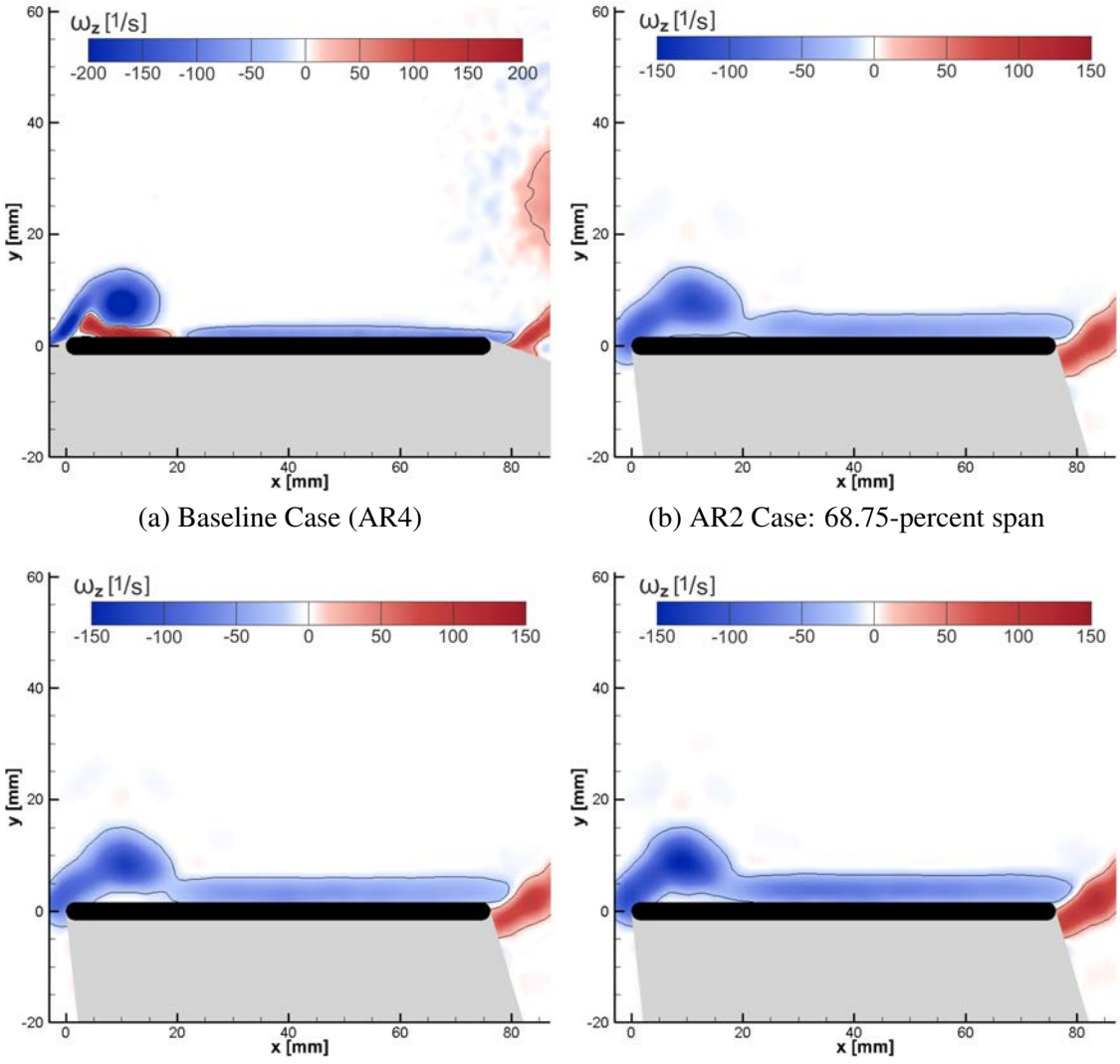

(a) Baseline Case (AR4)

(b) AR2 Case: 68.75-percent span

(c) AR2 Case: 75-percent span

(d) AR2 Case: 81.25-percent span

Figure 8.3: Comparison of the vorticity fields of the Baseline (AR4) Case with those from the 68.75-, 75- and 81.25-percent span locations of the AR2 Case at $\phi = 0°$.

www.manaraa.com

Figure 8.4 presents the results of the flux analyses. Similar to the baseline example, the shear-layer and diffusive fluxes were found to govern the circulation budget at all three spanwise locations. The flux of vorticity out of Boundary 3 was noted to be slightly larger than the baseline data; however, an analysis of the vorticity fields obtained during the down-stroke once again revealed it to be a result of the boundary layer convecting downstream and out of the control region. More relevant to the current analysis, the total three-dimensional flux of vorticity (i.e. the sum of the tilting and spanwise convection terms) was once again discovered to be negligible. On their own, the tilting and spanwise convection terms were observed to provide relevant fluxes of vorticity (shown later in Figure 8.11), and their effect on the flow will be the focus of Section 8.5. At this time it is sufficient to note that despite their ability to modify the distribution of vorticity within the xy-plane, these three-dimensional fluxes of vorticity have a negligible effect on the overall circulation budget within the control region. So while the three-dimensionality may cause the restabilization of the LEV by moving it down towards the surface of the airfoil, any response seen within the diffusive flux is solely expected to be a result of the modified orientation and not by a variation in the strength of the LEV.

As they represent the two principal sources of vorticity within the flow, Figures 8.5a-8.5c report the magnitude of the shear-layer and diffusive fluxes that were calculated throughout the plunge cycle at the 68-, 75- and 81-percent span locations respectively. Also reported is the sum of all the instantaneous sources of vorticity ("Total") as well as the time-rate-of-change in the total circulation of the control region ("$d\Gamma/dt$"), which can be seen to be approximately equal. Overall, the behavior of the shear-layer flux is fairly consistent

www.manaraa.com

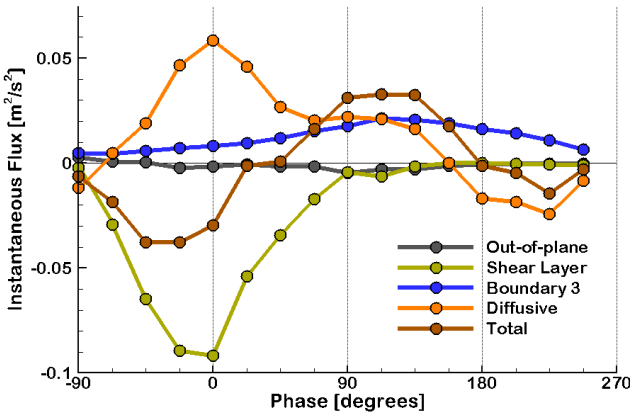

(a) 68.75-percent span

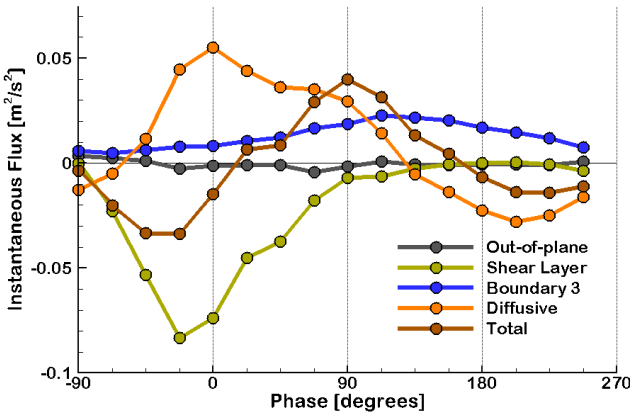

(b) 75-percent span

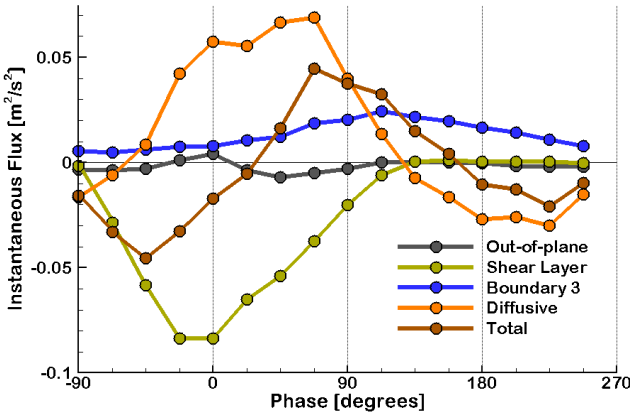

(c) 81.25-percent span

Figure 8.4: Instantaneous fluxes of vorticity at the three spanwise locations.

www.manaraa.com

for all three spanwise locations, as are the trends within the diffusive flux in the first half of the downstroke. However, during the second half of the downstroke, Figures 8.5a-8.5c begin to show a distinct variation between the diffusive fluxes of the three cases. In order to better visualize these variations, the diffusive fluxes measured for each of the three cases are plotted together in Figure 8.6. The diffusive flux calculated for the AR4 plunging case is also plotted within Figure 8.6 so as to establish the baseline, two-dimensional behavior. While the AR2 data varies significantly from this two-dimensional case in the first half of the downstroke, the baseline data does appear to provide a good reference dynamic after $\phi = 0°$. The major deviations of the AR2 data from this baseline trend are analyzed next in conjunction with the dynamics of the vorticity fields.

8.3 Reattachment of the LEV

Beginning within the 68-ps case, the appearance of a distinct OSV within Figure 8.7b indicates that the LEV has rolled-up by $\phi = 22.5°$. Furthermore, the pressure gradients within this figure depict the presence of two suction peaks on the surface of the airfoil. While causality has not been implied, this presence of the secondary suction-peak has been shown to be concomitant with the detachment of the LEV from the surface of the airfoil in the baseline case. The outline of the LEV within Figure 8.7c appears to indicate that it is on the verge of detaching from the leading-edge shear layer at $\phi = 45°$. Yet Figures 8.7d-8.7f show this detachment never takes place. Instead, the restabilization of the LEV begins around $\phi = 67.5°$ with a distinct weakening of the OSV. By $\phi = 90°$, the entire OSV–as well as the secondary suction-peak–has been eliminated and the LEV has reattached to the

www.manaraa.com

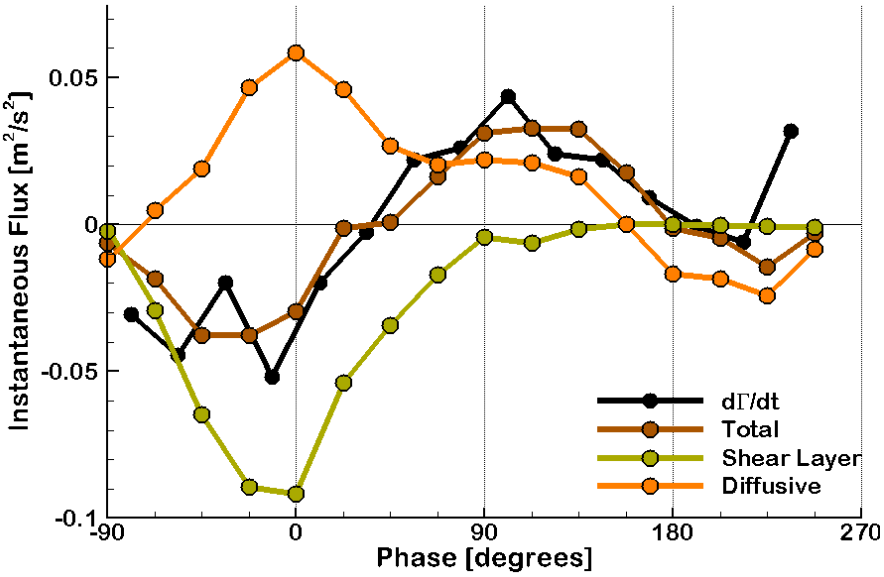

(a) 68.75-percent span

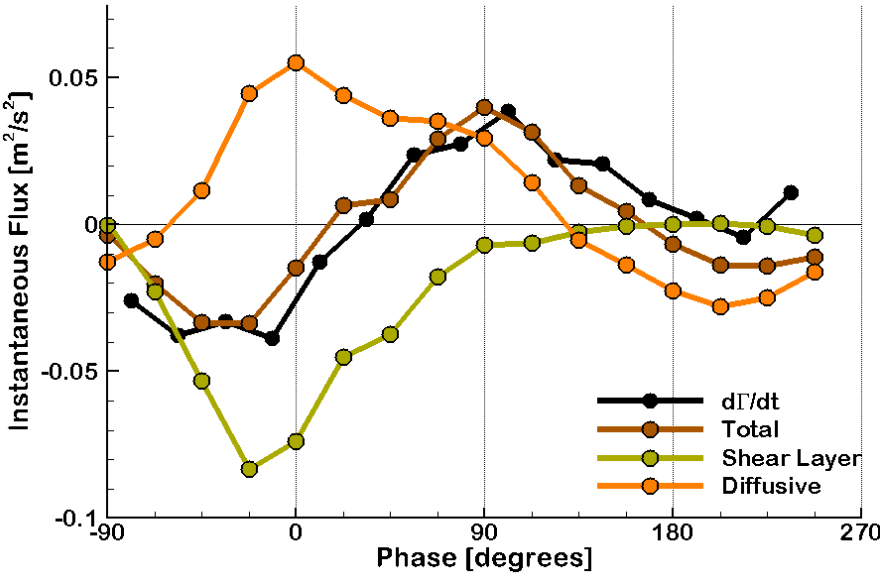

(b) 75-percent span

Figure 8.5: Instantaneous fluxes of vorticity at the three spanwise locations.

www.manaraa.com

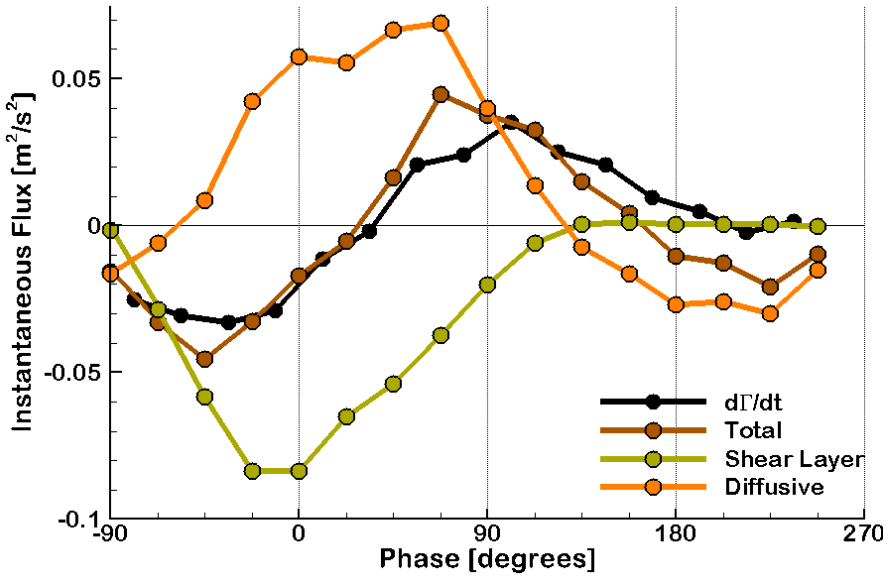

(c) 81.25-percent span

Figure 8.5: Instantaneous fluxes of vorticity at the three spanwise locations.

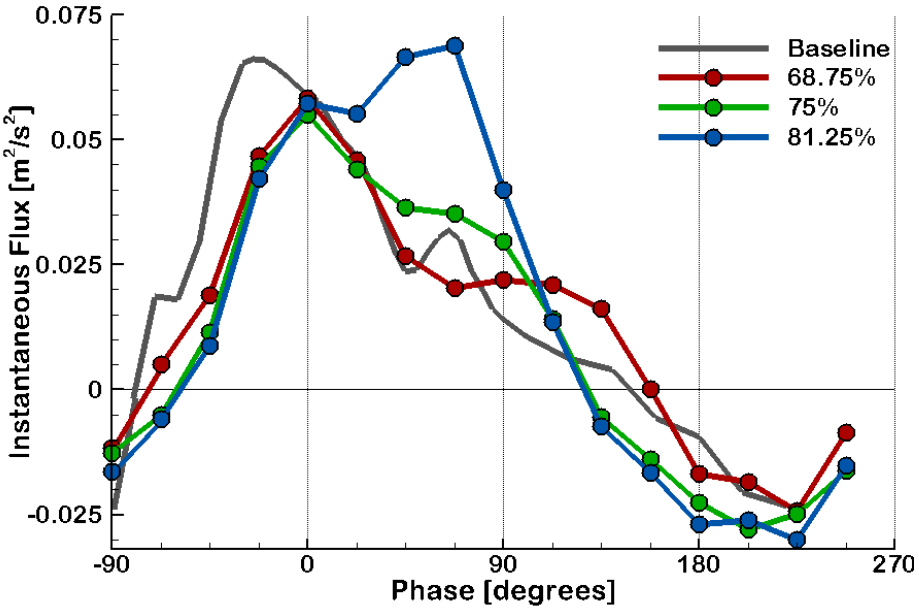

Figure 8.6: Comparison of the diffusive flux of vorticity calculated at the 68-, 75- and 81-percent span locations of the AR2 case. Also plotted is the diffusive flux calculated for the baseline (AR4) case.

www.manaraa.com

downstream boundary layer. Figure 8.6 shows that once the LEV actually reattaches to the downstream boundary layer at $\phi = 90°$, the diffusive flux data for the 68-ps case diverges from the baseline trend and temporarily plateaus. This increase persists until $\phi \approx 112.5°$, which Figure 8.7f shows to coincide with the LEV merging into the boundary layer.

The dynamics seen within the 75-ps case are very similar to those observed within the 68-ps case, yet there are some noteworthy variations. Figure 8.8 presents flow fields from the 75-ps case, wherein the LEV can be observed to have rolled-up by $\phi = 22.5°$. As opposed to what was seen within Figure 8.7b, the pressure gradients within Figure 8.8b do not seem to indicate the OSV has rolled-up, although it may be that the pressure taps simply do not have a spatial resolution small enough to resolve a secondary suction-peak. As the current plane of investigation is located further outboard than the previous case, the reattachment process appears to occur earlier in phase. Despite this temporal variation, the manner in which this reattachment is affected remains consistent. Figure 8.8c once again shows this reattachment process begins with the weakening/elimination of the OSV, after which the LEV reattaches and then merges with the downstream boundary layer (Figures 8.8d-8.8e). Consulting the 75-ps data from Figure 8.6 reconfirms that this reattachment produces a temporary plateau within the diffusive flux, which persists until the LEV merges with the boundary layer around $\phi \approx 90°$.

While both the 68-ps and 75-ps cases showed the LEV had rolled-up by $\phi = 22.5°$, the vorticity fields shown in Figure 8.9 indicate that the restabilization of the LEV occurs early enough in the 81-ps case to inhibit the formation of an OSV. Because the LEV never completely separates, the dynamics seen within Figures 8.9b-8.9d are much less pro-

www.manaraa.com

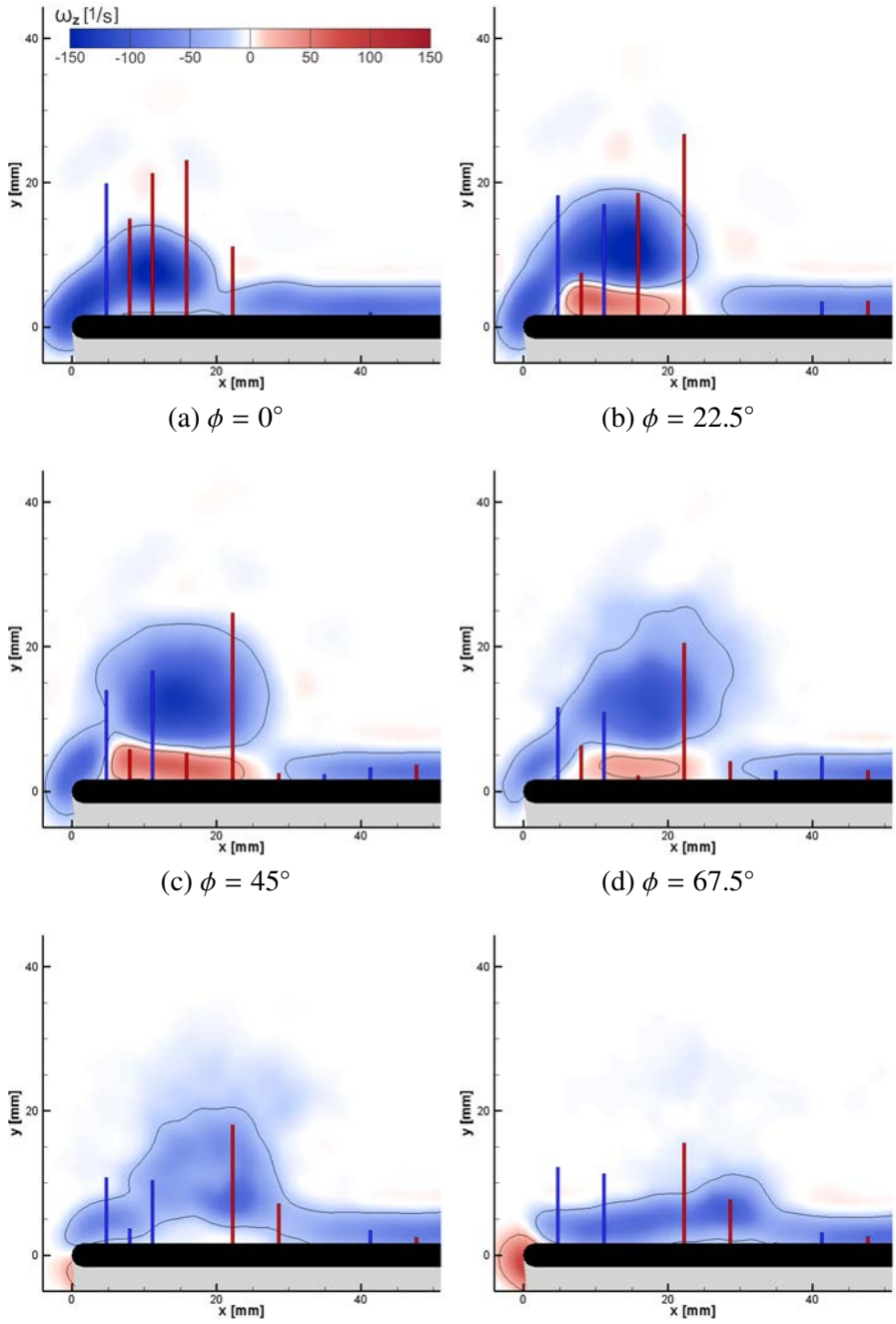

(a) $\phi = 0°$ (b) $\phi = 22.5°$

(c) $\phi = 45°$ (d) $\phi = 67.5°$

(e) $\phi = 90°$ (f) $\phi = 112.5°$

Figure 8.7: Vorticity isocountours from the AR2 case obtained at the 68.75-percent span.

www.manaraa.com

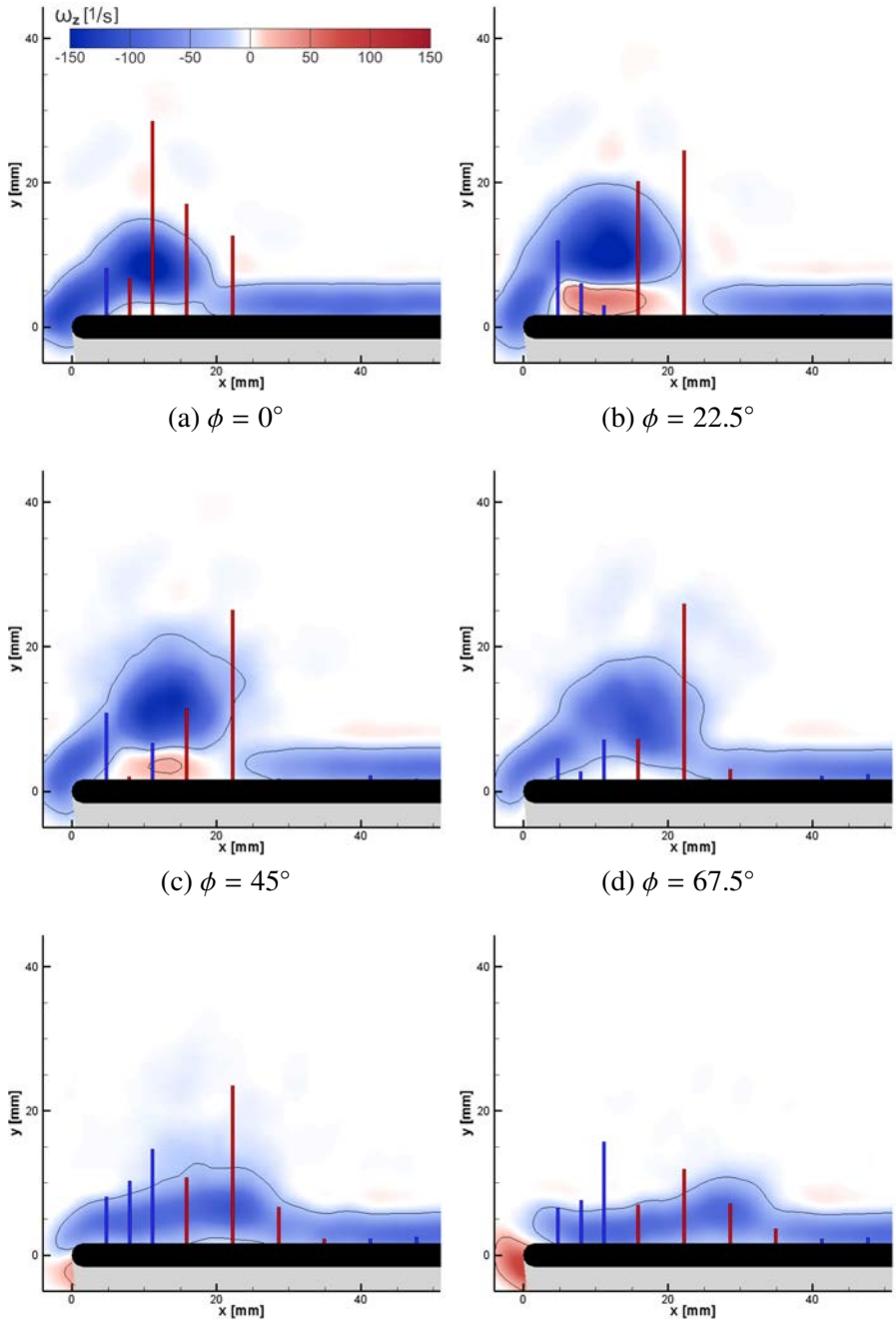

(a) $\phi = 0°$ (b) $\phi = 22.5°$

(c) $\phi = 45°$ (d) $\phi = 67.5°$

(e) $\phi = 90°$ (f) $\phi = 112.5°$

Figure 8.8: Vorticity isocountours from the AR2 case obtained at the 75-percent span.

www.manaraa.com

nounced than what was seen in the previous cases. Figures 8.9a-8.9c show hardly any variation in the size and position of the LEV; yet Figure 8.6 indicates that simply maintaining this reattaching LEV structure near the leading edge of the airfoil produces a significant increase in the diffusive flux of vorticity. This augmentation lasts until $\phi \approx 67.5°$, after which there is a major drop in the diffusive flux that once again accompanies the merging of the LEV into the boundary layer. Interestingly, Figure 8.6 shows this prolonged reattachment of the 81-ps LEV produces a peak within the diffusive flux data that is even larger than that of the baseline case, with a phase shift between the peaks of the two cases of approximately 90-degrees.

Summarizing the main points of this section, both the 68-ps and 75-ps cases showed that forcing the LEV to reattach to the downstream boundary layer results in a distinct (though temporary) plateau within the diffusive flux. While the three-dimensionality within the flow effectively reverses the roll-up of the LEV within these first two cases, the three-dimensionality is affected early enough within the 81-ps case to prevent the roll-up of the LEV in the first place. In contrast to the plateaus within the diffusive flux that Figure 8.6 shows to accompany the restabilization of the LEV–which first involves the elimination of the OSV–data for the 81-ps case indicates that maintaining a reattaching LEV affects a major increase in the diffusive flux. Based on these results, it appears that forcing the flow in a manner that prevents the roll-up of the LEV–as opposed to reversing the roll-up of the LEV after it has occurred–would be the most effective way of augmenting the diffusive flux.

www.manaraa.com

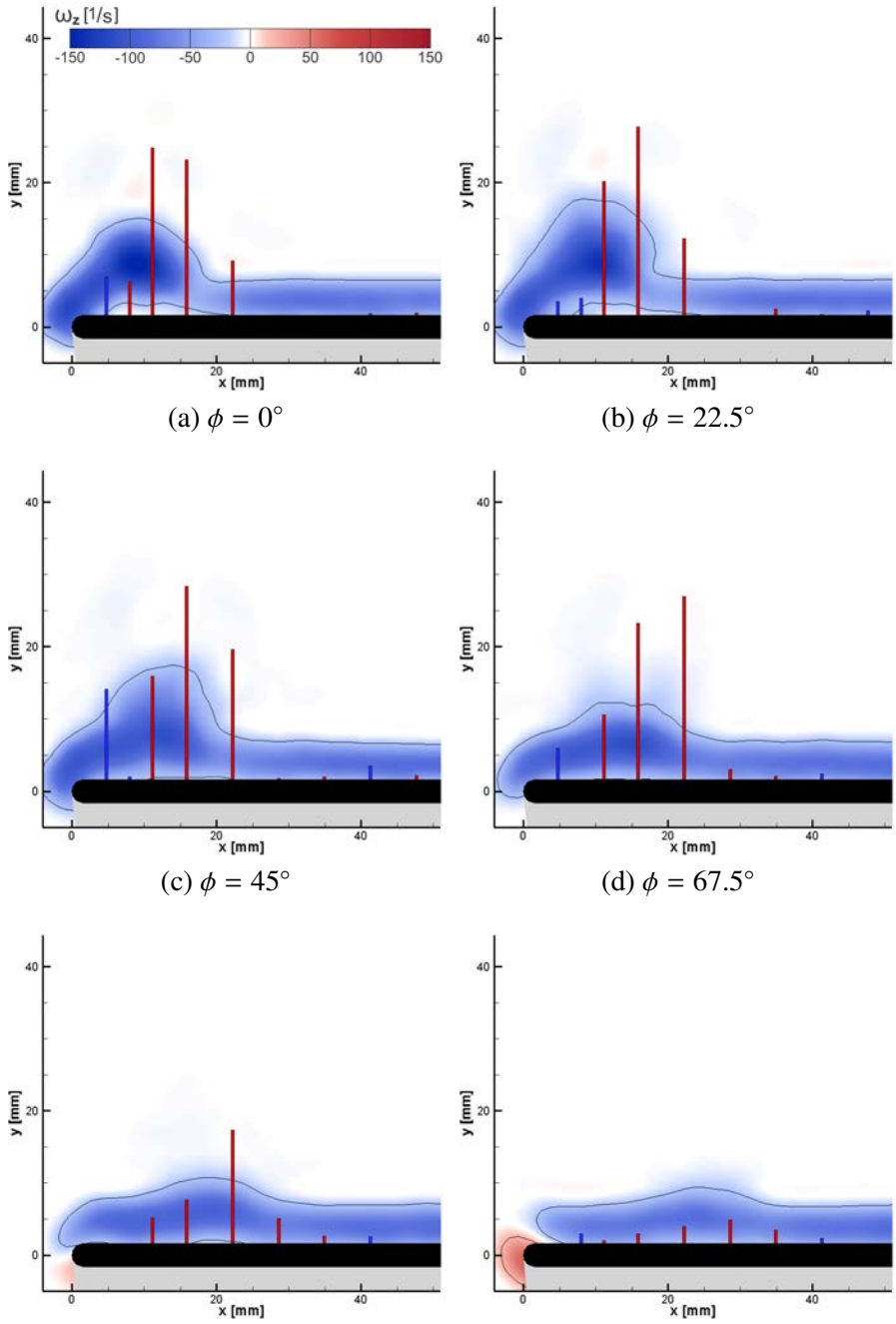

(a) $\phi = 0°$ (b) $\phi = 22.5°$

(c) $\phi = 45°$ (d) $\phi = 67.5°$

(e) $\phi = 90°$ (f) $\phi = 112.5°$

Figure 8.9: Vorticity isocountours from the AR2 case obtained at the 81.25-percent span.

www.manaraa.com

8.4 Aerodynamic Implications of LEV Reattachment

In order to establish the aerodynamic impact of the reattachment process, Figure 8.10 depicts the evolution of the chordwise pressure distributions for the 75-ps and 81-ps cases throughout the second half of the downstroke. The distribution measured at $\phi = -22.5°$ is also presented, primarily to show that the primary suction-peak of the 75-ps case reaches an approximate maximum around $\phi = 0°$.

Continuing to examine the 75-ps data within Figure 8.10a, the magnitude of the primary suction-peak can be seen to decrease after $\phi = 0°$ as the LEV rolls-up and–presumably–begins to detach. While the weakening of the OSV (which Figure 8.8c shows to occur at $\phi = 45°$) is indicative of the LEV beginning to be restabilized, the reduction of the primary suction-peak does not appear to stop until the LEV actually reattaches to the downstream boundary layer at $\phi = 67.5°$. As implied by the plateau within 75-ps diffusive flux data that Figure 8.6 shows at $\phi = 67.5°$, this initial reattachment of the LEV causes the leading-edge pressure to momentarily stop increasing–i.e. temporarily maintains some additional suction at the leading edge. It was demonstrated within Chapter 7 that the pressure measured near the leading edge acts as a good indicator of thrust production, and as such, the trends depicted within Figure 8.10a would seem to predict that the reattachment of the the LEV will temporarily prolong thrust production. However, once the LEV has merged with the boundary layer by $\phi = 90°$, the pressure measured at the leading edge begins to increase again, indicating the thrust would once again begin to drop.

Despite this loss of leading-edge suction, Figure 8.10a shows the merging of the LEV with the boundary layer causes the magnitude of the primary suction-peak to in-

www.manaraa.com

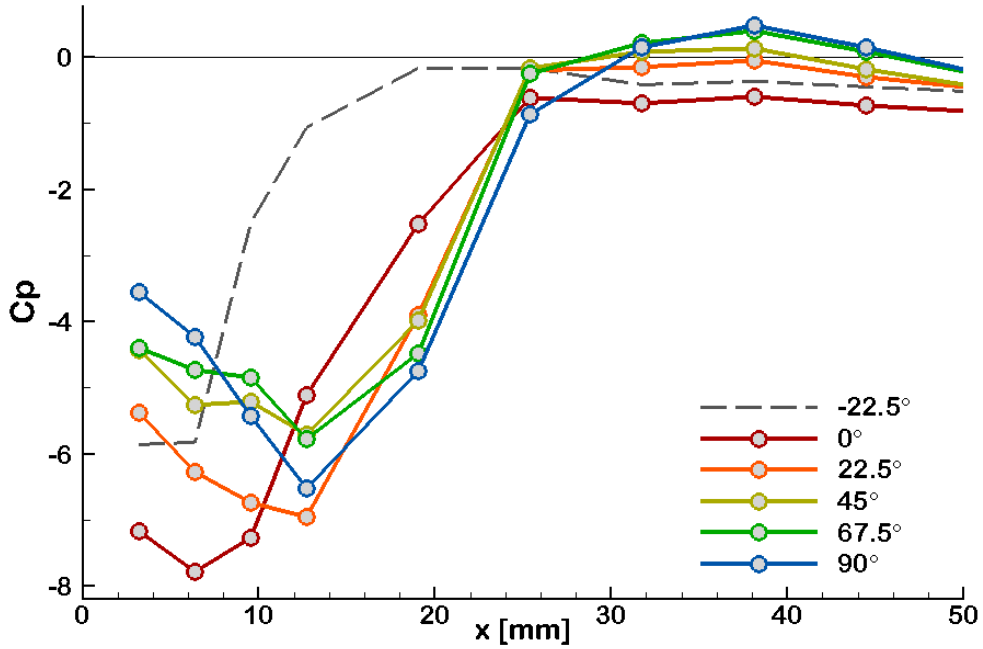

(a) 75-percent span

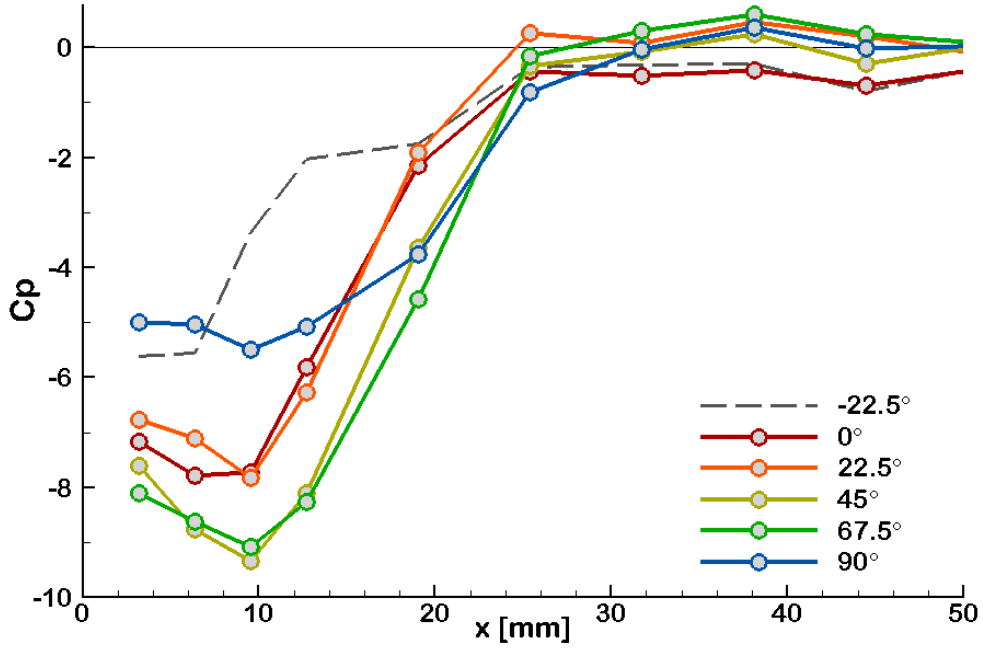

(b) 81.25-percent span

Figure 8.10: Evolution of the surface pressure distribution during the second half of the downstroke.

www.manaraa.com

crease. So while the three-dimensionality that causes the LEV to reattach to the downstream boundary layer may not have significant thrust benefits, it does appear to augment lift by repositioning the LEV closer to the surface of the airfoil. This result addresses a very important aerodynamic effect of the TiV that is often misinterpreted within the literature. It has been well documented within studies of plunging wings that the three-dimensionality introduced by a tip vortex leads to a reduction in lift over its two-dimensional counterpart, leading many studies to attribute this loss of lift to the downwash induced by the TiV [99, 97, 54]. However, Lee et al. [65] performed a unique analysis of a low aspect-ratio plunging plate wherein they used force element theory to quantify the lift production elements contained within the LEV and TiV. They eventually showed that both the LEV and TiV contained large, positive lift elements, indicating the TiV itself was a lift-producing structure that worked in parallel with the LEV. The pressure profiles shown in Figure 8.10a reaffirm this idea, as the primary suction-peak is augmented when the LEV becomes reattached to the downstream boundary.

While the roll-up of the LEV that occurs within the 75-ps case at $\phi = 22.5°$ leads to a drop in the leading-edge suction that is never recovered, Figure 8.10b shows the 81-ps pressure distribution remains approximately constant between $\phi = 0°$ and $\phi = 22.5°$ when the three-dimensionality prevents the roll-up of the LEV (see Figure 8.9b). As with the 75-ps case, Figure 8.10b shows the primary suction-peak is augmented when the LEV merges with the downstream boundary layer between $\phi = 45°$ and 67.5° (Figures 8.9c-8.9d). However, this suction peak is located close enough to the leading edge within the 81-ps data for the associated augmentation to affect an increase in the leading-edge suction,

www.manaraa.com

thereby leading to an additional rise within the diffusive flux from $\phi = 22.5°$ to 67.5° (see 81-ps data in Figure 8.6).

It was noted within Section 8.3 that maintaining the reattachment of the LEV leads to an increased diffusive flux, and the evolution of the pressure distributions within Figure 8.10b indicate that this increase is associated with an enhancement of both lift and thrust. While the effect on the total thrust may not be clear, it can be inferred from the current analysis that maintaining a reattaching LEV near the leading edge of a wing will lead to optimal lift production. This idea appears to be robustly validated by the natural kingdom, as stable, reattaching LEVs have been observed to be the primary lift-production mechanism used by insects [34, 14], small fliers like hummingbirds [113] and bats [78] as well as by carangiform swimmers [15].

8.5 Three-Dimensional Reorientation of the Flow

While Section 8.3 has clearly demonstrated the response of the diffusive flux to the reattachment of the LEV, the vorticity transport mechanism that drives the restabilization process has yet to be established. As this effect is related to the three-dimensionality within the flow, the three-dimensional fluxes of vorticity are characterized next. Figure 8.11 reports the total three-dimensional flux of vorticity (labeled "Out-of-plane") as well as the tilting and spanwise convection terms that were calculated using Equation 5.1 for the three spanwise locations. These plots indicate that all three cases contain significant tilting and spanwise convective fluxes, yet also demonstrate how their cumulative response has a negligible effect on the circulation budget. When comparing these figures to the vorticity

www.manaraa.com

budgets shown in Figure 8.5, the peaks within the tilting and spanwise convection terms can be seen to immediately precede the augmentation of the diffusive flux.

In order to characterize the effect of this three-dimensionality on the flow field, Figures 8.12-8.14 depict isocontours of the total three-dimensional flux of vorticity for the three cases during the phase interval over which the LEV was observed to reattach.

Once again, although there is no net-effect on the circulation budget, these isocontours clearly show how the three-dimensionality within the flow creates a source of negative vorticity near the surface of the airfoil and a sink of negative vorticity within the bulk flow. So as to provide an appropriate reference, an outline of the LEV and other relevant vortical structures has been superimposed upon these contours. Based on the position of these sources and sinks with respect to the LEV, it becomes apparent how the three-dimensional fluxes of vorticity induce the reattachment of the LEV by increasing the concentration of negative vorticity near the surface and decreasing the concentration within the separated region of the LEV.

The specific nature of this three-dimensionality within the flow is further elucidated within Figures 8.15-8.16, which decompose the total three-dimensional flux of vorticity from the 81-ps case into the spanwise convection and tilting terms respectively. The isocontours presented within these figures demonstrate that both mechanisms contribute an overall sink of vorticity within the bulk flow and source of vorticity near the surface of the airfoil. However, Figure 8.15 indicates that spanwise convective flux primarily acts to increase the concentration of negative vorticity–or decrease the amount of positive vorticity–within the region beneath the LEV. Conversely, the isocontours shown in Figure 8.16 indicate that the

www.manaraa.com

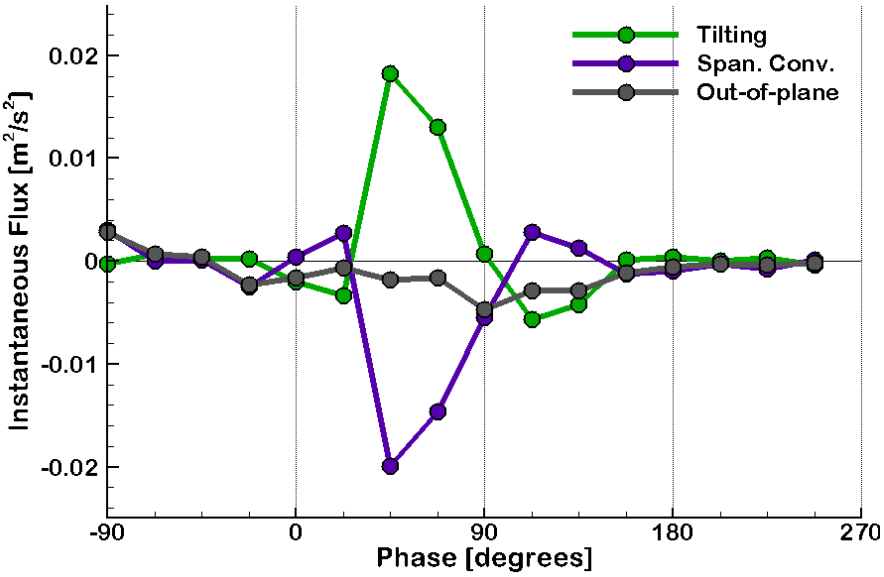

(a) 68.75-percent span

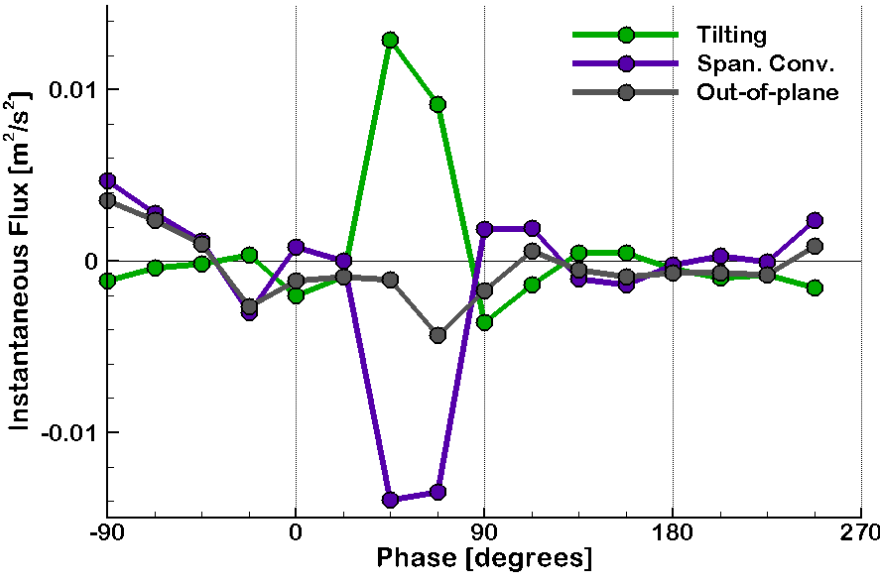

(b) 75-percent span

Figure 8.11: Three-dimensional fluxes of vorticity at the three spanwise locations.

www.manaraa.com

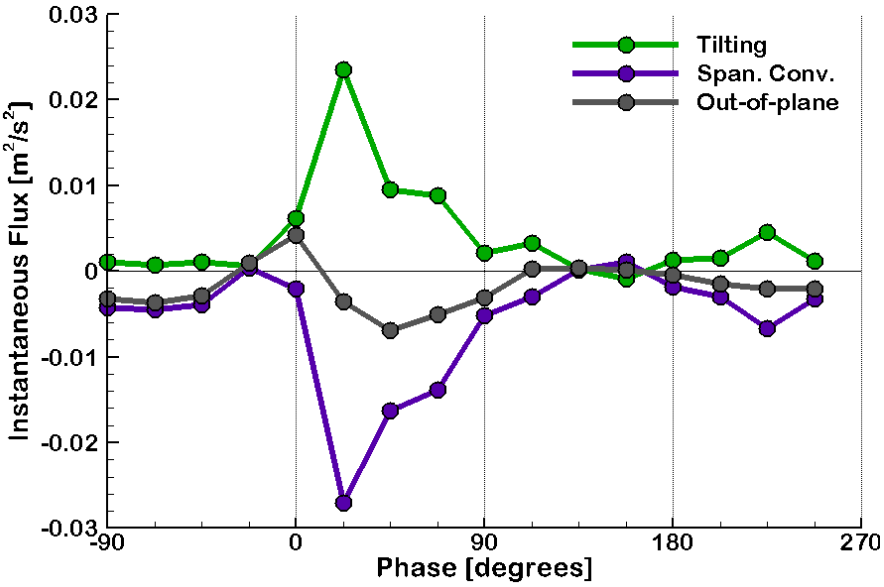

(c) 81.25-percent span

Figure 8.11: Three-dimensional fluxes of vorticity at the three spanwise locations.

tilting term primarily serves to remove negative vorticity from the separated portion of the LEV. This observation that spanwise convection acts predominantly as a source of negative vorticity while the tilting term acts as a sink of negative vorticity is consistent with the sign of the peaks plotted in Figure 8.11c.

Figure 8.17 presents isocontours of x-vorticity and the velocity vectors that were obtained within the vertically oriented yz-plane at $x/c = 0.166$. The three green lines within Figure 8.17a-8.17c depict the three spanwise locations being considered. The blue region within these isocontours is associated with the tip vortex and the red region is associated with the portion of the LEV that has been deflected into the streamwise direction. All three figures illustrate how the three-dimensionality within the flow leads to the formation of spanwise flow directed towards the root of the airfoil. Based on the spanwise gradient in

www.manaraa.com

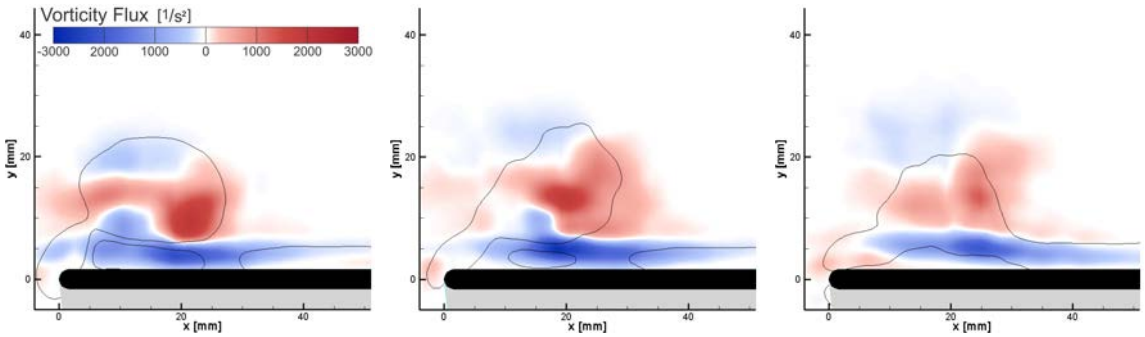

(a) $\phi = 45°$ (b) $\phi = 67.5°$ (c) $\phi = 90°$

Figure 8.12: Total three-dimensional flux of vorticity isocontours from the 68-ps case.

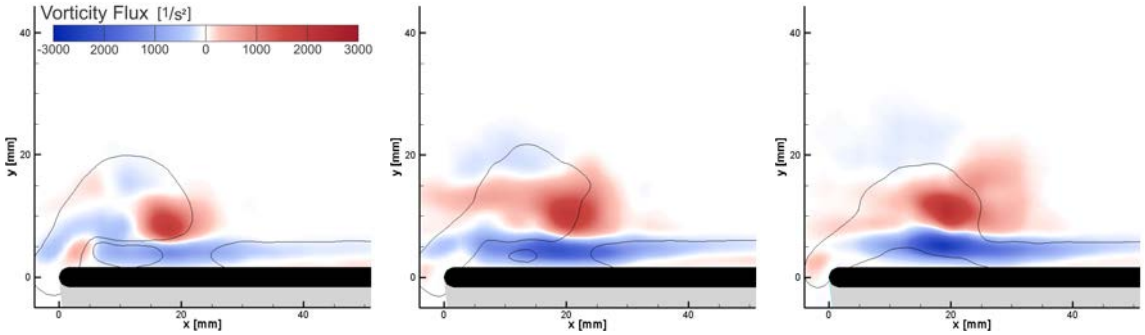

(a) $\phi = 22.5°$ (b) $\phi = 45°$ (c) $\phi = 67.5°$

Figure 8.13: Total three-dimensional flux of vorticity isocontours from the 75-ps case.

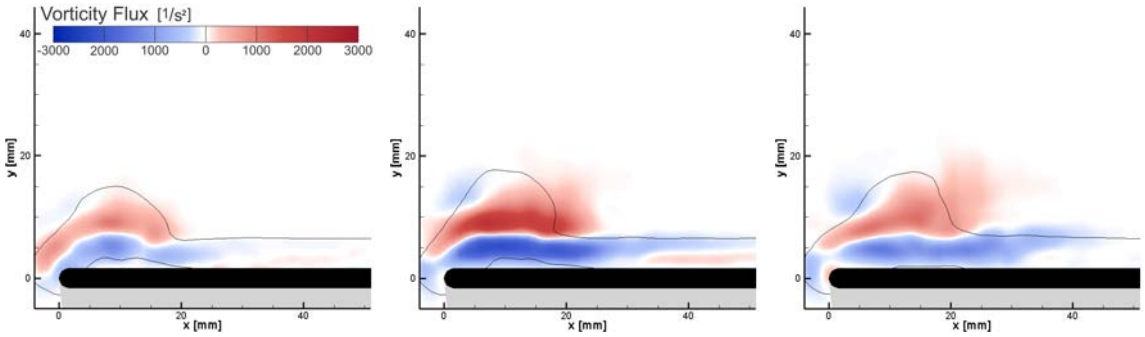

(a) $\phi = 0°$ (b) $\phi = 22.5°$ (c) $\phi = 45°$

Figure 8.14: Total three-dimensional flux of vorticity isocontours from the 81-ps case.

www.manaraa.com

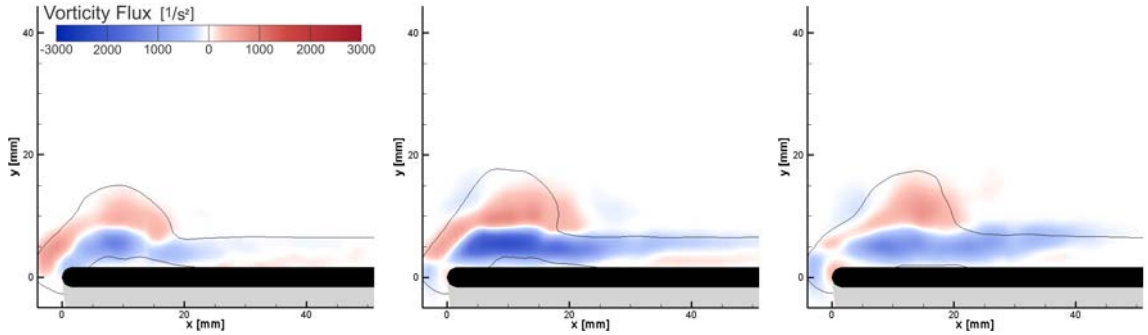

(a) $\phi = 0°$ (b) $\phi = 22.5°$ (c) $\phi = 45°$

Figure 8.15: Isocontours from the 81-ps case depicting the spanwise convection of vorticity.

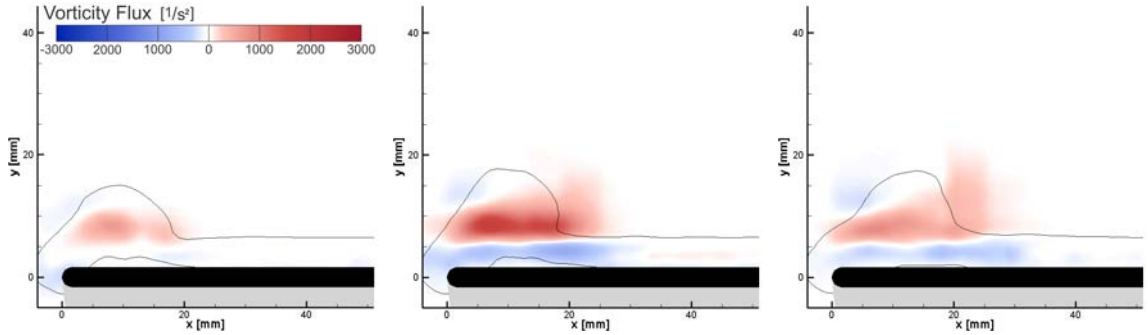

(a) $\phi = 0°$ (b) $\phi = 22.5°$ (c) $\phi = 45°$

Figure 8.16: Isocontours from the 81-ps case depicting the tilting of vorticity.

www.manaraa.com

the vorticity field that can be inferred from a comparison of Figures 8.7-8.9, it becomes clear how this spanwise flow produces the spanwise convective flux shown in Figure 8.15.

The isocontours depicted within Figures 8.15-8.16 indicate that the spanwise convective flux is the transport mechanism responsible for introducing negative vorticity into the xy-plane. Figures 8.2e-8.2h show the vorticity field near the tip of the plate primarily exists as an attached boundary layer, and the fact that the spanwise convective flux causes this boundary layer near the root to convect inboard is well represented by the fact that the negative isocontours (in blue) within Figure 8.15 take on a distribution that is reminiscent of an attached boundary layer. Based on this characterization, it can be understood that the restabilization of the LEV (as shown in Figures 8.7-8.9) is not caused by the in-plane convection of vorticity, but rather by the spanwise convection of *attached* vorticity into the plane. Therefore, while the surface-diffusive flux downstream of the LEV acts to deteriorate the connection between the LEV and the downstream boundary layer–and thus initiate the roll-up of the LEV–the spanwise flux retards and reverses this process by providing an additional source of primary (negative) vorticity within this region.

The three-dimensional flux analyses shown in Figures 8.11a-8.11c indicate that the source of negative vorticity produced by the spanwise convective flux is balanced by an equivalent sink of negative vorticity within the tilting term, which Figure 8.16 shows to be affected within the outer, separated portion of the LEV. Based on the three-dimensional vortex structure that is identified within Figure 8.1 using the Q-criterion, this sink appears to be characterized by the tilting of spanwise-vorticity into the y-direction in order to produce the leg of the half-arch vortex that develops.

www.manaraa.com

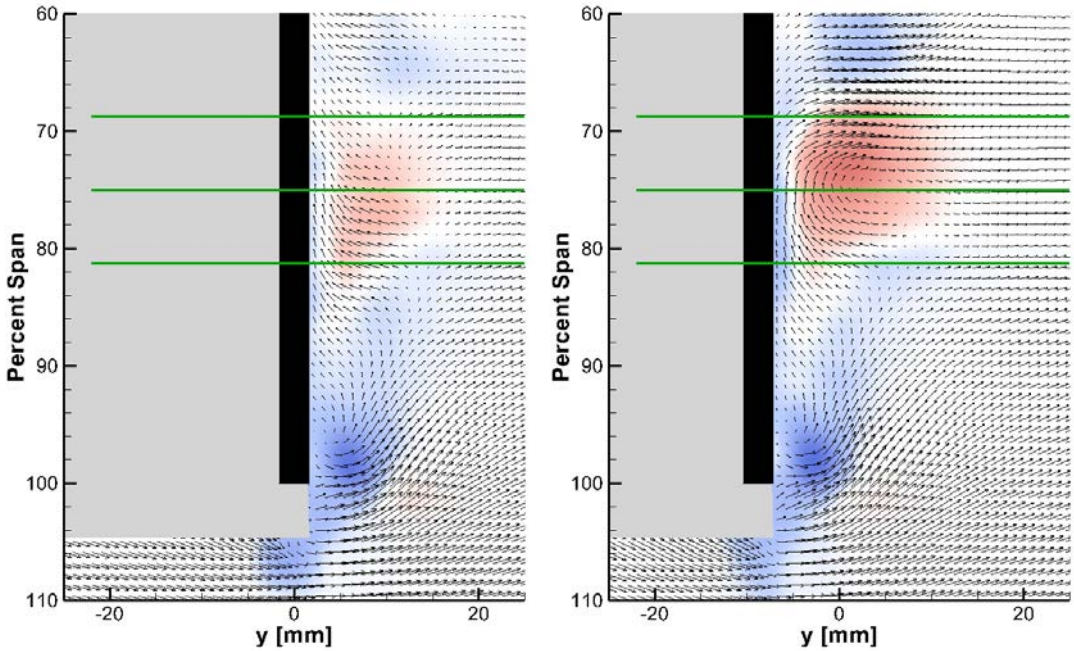

(a) $\phi = 0°$ (b) $\phi = 22.5°$

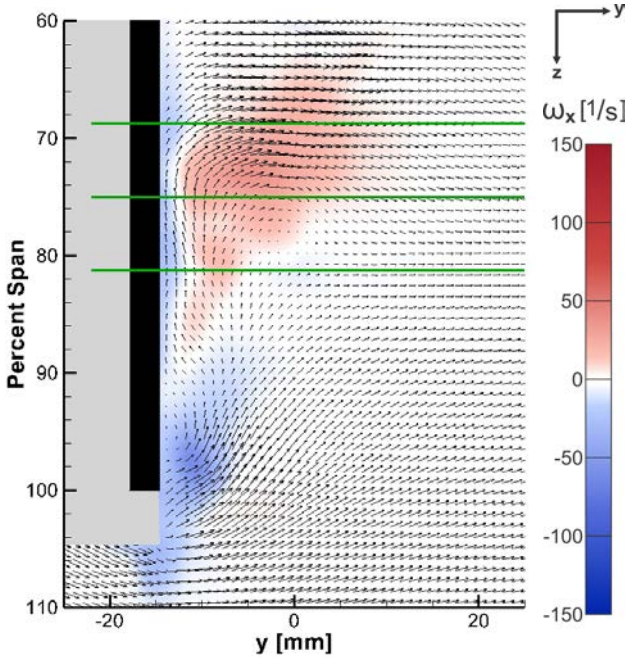

(c) $\phi = 45°$

Figure 8.17: Isocontours of streamwise vorticity and velocity vectors within the yz-plane at the 16.6-percent chordwise location.

www.manaraa.com

While there are a wide range of studies that have analyzed the three-dimensional evolution of an arch-shaped LEV, the dynamics described within this section appear to be novel. Taira and Colonius [99] characterized the pinning of the LEV to the surface of the airfoil as a result of the TiV inducing a downward velocity that would essentially push the LEV down towards the surface of the airfoil, and this mechanism of reattachment has also been proposed by Shyy et al. [97] and Lee et al. [65]. While it is possible that this downwash behavior is present within different experimental models, it is certainly not applicable within the current example, as the pinning of the LEV is associated with the spanwise convection of the outboard boundary layer.

On the other hand, Kim and Gharib [58] characterized the formation of an arched vortex as being caused by the spanwise flow from the TiV forcing the LEV inboard from the tip of a wing and up from the surface, while vorticity from the TiV extends upwards to maintain the pinned leg of the LEV. Indeed, this description of the inboard motion may be an apt characterization of the spanwise convection depicted within Figure 8.15. However, there is no evidence within the current data that suggest the LEV is being forced away from the surface of the airfoil, as this would imply that spanwise vorticity is being convected in the y-direction. Figure 8.16 indicates that this process is much more aptly characterized within the current example as the *tilting* of the spanwise vorticity into the y-direction.

8.6 Summary

The goal of this chapter was to further explicate the relationship between a reattaching LEV, the primary suction-peak and the diffusive flux of vorticity, as well as to charac-

www.manaraa.com

terize how the roll-up of the LEV might be expected to effect aerodynamic performance. Comparing the 75-ps and 81-ps vorticity fields presented within Figures 8.8 and 8.9, the two flows appear to be nearly identical at $\phi = 0°$. Yet while the 75-ps LEV rolls-up in Figure 8.8b, Figure 8.9b shows the LEV from the 81-ps case remains attached to the downstream boundary layer. The diffusive flux data plotted in Figure 8.6 illustrates how simply maintaining a reattaching LEV at $\phi = 22.5°$ produces a stronger diffusive flux within the 81-ps data than the case in which the LEV was seen to roll up (i.e. either the 68-ps or 75-ps data), which serves to validate the conclusion from Chapter 6 that the roll-up of the LEV limits the growth of the diffusive flux.

As with the vorticity fields, Figure 8.10 shows the pressure distributions of the 75-ps and 81-ps cases to be similar at $\phi = 0°$. While Figure 8.10a shows the primary suction-peak within the 75-ps data begins to decrease once the LEV rolls-up at $\phi = 22.5°$, Figure 8.10b shows the prolonged reattachment of the LEV in the 81-ps case prevents the magnitude of the primary suction-peak from dropping. The lift benefits associated with the conservation of this primary suction-peak indicate that optimal lift production is associated with maintaining an LEV that reattaches to the downstream boundary layer. It should be noted that this augmentation of the primary suction-peak cannot be maintained for an extended period of time. While the three-dimensional sources of vorticity do not alter the circulation of the LEV, augmenting the diffusive flux will affect a major sink of vorticity that will weaken the LEV. Figure 8.9e shows how this loss of LEV circulation eventually leads to it merging with the boundary layer–which appears to cause the flow to reattach near the leading edge. The $\phi = 90°$ data within Figure 8.10b depicts how this leads to a

www.manaraa.com

decrease in the magnitude of the primary suction-peak.

As discussed in Section 8.3, the restabilization of the LEV within the 68-ps and 75-ps cases produced a temporary plateau within the diffusive flux until the LEV merged with the boundary layer and the flow reattached at the leading edge. However, within the 81-ps case, the spanwise flux of vorticity was able to provide an additional source of negative vorticity within the reattachment region so that the roll-up of the LEV was prevented. This maintenance of a reattaching LEV led to a net increase in the diffusive flux, the peak of which is shown within Figure 8.6 to reach a higher magnitude than that of the baseline case. In terms of flow control, these results indicate that forcing the flow in a manner that prevents the roll-up of the LEV–as opposed to reversing the roll-up of the LEV after it has occurred–would be the most effective way of augmenting the diffusive flux.

In addition to elucidating this aerodynamic benefit of a reattaching LEV, determining why the LEV remains attached to the downstream boundary layer at the 81-percent span can inform our understanding of what incites the roll-up process. One of the major conclusions of Chapter 6 was that the reattachment of the LEV was governed by the balance between the diffusive and convective fluxes of vorticity within within the reattachment region. Using a modified interpretation of the Crabree criterion [30], it was noted that once the APG formed downstream of the LEV core became strong enough to cross-cancel all of the vorticity within the reattachment region, the LEV would roll up and the OSV would begin to form. Based on this characterization of the flow physics, the maintenance of a reattaching LEV at the 81-percent span requires that there be an additional source of negative vorticity within the reattachment region of the 81-ps case at $\phi = 22.5°$ that does not

www.manaraa.com

exist within the 75-ps and 68-ps cases.

Indeed, Figure 8.15b indicates this prolonged reattachment of the LEV is achieved through an additional source of negative vorticity into the reattachment region via a spanwise convective flux. These results not only justify the discussion from Chapter 6 about what incites the roll-up of the LEV, but also indicates that it is possible to prevent this roll-up by prescribing an additional source of negative vorticity within the reattachment region.

Many studies have asserted that spanwise flow can stabilize an LEV, yet the results of this chapter have found this to be incorrect on several different levels. First of all, unlike the spanwise convective flux that drains vorticity from the LEV on delta wings, the spanwise flow within the current example of a finite-AR plunging plate induces a spanwise convective flux of vorticity that primarily acts to strengthen the LEV. Yet it should be noted that this spanwise convection of vorticity does not alter the total circulation of the LEV because it is counteracted by an equivalent tilting term. The fact that the total three-dimensional flux of vorticity remains zero within the current example indicates that even when signification amounts are present, spanwise flow does not necessarily have the ability to alter the total circulation contained within the xy-plane. In reality, the results of this section have once again served to demonstrate that it is the diffusive flux of vorticity that actually mitigates the circulation of the LEV.

Despite this fact that spanwise flow does not appear to affect the circulation of the LEV, the point can still be made that spanwise flow is necessary for the stabilization of the LEV. While the total three-dimensional transport of vorticity may not be able to alter the

www.manaraa.com

circulation of the LEV, it can modify the vorticity field so that the LEV remains attached to the downstream boundary layer, thereby allowing for the enhancement of the diffusive flux.

The results of this discussion are summarized as follows: Maintaining an LEV that reattaches to the downstream boundary layer can lead to an increase in lift, as the associated augmentation of the diffusive flux of vorticity is indicative of the primary suction-peak being amplified. Furthermore, the spanwise convective flux of vorticity that develops within a finite aspect-ratio wing appears to be capable of prolonging this reattachment of the LEV by providing an additional source of negative vorticity within the reattachment region.

While the results of this chapter have helped to explicate how the reattachment of an LEV to the downstream boundary layer effects the vorticity transport of the flow and the aerodynamic performance of the airfoil, it has not provided significant insight into the role of the OSV within the evolution of the LEV. Thus, providing a characterization of the OSV will be the primary objective of the next chapter.

www.manaraa.com

CHAPTER 9
RESULTS FOR THE SUCTION CASE

9.1 Introduction

Similar to Chapter 8, the role of this chapter will be to extend our understanding of the LEV evolution by further characterizing the developmental stages that were identified within Chapter 6. The results from Chapter 8 were primarily concerned with roll-up of the LEV, and in order to further explicate the development of the LEV, it will be the goal of the current chapter to provide a similar analysis that is geared towards the roll-up of the OSV.

Using a modified interpretation of the Crabtree criterion [30], Section 6.2 established that the roll-up of the LEV was governed by the vorticity budget within the reattachment region. Because the spanwise convective flux of vorticity within the AR2 case acted to strengthen the reattachment region of the LEV, the roll-up process of the LEV varied between each of the three spanwise locations that were analyzed; it was the comparison of these unique cases that allowed the previous chapter to successfully characterize the roll-up of the LEV. The current chapter will take a similar approach in order to analyze the roll-up of the OSV.

While the Crabree criterion may govern the roll-up of the LEV, it was hypothesized within Section 6.3 that the amount of secondary vorticity within the flow governs the roll-up of the OSV. Thus, the approach of the suction case will be to apply suction beneath the OSV in order to remove secondary vorticity from the flow. While any modification of the OSV strength might be expected to affect the flow–as it will fundamentally alter the

www.manaraa.com

interaction between the LEV and the OSV–the primary goal of the current study will be to characterize how the roll-up of the OSV affects the development of the LEV. Since Chapter 6 has established this roll-up to be associated with the formation of a secondary suction-peak, suction will be applied within the current case so as to hinder the formation of this secondary suction-peak. Considering Figure 6.3 from Section 6.3, increasing the magnitude of the primary suction-peak seems to be the simplest way to eliminate the secondary peak. In order to achieve this augmentation of the primary suction-peak within the current case, suction will be applied at the 12.5% chordwise location (x = 9.5 mm) between $\phi = -30°$ and $\phi = 60°$.

The following results not only seek to characterize how the OSV affects the dynamics of the LEV, but also delve into the role of the diffusive flux of vorticity and surface pressure distribution within the evolution of the flow. The effectiveness of the suction application process will also be investigated in order to establish some fundamental guidelines for future flow control studies.

9.2 Global Flow Dynamics and Evolution

As was done with the baseline plunging case in Section 5.2, the first step in examining the suction experiment will be characterizing the global flow evolution. Figure 9.1 displays the vorticity isocontours from the suction case for all the phases that were measured. Similar to Figure 5.1, surface pressure gradients are also displayed over the flow field as vertical lines.

One major difference between the flow fields of the suction and baseline cases at

www.manaraa.com

$\phi = -90°$ is the position of the LEV from the previous cycle. Based on Figures 5.1a and 9.1a, the LEV of the baseline case has advected approximately $0.2c$ further downstream than the suction case (where c is the chord length). This delayed advection of the LEV significantly alters its interaction with the trailing-edge vortex being shed from the underside of the airfoil. Eslam Panah and Buchholz [35] showed that the reduced frequency of a rigid, plunging plate was the primary variable governing the wake vorticity distribution, as different wake patterns were characterized by different orientations of the LEV with respect to the TEV. Akkala et al. [4] extended these ideas and showed that if a vortex starts shedding from the underside of the trailing edge before the LEV from the upper surface had passed the trailing edge, the upstream LEV would induce a velocity that promotes the roll-up of the TEV.

This effect appears to be confirmed within the current data, as the delayed advection of the LEV within the suction case prevents it from aiding in the roll-up of the TEV. Because of this, the TEV depicted within Figures 9.1a-9.1e ($\phi = -90°$ to $\phi = -50°$) is shed from the trailing edge as a number of discrete vortices. Roll-up of the TEV into a single structure does not appear to occur until the LEV approaches the trailing edge at $\phi \approx -40°$ (Figure 9.1f). The orientation of the LEV upstream of the TEV within the suction case prevents it from immediately shedding into the wake, with Figures 9.1f-9.1t showing the LEV becoming trapped by the TEV and getting driven down towards the trailing-edge shear layer.

While these results identify a noteworthy variation in the interaction between the LEV and the TEV, there is no indication that trapping the LEV upstream of the TEV signif-

www.manaraa.com

icantly impacts the pressure distribution on the surface of the airfoil, as Figure 9.1 shows no noticeable pressure gradients anywhere along the downstream half of the airfoil.

Additional variations between the flow fields of the two cases are difficult to see when comparing Figures 5.1 and 9.1, as the formation of the LEV from the suction case occurs almost identically to the baseline case. Indeed, the stages in the development of the LEV (i.e. accumulation, roll-up, detachment) all correspond to the same approximate phase intervals. However, there are several important variations within these stages that will be identified in Sections 9.3.1-9.3.5 when the LEV is investigated more closely. While it is difficult to discern any variation between the two cases based on the vorticity field, the pressure gradients show some marked differences. The gradients that are depicted in Figures 5.1 and 9.1 evolve similarly throughout much of the downstroke, even after the initial application of suction at $\phi = -30°$. But once the airfoil enters the second half of its downstroke, the suction begins to modify the pressure gradients from their baseline values. Though this forcing appears small at first, the continued application of suction eventually reestablishes the single-suction-peak distribution on the surface of the airfoil by $\phi = 15°$ (Figure 9.1p). This reestablishment of the single-suction-peak distribution was also seen within the AR2 case at the 68.75-percent span location, which Figures 8.7d-8.7e showed to correspond to the elimination of the OSV and the restabilization of the LEV.

While the physics associated with the elimination of the secondary suction-peak within the current case are not yet clear, these preliminary results do serve as an initial confirmation that the suction was successful in forcing the flow. In order to establish a deeper understanding of the physics governing these changes, a vorticity flux analysis is

www.manaraa.com

performed next. By objectively quantifying the transport of vorticity, this analysis will help to reveal the precise nature in which the suction affects the flow.

9.3 Vorticity Flux Analysis

The vorticity flux analysis for the suction case was computed using the same control region and governing equations as the baseline case, and the vorticity budget was once again found to be governed by the shear-layer and diffusive fluxes. These primary fluxes are shown in Figure 9.2 along with the total flux of vorticity and the computed change in circulation–note that these last two terms should be equivalent if all of the sources and sinks of vorticity are being accounted for. While the total vorticity flux and $d\Gamma/dt$ are generally in very close agreement–as was seen with the baseline data in Figure 5.4–there is a region of mismatch between $\phi = 0°$ and $\phi = 10°$. Because the vorticity flux analysis was able to successfully resolve the circulation budget of the baseline case, it is expected that all of the terms from Equation 5.1 are still being properly characterized. As such, the discrepancy between $\phi = 0°$ and $\phi = 10°$ is presumably the result of an additional source/sink of vorticity that was not represented within Equation 5.1. Because the region in question occurs within the suction application interval, it seems appropriate to conclude that the missing term is associated with a net removal of circulation via the suction. It is interesting to note that this physical removal of circulation only occurs within a small phase interval, despite the fact that the suction is being applied over half the downstroke (i.e from $\phi = -30°$ to $\phi = 60°$). This result seems to imply that there is a condition that governs the effectiveness of the suction process, the specifics of which will be analyzed extensively

www.manaraa.com

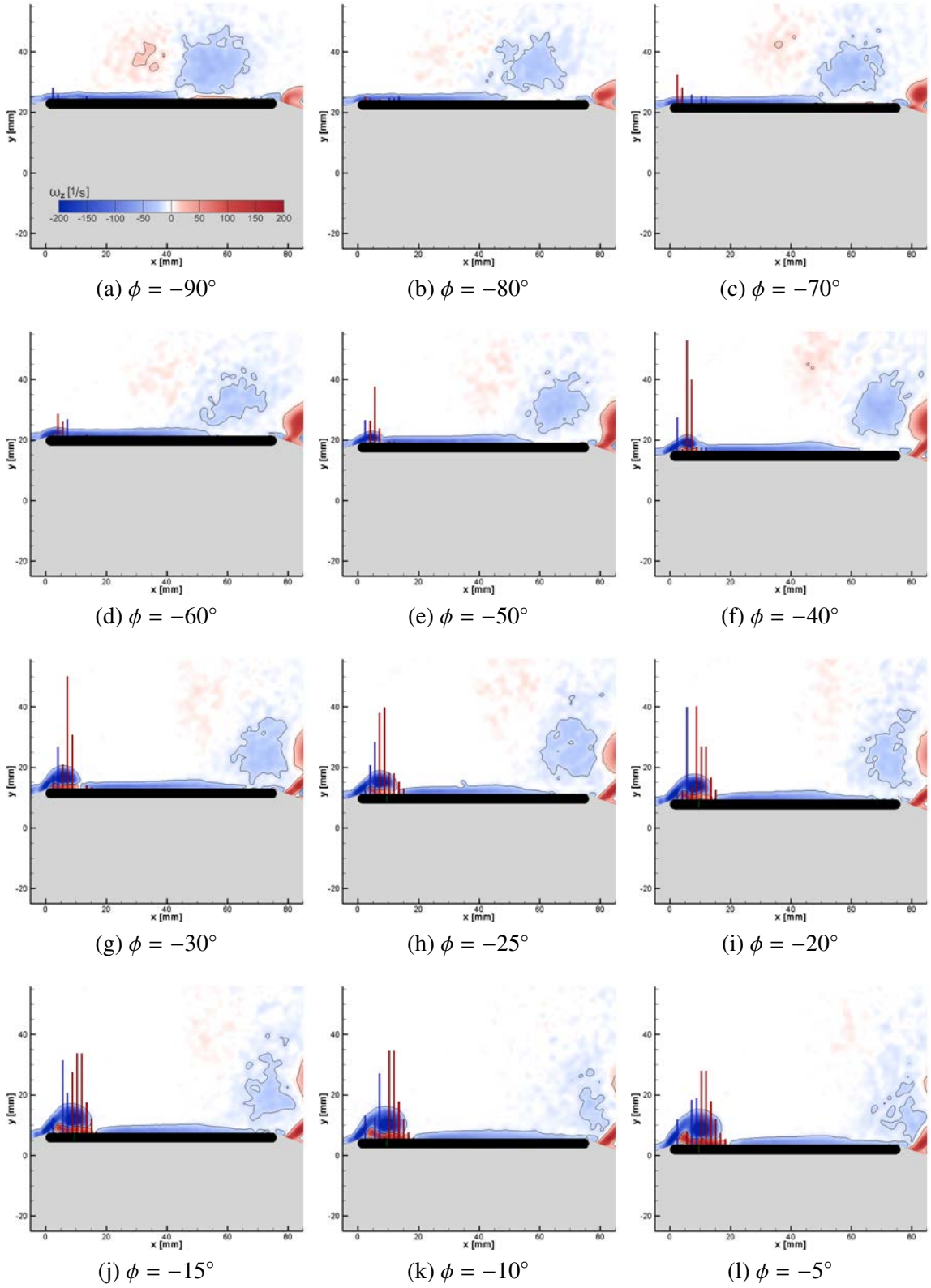

(a) $\phi = -90°$ (b) $\phi = -80°$ (c) $\phi = -70°$

(d) $\phi = -60°$ (e) $\phi = -50°$ (f) $\phi = -40°$

(g) $\phi = -30°$ (h) $\phi = -25°$ (i) $\phi = -20°$

(j) $\phi = -15°$ (k) $\phi = -10°$ (l) $\phi = -5°$

Figure 9.1: Evolution of the vorticity field from the suction case.

www.manaraa.com

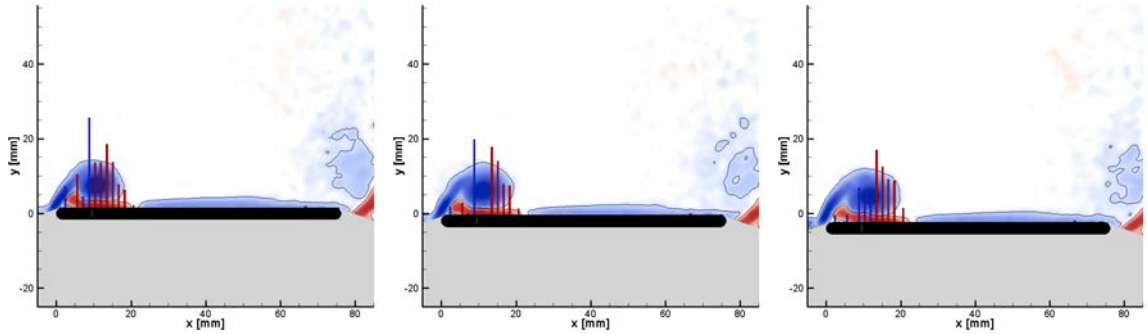

(m) $\phi = 0°$ (n) $\phi = 5°$ (o) $\phi = 10°$

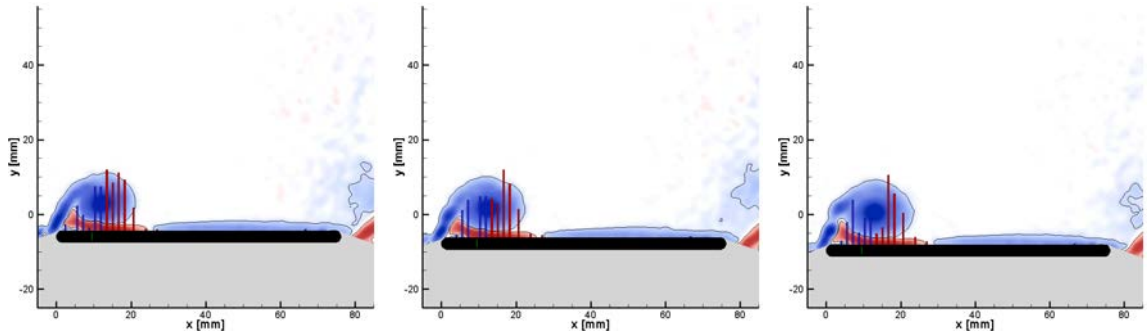

(p) $\phi = 15°$ (q) $\phi = 20°$ (r) $\phi = 25°$

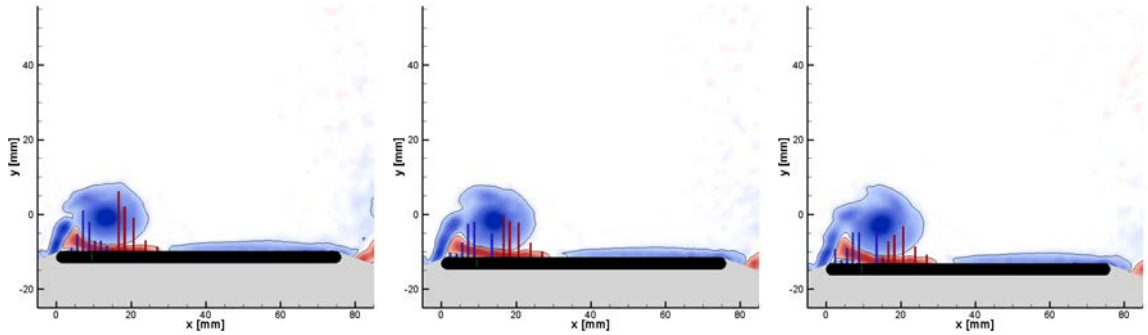

(s) $\phi = 30°$ (t) $\phi = 35°$ (u) $\phi = 40°$

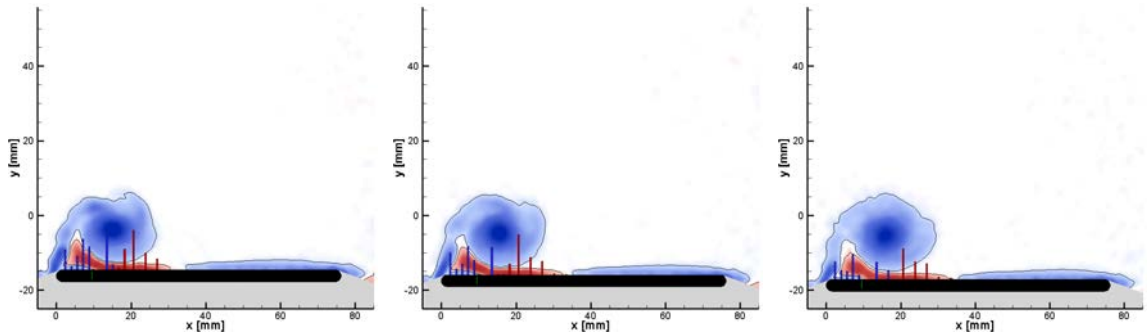

(v) $\phi = 45°$ (w) $\phi = 50°$ (x) $\phi = 55°$

Figure 9.1: Evolution of the vorticity field from the suction case.

www.manaraa.com

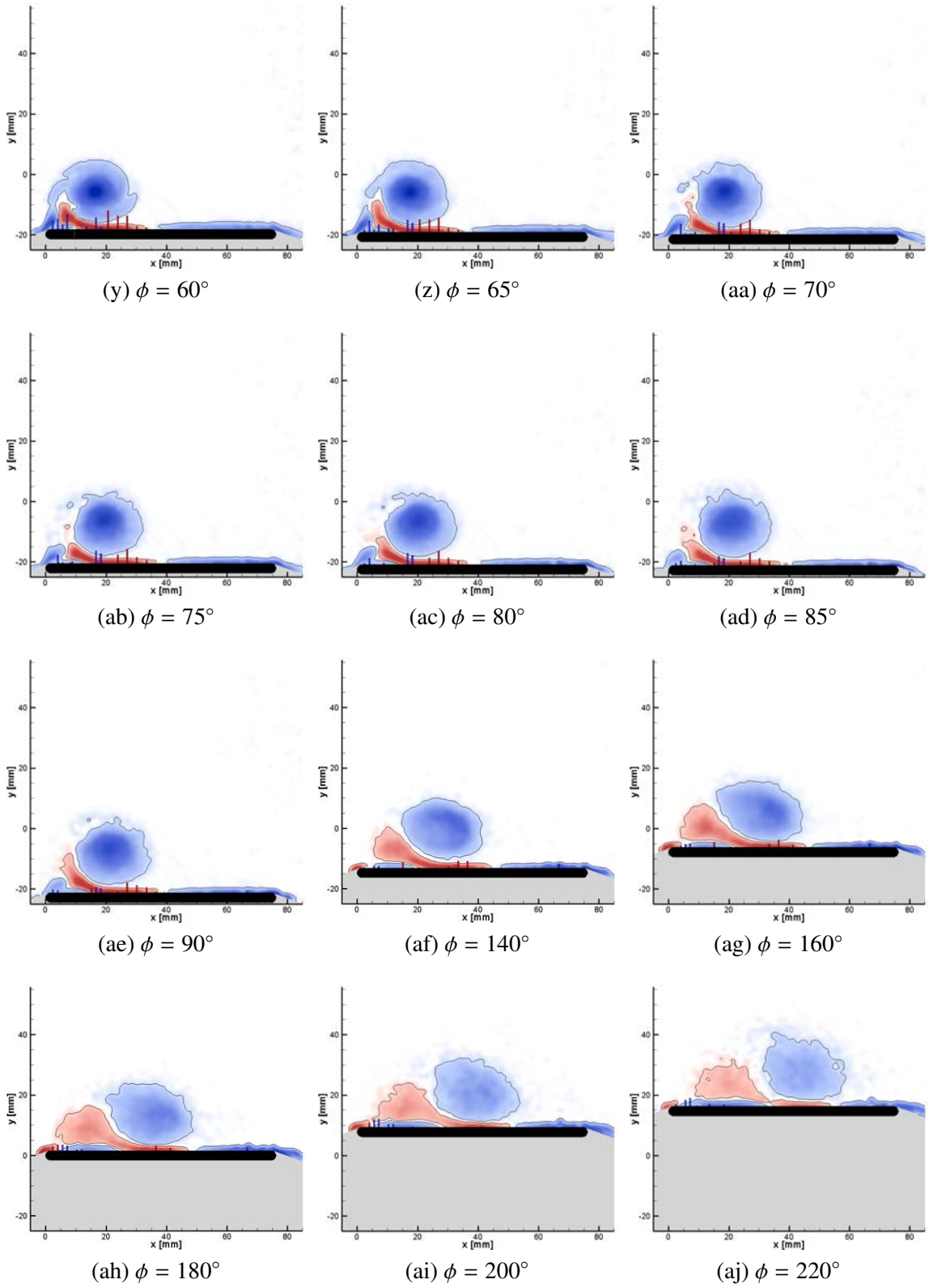

(y) $\phi = 60°$ (z) $\phi = 65°$ (aa) $\phi = 70°$

(ab) $\phi = 75°$ (ac) $\phi = 80°$ (ad) $\phi = 85°$

(ae) $\phi = 90°$ (af) $\phi = 140°$ (ag) $\phi = 160°$

(ah) $\phi = 180°$ (ai) $\phi = 200°$ (aj) $\phi = 220°$

Figure 9.1: Evolution of the vorticity field from the suction case.

www.manaraa.com

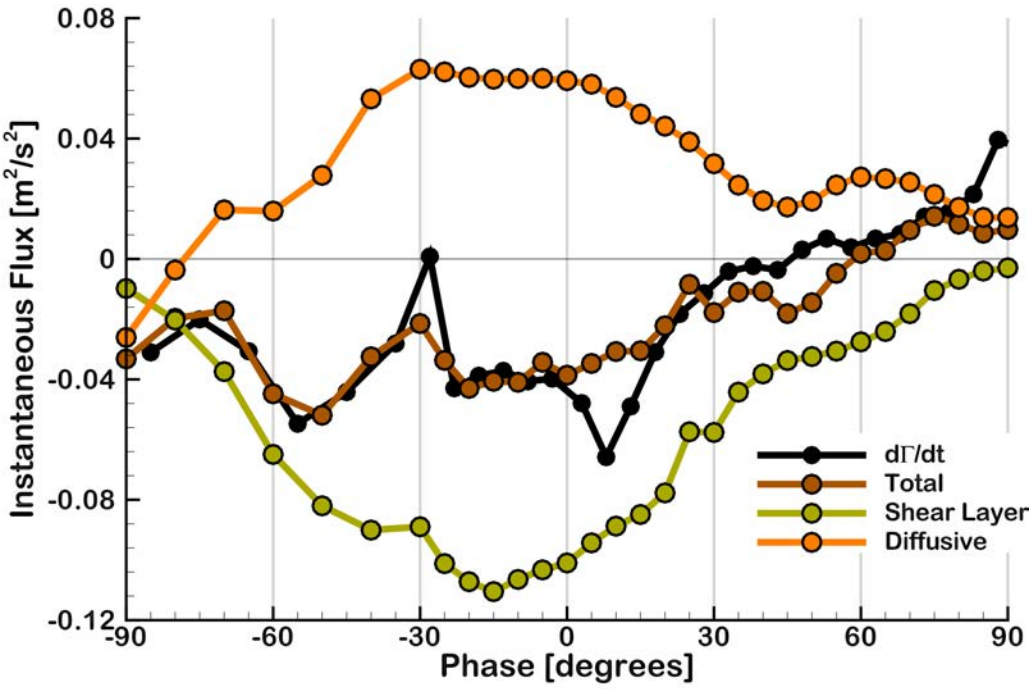

Figure 9.2: Primary fluxes of vorticity during the downstroke of the suction case.

within Sections 9.3.2-9.3.4.

Now that the fluxes of vorticity have been described, a comparison to the baseline data can be performed. In order to establish a fundamental picture of how the global flow differs between the suction and baseline cases, Figure 9.3a compares the total circulation measured within the two cases. To provide a more precise description, this data is then decomposed into the respective contributions from negative vorticity (primarily from the LEV) and positive vorticity (from the OSV) and presented within Figures 9.4b-9.4c. Because the fluxes of vorticity are of primary interest, Figures 9.4a-9.4c plot the time-derivatives of these circulation budgets in order to establish the net flux of vorticity. Figures 9.5 and 9.6 plot the shear-layer and diffusive fluxes against their respective terms from

www.manaraa.com

the baseline example, thereby characterizing the sources and sinks of vorticity within the flow. Variations within these specific vorticity transport mechanisms are analyzed next in conjunction with the major trends observed within the total fluxes.

Prior to the application of suction at $\phi = -30°$, Figure 9.3a shows some mild variation in the total circulation measured within the two cases. Figure 9.3b reveals this variation to be associated with the accumulation of more negative vorticity within the suction case, which appears to be a result of the enhanced shear-layer flux that Figure 9.5 shows at the beginning of the downstroke (i.e. for $-70° < \phi < -50°$). The shear-layer flux weakens slightly as the LEV rolls-up, resulting in a major deviation from the baseline value at $\phi = -30°$. Since the suction application system was triggered at the same time the PIV images were acquired for the $\phi = -30°$ dataset, it should be noted that this drop in the shear-layer flux is not a direct results of the suction process. Rather, these dynamics within the shear-layer flux–both the augmentation earlier in the stoke and the drop seen at $\phi = -30°$–are indicative of the LEV from the suction case evolving in a slightly different manner than the baseline LEV. Given that the prescribed kinematics were identical between the two cases up to and including $\phi = -30°$, these variations within the evolution of the two flows are expected to be a byproduct of slightly different initial conditions between the two cases.

Figure 9.5 shows the application of suction at $\phi = -30°$ increases the shear-layer flux up to its baseline values. At the same time, Figure 9.4 depicts a major discontinuity within the circulation budgets immediately after the application of suction. It is interesting to note that this event causes the circulation of the LEV to return to its baseline magnitude

www.manaraa.com

(Figure 9.3b) and dynamics (Figure 9.4b) for the rest of the suction application interval. However, the same does not hold true for the dynamics of the OSV; Figure 9.4c shows the growth of the OSV once again stagnates around $\phi = 5°$. In the context of the total vorticity-budget from Figure 9.2, this feature is associated with the small time-interval over which the suction removes secondary vorticity from the flow. While the duration of this forcing is short, the fact that it does not impact the circulation of the LEV allows the suction to produce a measurable increase within the total circulation plotted in Figure 9.3a. This appears to be a permanent modification to the flow, as Figure 9.3a shows the increased circulation of the suction case–with respect to the baseline circulation–persists through the rest of the downstroke. The robustness of this alteration is emphasized by the fact that both the LEV and OSV experience a significant drop in circulation after the suction is stopped at $\phi = 60°$, yet the net result of these dynamics do not appear to have an impact on the total circulation budget.

Once the suction stops removing secondary vorticity after $\phi = 15°$, Figures 9.5 and 9.6 both depict a significant reduction in the magnitudes of the shear-layer and diffusive fluxes that persist until the end of the suction application interval, yet their combined effect appears to have no net effect on the total flux of vorticity. While these dynamics apparently counteract each other so that the total circulation does not deviate from the baseline value, their presence is a good indication that the suction is still forcing the flow in some manner. Although Figure 9.5 shows the shear-layer flux returns to its baseline value at the end of the suction application interval ($\phi = 60°$), the diffusive flux does not experience the same behavior. The continued variation within the diffusive flux data alludes to the suction

www.manaraa.com

having fundamentally altered the vortex-airfoil interaction, which appears to be similarly implied by and overall increase in the total circulation of the flow.

Based on this comparison to the baseline data, there is now sufficient context to establish how the suction modifies the flow. While the flow fields of the two cases initially appear to evolve differently, the application of suction causes the circulation of the LEV to return to its baseline value. Throughout most of its application, the suction affects the shear-layer and diffusive fluxes without producing any major changes within the total circulation-budget. The exception to this behavior occurs between $\phi = 0°$ and $\phi = 10°$, when the diffusive flux experiences a distinct return to its baseline behavior while the suction is temporarily able to remove vorticity from the OSV. Not only is the suction able to remove secondary vorticity without changing the circulation of the LEV, but the process also can be inferred to have a distinct impact on the flow dynamics due to the fact that it increases the total circulation within the control region.

The primary goal of this chapter is to characterize the dynamics of the OSV, particularity with respect to its interaction with the LEV. To this end, the purpose of the suction experiment was to physically alter the strength of the OSV through the removal of secondary vorticity, after which the effect on both the surface pressure distribution as well as the overall vorticity field could be analyzed. Extending the approach of Chapter 6, interpreting any modifications to the flow in parallel with the behavior of the surface pressure distributions can provide unique insight into highly coupled vortex-surface interaction that appears to govern the evolution of the LEV. On the other hand, a cursory comparison of Figures 5.1ae-5.1aj and 9.1ae-9.1aj indicates the suction ultimately produces a distinctly

www.manaraa.com

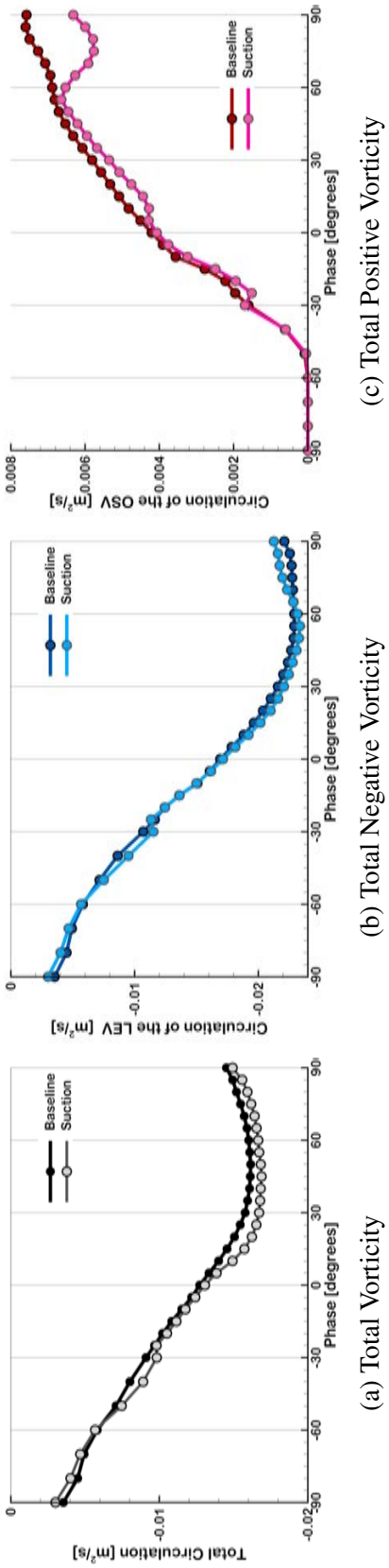

(a) Total Vorticity (b) Total Negative Vorticity (c) Total Positive Vorticity

Figure 9.3: Comparison of the circulation values calculated for the baseline and suction cases.

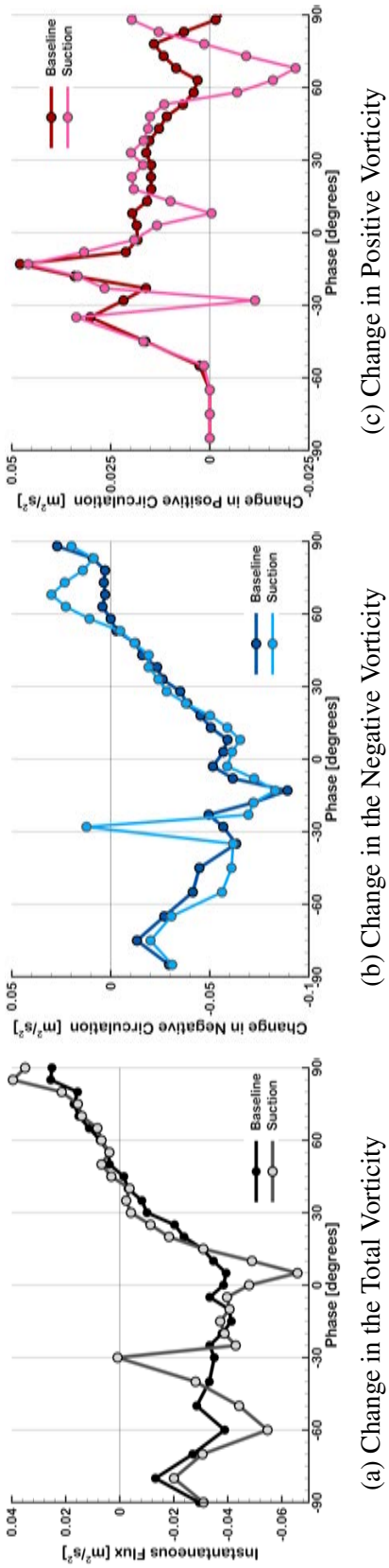

(a) Change in the Total Vorticity (b) Change in the Negative Vorticity (c) Change in Positive Vorticity

Figure 9.4: Comparison of the change in circulation calculated for the baseline and suction cases.

www.manaraa.com

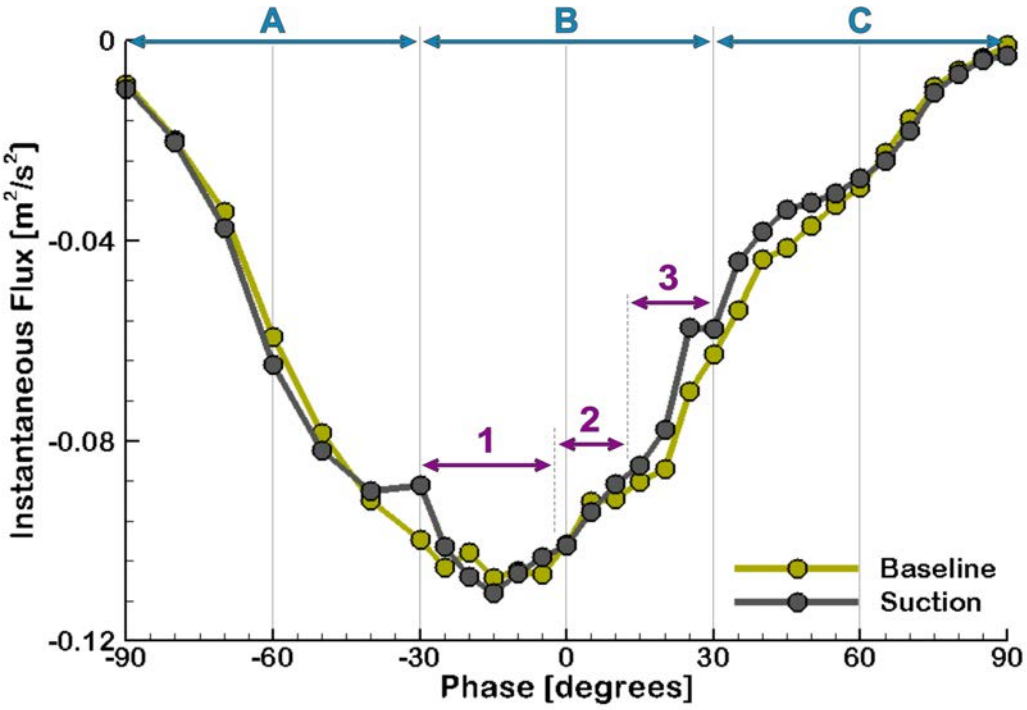

Figure 9.5: Comparison of the shear-layer fluxes from the baseline and suction cases.

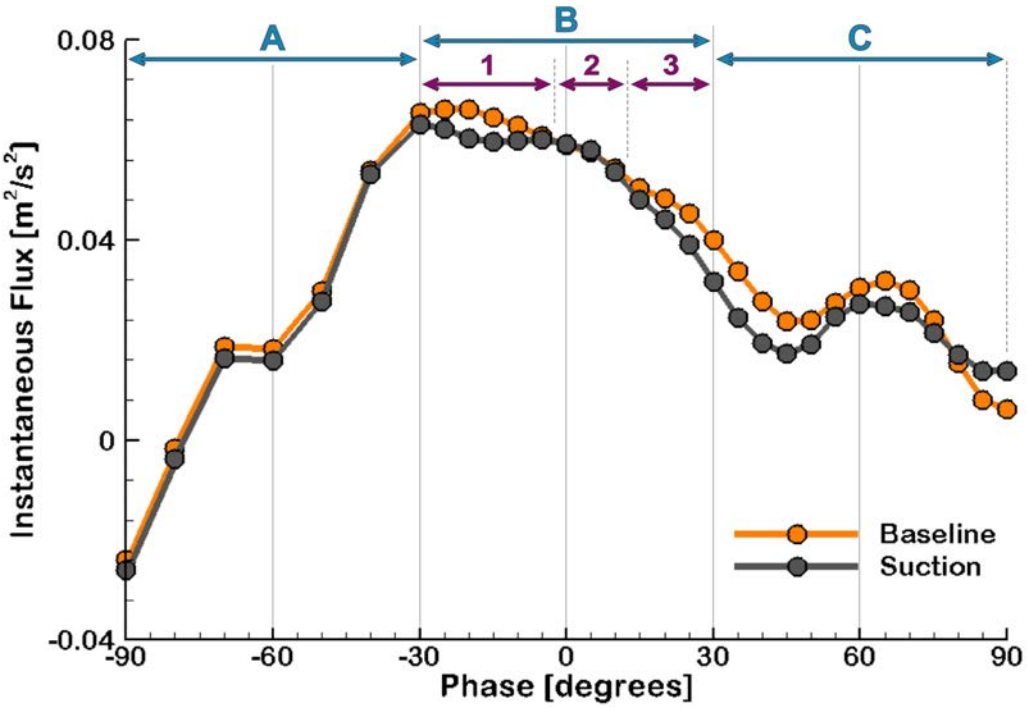

Figure 9.6: Comparison of the diffusive fluxes from the baseline and suction cases.

www.manaraa.com

different flow field, effectively redistributing the primary, secondary and tertiary vortices within the flow. As this is achieved without modifying the prescribed kinematics or model geometry, it provides a novel example for studying the vortex-vortex interactions within the flow, as it causes the evolution of the LEV to become highly dependent on its orientation with respect to other vortical structures. In order to streamline a more effective discussion of all these results, several phase intervals are defined throughout the downstroke of the airfoil based on what type of vortex-interaction will be discussed. These phase intervals are marked within Figures 9.5 and 9.6 and are characterized below.

Interval B identifies the portion of the downstroke where the correlation between the surface pressure distribution and the vorticity field are of primary interest, the interval for which begins at the start of the suction application interval ($\phi = -30°$) and ends just prior to the detachment of the LEV ($\phi = 30°$). The associated discussion will serve to validate the ideas from Section 6.4 regarding the correlation between the surface pressure distributions and the dynamics of the OSV, specifically how the roll-up of the OSV leads to the formation of a secondary suction-peak. Furthermore, by relating any changes within the secondary suction-peak to those found within the primary suction-peak, discussion within this phase interval will help to further characterize how the OSV influences the dynamics of the LEV as well as the aerodynamic loads. In anticipation of possible variations within this interval, it is split into three sub-intervals based on whether or not the suction is successful in altering the total circulation of the flow.

While the surface pressure distributions are the focus of Interval B, discussion within Section 7.4 has indicated that the suction produced by the LEV on the surface of

www.manaraa.com

the airfoil approaches zero once it detaches. Interval C is associated with the portion of the downstroke after this detachment begins ($30° < \phi < 90°$), wherein the evolution of the LEV becomes independent of any on-wall dynamics. Discussion of this interval will focus on how the dynamics of a single vortical structure are affected by its orientation with respect to other structures within the flow.

Interval A is defined by the portion of the downstroke prior to the application of suction, where the flux analysis has shown some variation in the vorticity budget of the LEV. This behavior is expected to be an extension of Interval C, in that the reorientation of the vorticity field–e.g. the delayed advection of the previous cycle's LEV–will create different initial conditions within the suction case at the beginning of the downstroke. Discussion of Interval A will not delve into the specifics of these initial conditions, but will instead describe how the LEV formation varies between the two cases.

These phase intervals are summarized as follows:

Interval A ($-90° \leq \phi \leq -30°$): Associated with the portion of the downstroke prior to the application of suction. Characterizes how the formation of the LEV differs between the two cases when the periodic application of suction alters the initial conditions of the suction case at the beginning of the downstroke.

Interval B ($-30° \leq \phi \leq 30°$): Includes the portion of the suction interval prior to the detachment of the LEV, where the suction affects distinct variations within the flow that fundamentally alter the interaction between the vorticity field and the surface of the airfoil. This interval is split into three sub-intervals based on the effectiveness of the suction in altering the circulation of the control region, as

www.manaraa.com

well as the change produced within the diffusive flux data.

Interval B1 ($-30° \leq \phi \leq -5°$): Initial application of suction causes the circulation of the control region to revert to its baseline value, after which the suction appears to have no effect on the total circulation budget. Figure 9.6 depicts a marked divergence within the diffusive flux of the two cases over this interval.

Interval B2 ($0° \leq \phi \leq 10°$): The suction successfully removes secondary vorticity from the flow so that the total circulation of the control region decreases. Figure 9.6 shows no variation in the diffusive flux of the two cases over this interval.

Interval B3 ($15° \leq \phi \leq 30°$): The suction stops removing secondary vorticity and $d\Gamma/dt$ reverts to its baseline behavior. Over this interval, Figure 9.6 once again shows the diffusive flux of the suction case as decreasing with respect to the baseline data.

Interval C ($30° \leq \phi \leq 90°$): Contains the portion of the cycle where the LEV is detaching or has already detached, where the suction has significantly modified the configuration of vortices within the flow. Characterizes how the evolution of the LEV depends on its position with respect to the secondary and tertiary vortical structures.

Sections 9.3.1-9.3.5 delve into these specific phase intervals in order to better characterize how the evolution of the LEV varies between the two cases. To aid in this process,

www.manaraa.com

magnified vorticity isocontours are presented for both flows in Figures 9.7, 9.8, 9.11, 9.14, 9.19 and 9.21 with the baseline case shown on the left and the suction case on the right. Velocity vectors are overlaid upon the isocontours, as are lines representing the surface pressure gradients. In the phases where suction is being applied, there is a small green line drawn on the airfoil's cross section at the chordwise-location of the suction ports.

9.3.1 Phase Interval A: $\phi = -90°$ to $\phi = -30°$

Ideally, the LEV within the suction case would follow the baseline formation process prior to the application of suction. However, an analysis of the vorticity fields shows this is not the case, and Figures 9.7k-9.7l show a significant variation has developed between the cases by $\phi = -30°$. The deviation of the two flows that is depicted within Figure 9.7 appears to be a gradual process that develops over time, yet the deviation becomes exacerbated once the LEV separates. This overall trend is consistent with the behavior that was observed within Figures 9.3b, in that the beginning of the downstroke is characterized by a gradual divergence in the amount of negative vorticity within the flow.

In terms of the variation seen in Figure 9.5, it appears that augmenting the shear-layer flux while the LEV remains attached to the downstream boundary layer does not significantly alter the appearance of the vorticity field. However, increasing the circulation of the LEV seems to have a significant effect on the flow field once the structure rolls-up, though this could be a time integrated effect–i.e. the LEV has not accumulated enough circulation to noticeably alter the vorticity field until after it rolls-up. Comparing the vorticity fields of Figures 9.7k-9.7l, it appears that the formation of a larger LEV structure leads to

www.manaraa.com

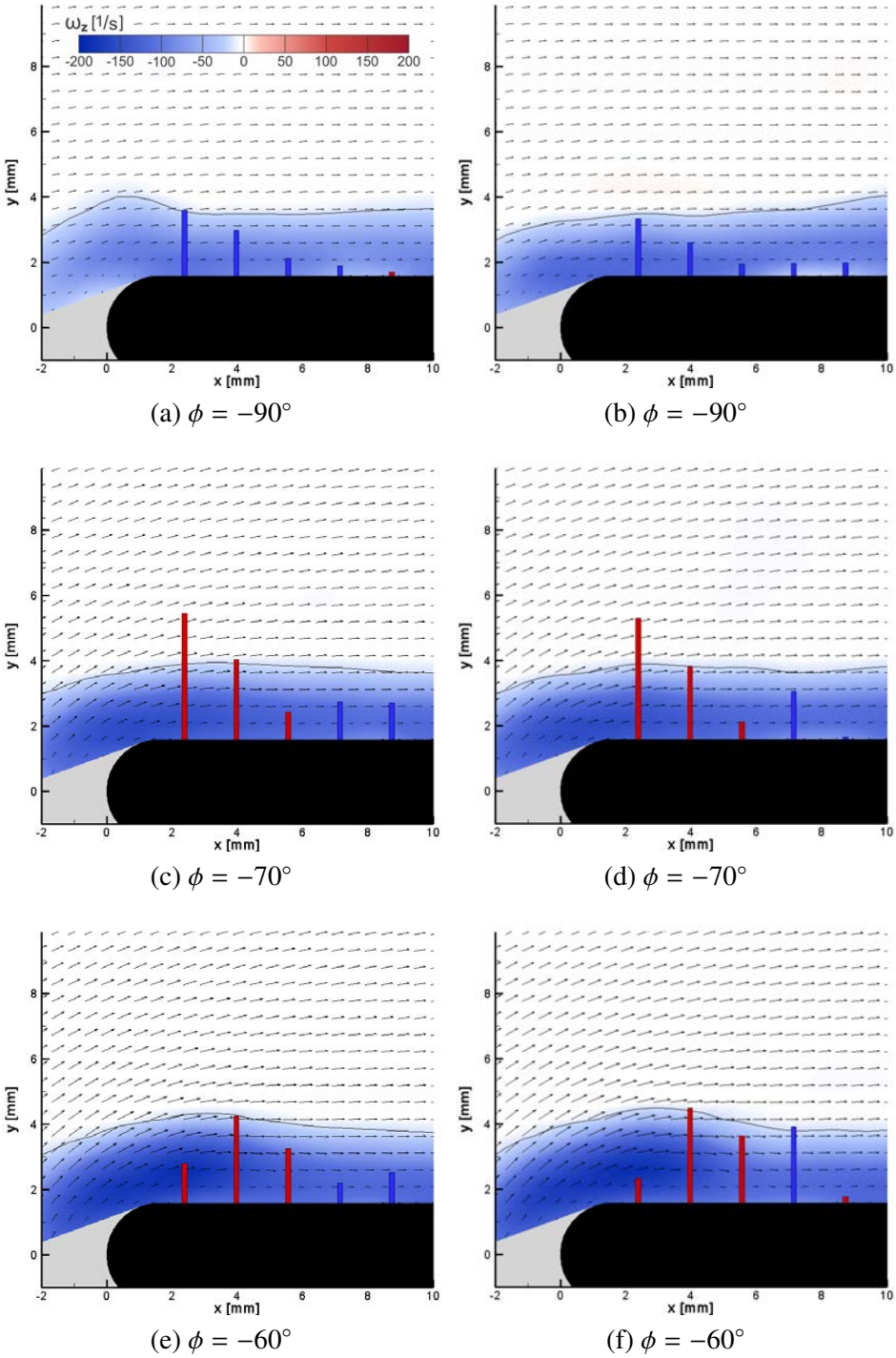

(a) $\phi = -90°$ (b) $\phi = -90°$

(c) $\phi = -70°$ (d) $\phi = -70°$

(e) $\phi = -60°$ (f) $\phi = -60°$

Figure 9.7: Evolution of the vorticity field from the baseline (left) and suction (right) cases prior to the application of suction.

www.manaraa.com

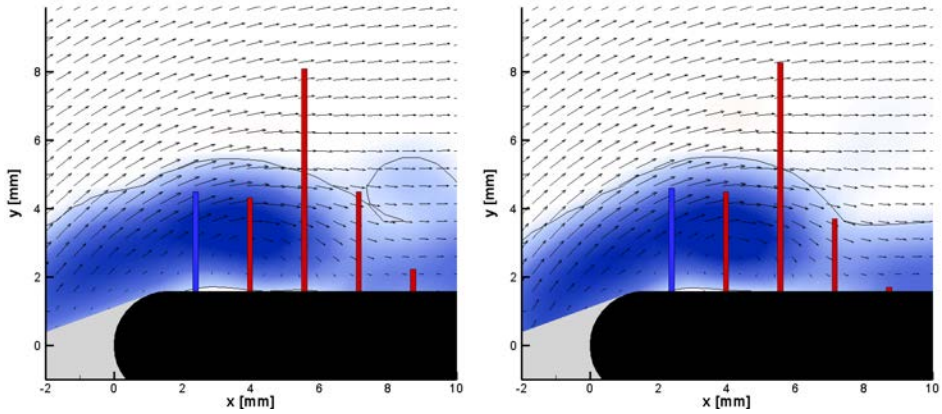

(g) $\phi = -50°$ (h) $\phi = -50°$

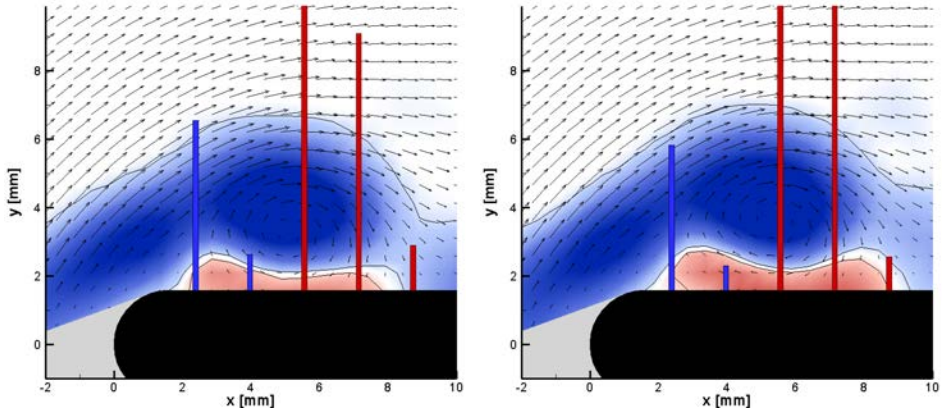

(i) $\phi = -40°$ (j) $\phi = -40°$

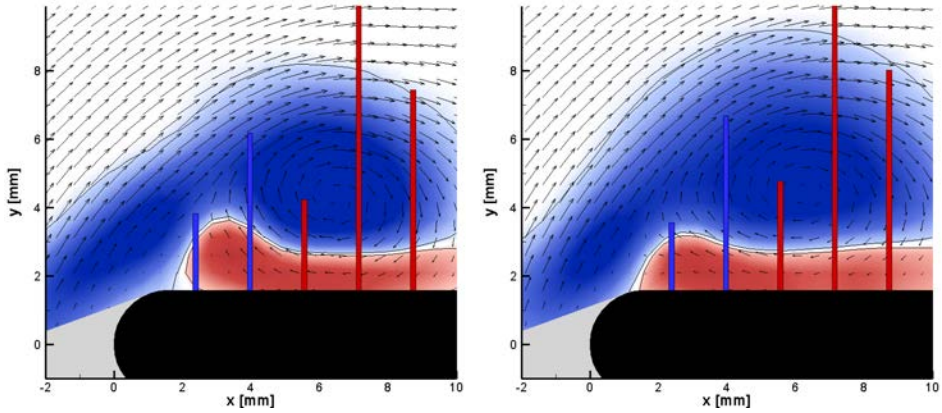

(k) $\phi = -30°$ (l) $\phi = -30°$

Figure 9.7: Evolution of the vorticity field from the baseline (left) and suction (right) cases prior to the application of suction.

www.manaraa.com

the premature leveling-off of the shear-layer flux that Figure 9.5 shows as occurring within the suction at $\phi = -30°$.

While Interval A highlights some interesting variations between the two cases regarding the formation of the LEV, the behaviors have not been sufficiently resolved within the current experiments to establish any form of causality. With regard to the current analysis, it is sufficient to say that vorticity field of the suction case moderately differs from that of the baseline example at the beginning of the suction interval. In addition to this point, it is interesting to note that even while the LEV of the suction case departs from the baseline evolution, the distribution of the pressure gradients remains fairly constant. This is not only indicated by the similarity in the pressure gradients between the left and right column of Figure 9.7, but also within the diffusive flux data plotted in Figure 9.6.

9.3.2 Phase Interval B1: $\phi = -30°$ to $\phi = -5°$

Figures 9.8a-9.8b once again show the flow fields obtained at $\phi = -30°$, and a comparison of Figures 9.8b and 9.8d illustrates how the initial application of suction essentially draws the flow towards the suction port. Figures 9.4a, 9.4b and 9.4c all allude to the suction affecting a major change within the flow after it is applied at $\phi = -30°$, as it temporarily halts the accumulation of both positive and negative vorticity. Because Figures 9.5 and 9.6 show the shear-layer and diffusive fluxes are still introducing vorticity of either sign into the flow during this time, the suction must be able to eliminate similar amounts of positive and negative vorticity in order to achieve the zero-sum result. While the exact nature is not clear, the simplest way for the suction to accomplish this dual-signed sink of vorticity is for

www.manaraa.com

it to enhance the cross-cancellation between the LEV and OSV, which seems to be an apt characterization of what is shown in Figure 9.8d.

By accelerating the flow towards the suction port, the suction effectively "pulls" the LEV down into the OSV. Although this decreases the circulation of both structures, the local balance of vorticity is such that the OSV becomes weakened while a portion of the LEV is completely eliminated–i.e. Figure 9.8d depicts a weakening of the OSV directly above the suction port within the same region that a portion of the otherwise-circular LEV appears to have been eliminated. However, this enhanced cross-cancellation does not persist for very long, as Figures 9.8f and 9.8h show the OSV growing stronger above the suction port and the LEV being pushed away from the surface of the airfoil by $\phi = -20°$. Based on these qualitative observations of the flow field, it appears that the initial application of suction is able to forcibly reposition the vortical structures within the flow, with the vorticity field settling into a new orientation once the suction pressure approaches steady state at $\phi = -20°$. (Recall from Figure 3.6 that the negative pressure imposed at the suction ports has a 65-percent rise time of 0.0264 seconds, which corresponds to 8.08 degrees within the motion of the airfoil.)

When comparing the vorticity fields of the two cases before (Figures 9.7k-9.7l) and after (Figures 9.8e-9.8f) this effective reorientation of the vorticity field, it is interesting to note that the suction actually modifies the LEV so that it once again resembles the base-line distribution. This observation is emphasized within Figure 9.9, which overlays the vorticity-threshold outlines of the LEV from the two cases atop one another. Figure 9.9a shows a clear distinction between the LEV of the suction and baseline cases (show in green

www.manaraa.com

and black respectively) at $\phi = -30°$, and Figure 9.9b illustrates how the application of suction reorients the LEV so that it approaches the baseline configuration. While Figures 9.9c-9.9d show some minor variations persisting between the two LEVs until $\phi = -15°$, it is apparent that the primary modification of the flow field occurs at $\phi = -25°$ near the initiation of suction.

The transient application of suction certainly may have a pronounced effect on the flow field, but once the suction approaches steady state at $\phi = -20°$, it is no longer effective in altering the vorticity field. Despite the fact that suction continues to be applied beneath a region of positive vorticity, Figure 9.4c shows the OSV once again begins to accumulate circulation at the same rate as the baseline case after $\phi = -20°$. While there is no obvious explanation for how the OSV remains unaffected while the suction is physically removing rotational fluid, it is likely a three-dimensional effect. It is important to remember that the PIV data was acquired within an imaging plane that was located halfway between two suction ports, meaning the application of suction does not inherently require the removal of vorticity from the two-dimensional, spanwise-slice of the OSV represented within Figure 9.8. Based on the available data, it appears that there is some sort of three-dimensionality within the flow that preserves the circulation of the OSV between $\phi = -25°$ and $\phi = -5°$, which is alluded to within Figure 9.8f by the appearance of a small region of negative vorticity forming beneath the OSV, directly above the suction port. The exact nature of this effect is not clear–as the dynamics were not resolved within the PIV data–but the next section will provide some insight into what sort of flow conditions are necessary for the effective removal of vorticity from the OSV.

www.manaraa.com

There was a significant amount of discussion within Chapter 6 regarding the roll-up of the LEV and appearance of the OSV. In a modified interpretation of the Crabree criterion, Section 6.2 established that the balance between convective and diffusive fluxes downstream of the LEV governs its reattachment to the downstream boundary layer. Although the initial application of suction was not successful in reattaching the LEV, Figure 9.8d does show the LEV being drawn down towards the surface of the airfoil and extending towards the downstream boundary layer. However, Figure 9.6 shows this trend towards the reattachment of the LEV does not augment the diffusive flux, which is in agreement with the results of the finite-AR case. It was shown in Section 8.3 that reversing the roll-up of the LEV did not augment the diffusive flux until after the OSV has been completely eliminated and the LEV actually reattached to the downstream boundary layer. The suction case reaffirms this concept and provides further evidence of the diffusive flux being unable to increase so long as the OSV remains present within the flow.

A cursory analysis of Figure 9.8 indicates the application of suction does not significantly change the pressure gradients beneath the LEV, further emphasizing their robustness. To allow for a more precise comparison, Figure 9.10 plots the actual pressure distributions that were measured. Generally, these pressure distributions remain fairly constant between the two cases, although the application of suction between $\phi = -20^\circ$ and $\phi = -10^\circ$ does appear to alleviate some of the suction at the leading edge, which also accounts for the drop in the diffusive flux that is shown in Figure 9.6. This variation in the pressure decreases over time, until it is effectively eliminated by $\phi = -5^\circ$ (Figure 9.10d). Examination of the pressure gradients depicted in Figures 9.8i-9.8l confirms that the only major difference

www.manaraa.com

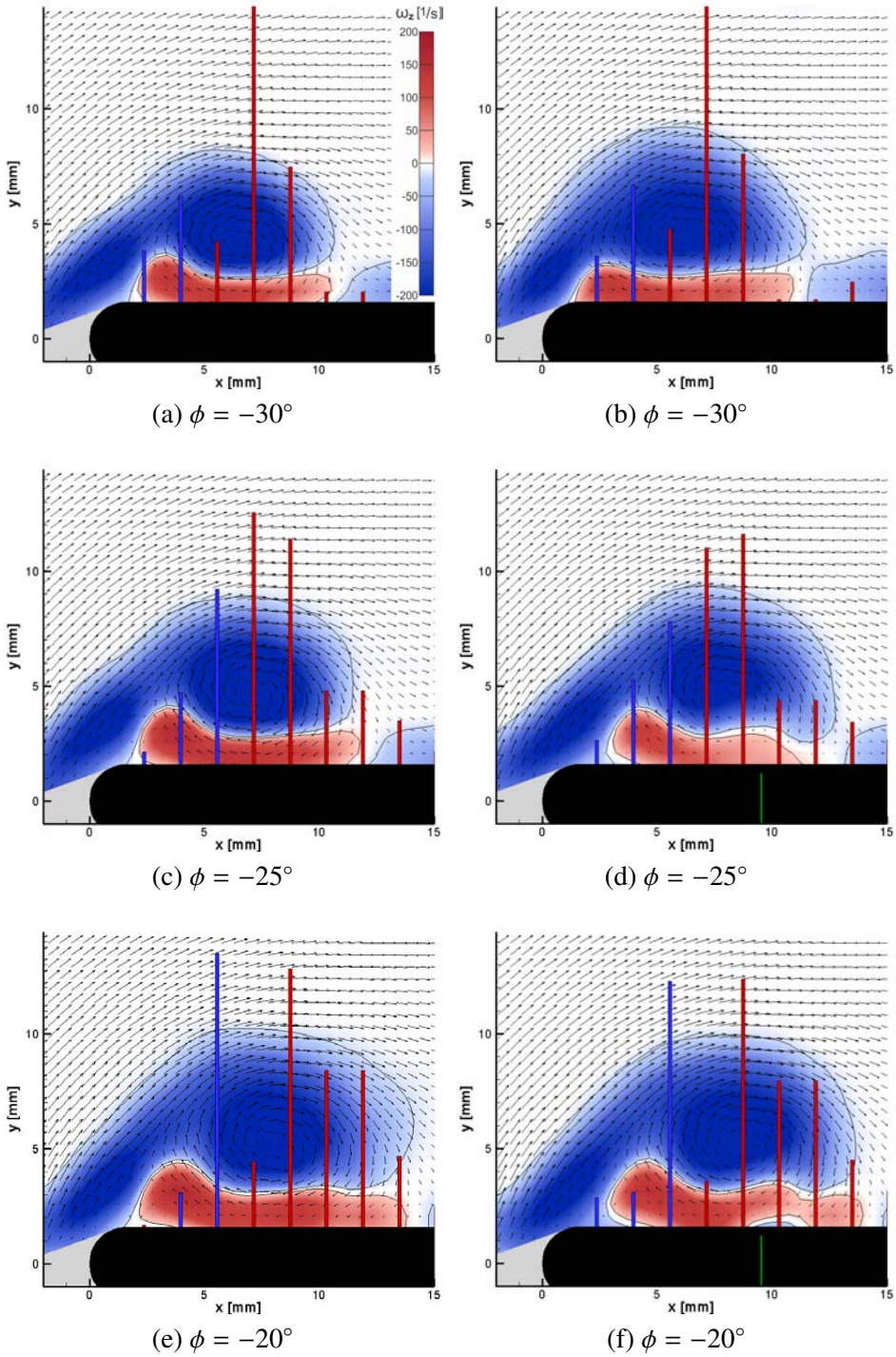

(a) $\phi = -30°$ (b) $\phi = -30°$

(c) $\phi = -25°$ (d) $\phi = -25°$

(e) $\phi = -20°$ (f) $\phi = -20°$

Figure 9.8: Evolution of the vorticity field from the baseline (left) and suction (right) cases during the initial roll-up of the LEV.

www.manaraa.com

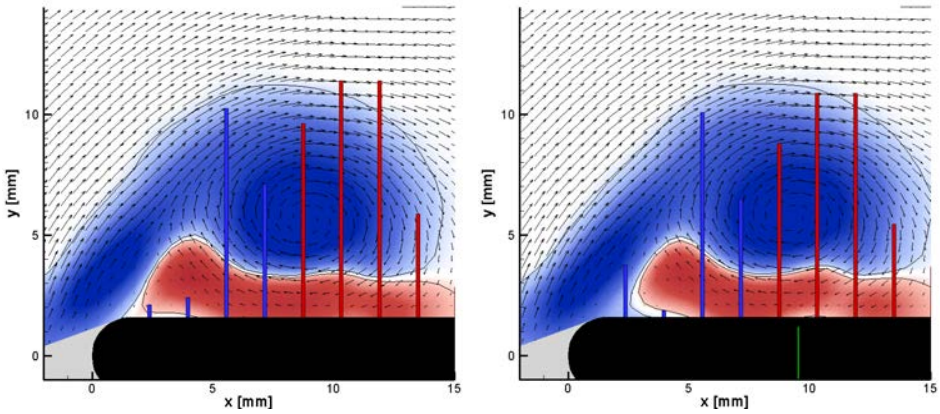

(g) $\phi = -15°$ (h) $\phi = -15°$

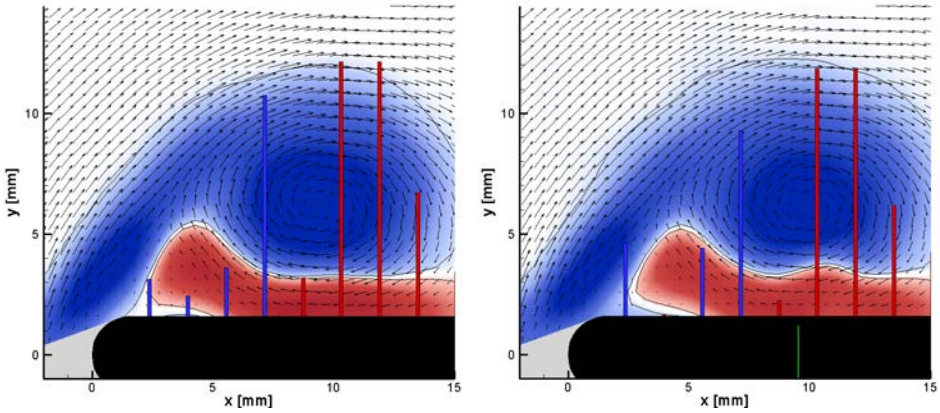

(i) $\phi = -10°$ (j) $\phi = -10°$

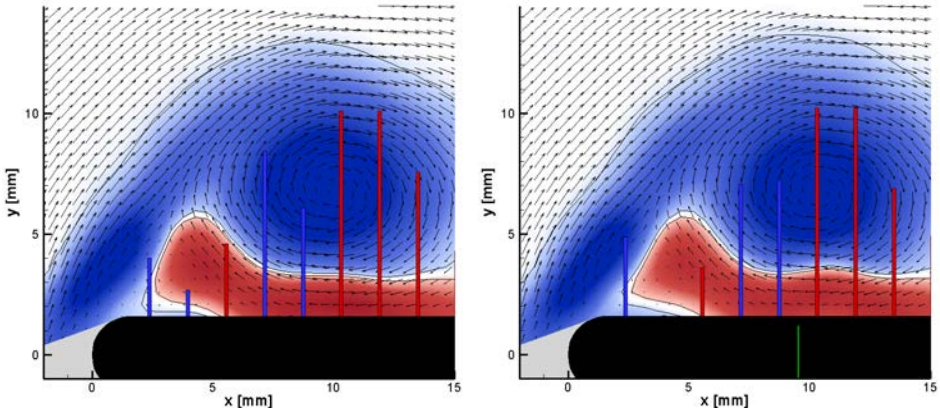

(k) $\phi = -5°$ (l) $\phi = -5°$

Figure 9.8: Evolution of the vorticity field from the baseline (left) and suction (right) cases during the initial roll-up of the LEV.

www.manaraa.com

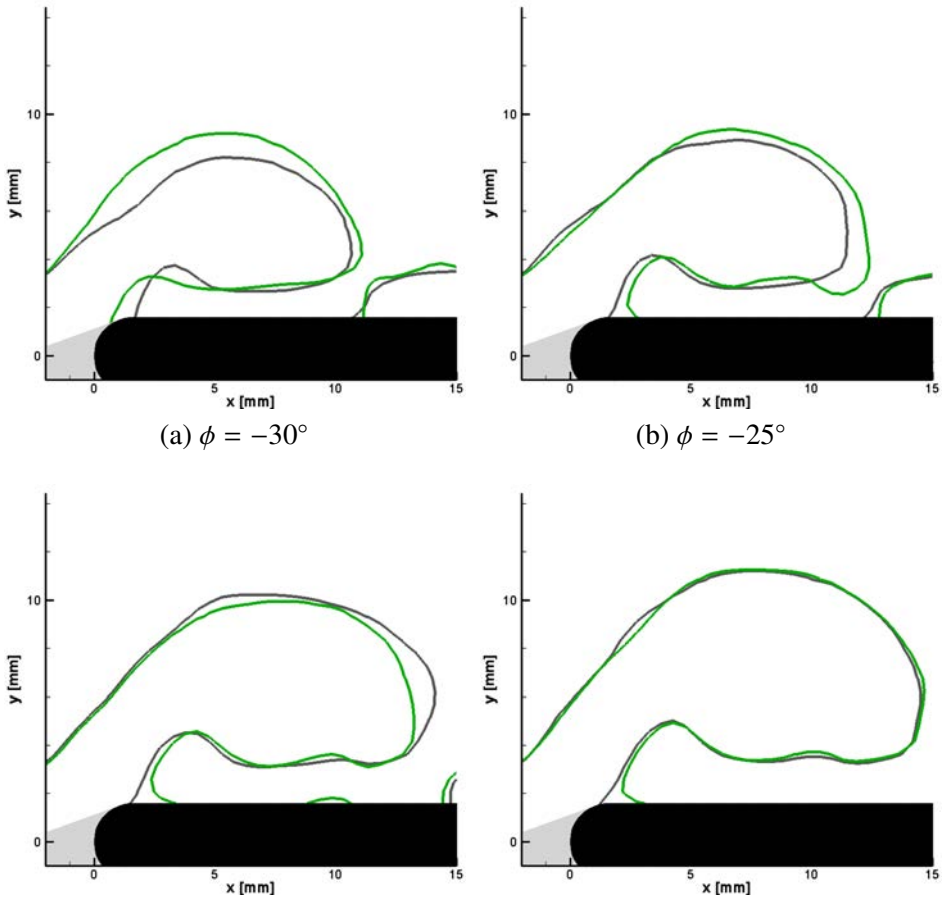

(a) $\phi = -30°$ (b) $\phi = -25°$

(c) $\phi = -20°$ (d) $\phi = -15°$

Figure 9.9: Outlines of the LEV from the baseline (black) and suction (green) cases during the initial application of suction, as determined by the vorticity isocontour obtained at 5-percent of the maximum vorticity magnitude (only negative-vorticity threshold outline is shown).

www.manaraa.com

between the two cases is an enhanced FPG right at the leading edge of the airfoil within the suction case, which appears to produce a very small region of attached flow upstream of the OSV. By drawing the separation point further downstream, the suction appears to be decreasing the effective angle of attack, which is to be expected based on the fact that the suction is essentially producing a downwash effect on the leading edge.

9.3.3 Phase Interval B2: $\phi = 0°$ to $\phi = 10°$

Between $\phi = 0°$ and $\phi = 10°$, the diffusive flux plotted within Figure 9.6 exhibits a distinct return to its baseline behavior. Interestingly, Figure 9.4c shows this to correspond to the phase interval over which the suction is finally able to remove positive vorticity from the flow. Referencing the flow fields within Figure 9.11, this effect is observed to gradually reduce the amount of secondary vorticity near the leading edge until there is a significant variation in the strength of the upstream portion of the OSV by $\phi = 10°$ (Figures 9.11e-9.11f)

Since the objective of the suction application process was to remove secondary vorticity from the flow, it is important to understand why this phenomenon suddenly becomes possible between $\phi = 0°$ and $\phi = 10°$. The fact that this interval begins at $\phi = 0°$ indicates there might be some dependence on the acceleration of the airfoil, e.g. the suction becomes effective once the airfoil starts to decelerate. It is difficult to rule this idea out entirely, however preliminary tests of the system showed that suction applied from $\phi = -30°$ to $\phi = 0°$ removed the same volume of fluid as when it was applied from $\phi = 0°$ to $\phi = 30°$ (see Section 3.3). Although there is no way to verify the spanwise distribution of this removal,

www.manaraa.com

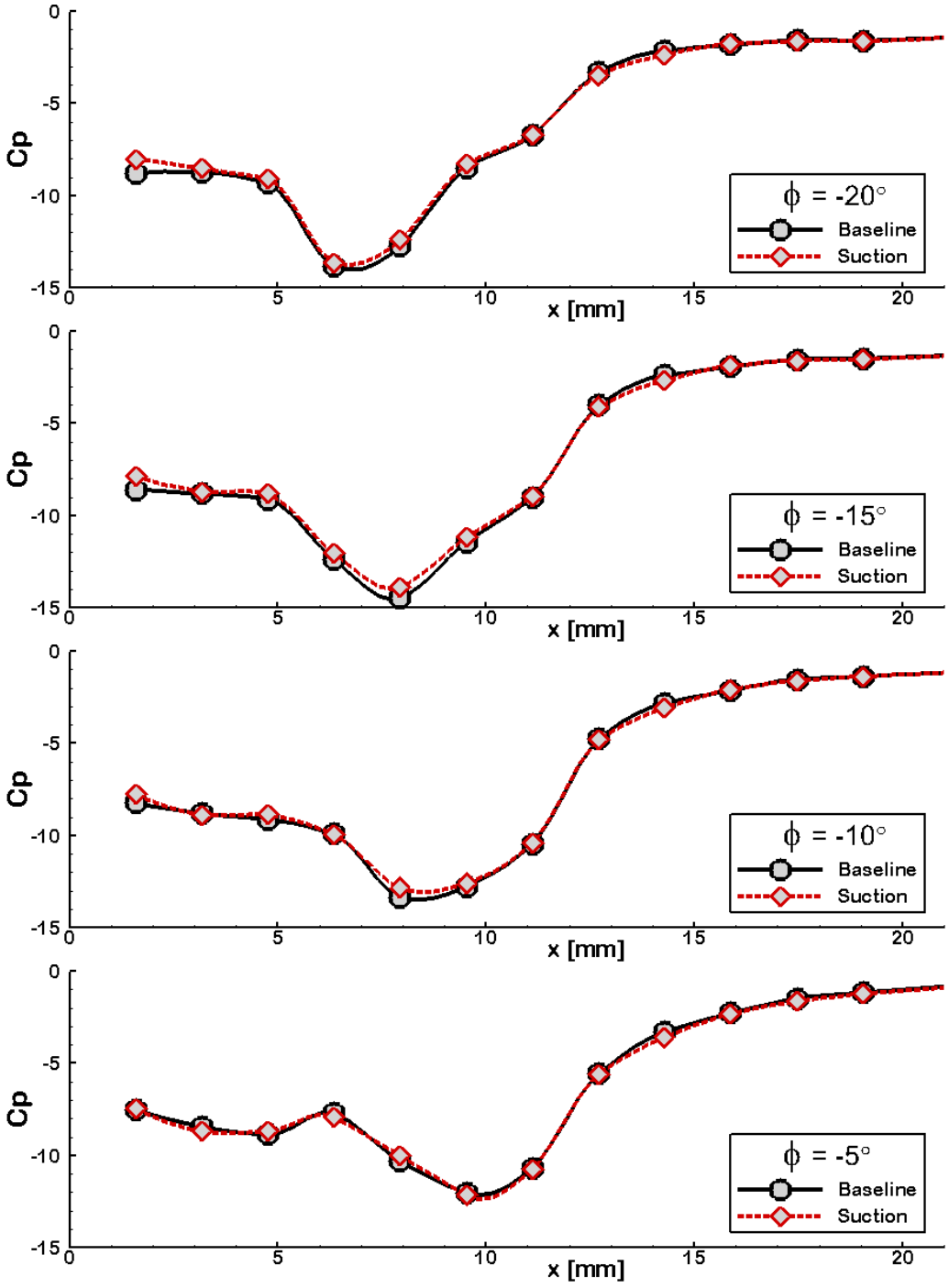

Figure 9.10: Comparison of the surface pressure distributions near the leading edge for select phases within the baseline and suction cases.

www.manaraa.com

the invariance of the average suction velocity seems to imply that the suction process is not greatly affected by the acceleration of the airfoil. A more promising characterization of the suction's effectiveness relates to the location of the LEV with respect to the suction port.

Within the pressure distributions shown in Figure 9.10, for phases prior to $\phi = 0°$, the suction peak produced by the LEV is seen to be situated either upstream or directly over the suction port (located at x = 9.525 mm). Similarly, Figure 9.8 shows the suction slot located within the APG downstream of the LEV. However, it can be inferred from both Figure 9.8l and Figure 9.10d that $\phi = -5°$ marks the point at which this primary suction-peak moves past the suction port, after which secondary vorticity begins to be removed from the flow. Despite the fact that the suction had always been applied beneath a region of secondary vorticity, these results indicate that the suction system employed within the current experiment is only capable of removing secondary vorticity when it is applied upstream of the primary suction-peak produced by the LEV. When the suction is applied downstream of the primary suction-peak, the unidentified three-dimensional effect proposed in the previous section acts to prevent a net change in the total circulation.

Figure 9.12 compares the pressure distributions of the two cases over Interval B2 and reveal some additional physics of the flow. Although the pressure at the leading edge remains constant between the two cases–which causes the diffusive flux to remain consistent as well–the suction finally begins to decrease the pressure around the point of application once it starts removing secondary vorticity. This forcing appears small at first, but Figure 9.12 shows it not only growing larger over time, but also extending further upstream. While the suction reduces the pressure beneath the primary suction-peak, Figures 9.12b-

www.manaraa.com

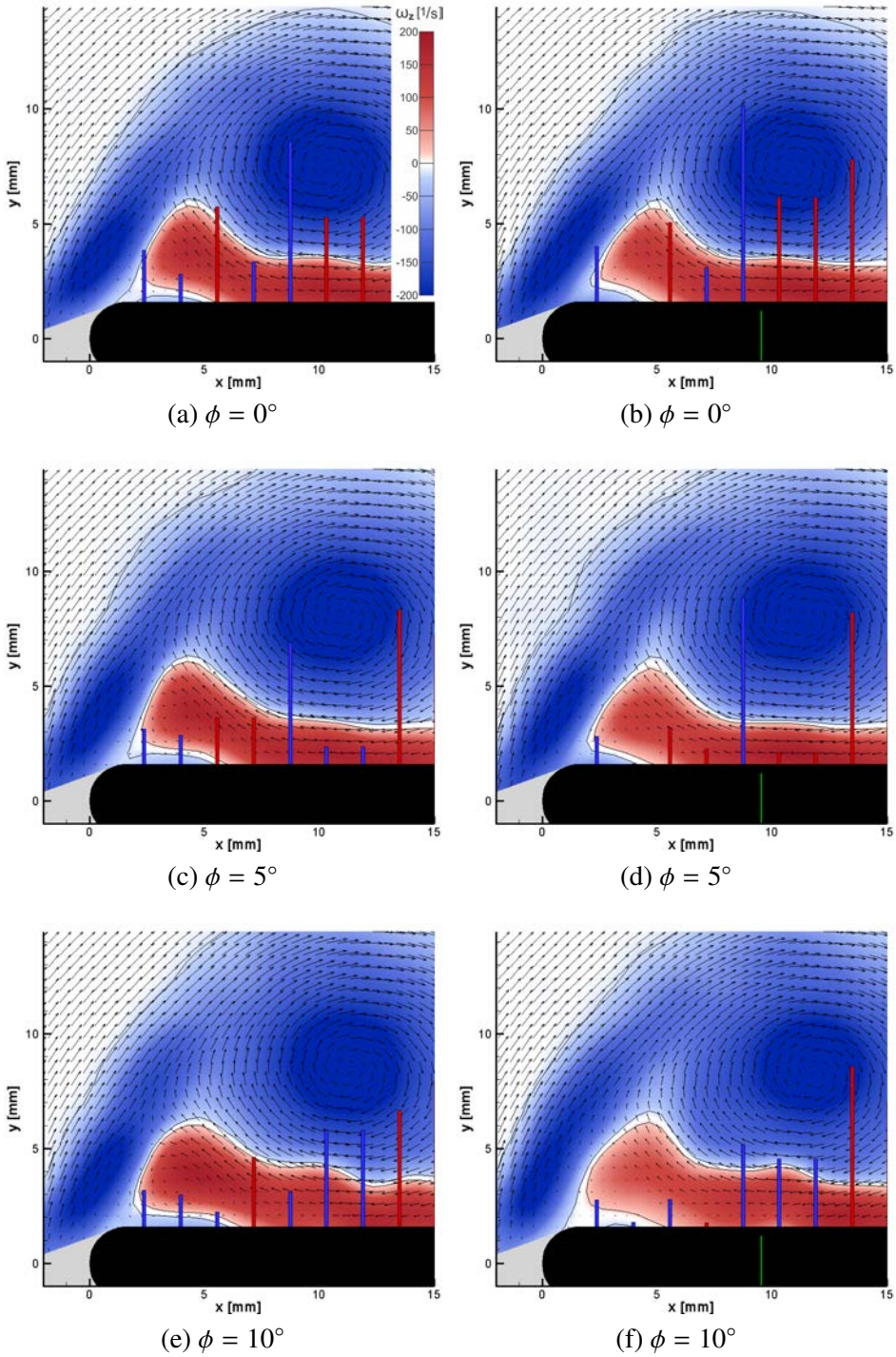

(a) $\phi = 0°$ (b) $\phi = 0°$

(c) $\phi = 5°$ (d) $\phi = 5°$

(e) $\phi = 10°$ (f) $\phi = 10°$

Figure 9.11: Evolution of the vorticity field from the baseline (left) and suction (right) cases during the suction's effective removal of secondary vorticity.

www.manaraa.com

9.12c show it to increase the pressures beneath the secondary suction-peak once the effects have propagated upstream. The net result of this process is an augmentation of the suction peak beneath the LEV and a simultaneous regression of the pressure distribution beneath the OSV back into a pressure plateau.

As discussed in Section 6.3, the initial formation of the OSV slows down the flow near the leading edge to create a region of separated flow. However, as the circulation of the OSV grows, it eventually reaches a point where it can roll up and create a secondary suction-peak. This OSV roll-up occurs at $\phi \approx -10^{\circ}$ for both the suction and baseline cases. By removing secondary vorticity from the flow, the suction is effectively reversing the roll-up of the OSV. In order to illustrate this process more clearly, Figure 9.13 presents a magnified view of the vorticity field near the leading edge for the baseline and suction cases both prior to (Figures 9.13a-9.13b) and after (Figures 9.13c-9.13d) the suction begins to remove secondary vorticity. The velocity vectors shown within Figures 9.13a-9.13b indicate that the OSV of the suction case is exhibiting a distinct, rotational behavior that is comparable to that of the baseline case at $\phi = -5^{\circ}$. However, by $\phi = 10^{\circ}$ enough secondary vorticity has been removed from the flow to significantly hinder the vortical-nature of the OSV; while the velocity vectors within Figure 9.13c depict a distinct rotation within the baseline OSV, the vectors shown within Figure 9.13d for the suction case are more reminiscent of an attached shear layer.

These results have two important implications for the model of the LEV formation that was laid out in Chapter 6. First, it provides additional validation of the correlation between the secondary suction-peak and the strength of a counter-rotating OSV, as revers-

www.manaraa.com

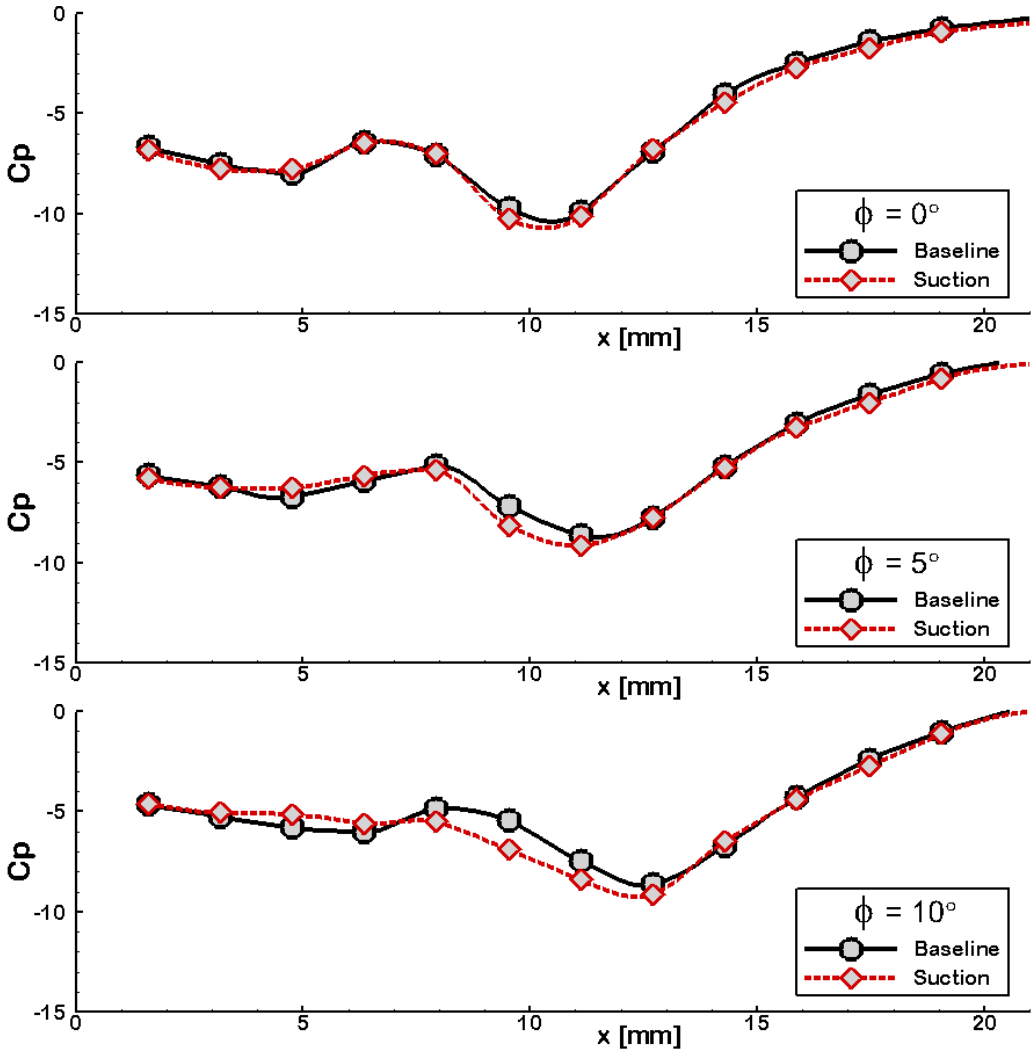

Figure 9.12: Comparison of the surface pressure distributions near the leading edge for select phases within the baseline and suction cases.

www.manaraa.com

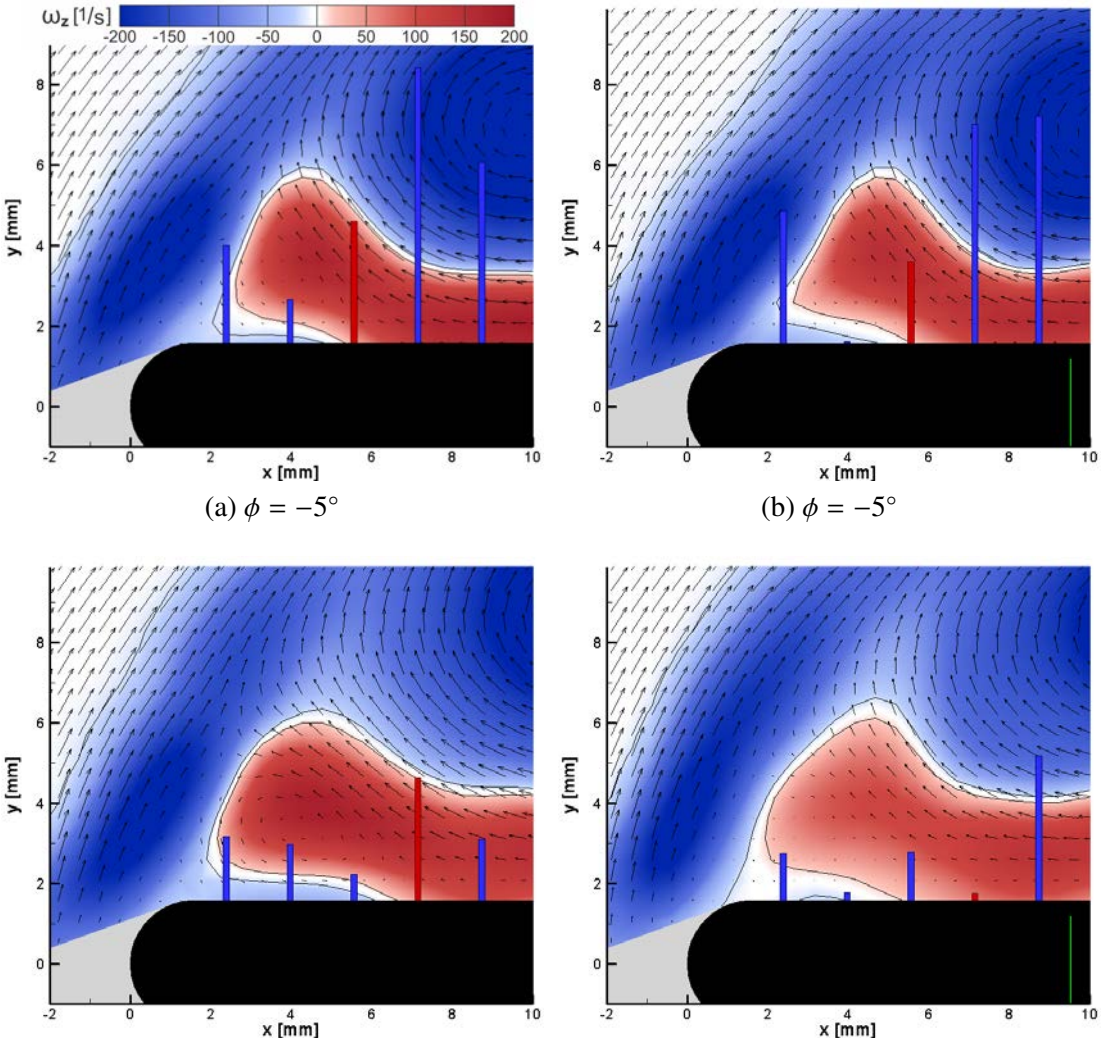

(a) $\phi = -5°$ (b) $\phi = -5°$

(c) $\phi = 10°$ (d) $\phi = 10°$

Figure 9.13: Comparison of the OSV within the baseline (left) and suction (right) cases both prior to and after the suction's removal of secondary vorticity.

www.manaraa.com

ing the roll-up of the OSV leads to the secondary suction-peak reverting into a pressure plateau. Secondly, it demonstrates that the dynamics of the secondary suction-peak are correlated to those of the primary suction-peak. The fact that the primary peak increases when the secondary peak is reduced indicates that removing secondary vorticity from the flow promotes the interaction between the LEV and the airfoil. Based on these results, the accumulation of secondary vorticity beneath the LEV can essentially be characterized as producing a "buffer" region between the LEV and the airfoil.

9.3.4 Phase Interval B3: $\phi = 15°$ to $\phi = 30°$

Figure 9.14b shows that by $\phi = 15°$ enough secondary vorticity has been removed from the flow to reestablish the single-suction-peak profile beneath the LEV. The total vorticity budget shown in Figure 9.2 indicates that once this has occurred, the suction stops removing vorticity from the flow and the circulation of the OSV once again begins to increase (see Figure 9.4c). Based on these results, it appears that suction applied at a steady state can only remove vorticity from the OSV if it has rolled-up. A possible explanation for this limitation is proposed next.

When the OSV has rolled-up, it essentially contains an excess amount of energy that can be removed via the suction. However, reconciling the reverse flow beneath the LEV and the inclined flow of the shear layer within a continuous vorticity field requires the presence of some finite amount of secondary vorticity. The OSV must therefore maintain a minimum circulation in order to satisfy the topology of the flow field. Once the OSV has been reverted to its low-energy, separated state, these topological restrictions would require

www.manaraa.com

any additional removal of secondary vorticity to be accompanied by a major reorientation of the entire flow field–presumably by means of a reattaching shear layer. While Figures 8.7c-8.7e from Section 8.3 show this process occurring within the finite-AR case, the inability for the suction to continue removing secondary vorticity from the flow after $\phi = 15°$ simply appears to be a matter of the suction system not being strong enough to force the reattachment of the shear layer and reverse the roll-up of the LEV.

Figure 9.12 depicts the suction effects propagating upstream from the suction port, in that the difference between the baseline and suction data upstream of the suction port grows larger with time. Figure 9.15 shows this variation in the pressure distributions reaches the leading edge at $\phi = 15°$–i.e. within Figure 9.15a (as well as the rest of Figure 9.15) there is a measurable difference between the leading-edge pressure of the two cases. As the leading-edge pressure governs the total diffusive flux through Boundary 4 of the control region, Figure 9.6 shows the diffusive flux once again begins to deviate from the baseline behavior after this point. While the implications are not clear, this reveals a characteristic trend within the data. The initial application of suction produced an almost instantaneous change within the leading-edge pressure, the magnitude of which decreased as the primary suction-peak approached the suction port. As the primary peak moved past the suction port, the leading-edge pressure reverted to its baseline behavior and the suction process began to remove secondary vorticity from the flow, thereby inciting changes within the local pressure distribution that slowly propagated towards the leading edge. When the effects of the suction were once again able to produce a change in the pressure at the leading edge, secondary vorticity stopped being removed from the flow. The distinct pattern

www.manaraa.com

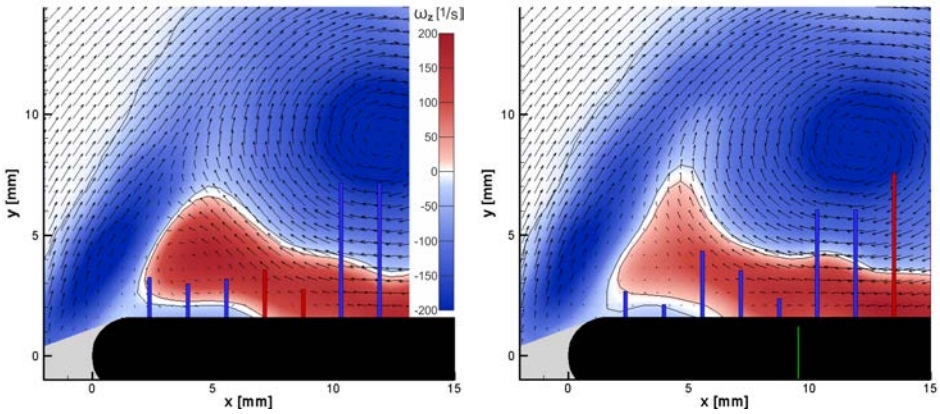

(a) $\phi = 15°$ (b) $\phi = 15°$

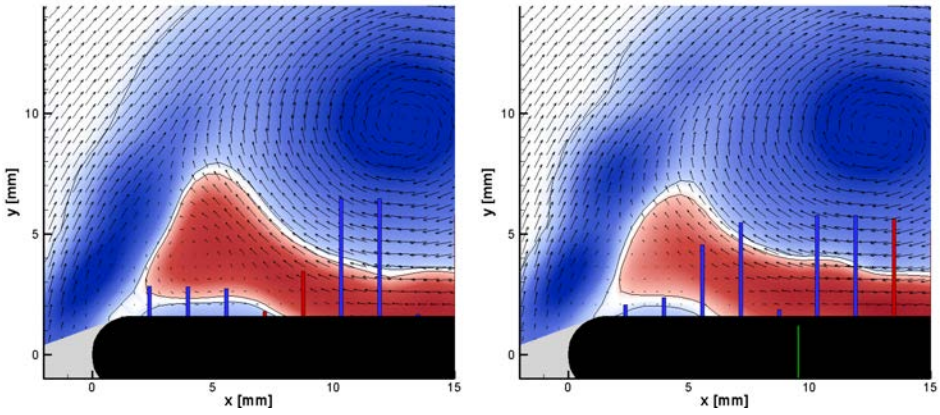

(c) $\phi = 20°$ (d) $\phi = 20°$

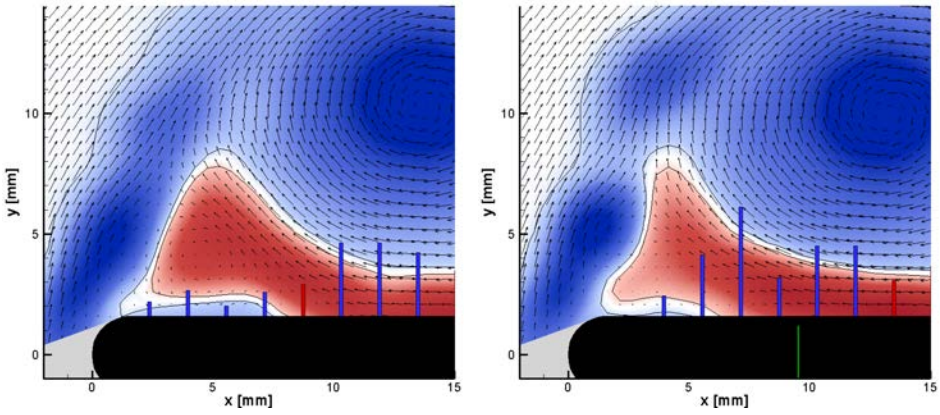

(e) $\phi = 25°$ (f) $\phi = 25°$

Figure 9.14: Evolution of the vorticity field from the baseline (left) and suction (right) cases after the suction's elimination of the secondary suction-peak.

www.manaraa.com

within this behavior seems to imply that the suction will not remove vorticity if it is able to alter the pressure at the leading edge.

It should be noted that even if the effectiveness of the suction is governed by its effect on the leading-edge pressure, it does not discount the earlier statement about the suction only being able to remove secondary vorticity if the OSV has rolled-up. This characterization still applies within the current example due to the fact that the effects from the suction are not able to propagate all the way to the leading edge so long as the OSV remains rolled-up.

Figure 9.15 makes it clear that weakening the OSV allows the LEV to induce more suction upon the surface of the airfoil. As per the discussion at the end of the previous section, this indicates that the presence of the OSV beneath the LEV essentially causes the secondary vorticity to act as a buffer region that weakens the interaction between the LEV and the surface of the airfoil, which has important aerodynamic implications.

The point was made within Section 6.4 that this dissertation has been the first to characterize the dynamics of the pressure plateau and subsequent secondary suction-peak that are produced by the OSV. As the specifics have never been addressed within the literature, one might be inclined to believe that by producing a secondary suction-peak out of the pressure plateau, the roll-up of the OSV would increase the total amount of suction on the surface of the airfoil and thereby increase the total lift. Indeed, Figure 9.15 does show the secondary suction-peak within the baseline data producing more suction near the leading edge than the pressure plateau observed within the suction case. However, these figures also indicate that any additional suction produced near the leading edge by the sec-

www.manaraa.com

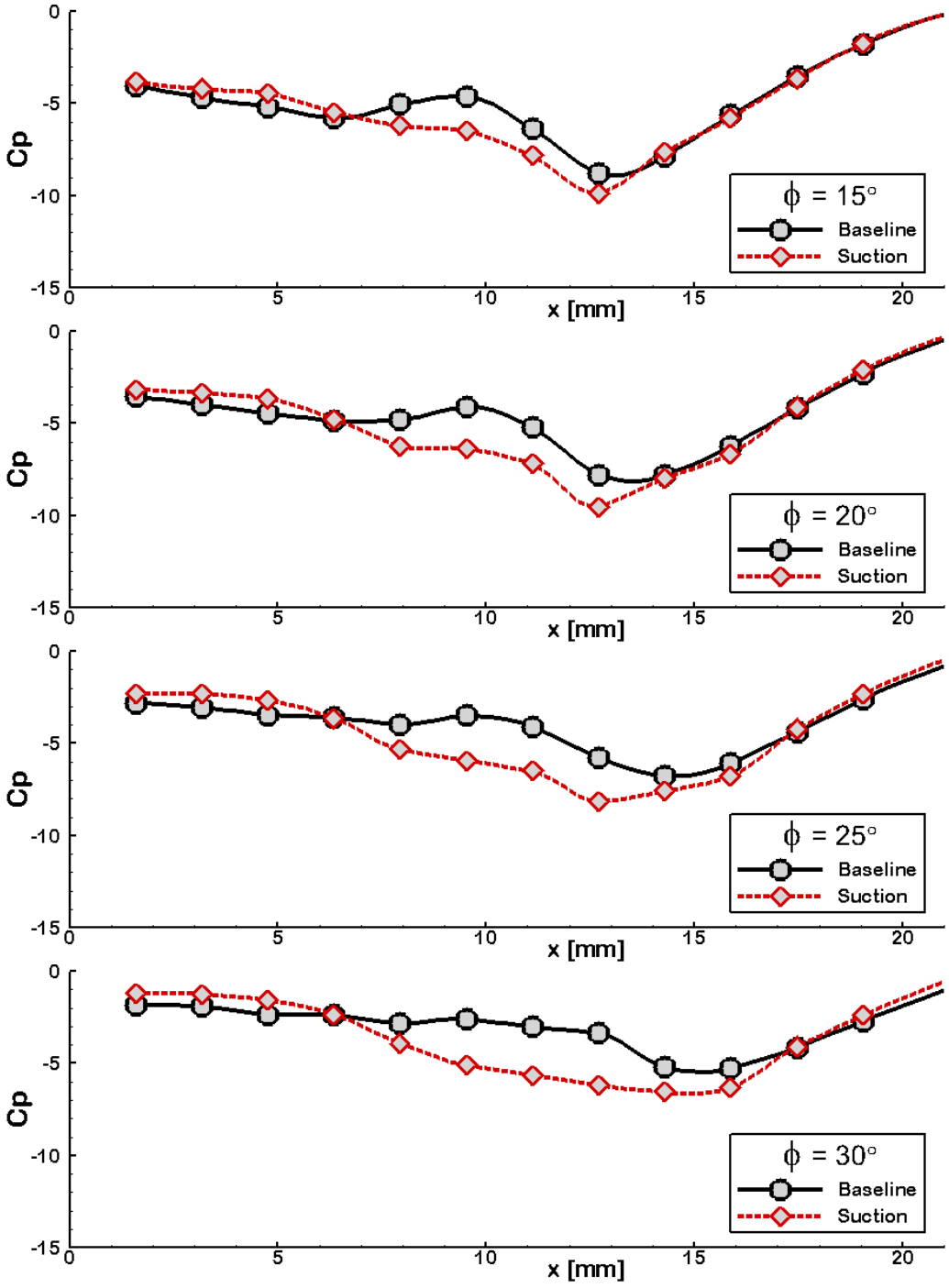

Figure 9.15: Comparison of the surface pressure distributions near the leading edge for select phases within the baseline and suction cases.

www.manaraa.com

ondary peak is far outweighed by a subsequent loss of suction within the primary peak. Put simply, while a counter-rotating OSV can induce lift upon the surface of the airfoil, the accumulation of secondary vorticity hinders the ability of the LEV to produce lift.

Figure 9.16a compares the lift data measured for the baseline and suction cases, and confirms that the total lift increases as the suction removes secondary vorticity from the flow. The same holds true for the data reported in Figure 9.16b, which compares the component of the lift that is acting on the suction side of the airfoil as a means of verifying the trends reported in Figure 9.16a. As per Chapter 7, this suction-lift was obtained through a chordwise integration of the pressure data from the suction side of the airfoil. The total uncertainty for the data plotted in Figures 9.16a and 9.16b is 0.0046 N and 0.0049 N respectively, which is approximately the width of the line being plotted in either figure. It is important to note that these results being reported within Figure 9.16 are also in agreement with the Kutta-Joukowski Lift Theorem, as they demonstrate that removing positive vorticity–and thus increasing the magnitude of the net circulation associated with the airfoil as per Figure 9.3a–leads to an increase in lift.

Although these results indicate that the roll-up of the OSV is detrimental to the total lift of the airfoil, the fact that the secondary peak does slightly augment the pressure at the leading edge implies that it will have a positive impact on the leading-edge suction term. Thus, while the removal of secondary vorticity enhances lift, the subsequent loss of leading-edge suction that occurs when the secondary suction-peak is reverted back into a pressure plateau is expected to decrease the thrust. Figure 9.17 compares the thrust data measured for the baseline and suction cases and indeed shows that eliminating the secondary suction-

www.manaraa.com

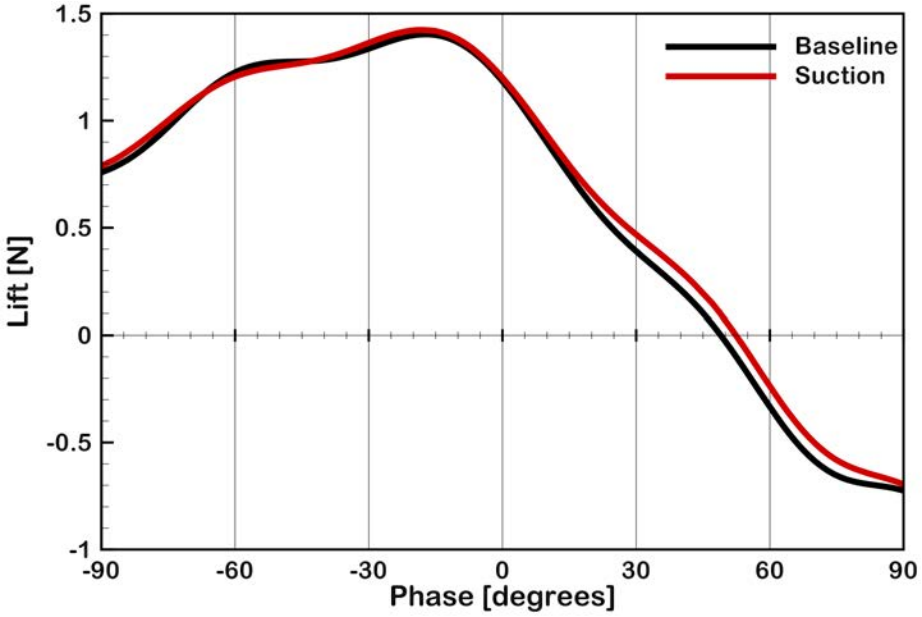

(a) Lift

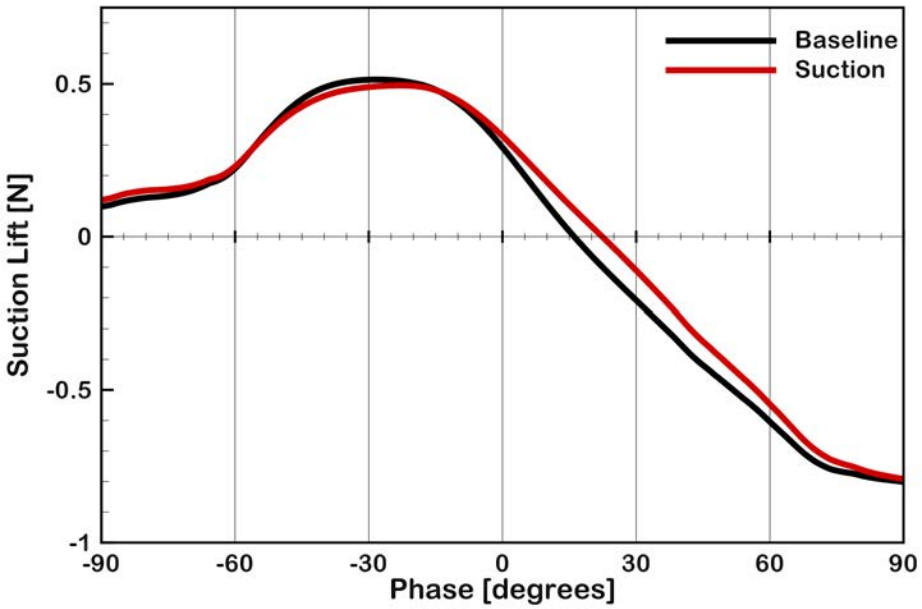

(b) Suction-Lift

Figure 9.16: Comparison of (*a*) the lift measurements from the baseline (black) and suction (red) cases (total uncertainty = 0.0046 N), as well as (*b*) the pressure-integrated lift from the suction side of the airfoil (total uncertainty = 0.0049 N). Total uncertainty within either plot can be approximated by the width of the line.

www.manaraa.com

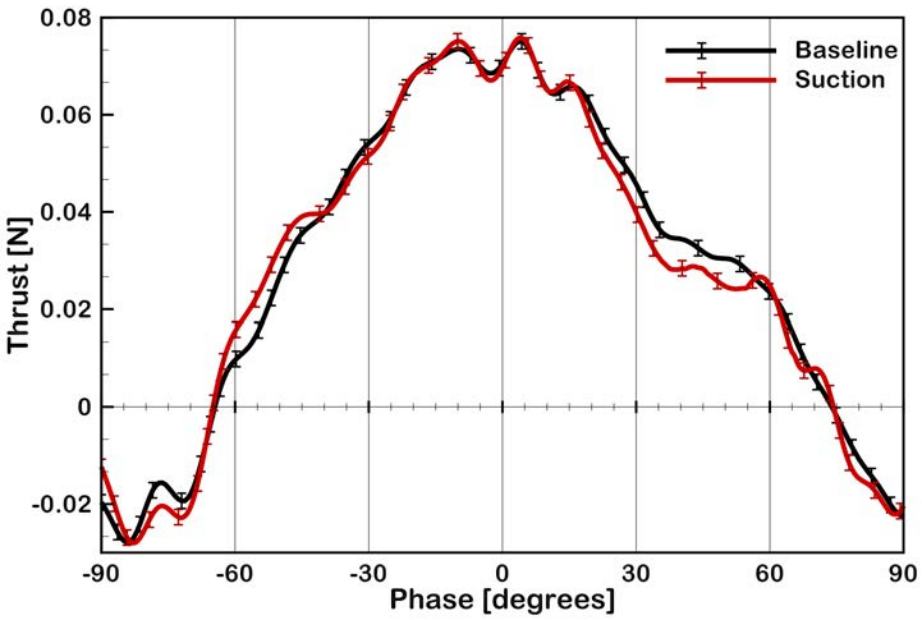

Figure 9.17: Comparison of the thrust measurements from the baseline (black) and suction (red) cases (total uncertainty due to random errors = 0.0016 N). Error bars depicting this total uncertainty are plotted for both data sets.

peak at $\phi = 15°$ results in a loss of thrust within the suction case.

Although the total uncertainty of the thrust data plotted in Figure 9.17 was calculated to be 0.0046 N, this value included systematic errors as well as random errors. Since the main purpose of Figure 9.17 is to compare the thrust data between the two cases–which was measured using the exact same experimental setup–it would be more appropriate to only consider the random errors. Calculating the total uncertainty based solely on the random errors within the data yields a value of 0.0016 Newtons; this value is indicated within the figure via error bars. It should be noted that the deviation in the thrust data of the two cases that occurs between $\phi = 15°$ and $\phi \approx 60°$ can in fact be resolved within the

www.manaraa.com

uncertainty of the data.

While most of the discussion within this section has focused on the interaction between the vorticity field and the surface of the airfoil, there are some pertinent dynamics within the bulk flow as well. When it was first presented in Section 9.2, one of the most prominent variations that was seen within the flow field of the suction case was the delayed advection of the LEV. In order to establish when and how this delay was affected, the Γ_1 criterion developed by Graftieaux et al. [41] was used to identify and track the core of the LEV within the baseline and suction cases. Figure 9.18 plots the x-coordinates of these cores throughout the downstroke and shows the streamwise location of the two structures beginning to diverge after $\phi = 15°$. These results seem to indicate that the roll-up of the OSV enhances the advection of the LEV.

In addition to modifying the dynamics of the LEV, weakening the OSV also appears to have an effect on the shear layer. Many studies have sought to establish the relevance of the OSV based on its interaction with the shear layer [1, 33, 92, 85, 115], and the most well-regarded characterization was introduced by Acharya and Metwally [1], who postulated that the detachment of the LEV would occur once the OSV became strong enough to cut through the shear layer. However, both Wojcik and Buchholz [118] and Eslam Panah et al. [85] have found evidence that this process is not a distinct eruption of secondary vorticity through the shear layer, but rather a gradual entrainment of blobs of secondary vorticity into the shear layer after they have broken off of the OSV. Evidence of this modified interpretation can be seen in the phase-averaged representation of the flow field shown in Figures 9.14a-9.14b. In the baseline example, Figure 9.14a illustrates how the region of

www.manaraa.com

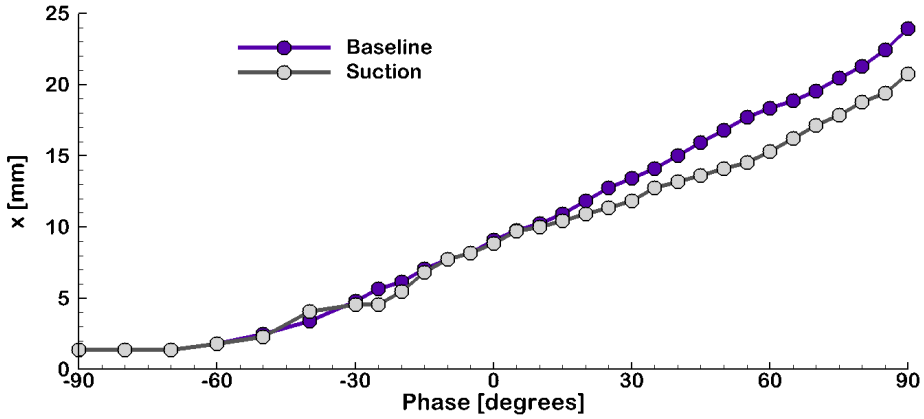

Figure 9.18: Position of the LEV core from the baseline (purple) and suction (gray) cases.

negative vorticity that connects the shear layer and LEV appears to be significantly weakened in the presence of a strong OSV. On the other hand, because weakening the OSV would cause less secondary vorticity to be entrained, Figure 9.14b shows this region to be much stronger in the suction case.

9.3.5 Phase Interval C: $\phi = 30°$ to $\phi = 90°$

In Section 5.3.3, the detachment of the LEV was observed to coincide with the formation of a small FPG at the leading edge of the airfoil that appeared to be correlated to the formation of a tertiary vortex (TrV)–i.e. a small region of negative vorticity directly downstream of the leading edge that is constrained beneath the OSV. Figure 9.6 shows that the temporary drop in the diffusive flux between $\phi \approx 35°$ and $\phi \approx 65°$ that characterizes this process has become much more pronounced within the suction case. But in spite of this variation in magnitude, these features within the baseline and suction dataset are approximately in phase with each other, although it does appear to be slightly advanced

www.manaraa.com

within the suction case. While Figures 9.14a-9.14b within the previous section illustrated how reducing the circulation of the OSV leads to less entrainment of secondary vorticity within the shear layer, the similar detachment intervals that Figure 9.6 reveals within the diffusive flux suggest that this interaction between the OSV and the shear layer does not have a substantial impact on the detachment of the LEV.

The vorticity fields associated with this detachment process are summarized within Figure 9.19, and they do indeed confirm that the FPG formed at the leading edge has been exacerbated within the suction case, thereby accounting for the larger drop in the diffusive flux. When the detachment of the LEV within the baseline case was discussed within Section 5.3.3, it was noted that the local minimum within the diffusive flux coincided with the time at which the tertiary vortex (TrV) was able to connect with the shear layer at the leading edge. More importantly, it was shown that the shear layer detached from the LEV and began to rotate down towards the surface of the airfoil once this connection occurred. As this process was concomitant with the loss of the FPG at the leading edge, it was hypothesized that the TrV plays an important role in the detachment of the LEV by promoting the reattachment of the shear layer. This idea appears to be well-applied within the suction case as well.

Figures 9.19a-9.19b depict similar regions of negative vorticity developing beneath the OSV, and Figures 9.19c-9.19d show these features continue to remain similar as they extend upstream and eventually coalesce with the shear layer. So as to better explicate the process of the TrV extending towards the leading edge and connecting with the shear layer, Figure 9.20 presents a magnified view of the vorticity fields measured near the leading

www.manaraa.com

edge between $\phi = 40°$ and $\phi = 50°$. While the pertinent measurements are located near the wall–and thus have diminished accuracy–Figure 9.20 does illustrate how the process of the TrV connecting to the shear layer appears to be slightly advanced in time within the suction case, thus accounting for the local minimum seen at $\phi \approx 50°$ within Figure 9.6 for the diffusive flux of the suction case as occurring slightly before that of the baseline case.

Because both the strength of the OSV and the amount of secondary vorticity being entrained into the shear layer vary between the two cases, it is unlikely that either of them directly impact on the detachment process–which is seen to be approximately the same for both cases. As the dynamics of the tertiary vortex–and its eventual connection to the shear layer–were also observed to also remain fairly consistent between the two cases, its correlation to the detachment of the LEV from the shear layer appears to be much more relevant. Because it seems improbable that the TrV would actually cause the detachment of the LEV, it is likely that the dynamics observed within the TrV stem from another, unidentified mechanism within the flow (e.g. the lifting of the secondary vortex from the surface) that actually governs the detachment of the LEV.

Once the shear layer has detached from the LEV and it begins to rotate down towards the surface of the airfoil, the stronger FPG that Figure 9.19f shows at the leading edge of the suction case enhances the reattachment of the shear layer, drawing it closer to the surface of the airfoil than its baseline counterpart. This difference may be small within Figures 9.19e-9.19f, but Figure 9.21 shows how enhancing the reattachment of the shear layer prevents it from rolling up into a discrete structure upstream of the LEV. It should be noted that within the literature, this structure that develops out of the shear layer is some-

www.manaraa.com

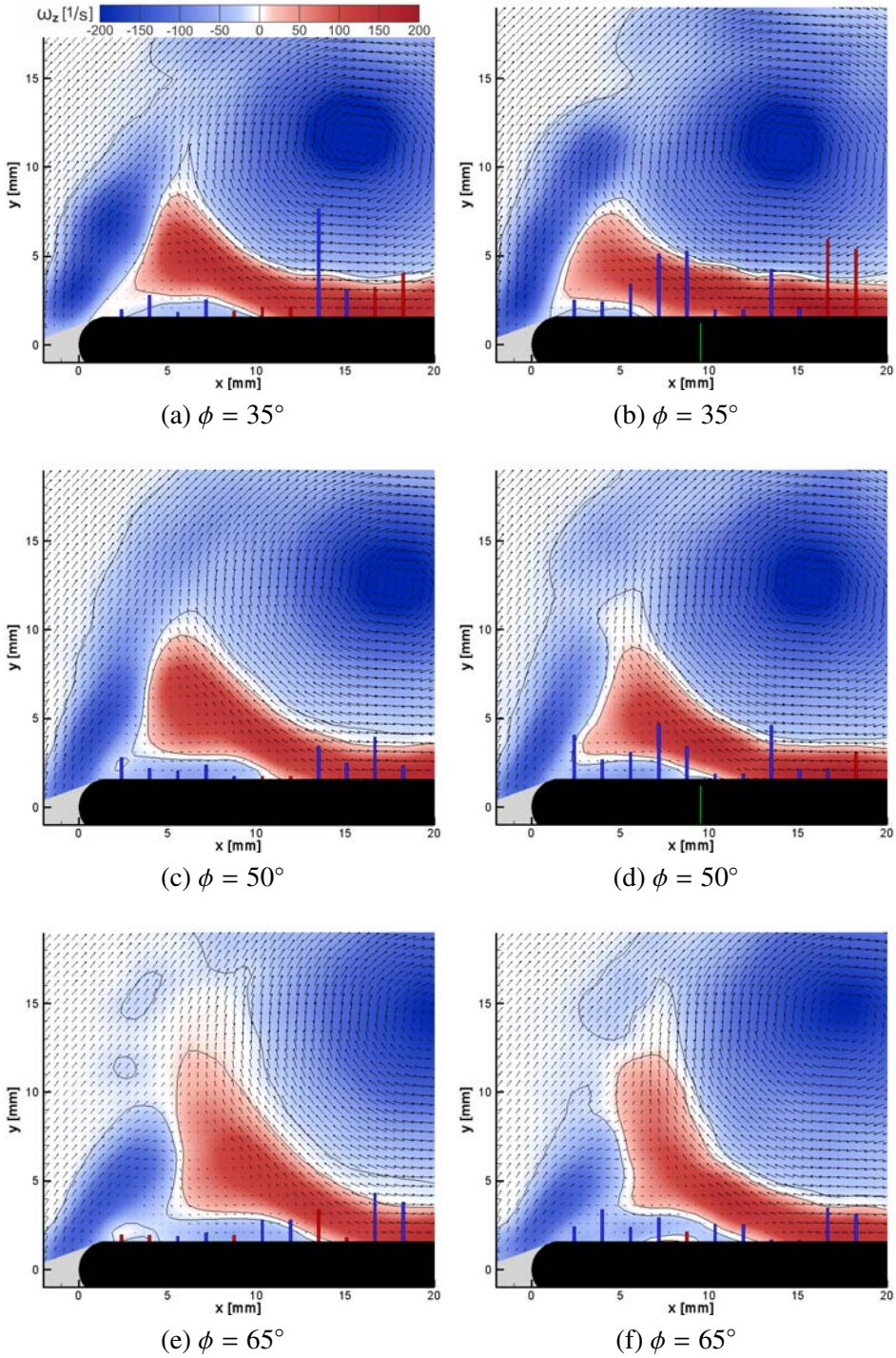

(a) $\phi = 35°$ (b) $\phi = 35°$

(c) $\phi = 50°$ (d) $\phi = 50°$

(e) $\phi = 65°$ (f) $\phi = 65°$

Figure 9.19: Evolution of the vorticity field from the baseline (left) and suction (right) cases during the detachment of the LEV.

www.manaraa.com

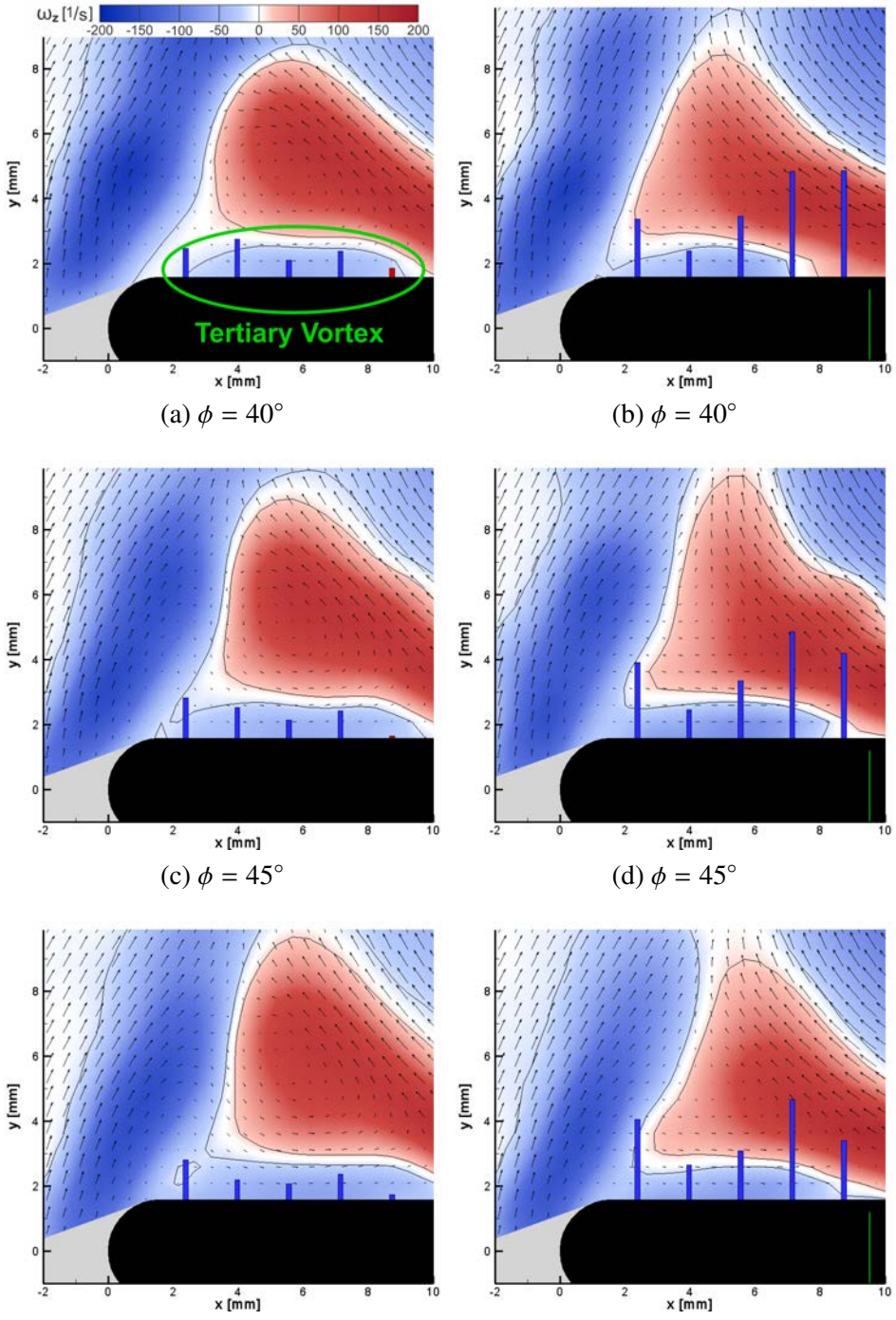

(a) $\phi = 40°$ (b) $\phi = 40°$

(c) $\phi = 45°$ (d) $\phi = 45°$

(e) $\phi = 50°$ (f) $\phi = 50°$

Figure 9.20: Evolution of the tertiary vortex in the baseline (left) and suction (right) cases.

www.manaraa.com

times referred to as the "tertiary vortex"; however, in order to continue with the terminology defined within this dissertation, this structure will be referred to as the Shear-Layer Vortex (SLV). For consistency purposes, the structure that is formed by the shear layer coalescing with the tertiary vortex within the suction case will also be denoted as an SLV.

The small size of the SLV generally causes it to be neglected, yet Akkala [3] showed that its presence within the flow can help to prevent the OSV from circumnavigating the leading edge. The results obtained in this experiment also illustrate this phenomenon. The vorticity fields obtained during the beginning of the upstroke are displayed in Figure 9.22 for the two cases. While the SLV that is present in Figure 9.22a has disappeared by Figure 9.22c, its presence near the leading edge has already helped to prevent the OSV from attaching to the shear layer that is feeding the LEV on the underside of the airfoil by inducing a velocity up and away from the leading edge. Conversely, the SLV of the suction case has endured a greater degree of reattachment, causing it to become a less effective barrier to the OSV. As such, Figures 9.22d and 9.22f show the OSV spreading upstream and closer to the surface of the airfoil within the suction case.

While the OSV of the suction case does not circumnavigate the leading edge–which is typically seen once the OSV forms a strong connection with the underside shear layer [3]–modifying the orientation of the OSV with respect to the LEV enhances the upstream component of the dipole made between the two structures. Figure 9.23 plots the stream-wise location of the LEV core through the entire plunge cycle and shows that much of the delayed LEV advection within the suction case is affected during the upstroke. Because the dynamics of the LEV become relatively independent of the airfoil once it has detached

www.manaraa.com

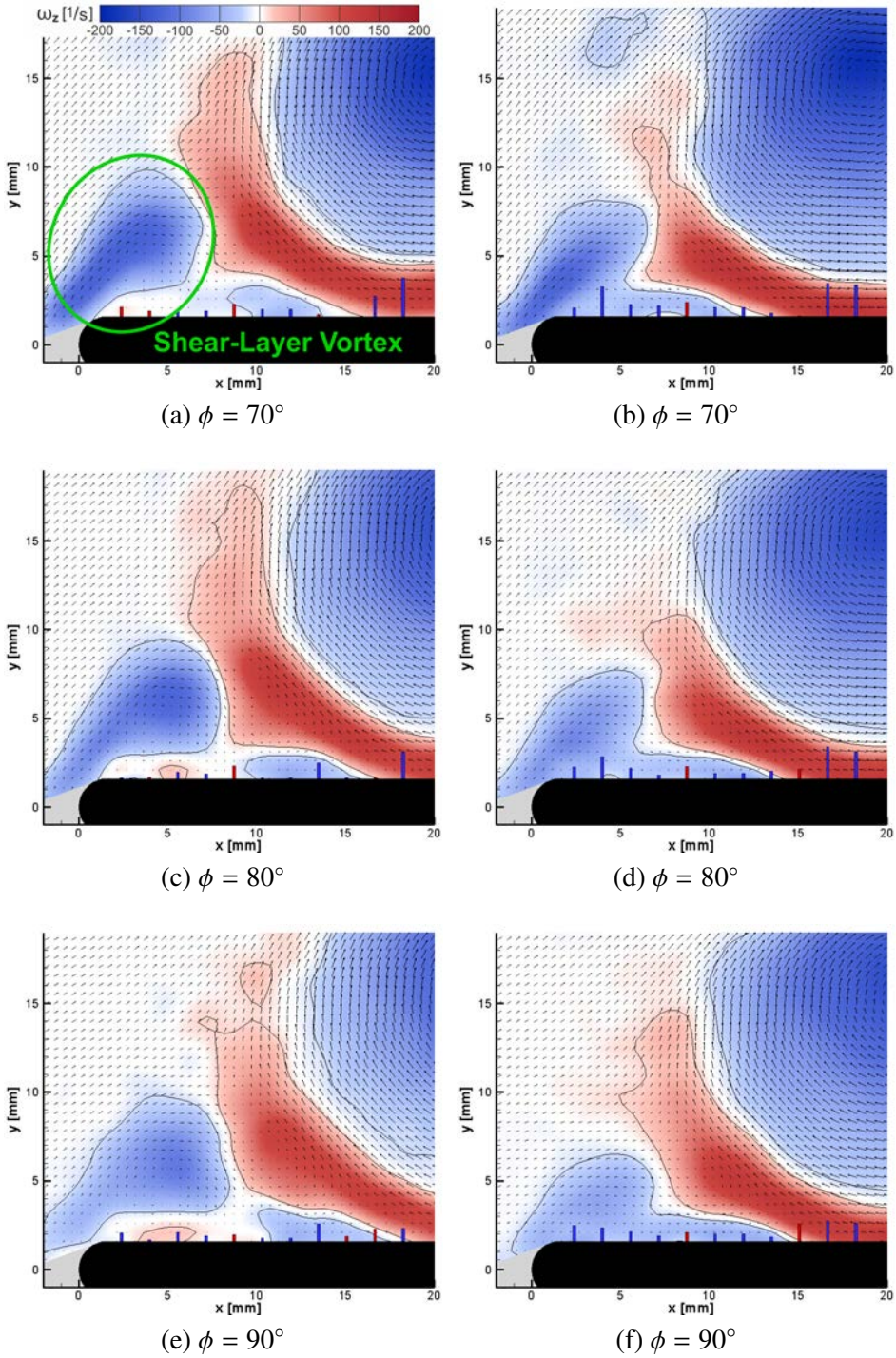

(a) $\phi = 70°$ (b) $\phi = 70°$

(c) $\phi = 80°$ (d) $\phi = 80°$

(e) $\phi = 90°$ (f) $\phi = 90°$

Figure 9.21: Evolution of the vorticity field from the baseline (left) and suction (right) cases after the detachment of the LEV.

www.manaraa.com

[96, 63], realigning the LEV-OSV dipole can be understood to be the primary source of the delayed LEV advection during the upstroke.

9.3.6 Summary

The primary motivation for the suction experiment was to examine how removing secondary vorticity from the flow would modify the evolution of the LEV. While this primary goal was achieved, the effectiveness of the suction was limited by topological constraints. However, when the suction was able to remove secondary vorticity, it did so without modifying the circulation of the LEV so that the total circulation of the flow was increased. Based on the vorticity budget shown in Figure 9.2, the suction was only able to remove secondary vorticity from the flow if the pressure at the leading edge of the airfoil was not forced from its baseline value. A concise summary of this process is as follows:

- No vorticity was removed if the suction was applied downstream of the pressure minimum created by the LEV. However, doing so resulted in an immediate loss of suction at the leading edge, the magnitude of which decreased as the suction was applied closer to the pressure minimum.

- Secondary vorticity was removed when the suction was applied upstream of the pressure minimum beneath an OSV that had rolled-up. However, this led to the modification of the local pressure distribution, the effects of which slowly propagated upstream.

- No vorticity was removed after the OSV was reverted to its minimum-energy state, as the topology of the flow required a finite amount of circulation be maintained within the OSV. This limit was reached once the effects from the suction propagated all the way

www.manaraa.com

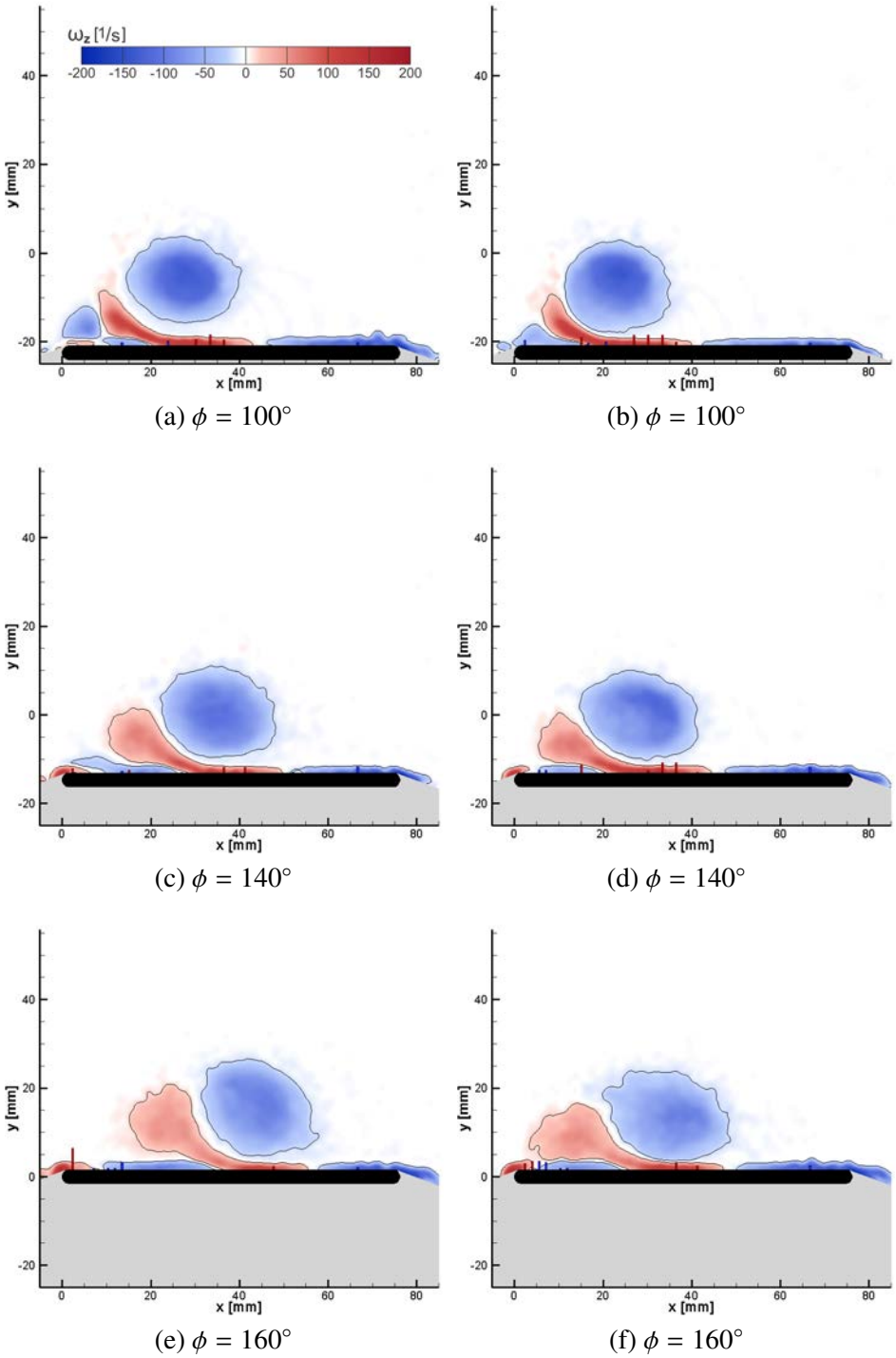

(a) $\phi = 100°$ (b) $\phi = 100°$

(c) $\phi = 140°$ (d) $\phi = 140°$

(e) $\phi = 160°$ (f) $\phi = 160°$

Figure 9.22: Evolution of the vorticity field from the baseline (left) and suction (right) cases during the upstoke.

www.manaraa.com

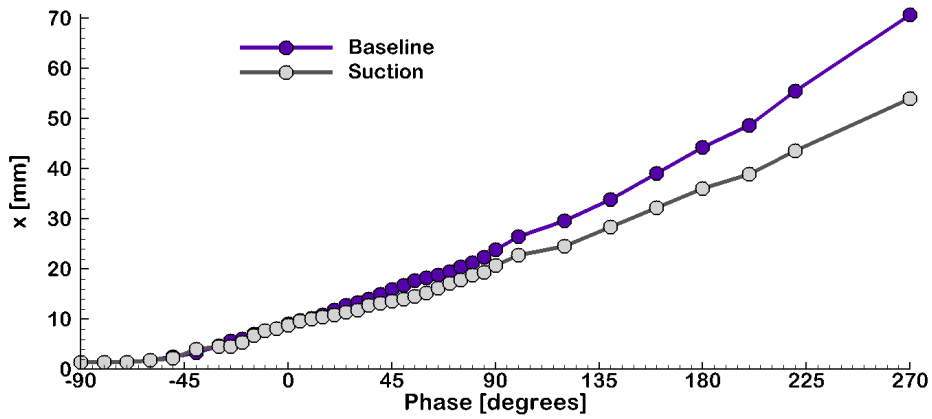

Figure 9.23: Position of the LEV core from the baseline (purple) and suction (gray) cases.

to the leading edge, causing the secondary suction-peak to be reverted into a pressure plateau.

Within the experiment that was performed, the application of suction was effectively able to reverse the roll-up of the OSV and revert the counter-rotating flow at the leading edge into a low-energy region of separated flow. It was found that turning the secondary suction-peak back into a pressure plateau reduced the amount of suction near the leading edge. However, any additional suction that the counter-rotating OSV produced at the leading edge was far outweighed by the reduction it caused within the primary suction-peak beneath the LEV. As characterized by these two effects, it was shown that the roll-up of the OSV leads to a loss of lift but an increase in thrust. In addition to these aerodynamic implications, reversing the roll-up of the OSV caused the dynamics within the flow of the suction case to experience a distinct departure from the baseline behavior. Most importantly, the trajectory of the LEV core showed that reversing the roll-up of the OSV caused the LEV to advect slower. Furthermore, weakening the OSV was found to strengthen the portion of

www.manaraa.com

the shear layer that connects to the LEV, presumably because it decreases the amount of secondary vorticity that becomes entrained by the shear layer. However, the variation in this entrainment was observed not to have an effect on the detachment process.

While removing secondary vorticity from the OSV allowed for the alteration of the surface pressure distribution, the associated diffusive flux was not seen to have a pronounced effect on the flow field. This is primarily because of the fact that any reduction in the diffusive flux after $\phi = 15^\circ$ was similarly imposed upon the shear-layer flux so that the total flux of vorticity did not vary from the baseline example. However, once the shear layer detached from the LEV, the enhanced FPG that the suction produced at the leading edge of the airfoil was observed to promote the reattachment of the shear layer so that it rotated down closer to the surface of the airfoil. This is a prominent result in itself, as the reattachment of a leading-edge shear layer is one of the preeminent objectives for the application of flow control [56, 128]. Additionally, within the current example, the degree to which the shear layer reattaches was observed to play a substantial role within the evolution of the flow, in that it altered the streamwise position of the OSV. This was found to modify the orientation of the LEV-OSV dipole so as to significantly delay their advection during the upstroke.

www.manaraa.com

CHAPTER 10
CONCLUSIONS AND FUTURE WORK

10.1 Conclusions

Analysis of a nominally two-dimensional, pure-plunging of the AR4 airfoil within Chapter 5 served to characterize the baseline behavior of the vorticity transport associated with the development of a leading-edge vortex. After characterizing the vorticity budget of the LEV, the growth of the structure was observed to be governed by two dominant sources of vorticity. The shear-layer flux was identified as the larger source, and its dynamics appeared to be governed by the plunge velocity. However, the total circulation of the flow was substantially reduced by the diffusive flux of vorticity emanating from the surface of the airfoil beneath the LEV.

It was further shown within Sections 5.3.1-5.3.3 that the trends within the diffusive flux correlated very well with the evolution of the flow field. Specifically, the diffusive flux experienced a major increase during the phase interval in which the LEV remained attached to the downstream boundary layer. Once the LEV rolled-up and the OSV began to form, the magnitude of the diffusive flux leveled off. The detachment of the LEV was also observed to be concomitant with a temporary drop in the diffusive flux, which was correlated to the formation of a tertiary vortex near the leading edge. In accordance with the limited amount of literature [96, 63], these results suggest that the diffusive flux of vorticity plays a significant role in the development of the LEV.

Within Chapter 6, the on-wall pressure-signature of the vorticity field was used to

www.manaraa.com

further characterize the evolution of the flow. Using this method of analysis, it was shown that the reattachment of the LEV to the downstream boundary layer caused the diffusive flux of vorticity to be affected as a sink of negative vorticity, which served to cross-cancel the negative vorticity within the reattachment region. Furthermore, it was demonstrated that once all of the vorticity within the reattachment region had been cross-canceled, the LEV would roll up and positive vorticity would begin to be diffused into the flow.

Upon the roll-up of the LEV, the initial appearance of a wall-bounded opposite-signed vortex was observed to form of a pocket of separated flow between the shear layer and the LEV, thereby producing a pressure plateau upstream of the primary suction-peak. This pressure plateau was observed to prevent the LEV from imposing any additional suction on the leading edge, thus identifying why the diffusive flux of vorticity stopped increasing once the LEV rolls-up. It was therefore discerned that–at least within the current example–the diffusive flux of vorticity produced by the interaction between the LEV and the airfoil can only be increased if it is affected as a sink of negative vorticity.

It was also demonstrated within Chapter 6 that when the opposite-signed vortex rolled-up, it caused the pressure plateau to deform into a secondary suction-peak. For the experiments performed within this dissertation, it was noted that the formation of this secondary suction-peak was concomitant with a reduction of the primary suction-peak, marking the beginning of the detachment of the LEV from the surface of the airfoil.

In Chapter 8, the three-dimensional flow field of a plunging flat-plate airfoil with aspect-ratio 2 was studied. Vorticity flux analyses were performed at three different spanwise locations of the airfoil, and the associated vorticity field of these planes were reviewed

www.manaraa.com

in parallel with surface pressure measurements. Examination of the 81.25-percent spanwise location lead to the identification of an LEV that was never observed to roll up. Through a comparison of this data to that obtained at the 68.75- and 75-percent spanwise locations, it was determined that an additional source of negative vorticity–via a spanwise convective flux–within the reattachment region of the 81.25-percent span prevented the roll-up of the LEV. This served to validate the results from Chapter 6, as it demonstrated that the roll-up of the LEV–and appearance of the OSV–was governed by the local vorticity balance within the reattachment region.

In Chapter 9, a nominally two-dimensional, plunging flat-plate airfoil was once again studied, but this time suction ports on the surface of the airfoil were used to alter the circulation of the OSV by removing vorticity-carrying fluid particles. While the suction system being employed was unable to prevent the detachment of the LEV, enough secondary vorticity was removed from the flow to eliminate the secondary suction-peak and cause the OSV to be reverted into a wall-bounded shear layer. While this was observed to reduce the amount of suction imposed right at the leading edge, it also caused a measurable increase in the magnitude of the primary suction-peak. In accordance with these results, lift and thrust data were used to confirm that the roll-up of the OSV enhances thrust but leads to a loss of lift.

In addition to characterizing this aerodynamic effect, modifying the strength of the OSV was seen to affect the evolution of the LEV. While modifying the strength of the OSV did not significantly alter the detachment of the LEV, the enhanced FPG that the suction produced at the leading edge of the airfoil was observed to promote the reattachment of the

www.manaraa.com

shear layer once it detached from the LEV so that it rotated down closer to the surface of the airfoil. Within the current example, the degree to which the shear layer reattaches was observed to play an important role within the evolution of the flow, in that it altered the streamwise position of the OSV. This was found to modify the orientation of the LEV-OSV dipole so as to significantly delay their advection during the upstroke.

10.2 Future Work

Throughout this dissertation, the appearance of secondary vorticity beneath the LEV has been characterized as being detrimental to the production of lift due to the fact that it hinders the amount of suction that the LEV can impose on the surface of the airfoil. It is therefore understood that flow control strategies aimed at maximizing lift should be developed with the intent of eliminating the OSV and reattaching the LEV to the downstream boundary layer.

Attempts were made within Chapter 9 to remove secondary vorticity from the flow, but the suction was unable to completely eliminate the OSV. Furthermore, because the suction was only observed to remove vorticity from the flow when it was applied upstream of the LEV, the effective removal of secondary vorticity was not seen until after both the LEV and OSV had rolled-up. The results presented in Chapter 8 demonstrated that forcing the flow in a manner that prevents the roll-up of the LEV–as opposed to "restabilizing" the LEV after it has already rolled-up–is much more effective in augmenting the magnitude of the primary suction-peak. Thus, even if the suction applied within Chapter 9 had been able to completely eliminate the OSV, the aerodynamic benefits may not have been as

www.manaraa.com

impressive as if the roll-up had been prevented in the first place.

Based on these results, the first proposal for future work would be to perform additional suction experiments with the suction ports oriented closer to the leading edge so that flow control attempts could be made earlier in the evolution of the LEV. It is anticipated that by altering the position of these ports, the suction would be able to remove secondary vorticity from the flow as soon as it is diffused from the surface. The goal of this process would be to hinder the formation of the pressure plateau at the leading edge by preventing any secondary vorticity from accumulating within the flow and hopefully delaying the roll-up of the LEV.

While the method of flow control that was utilized within the suction case is based on the removal of secondary vorticity from the flow, Chapters 6 and 8 have indicated that a reattaching LEV can be maintained by providing an additional source of negative vorticity within the reattachment region. It is therefore proposed that rather than using sinks of positive vorticity to alter the roll-up process of the LEV, future work should also attempt to utilize sources of negative vorticity to prevent the roll-up of the LEV altogether.

Although generating a source of negative vorticity may be more difficult than producing a sink of positive vorticity, a variety of techniques for affecting sources of negative vorticity have been developed within dynamic stall studies, including: wall-normal jet actuation [39, 40, 45], spanwise blowing [21, 119] and rotating cylinders in airfoils [75, 5, 134]. When applied under the right conditions, each of these techniques has been shown to enhance lift by reducing the length of–and thereby stabilizing–the laminar separation bubble. As the work presented within this dissertation has indicated that the bursting of an LSB and

www.manaraa.com

the roll-up of an LEV appear to be governed by the same physics, it seems likely that the success of these flow control techniques within dynamic stall studies could be reproduced at lower Reynolds numbers within studies that consider a distinct leading-edge vortex.

Based on the impressive "restabilization" that was observed within Chapter 8 for the AR2 case, spanwise blowing might be one of the most effective ways to delay the roll-up of the LEV. This would also be the most intuitive next step of the present study, as it could by implemented by modifying the suction ports so that they were angled towards the spanwise centerline of the airfoil and then affecting a positive gauge pressure within the vacuum tank of the suction system–so as to produce a pressure reservoir rather than a suction reservoir–that would allow the system to produce a blowing effect at the surface of the airfoil. The end goal of these experiments would be to use this spanwise blowing to create an additional source of negative vorticity within the reattachment region of the LEV by essentially "pushing" more negative vorticity towards the mid-span of the airfoil, thus prolonging its reattachment to the downstream boundary layer.

www.manaraa.com

APPENDIX
UNCERTAINTY ANALYSIS

This Appendix provides an analysis that serves to quantify the uncertainties within the vorticity transport mechanism from Equation 5.1, the approach for which follows a technique developed by Wojcik [116]. In order to determine an appropriate estimate of the (maximum) uncertainty within the flux analyses that have been reported and discussed within Chapters 5-9, this analysis will be performed on the data from the baseline case that was obtained at $\phi = -10°$, which is where Figure 5.3 shows the fluxes of vorticity to reach an approximate maximum.

A.1 Velocity and Vorticity

The velocity vectors were calculated from the PIV images by using a direct-correlation analysis to determine a mean displacement of the particles within a small interrogation window–specified as 24 px × 24 px on the final round of calculations, yielding a total of 29,928 vectors–between the two images captured by a camera.

Once all of the pixel displacements have been determined for each of the interrogation windows, the pixel values are converted to millimeters and divided by the time interval separating the image pair.

For example, the x-direction velocity component, U_x, can be defined as:

$$U_x = \frac{M\Delta x}{\Delta t} \tag{A.1}$$

Where M is the magnification ratio (mm/pixels). The total uncertainty in the streamwise velocity can be obtained by taking partial derivatives of U_x with respect to the terms that

www.manaraa.com

will contribute error.

$$\epsilon_{Ux} = \frac{M\epsilon_{\Delta x}}{\Delta t} \tag{A.2}$$

The camera was calibrated using a LaVision type # 20 calibration plate that was placed at the imaging plane. The 2048 × 2048 pixel field of the image was then calibrated to match the "real-world" coordinate system by mapping the recorded image to the "known" standard (the calibration plate) that was located within the imaging plane using a third-order polynomial fit. The root-mean-square (RMS) of the fit was 0.063 pixels which is in the range (less than 0.3) that is considered to be high quality. Based on this high quality data, the literature [48] indicates that the uncertainty in the pixel displacements ($\epsilon_{\Delta x}$, $\epsilon_{\Delta y}$, $\epsilon_{\Delta z}$) can be assumed to be 0.1, 0.1, and 0.3 pixels respectively. Both the uncertainty in the magnification ratio (M) and in the time interval Δt are assumed to be negligible.

The calibration process yielded a magnification ratio of 0.0507 mm/pixel, and a time delay (Δt) of 2500 μs was specified between images during data acquisition. Plugging the reported values into Equation A.2 results in the following uncertainties:

$$\epsilon_{Ux} = \epsilon_{U_y} = 2.03 \ \text{(mm/s)} \tag{A.3}$$

$$\epsilon_{Uz} = 6.08 \ \text{(mm/s)} \tag{A.4}$$

These values characterize the measurement uncertainty of a single velocity vector within a single set of PIV images. However, the velocity and vorticity fields that have been used within this dissertation were obtained by averaging the results of 100 PIV image sets. In order to characterize the total uncertainty of a single velocity vector within the phase-averaged results, the random error associated with the calculation of a single component of

www.manaraa.com

the velocity vector should be added in quadrature with the standard deviation of that vector component obtained over the 100 trials.

The standard deviation in the x-component of the velocity vector (SD_{Ux}) located at point P_1 within the computed velocity field is given by:

$$SD_{Ux} = \sqrt{\frac{1}{N}\sum_{n=1}^{N}\left((U_x)_n - \overline{U}_x\right)^2} \tag{A.5}$$

where N is the total number of trials (i.e. 100), $(U_x)_n$ is the x-component of the velocity vector at point P_1 given by the nth set of PIV images and $\overline{U_x}$ is the x-component of the phase-averaged velocity vector at point P_1 being computed from the 100 trials. It should be noted that from this point forward, the over-bar will be dropped from the phase-averaged velocity vector and all references to the velocity field will be associated with the phase-averaged results.

The total measurement uncertainty in the x-component of the velocity vector at point P_1 can now be found as:

$$\sigma_{Ux} = \sqrt{\epsilon_{Ux}^2 + SD_{Ux}^2}\frac{1}{\sqrt{N}} \tag{A.6}$$

The true value of the x-component of the velocity vector located at any given point within the flow can thus be represented as $U_x \pm \sigma_{Ux}$ at a 65-percent confidence interval.

Figure A.1a presents isocontours of the x-velocity field obtained at $\phi = -10°$ within the baseline case that have been scaled by the free-stream velocity–i.e. contours are of U_x/U_∞. The gray box within this figure identifies the control region used for the flux analysis calculations. By evaluating Equation A.6 at all 29,928 points within the vector field, the total uncertainty of the x-velocity field depicted in Figure A.1a was calculated

www.manaraa.com

and plotted in Figure A.1b as a percent of the free-stream velocity–i.e. contours are of $(100 \times \sigma_{Ux})/U_{\infty}$). Thus, the scaling of the Figures A.1a and A.1b vary by a factor of 100.

Scaled isocontours of the y- and z-velocity fields obtained at $\phi = -10^{\circ}$ within the baseline case have also been plotted within Figures A.2a and A.2c, with the associated uncertainties being represented within Figures A.2b and A.2d.

While Figure A.1b depicts significant uncertainty values within the TEV, the work presented within this dissertation focuses on the control region identified within Figures A.1-A.3 as a gray box. It can be noted that the maximum uncertainty of the x-, y- and z-components of the velocity field within this control region were found to be:

$$\sigma_{Ux-MAX} = 8.47 \ \text{(mm/s)} \tag{A.7}$$

$$\sigma_{Uy-MAX} = 6.16 \ \text{(mm/s)} \tag{A.8}$$

$$\sigma_{Uz-MAX} = 19.7 \ \text{(mm/s)} \tag{A.9}$$

which correspond to approximately 6.54%, 4.76% and 15.2% of free-stream velocity respectively.

The spanwise vorticity component was calculated via a central difference approximation. Using the uncertainties in the velocity components, the uncertainty in the vorticity values at any given point within the flow can be determined by:

$$\sigma_{\omega z} = \sqrt{\frac{\sigma_{U_y}^2}{2X_g^2} + \frac{\sigma_{U_x}^2}{2Y_g^2}} \tag{A.10}$$

where the X_g and Y_g represent the horizontal and vertical vector spacing, both of which are 0.6084 mm (or 12 pixels) within the current case.

www.manaraa.com

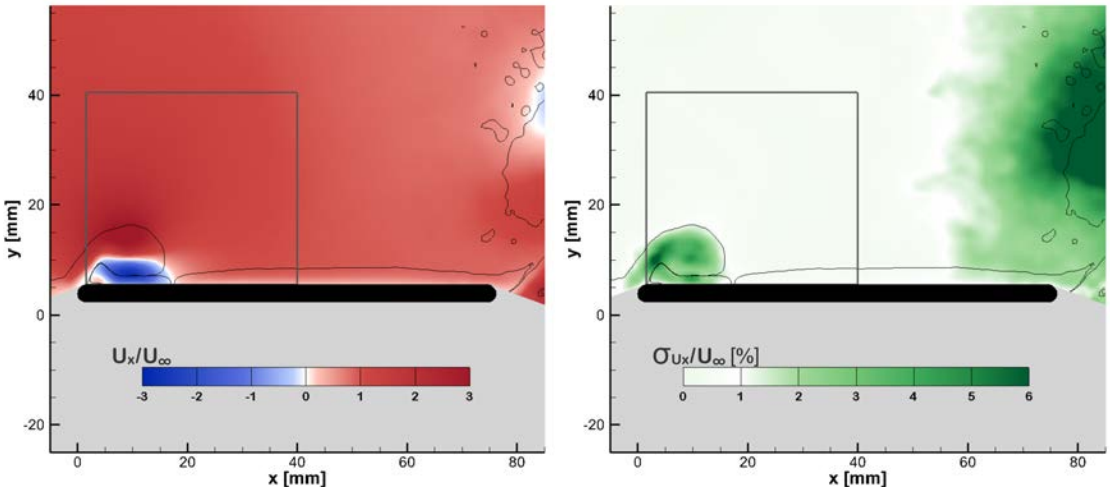

(a) (b)

Figure A.1: (a) Isocontour of the x-velocity field obtained at $\phi = -10°$ within the baseline case (scaled by U_∞) and (b) the associated isocontour showing the total uncertainty of these measurements (scaled by $U_\infty/100$).

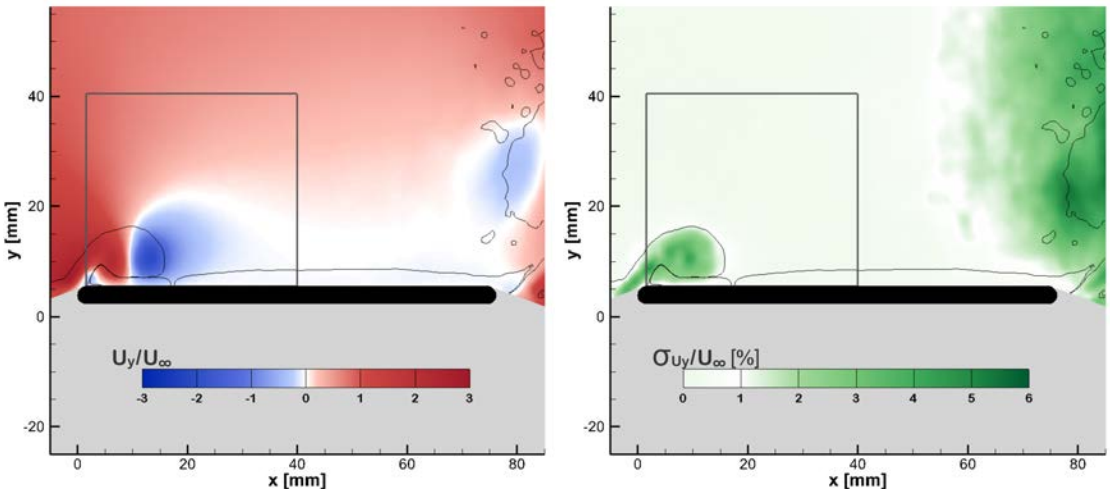

(a) (b)

Figure A.2: (a) Isocontour of the y-velocity field obtained at $\phi = -10°$ within the baseline case (scaled by U_∞) and (b) the associated isocontour showing the total uncertainty of these measurements (scaled by $U_\infty/100$).

www.manaraa.com

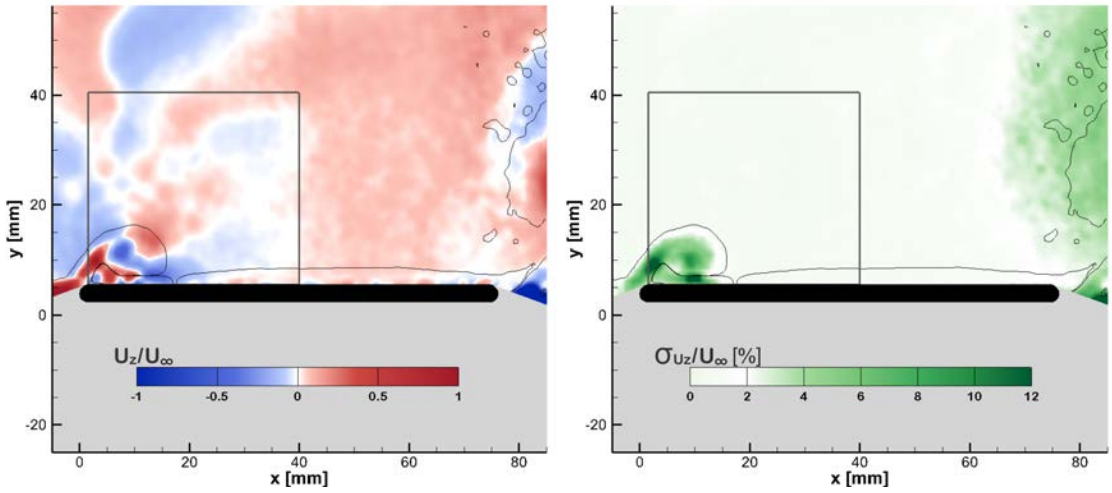

(c) (d)

Figure A.2: (a) Isocontour of the z-velocity field obtained at $\phi = -10°$ within the baseline case (scaled by U_∞) and (b) the associated isocontour showing the total uncertainty of these measurements (scaled by $U_\infty/100$).

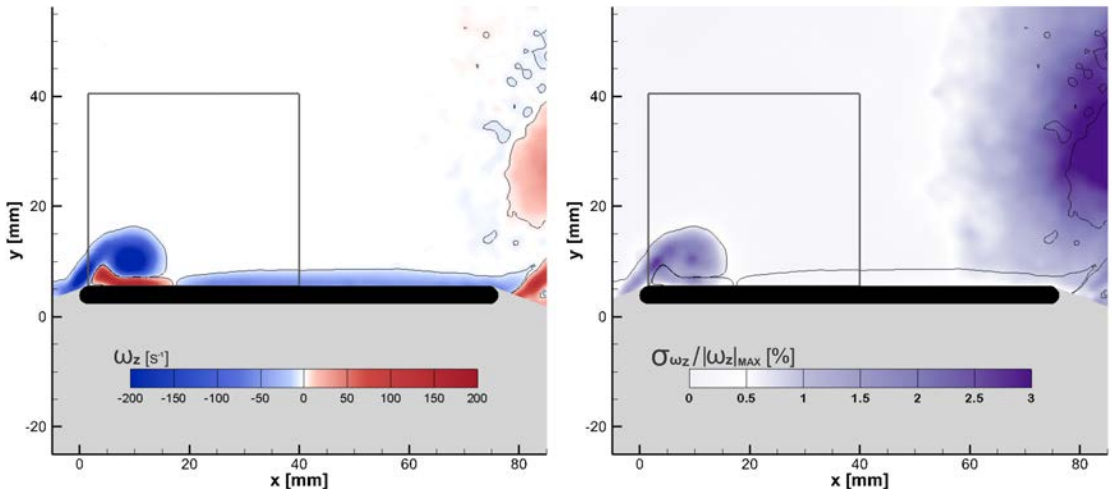

(e) (f)

Figure A.3: (a) Isocontour of the z-vorticity field obtained at $\phi = -10°$ within the baseline case and (b) the associated isocontour showing the total uncertainty of these measurements (presented as a percent of the maximum vorticity magnitude).

www.manaraa.com

Isocontours of the z-vorticity field obtained at $\phi = -10^{\circ}$ within the baseline case are reported in Figure A.3e. The total uncertainty of these measurements is obtained by evaluating Equation A.10 at each point within the vorticity field, the results of which are shown in Figure A.3f as a percentage of the maximum vorticity magnitude measured within the flow. The maximum uncertainty in the spanwise vorticity data calculated within the control region was found to be:

$$\sigma_{\omega z-MAX} = 12.2 \ (\mathrm{s}^{-1}) \tag{A.11}$$

or 2.95% of the maximum vorticity magnitude within the flow.

A.2 LEV Circulation

The circulation of the control region was found by multiplying the z-vorticity data by the differential area element given by $(X_g \cdot Y_g)$ and the summing all of the points within the control region. The total uncertainty of this area integral can be derived by adding the uncertainty from each point in quadrature. Thus, the uncertainty of the circulation calculations can be found as:

$$\sigma_{\Gamma} = X_g Y_g \sqrt{\sum_{m=1}^{M} (\sigma_{\omega z})_m^2} \tag{A.12}$$

where $(\sigma_{\omega z})_m$ is the total uncertainty in the z-component of the vorticity vector located at a point within the control region and M is the total number of points within the control region. Evaluating Equation A.12 for the data obtained at $\phi = -10^{\circ}$ within the baseline case yields:

$$\sigma_{\Gamma} = 41.8 \ (\mathrm{mm}^2/\mathrm{s}) \tag{A.13}$$

www.manaraa.com

which is approximately 0.36% of the total circulation measured within the control region at that phase.

To calculate the time-rate-of-change of the circulation ($d\Gamma/dt$), a finite difference approximation was performed using two sequential values of LEV circulation.

$$\frac{d\Gamma}{dt} = \frac{\Gamma_2 - \Gamma_1}{t_2 - t_1} \tag{A.14}$$

Assuming that the uncertainty in the time difference between two consecutive phases is negligible, the uncertainty in $d\Gamma/dt$ can be found:

$$\sigma_{d\Gamma/dt} = \frac{\sqrt{\sigma_{\Gamma 2}^2 + \sigma_{\Gamma 1}^2}}{t_2 - t_1} \tag{A.15}$$

Using the uncertainties in the circulation values obtained at $\phi = -10°$ and $\phi = -5°$, the uncertainty in the $d\Gamma/dt$ measurement plotted at $\phi = -7.5°$ in Figure 5.4 is found to be:

$$\sigma_{d\Gamma/dt} = 3,630 \ \ (\mathrm{mm}^2/\mathrm{s}^2) \tag{A.16}$$

Figure 5.4 indicates that $d\Gamma/dt \approx 0.04 \ \ \mathrm{m}^2/\mathrm{s}^2$ at $\phi = -7.5°$, meaning A.16 has an error relative to $d\Gamma/dt$ of approximately 9.1%.

A.3 Convection of Vorticity Across Boundaries

As laid out in Section 2.3, the in-plane convective flux is evaluated as:

$$\int_{1-3} \omega_z \, (\vec{u} \cdot \hat{n}) \, d\ell \tag{A.17}$$

The uncertainty in the convective flux through Boundaries 1-3 is found by summing the errors from each point along the boundary in quadrature:

$$\sigma_{Boundary\,1} = \sqrt{\sum_{i=1}^{N_y} \left(\omega_z Y_g \sigma_{Ux}\right)_i^2 + \left(U_x Y_g \sigma_{\omega z}\right)_i^2} \tag{A.18}$$

www.manaraa.com

$$\sigma_{Boundary\,2} = \sqrt{\sum_{j=1}^{N_x} \left(\omega_z X_g \sigma_{Uy}\right)_j^2 + \left(U_y X_g \sigma_{\omega z}\right)_j^2} \tag{A.19}$$

$$\sigma_{Boundary\,3} = \sqrt{\sum_{k=1}^{N_y} \left(\omega_z Y_g \sigma_{Ux}\right)_k^2 + \left(U_x Y_g \sigma_{\omega z}\right)_k^2} \tag{A.20}$$

where i, j and k specify a single point located on Boundaries 1, 2 and 3 respectively, N_y is the total number of points located on Boundaries 1 and 3 and N_x is the total number of points located on Boundary 2. Upon evaluating Equations A.18-A.20 the total uncertainty in the convective flux through the three boundaries comes out to be:

$$\sigma_{Boundary\,1} = 2,800 \ \ (\mathrm{mm}^2/\mathrm{s}^2) \tag{A.21}$$

$$\sigma_{Boundary\,2} = 37.9 \ \ (\mathrm{mm}^2/\mathrm{s}^2) \tag{A.22}$$

$$\sigma_{Boundary\,3} = 521 \ \ (\mathrm{mm}^2/\mathrm{s}^2) \tag{A.23}$$

A.4 Diffusive Flux

Within this dissertation, the diffusive flux was characterized using the following:

$$\text{Diffusive} = \frac{1}{\rho}\int_4 \frac{\partial p}{\partial x} dx \tag{A.24}$$

Which can be physically calculated as:

$$\text{Diffusive} = \frac{1}{\rho}\left(p_b - p_a\right) \tag{A.25}$$

where p_a and p_b are the pressures on the surface of the airfoil at the start and end of the control region respectively. Assuming that the total uncertainty in the pressure data is the same at both points ($\sigma_p = 0.84$ Pa), the total uncertainty in the diffusive flux can be calculated as:

$$\sigma_{Diffusive} = \frac{\sigma_p}{\rho\sqrt{2}} \tag{A.26}$$

www.manaraa.com

$$\sigma_{Diffusive} = 595 \ (\mathrm{mm}^2/\mathrm{s}^2) \tag{A.27}$$

which is approximately 0.17% of the maximum diffusive flux.

www.manaraa.com

REFERENCES

[1] M. Acharya and M. H. Metwally. Unsteady pressure field and vorticity production over a pitching airfoil. *AIAA J.*, 30(2):403–411, 1992.

[2] T. Akiyama. Pressure estimation from oscillatory signals obtained through bwr's instrument lines. *Journal of Dynamic Systems , Measurement, and Control*, 108:80–85, March 1986.

[3] J. M. Akkala. Flow structure and performance of a flexible plunging airfoil. Master's thesis, University of Iowa, 2013.

[4] J. M. Akkala, A. Eslam Panah, and J. H. J. Buchholz. Vortex dynamics and performance of flexible and rigid plunging airfoils. *J. Fluid Eng.*, 54:103–121, April 2015.

[5] A. M. Al-Garni and A. Z. Sahin. Flow control for an airfoil with leading-edge rotation: An experimental study. 37(4):617–622, 2000.

[6] M. Amitay, A. Honohan, M. Trautman, and A. Glezer. Modification of the aerodynamic characteristics of bluff bodies using fluidic actuators. 1997. AIAA Paper 97-2004.

[7] J.-Z. Wu an Y.-T. Yan, Y.-B. Luo, and C. Pozrikidis. Fluid kinematics on a deformable surface. *J. Fluid Mech.*, 541:371–381, 2005.

[8] J. M. Anderson, K. Streitlien, D. S. Barrett, and M. S. Triantafyllou. Oscillating foils of high propulsive efficiency. *J. Fluid Mech.*, 360:41–72, 1998.

[9] J. Andreopoulos and J.H. Agui. Wall-vorticity flux dynamics in a two-dimensional turbulent boundary layer. *J. Fluid Mech.*, 309:45–84, 1996.

[10] Y.S. Baik, L.P. Bernal, K. Granlund, and M.V. Ol. Unsteady force generation and vortex dynamics of pitching and plunging aerofoils. *J. Fluid Mech.*, 709:37–68, 2012.

[11] S. M. Batil and J. V. Nebres. Application of digital filtering techniques to unsteady pressure measurements. In *29th AIAA Aerospace Sciences Meeting*, Reno, NV, January 1991. AIAA Paper 91-0061.

[12] H. R. Beem, D. E. Rival, and M. S. Triantafyllou. On the stabilization of leading-edge vortices with spanwise flow. *Expts. Fluids*, 52:511–517, 2012.

www.manaraa.com

[13] J. M. Birch and M. H. Dickinson. Spanwise flow and the attachment of the leading-edge vortex on insect wings. 412:729–733, 2001.

[14] R. J. Bomphrey, N. J. Lawson, N. J. Harding, G. K. Taylor, and A. L. R. Thomas. The aerodynamics of manduca sexta: Digital particle image velocimetry analysis of the leading edge vortex. *J. Exp. Biol.*, 208:1079–1094, 2005.

[15] I. Borazjani and M. Daghooghi. The fish tail motion forms and attached leading edge vortex. *Proc. R. Soc. B*, 280, 2013.

[16] M. Brons, M. C. Thompson, T. Leweke, and K. Hourigan. Vorticity generation and conservation for two-dimensional interfaces and boundaries. *J. Fluid Mech.*, 758:63–93, 2014.

[17] S. L. Brunton and C. W. Rowley. Modeling the unsteady aerodynamic forces on small-scale wings. In *47th AIAA Aerospace Sciences Meeting*, January 2009. AIAA Paper 2009-1127.

[18] J. H. J. Buchholz, M. A. Green, and A. J. Smits. Scaling the circulation shed by a pitching panel. *J. Fluid Mech.*, 688:591–601, 2011.

[19] D. E. Calderon, Z. Wang, I. Gursul, and M. R. Visbal. Volumetric measurements and simulations of the vortex structures generated by low aspect ratio plunging wings.

[20] D. E. Calderon, Z. Wang, I. Gursul, and M. R. Visbal. Volumetric measurements and simulations of the vortex structures generated by low aspect ratio plunging wings. In *50th AIAA Aerospace Sciences Meeting*, Nashville, TN, January 2012. AIAA Paper 2012-0914.

[21] J. F. Campbell. Effects of spanwise blowing on the pressure field an vortex-lift characteristics of a 44° swept trapezoidal wing. Technical Report NASA TN D-7907, Langley Research Center, Hampton, VA, June 1975.

[22] Z. Carr, C. Chen, and M. J. Ringuette. The effect of aspect ratio on the three-dimensional vortex formation of rotating flat-plate wings. In *50th AIAA Aerospace Sciences Meeting including the New Horizons Forum and Aerospace Exposition*, Nashville, Tennessee, 9–12 January 2012. AIAA Paper 2012-912.

[23] M. S. Chandrasekhara and M. C. Wilder. Unsteady stall control using dynamically deforming airfoils. *AIAA J.*, 36(10), 1998.

[24] M. S. Chandrasekhara, M. C. Wilder, and L. W . Carr. Compressible dynamic stall control using a shape adaptive airfoil. 1999. AIAA Paper 99-16516.

www.manaraa.com

[25] B. Cheng, S. Sane, G. Barbera, D. Troolin, T. Strand, and X. Deng. Three-dimensional flow visualization and vorticity dynamics in revolving wings. *Expts. Fluids*, 54, 2013.

[26] J. Choi, T. Colonius, and D. R. Williams. Surging and plunging oscillations of an airfoil at low reynolds number. *J. Fluid Mech.*, 763:237–253, 2015.

[27] D. J. Cleaver, Z. Wang, and I. Gursul. Oscillating flexible wings at low reynolds numbers. In *51st AIAA Aerospace Sciences Meeting*, Dallas, TX, January 2013. AIAA Paper 2013-0674.

[28] R. N. Conger and B. R. Ramaprian. Correcting for response lag in unsteady pressure measurements in water. *J. Fluid and Struct.*, 115:676–679, December 1993.

[29] R. N. Conger and B. R. Ramaprian. Pressure measurements on a pitching airfoil in a water channel. *AIAA J.*, 32(1):108–115, 1994.

[30] L. F. Crabtree. The formation of regions of separated flow on wing surfaces. Technical Report R&M 3122, Aeronautical Research Council, 1959.

[31] P. Czop. Application of an inverse data-driven model for reconstructiong wheel movement signals. *Metrol. Meas. Syst.*, 18(3):491–500, 2011.

[32] N. Didden. On the formation of vortex rings: Rolling-up and production of circulation. *J. Applied Math. and Physics*, 30:101–116, 1979.

[33] T. L. Doligalski, C. R. Smith, and J. D. A. Walker. Vortex interactions with walls. *Annu. Rev. Fluid Mech.*, 26:573–616, 1994.

[34] C. P. Ellington, C. van den Berg, A. P. Willmott, and A. L. R. Thomas. Leading-edge vortices in insect flight. *Nature*, 384:626–630, 1996.

[35] A. Eslam Panah and J. H. J. Buchholz. Parameter dependence of vortex interactions on a two-dimensional plunging plate. *Expts. Fluids*, 55(3):1687, 2014.

[36] P. Freymuth. Flow visualization in fluid mechanics. 64(1):1–18, 1993.

[37] R. Garmann, M. Visbal, and P. Orkwis. Three-dimensional flow structure and aerodynamic loading on a low aspect ratio, revolving wing. In *42nd AIAA Fluid Dynamics Conference and Exhibit*, New Orleans, Louisiana, 2012. AIAA Paper 2012-3277.

[38] M. Ghil, J.G. Liu, C. Wang, and S. Wang. Boundary-layer separation and adverse pressure gradient for 2-d viscous incompressible flow. *Physica D.*, (197):149–173, 2004.

www.manaraa.com

[39] A. Glezer. Some aspects of aerodynamic flow control using synthetic-jet actuation. *Phil. Trans. R. Soc. A.*, 369:1476–1494, 2011.

[40] M. Goodarzi, M. Rahimi, and R. Fereidouni. Investigation of active flow control over naca0015 airfoil via blowing. *Int. J. Aero. Sci., Year = 2012, Number = 4, Pages = 57–63, Volume = 1.*

[41] L. Graftieaux, M. Michard, and N. Grosjean. Combining PIV, POD and vortex identification algorithms for the study of unsteady turbulent swirling flows. *Meas. Sci. Tech.*, 12(9):1422–1429, 2001.

[42] K. Granlund, M. V. OL, and L. P. Bernal. Experiments on pitching plates: Force and flowfield measurements at low reynolds numbers. In *49th AIAA Aerospace Sciences Meeting*, Orlando, FL, January 2011. AIAA Paper 2011-872.

[43] D. Greenblatt, J. Kiedaisch, and H. Nagib. Unsteady-pressure corrections in highly attenuated measurements at moderate mach numbers. In *31st AIAA Fluid Dynamics Conference & Exhibit*, Anaheim, CA, June 2001. AIAA Paper 2001-2983.

[44] P.W. Hammerton and E.J. Kerschen. Leading-edge receptivity for bodies with mean aerodynamic loading. *J. Fluid Mech.*, 535:1–32, 2005.

[45] K. D. Hipp, S. I. Benton, M. M. Walker, and J. P. Bons. Parametric optimization of control for a post-stall airfoil using pulsed jets. In *53rd AIAA Aerospace Sciences Meeting*, Kissimmee, FL, January 2015. AIAA Paper 2015-1268.

[46] A. Hondan and J. Andreopoulos. Instantaneous three-dimensional vorticity measurements in vortical flow over a delta wing. *AIAA J.*, 35(10):1612–1620, 1997.

[47] H. P. Horton. *Laminar Separation Bubbles in Two and Three Dimensional Incompressible Flow*. PhD thesis, Queen Mary College, 1968.

[48] H. Huang, D. Dabiri, and M. Gharib. On errors of digital particle image velocimetry. *Meas. Sci. Tech.*, 8:1427–1440, 1997.

[49] A. S. Iberall. Attenuation of oscillatory pressures in instrument lines. *J. Reseach of the National Bureau of Standards*, 45:85–108, July 1950.

[50] M. V. Jain, J. G. Wong, and D. E. Rival. Investigation of vortex development on accelerating spanwise-flexible wings. *J. Fluid Eng.*, 53:466–478, 2015.

[51] R. Jantzen, K. Taira, K. Granlund, and M. Ol. Vortex dynamics around pitching plates. *Phys. Fluids*, 26, 2014. Art. 053606.

www.manaraa.com

[52] A. R. Jones and H. Babinsky. Reynolds number effects on leading edge vortex development on a waving wing. *Expts. Fluids*, 51:197–210, 2011.

[53] H.Y. Ma J.Z. Wu and M.D. Zhou. *Vorticity and Vortex Dynamics*. Springer, 2007.

[54] C.-K. Kang, H. Aono, Y.S. Baik, L.P. Bernal, and W. Shyy. Fluid dynamics of pitching and plunging flat plate at intermediate reynolds numbers. *AIAA J.*, 51(2), 2013.

[55] C. K. Kang, H. Aono, C. E. S. Cesnik, and W. Shyy. Effects of flexibility on the aerodynamic performance of flapping wings. *J. Fluid Mech.*, 689:32–74, 2011.

[56] M. A. Karim and M. Acharya. Control of the dynamic-stall vortex over a pitching airfoil by leading-edge suction. In *AIAA Shear Flow Conference*, Orlando, FL, 1993. AIAA Paper 93-3267.

[57] J. Kiedaisch and M. Acharya. Investigation of incipient dynamic stall over pitching airfoils using hot-film sensors. In *35th AIAA Aerospace Science Meeting & Exhibit*, Reno, Nevada, 1997. AIAA Paper 97-0656.

[58] D. Kim and M. Gharib. Experimental study of three-dimensional vortex structures in translating and rotating plates. *Expts. Fluids*, 49:329–339, 2010.

[59] D. Kim and M. Gharib. Flexibility effects on vortex formation of translating plates. *J. Fluid Mech.*, 677:255–271, 2011.

[60] M. M. Koochesfahani. Vortical patterns in the wake of an oscillating airfoil. *AIAA J.*, 27(9):1200–1205, 1989.

[61] J. Kriegseis, M. Kinzel, and D. Rival. On the persistence of memory: do initial conditions impact vortex formation? *J. Fluid Mech.*, 736:91–106, 2013.

[62] D. Kuchemann. Report on iutam symposium on concentrated vortex motion in fluids. *J. Fluid Mech.*, 21:1–20, 1965.

[63] C.H. Kuo and J.K. Hsieh. Unsteady flow structure and vorticity convection over the airfoil oscillating at high reduced frequency. *Exp. Therm. and Fluid Science*, 24:117–129, 2001.

[64] J. C. S. Lai and M. F. Platzer. Jet characteristics of a plunging airfoil. *AIAA J.*, 37(12):1529–1537, 1999.

[65] J.J. Lee, C.T. Hsieh, C. Chang, and C.C. Chu. Vorticity forces on an impulsively started finite plate. *J. Fluid Mech.*, 694:464–492, 2012.

www.manaraa.com

[66] T. Lee and Y.Y. Su. Surface pressures developed on an airfoil undergoing heaving and pitching motion. *J. Fluid and Struct.*, 137, 2015.

[67] G. C. Lewin and H. Haj-Hariri. Modelling thrust generation of a two-dimensional heaving airfoil in a viscous flow. *J. Fluid Mech.*, 492:339–362, 2003.

[68] M. J. Lighthill. Introduction. boundary layer theory. In L. Rosenhead, editor, *Laminar boundary Layers*, pages 46–113. Oxford University Press, London, 1963.

[69] T. T. Lim, C. J. Teo, K. B. Lua, and K. S. Yeo. On the prolong attachment of leading edge vortex on a flapping wing. *Mod. Phys. Lett. B*, 23(3):357–360, 2009.

[70] K. B. Lua, T. T. Lim, K. S. Yeo, and G. Y. Oo. Wake-structure formation of a heaving two-dimensional elliptic airfoil. *AIAA J.*, 45(7):1571–1583, 2007.

[71] K. W. Mangler and J. H. B. Smith. A theory of the flow past a slender delta wing with leading edge separation. *P. Roy. Soc. Lond. A Mat.*, 251(1265):200–217, 1959.

[72] G. Z. McGowan, K. Granlund, M. Ol, A. Gopalarathnam, and J. R. Edwards. Investigations of lift-based pitch-plunge equivalence for airfoils at low reynolds numbers. *AIAA J.*, 49(7):1511–1524, 2011.

[73] M. Milano and M. Gharib. Uncovering the physics of flapping flat plates with artificial evolution. *J. Fluid Mech.*, 534:403–409, 2005.

[74] A. Mitchell, S. Morton, J. Forsythe, and R. Cummings. The effect of aspect ratio on the three-dimensional vortex formation of rotating flat-plate wings. In *32nd AIAA Fluid Dynamics Conference and Exhibit*, St. Louis, MO, 24–26 June 2002. AIAA Paper 2002-2968.

[75] V. J. Modi, S. R. Munshi, G. Bandyopadhyay, and T. Yokomizo. High-performance airfoil with moving surface boundary-layer control. 35(4):544–553, 1998.

[76] M. Molki and N. Sattari. Vortex generation in low-speed flow over an oscillating and deforming arc airfoil. *J. Fluids Eng.*, 135, 2013.

[77] B. R. Morton. The generation and decay of vorticity. 28:277–308, 1984.

[78] F. T. Muijres, L. C. Johansson, R. Barfield, M. Wolf, G. R. Spedding, and A. Hedenstrom. Leading-edge vortex improves lift in slow-flying bats. *Science*, 319:1250–1253, 2008.

[79] A. Nassirharand and H. Karimi. Closed-form solution for design of lead-lag compensators. *International Journal of Electrical Engineerings Education*, 41(2):172–180, 2004.

www.manaraa.com

[80] R. C. Nelson and A. Pelletier. The unsteady aerodynamics of slender wings and aircraft undergoing large amplitude maneuvers. *Progress in Aerospace Sciences*, 39:185–248, 2003.

[81] H. G. Nepomuceno and R. M. Lueptow. Pressure and shear stress measurements at the wall in a turbulent boundary layer on a cylinder. *Phys. Fluids*, 9(9):2732–2739, 1997.

[82] M. Ol. The high-frequency, high-amplitude pitch problem: Airfoils, plates and wings. 2009. AIAA Paper 2009-3686.

[83] M. V. Ol, L. Bernal, C.-K. Kang, and W. Shyy. Shallow and deep dynamic stall for flapping low reynolds number airfoils. *Expts. Fluids*, 46:883–901, 2009.

[84] A. Eslam Panah. *Flow Structure and Vorticity Transport on a Plunging Wing*. PhD thesis, University of Iowa, 2014.

[85] A. Eslam Panah, J.M. Akkala, and J.H.J. Buchholz. Vorticity transport and the leading-edge vortex of a plunging airfoil. *Expts. Fluids*, 2015. in review.

[86] J. Panda and K. B. M. Q. Zaman. Experimental investigation of the flow field of an oscillating airfoil and estimation of lift from wake surveys. *J. Fluid Mech.*, 265:65–95, 1994.

[87] A. Patterson, P. Rymarz, and B. R. Ramaprian. Surface pressure measurements on a pitching swept wing in a water channel. *AIAA J.*, 33(10):1871–1879, 1995.

[88] C. W. Pitt Ford and H. Babinsky. Lift and the leading edge vortex. In *50th AIAA Aerospace Sciences Meeting*, Nashville, TN, January 2012. AIAA Paper 2012-911.

[89] E. Polhamus. Application of the leading-edge-suction analogy of vortex lift to the drag due to lift of sharp-edge delta wings. Technical Report NASA TN D-4739, Langley Research Center, Hampton, VA, August 1968.

[90] L. R. Pujara. A computer aided multivariable control systems design technique with application to aircraft flying qualitiesl. Report WRDC-TR-90-3069, Wright Laboratory, 1991.

[91] K. Ramesh, A. Gopalarathnam, K. Granlund, M. Ol, and J. Edwards. Discrete-vortex method with novel shedding criterion for unsteady aerofoil flows with intermittent leading-edge vortex shedding. *J. Fluid Mech.*, 751:500–538, 2014.

[92] D. Rival, J. Kriegseis, P. Schaub, A. Windmann, and C. Tropea. A criterion for

www.manaraa.com

vortex separation on unsteady aerodynamic profiles. January 2013. AIAA Paper 2013-0836.

[93] D. Rival, T. Prangemeier, and C. Tropea. The influence of airfoil kinematics on the formation of leading-edge vortices in bio-inspired flight. *Expts. Fluids*, 46:823–833, 2009.

[94] D. Rockwell. Vortex-body interactions. *Annu. Rev. Fluid Mech.*, 30:199–229, 1998.

[95] D. M. Sharma and K. Poddar. Investigation on quasi-steady characteristics for an airfoil oscillating at low reduced frequencies. *Int. J. of Aero. Eng.*, 2010.

[96] C. Shih and C.M. Ho. Vorticity balance and time scales of a two-dimensional airfoil in an unsteady free stream. *Phys. Fluids*, 6, 1994.

[97] W. Shyy, H. Aono, S. K. Chimakurthi, P. Trizila, C. K. Kang, C. E. S. Cesnik, and H. Liu. Recent progress in flapping wing aerodynamics and aeroelasticity. *Prog. Aerosp. Sci.*, 46:284–327, 2010.

[98] W. Shyy, P. Trizilla, C. k. Kang, and H. Aono. Can tip vortices enhance lift of a flapping wing? *AIAA J.*, 47(2):289–293, 2009.

[99] K. Taira and T. Colonius. Three-dimensional flows around low-aspect-ratio flat-plate wings at low reynolds numbers. *J. Fluid Mech.*, 623:187–207, 2009.

[100] I. Tani. Low-speed flows involving bubble separations. *Progress in Aerospace Sciences*, 5:70–103, 1964.

[101] G. K. Taylor, R. L. Nudds, and A. L. R. Thomas. Flying and swimming animals cruise at a strouhal number tuned for high power efficiency. 425:707–711, 2003.

[102] T. Theodorsen. General theory of aerodynamic instability and the mechanism of flutter. Report 496, NACA, 1935.

[103] G. S. Triantafyllou, M. S. Triantafyllou, and M. A. Grosenbaugh. Optimal thrust development in oscillating foils with application to fish propulsion. 7:205–224, 1993.

[104] M. S. Triantafyllou, G. S. Triantafyllou, and R. Gopalkrishnan. Wake mechanics for thrust generation in oscillating foils. 3(12):2835–2837, 1991.

[105] P. Trizila, C. K. Kang, H. Aono, W. Shyy, and M. Visbal. Low-reynolds-number aerodynamics of a flapping rigid flat plate. *AIAA J.*, 49:806–823, 2011.

[106] L.L. van Dommelen and S.F. Shen. The spontaneous generation of the singularity in a separating laminar boundary layer. *J. Comp. Phys.*, 38:125–140, 1980.

www.manaraa.com

[107] M. Visbal, T. O. Yilmaz, and D. Rockwell. Three-dimensional vortex formation on a heaving low-aspect-ratio wing: Computations and experiments. *JFS*, 38:58–76, January 2013.

[108] M. R. Visbal. High-fidelity simulation of transitional flows past a plunging airfoil. *AIAA J.*, 47(11):2685–2697, 2009.

[109] M. R. Visbal. Flow structure and unsteady loading over a pitching and perching low-aspect-ratio wing. In *42nd AIAA Fluid Dynamics Conference.*, New Orleans, Louisiana, 2012. AIAA Paper 2012-3279.

[110] M. R. Visbal. Analysis of the onset of dynamic stall using high-fidelity large-eddy simulations. In *52nd AIAA Aerospace Sciences Meeting.*, National Harbor, MD, 2014. AIAA Paper 2014-0591.

[111] M. R. Visbal and J. S. Shang. Investigation of the flow structure around a rapidly pitching airfoil. *AIAA J.*, 27(8):1044–1051, 1989.

[112] C. Wang and J. D. Eldredge. Low-order phenomenological modeling of leading-edge vortex formation. *Theo. Comp. Fluid Dyn.*, 27:577–598, 2013.

[113] D. R. Warrick, B. W. Tobalske, and D. R. Powers. Lift production in the hovering hummingbird. *Proc. R. Soc. B*, 276:3747–3752, 2009.

[114] M. S. Wibawa, S. C. Steele, J. M. Dahl, D. E. Rival, G. D. Weymouth, and M. S. Triantafyllou. Global vorticity shedding for a vanishing wing. *J. Fluid Mech.*, 695:112–134, 2012.

[115] A. Widmann and C. Tropea. Parameters influencing vortex growth and detachment on unsteady aerodynamic profiles. *J. Fluid Mech.*, 773:432–459, 2015.

[116] C. J. Wojcik. The dynamics of spanwise vorticity on a rotating flat plate in a starting motion. Master's thesis, University of Iowa, 2012.

[117] C. J. Wojcik and J. H. J. Buchholz. Parameter variation and the leading-edge vortex of a rotating flat plate. *AIAA J.*, 52(2):348–357, 2014.

[118] C. J. Wojcik and J. H. J. Buchholz. Vorticity transport in the leading-edge vortex on a rotating blade. *J. Fluid Mech.*, 743:249–261, 2014.

[119] C. Wong and K. Kontis. Flow control by spanwise blowing on a naca 0012. 44(1):338–340, 2007.

www.manaraa.com

[120] J. G. Wong, J. Kriegseis, and D. E. Rival. An investigation into vortex growth and stabilization for two-dimensional plunging and flapping plates with varying sweep. *J. Fluid Eng.*, 43:231–243, 2013.

[121] C.J. Wu, L. Wang, and J.Z. Wu. Suppression of the von karman vortex street behind a circular cylinder by a traveling wave generated by a flexible surface. *J. Fluid Mech.*, 574:365–391, 2007.

[122] J. Wu and J. Wu. Boundary vorticity dynamics since lighthill's 1963 article: Review and development. *Theo. Comp. Fluid Dyn.*, pages 459–474, 1998.

[123] J. Z. Wu, X. H. Wu, and J. M. Wu. Streaming vorticity flux from oscillating walls with finite amplitude. *Phys. Fluids*, 5(8):1933–1938, 1993.

[124] Jiezhi Wu, Xiyun Lu, Yantao Yang, and Rikui Zhang. Vorticity dynamics in complex flow diagnosis and management. In *13th Asian Congress of Fluid Mechanics*, Dhaka, Bangladesh, December 2010.

[125] J.Z. Wu, R.L. Roach, C.F. Lo, F.L. Zhu, R. M. Dowgwillo, L.B. Jiang, and R.W. Tramel. Aerodynamic diagnostics and design based on boundary vorticity dynamicsl. In *17th AIAA Applied Aerodynamics Conference*, Norfolk, Virginia, June-July 1999. AIAA 99-3103.

[126] J.Z. Wu and J.M. Wu. Interactions between a solid surface and a viscous compressible flow field. *J. Fluid Mech.*, 254:183–211, 1993.

[127] K. Yamamoto and O. Inoue. Application of genetic algorithm to aerodynamic shape optimization. 1995. AIAA Paper 95-1650.

[128] J. Yen and N. A. Ahmed. Parametric study of dynamic stall flow field with synthetic jet actuation. *J. Fluid and Struct.*, 134, 2012.

[129] T. Yilmaz, M. Ol, and D. Rockwell. Scaling of flow separation on a pitching low aspect ratio plate. 26:1034–1041, 2010.

[130] T. Yilmaz and D. Rockwell. Three-dimensional flow structure on a maneuvering wing. *Expts. Fluids*, 48:539–544, 2010.

[131] M. L. Yu, H. Hu, and Z. J. Wang. Experimental and numerical investigations on the asymmetric wake vortex structures around an oscillating airfoil. In *50th AIAA Aerospace Sciences Meeting*, Nashville, TN, January 2012. AIAA Paper 2012-0299.

[132] M. Y. Zakaria, D. A. Pereira, S. Ragab, M. R. Hajj, and F. D. Marques. An experimental study of added mass on a plunging airfoil oscillating with high frequencies

www.manaraa.com

at high angles of attack. In *33rd AIAA Applied Aerodynamics Conference*, Dallas, TX, June 2015. AIAA Paper 2015-3166.

[133] H. Zhao, J.-Z. Wu, and J.-S. Luo. Turbulent drag reduction by traveling wave of flexible wall. *Fluid Dyn. Res.*, 34:175–198, 2004.

[134] Y. Zhuang, X. Sun, D. Huang, and G. Wu. Numerical study on aerodynamic performances of the wind turbine rotor with leading-edge rotation. *J. Renewable Sustainable Energy*, 4, 2012.

www.manaraa.com